DOE Award Number:	DE-FG26-05NT42545
Report Title:	New Adsorption Cycles for Carbon Dioxide Capture and Concentration
Principal Author:	James A. Ritter (PI) with Armin D. Ebner (co-PI), Steven P. Reynolds (PhD granted), Hai Du (PhD candidate) and Amal Mehrotra (PhD candidate)
Report Type:	Final Report
Reporting Period Start Date:	August 1, 2005
Reporting Period End Date:	July 31, 2008
Report Issue Data:	May 14, 2009
Organization:	University of South Carolina, Department of Chemical Engineering, Columbia, SC 29208

ABSTRACT

The objective of this three-year project was to study new pressure swing adsorption (PSA) cycles for CO_2 capture and concentration at high temperature. The heavy reflux (HR) PSA concept and the use of a hydrotalcite like (HTlc) adsorbent that captures CO_2 reversibly at high temperatures simply by changing the pressure were two key features of these new PSA cycles. Through the completion or initiation of nine tasks, a bench-scale experimental and theoretical program has been carried out to complement and extend the process simulation study that was carried out during Phase I (DE-FG26-03NT41799). This final report covers the entire project from August 1, 2005 to July 31, 2008.

This program included the study of PSA cycles for CO_2 capture by both rigorous numerical simulation and equilibrium theory analysis. The insight gained from these studies was invaluable toward the applicability of PSA for CO_2 capture, whether done at ambient or high temperature. The rigorous numerical simulation studies showed that it is indeed possible to capture and concentrate CO_2 by PSA. Over a wide range of conditions it was possible to achieve greater than 90% CO_2 purity and/or greater than 90% CO_2 recovery, depending on the particular heavy reflux (HR) PSA cycle under consideration. Three HR PSA cycles were identified as viable candidates for further study experimentally. The equilibrium theory analysis, which represents the upper thermodynamic limit of the performance of PSA process, further validated the use of certain HR PSA cycles for CO_2 capture and concentration.

A new graphical approach for complex PSA cycle scheduling was also developed during the course of this program. This new methodology involves *a priori* specifying the cycle steps, their sequence, and the number of beds, and then following a systematic procedure that requires filling in a 2-D grid based on a few simple rules, some heuristics and some experience. It has been tested successfully against several cycle schedules taken from the literature, including a 2-bed 4-step Skarstrom cycle, a 4-bed 9-step process with 2 equalization steps, a 9-bed 11-step process with 3 equalization steps, and a 6-bed 13-step process with 4 equalization steps and 4 idle steps. With respect to CO_2 capture and concentration by PSA, this new approach is now providing a very straightforward way to determine all the viable 3-bed, 4-bed, 5-bed, n-bed, etc. HR PSA cycle schedules to explore using both simulation and experimentation.

This program also touted the use of K-promoted HTlc as a high temperature, reversible adsorbent for CO_2 capture by PSA. This program not only showed how to use this material in HR PSA cycles, but it also proposed a new CO_2 interaction mechanism in conjunction with a non-equilibrium kinetic model that adequately describes the uptake and release of CO_2 in this material, and some preliminary fixed bed adsorption breakthrough and desorption elution experiments were carried out to demonstrate complete reversibility on a larger scale. This information was essentially missing from the literature and deemed invaluable toward promoting the use of K-promoted HTlc as a high temperature, reversible adsorbent for CO_2 capture by PSA.

Overall, the objectives of this project were met. It showed the feasibility of using K-promoted hydrotalcite (HTlc) as a high temperature, reversible adsorbent for CO_2 capture by PSA. It discovered some novel HR PSA cycles that might be useful for this purpose. Finally, it revealed a mechanistic understanding of the interaction of CO_2 with K-promoted HTlc.

TABLE OF CONTENTS

1.0 Overview: Global Warming and CO_2 Capture, and Overall Objectives

It is now generally accepted by most climate scientists that increasing global temperatures over the last 50 years are the result of increased atmospheric concentrations of greenhouse gases such as methane (CH_4), nitrous oxide (N_2O) and, most especially, carbon dioxide (CO_2). Since the beginning of the industrial revolution, atmospheric concentrations of CO_2 have increased nearly 30%, CH_4 concentrations have more than doubled, and N_2O concentrations have risen by about 15%. These increases have enhanced the heat-trapping capability of the earth's atmosphere via the greenhouse effect. Predictions of global energy use in the next century suggest a continued increase in carbon emissions and rising concentrations of CO_2 in the atmosphere unless major changes are made in the way humans produce and use energy, in particular how humans manage carbon (Reichle et al., 1999).

There are three courses of action that can be taken to stabilize the CO_2 concentration in the atmosphere. The first approach is increased efficiency of primary energy conversion. This will decrease the amount of fossil fuels needed to provide the same energy service. The second approach is to use lower-carbon or carbon-free energy sources, with the obvious outcomes of less or no CO_2 production. The final approach is carbon sequestration, which involves the capture and storage of carbon. This last approach is probably the newest means being studied to manage CO_2 in the environment (White et al., 2003).

A considerable effort is underway worldwide to curb CO_2 emissions from coal fired and other fossil fuel based power plants, because these plants are responsible for over 40% of the carbon dioxide emissions in the USA alone (Ebner and Ritter, 2007). The goal is to capture CO_2 from stack or flue gas, concentrate it to around 90 to 95 vol%, and sequester it somewhere in the Earth. The most likely options for CO_2 separation and capture include (1) chemical and physical absorption, (2) physical and chemical adsorption, (3) low-temperature distillation, and (4) gas separation membranes. Among these, physical absorption using amines is currently the most widely deployed commercial technology; however, there is a significant energy penalty associated with this technology from the heat required to regenerate the solvent. Cryogenic distillation is certainly feasible and widely practiced for CO_2 recovery; but, it is only viable for CO_2 concentrations higher that 90 vol%, which is outside the range for flue gas streams. Polymeric, ceramic and metallic membranes are all viable for CO_2 recovery from flue gas streams; however, they each have their own issues involving low fluxes, degradation, fouling, cost, etc. Various adsorption processes for concentrating CO_2 from flue gas streams have also been proposed and explored, with many of the results being controversial (IEA, 1994; White et al., 2003).

An International Energy Agency (IEA, 1994) study evaluated CO_2 separation and capture using 13X zeolite in both pressure swing adsorption (PSA) and temperature swing adsorption (TSA) processes. They concluded that PSA and TSA are too energy intensive for use with gas- and coal-fired power systems. But little information was offered in the IEA study on the type of cycle employed. Nevertheless, this conclusion has led others to extrapolate these findings and further conclude that adsorption systems, in general, are not applicable for CO_2 separation and capture. It is strongly suggested that this may not be the case. It is true that the commonly studied adsorbents (e.g., zeolites and activated carbons), which have a very high capacity for

CO_2 at ambient temperatures, suffer from low CO_2 capacity at elevated temperatures (Yong et al., 2002). It is also true that it may be too costly to pre-dry, cool and/or pressurize the feed and/or purge streams, which appears to be the basis for the pessimistic conclusions made in the IEA study about adsorption technology. This has not stopped research on ambient temperature CO_2 capture by PSA, however, as evidenced by some recent studies (Gomes and Yee, 2002; Ko et al., 2003). Moreover, there are some new adsorbents, generally referred to as hydrotalcite-like compounds (HTlcs), that are selective to CO_2 at elevated temperatures, even in the presence of H_2O; and they release CO_2 simply by decreasing the pressure (Yong et al., 2002). Hence, HTlc may be a viable adsorbent for use in a high temperature PSA process for CO_2 capture.

HTlcs are anionic clays consisting of positively charged layers of metal oxides (or metal hydroxides) with inter-layers of anions, such as carbonate (Yong et al., 2002). Exchange of the metal cations, as well as intercalation of the anionic layer, allow the hydrotalcites to have stability under wet conditions and high temperatures (Ding and Alpay, 2000). Experimental results show that hydrotalcites have a reversible capacity of about 0.83 mol/kg at 575 K and 1 atm under dry or wet conditions (Yong et al., 2002). In comparison, zeolites and activated carbons have a relatively high adsorption capacity for CO_2 of 4 mol/kg and 1.5-2.5 mol/kg, respectively, at 300 K and 1 atm; however, at 575 K and 1 atm their capacities decrease substantially to about 0.10-0.25 mol/kg (Yong et al., 2002). Although, basic alumina has a CO_2 capacity ranging from 0.39 to 0.62 mol/kg under the same conditions (Yong et al., 2000), HTlcs not only exhibit a higher CO_2 capacity at elevated temperatures, but they also tend to be H_2O insensitive, which is not necessarily true for zeolites, activated carbons, and basic aluminas.

The overall objective of this three-year continuation project was to study new pressure swing adsorption (PSA) cycles for CO_2 capture and concentration at high temperature. The heavy reflux (HR) PSA concept and the use of a HTlc adsorbent that captures CO_2 reversibly at high temperatures simply by changing the pressure were two key features of these new PSA cycles. A bench-scale experimental and theoretical program has been carried out to complement and extend the process simulation study that was carried out during Phase I (DE-FG26-03NT41799). This final report covers the entire project from August 1, 2005 to July 31, 2008 and provides details about the tasks that were carried out and the results from those tacks.

Those tasks were: 1. Construct High Temperature Fixed Bed Unit (Section 7.2); 2. Modify Fixed Bed Unit to Mimic Multi-Bed Operation (Section 7.3); 3. Perform Breakthrough and Elution Experiments in the Fixed Bed Unit (Section 7.0); 4. Perform Varying Pressure Cycling Experiments in the Fixed Bed Unit; 5. Modify and Validate Existing PSA Code (Sections 2.0 and 4.0); 6. Carry Out Rapid Adsorbent Characterization (Section 5.0); 7. Carry out Simulations with Validated PSA model (Sections 2.0 and 3.0); 8. Carry out Detailed Adsorbent Characterization (Section 6.0); and 9. Carry out Economic Analyses. The sections listed in parentheses correspond to sections throughout the report. Tasks without a section listed were not initiated and thus not discussed anywhere in the report.

2.0 Study of PSA Cycles for CO_2 Capture by Rigorous Numerical Simulation

2.1 Introduction and Objectives

Many pressure swing adsorption (PSA) processes employed today use a typical 4-step, stripping PSA cycle with light reflux, which is commonly referred to as the Skarstrom cycle (Ruthven et al., 1994). In this kind of PSA cycle, typical steps consist of a cocurrent high pressure feed step, a countercurrent depressurization step, a countercurrent low pressure purge step with light product (a light reflux step), and a countercurrent pressurization step with light product. The word "stripping" is used to denote that the feed step is carried out at the high pressure and that the adsorbent bed strips the heavy component from the gas phase due to selective adsorption. This is in contrast to an enriching PSA cycle where the word "enriching" is used to denote that the feed step is carried out at the low pressure and that the adsorbent bed enriches the gas phase with the heavy component due to desorption (Ebner and Ritter, 2002; Yoshida et al., 2003). Only stripping PSA cycles are considered in this work.

A multitude of stripping PSA cycles with light reflux have been developed for producing a relatively pure or even highly pure light component, depending on the application, with the number of beds varying from one to more than ten (Ruthven et al., 1994). However, a significant limitation exists with the use of this conventional stripping PSA cycle for concentrating the heavy component in a feed stream because of the fact that the light reflux step uses a portion of the light product gas for purge, which necessarily dilutes the heavy component in the heavy product stream (Liu and Ritter, 1996; Subramanian and Ritter, 1997). Therefore, it follows that for the separation of a binary gas mixture, for example, a pure light component is easy to attain from such a cycle, but not a pure heavy component. In fact, Subramanian and Ritter (1997) showed theoretically that the enrichment of the heavy component is limited by the pressure ratio for a stripping PSA cycle with light reflux.

Over the years, many modifications to the 4-step Skarstrom cycle have been purposed and implemented. Two such modifications to improve the heavy product purity or enrichment are the addition of a cocurrent depressurization step and/or adding a high pressure rinse (i.e., heavy reflux) step (Ruthven et al., 1994). The addition of a cocurrent depressurization step just after the high pressure feed step allows the pressure in the column to drop to some specified intermediate pressure, which in turn improves the heavy product enrichment by causing the heavy gas to desorb and fill the interstitial void spaces in the column while continuing to produce light product (Ruthven et al., 1994). This interstitial gas, now enriched in the heavy component, is recovered during the subsequent countercurrent depressurization step and countercurrent purge step with light product reflux, resulting in a heavy product that is more enriched in the heavy component.

The addition of a high pressure cocurrent rinse or purge step (i.e., a heavy reflux step) just after the high pressure feed step also improves the heavy product enrichment (Ruthven et al., 1994). This heavy reflux step recycles a portion of the heavy product gas obtained from a low pressure column during the countercurrent depressurization step, countercurrent low pressure purge step, or both steps back to the high pressure column. This gas, already being highly enriched in the heavy component, displaces the light component from the adsorbed phase near

the heavy product or feed end of the column and flushes it downstream toward the light product end of the column, effectively filling both the adsorbed and gas phases in much of the column with the heavy component, while continuing to produce either a pure light product or a gas stream with a composition similar to that of the feed gas. Much, if not all, of this heavy reflux gas is recovered during the subsequent countercurrent depressurization step and countercurrent purge step with light product reflux, again resulting in a heavy product that is more enriched in the heavy component.

The objective of this work was two-fold. The first objective was to carry out a systematic study that explored the advantages and disadvantages associated with both simple and more complex PSA cycles. The second objective was to exploit the use of K-promoted hydrotalcite-like compound (HTlc) adsorbent as a high temperature adsorbent for capturing and concentrating CO_2 from a stack gas. Results are presented that show markedly improved process performances when simple modifications were made to a variety of stripping PSA cycles. These results disclosed the importance of the PSA cycle configuration to the process performance by gaining an understanding of and appreciation for the use of heavy reflux, and they exposed the rigor involved in determining the best PSA cycle sequence for a given application.

2.2 Literature Review of PSA Cycles for CO_2 Capture

A variety of different stripping PSA cycle configurations have been developed for concentrating the heavy component in a feed stream; the ones of interest to this work are those that have been explored for concentrating CO_2 from stack and flue gases. Table 1 provides a summary of the performances of these various stripping PSA cycles investigated for concentrating CO_2 from flue gas. All of them utilize in some fashion a light, heavy, dual or surprisingly even a no reflux PSA cycle configuration, intermixed with various cocurrent and or countercurrent depressurization steps, feed, light product and heavy product pressurization steps, and null (delay) and pressure equalization steps. In addition, they also utilize either a vacuum swing cycle with the high pressure set just above but very near atmospheric pressure and the low pressure set at some vacuum level, or a more conventional pressure swing cycle, for example, with the purge or low pressure set at or near atmospheric pressure and the feed or high pressure set at some higher level. Finally, they all utilize one or more commercially available adsorbents that exhibit a high capacity for CO_2 at ambient temperature and pressure (e.g., activated carbon, carbon molecular sieve, and X and Y zeolites), in an attempt to concentrate and recover the heavy component, in this case CO_2, from a typical flue or stack gas.

For example, Suzuki et al (1997) studied a rapid cycle, 2-bed 2-step PSA cycle consisting of feed pressurization and countercurrent depressurization steps. Although they obtained very high feed throughputs in the range of 12,600 L STP/hr/kg (as expected from a rapid cycle PSA process), the purity of CO_2 in the heavy product was extremely low at around 18 vol%, but with a reasonable CO_2 recovery of 90% when processing a feed stream containing 15 vol% CO_2. This relatively poor process performance with respect to the CO_2 enrichment was most likely due to the lack of any kind of a reflux step in their stripping PSA cycle configuration.

Table 1. Performances of various stripping PSA cycle configurations investigated for CO_2 concentration from flue gas, with the process performance judged primarily in terms of the CO_2 purity in the heavy product ($y_{CO2,F}$), with the CO_2 recovery (R_{CO2}) and the feed throughput (θ) being secondary but also important process performance indicators.

Cycle Configuration	Cycle Step Sequence*	Adsorbent	P_H (atm)	π_T	$y_{CO2,F}$ (%)	$y_{CO2,HP}$ (%)	R_{CO2} (%)	θ (LSTP/hr/kg)	Reference
2-bed 2-step	FP, CnD	Y	2.0	2.0	15	18	90	12,600	Suzuki et al (1997)
2-bed 4-step	FP, F, CnD, LR	13X	3.0	3.0	8.3	--	--	15	Gomes and Yee (2002)
1-bed 4-step	LPP, F, CnD, LR	13X	1.7	1.9	15	24.4	9	17	Ko et al., (2003)
2-bed 4-step	FP, F, Cnd, LR	13X	1.1	17.2	10	68	50	507	Park et al., (2002)
1-bed 4-step	FP, F, Cnd, LR	13X	14.0	15.9	15	56.4	98	908	Ko et al., (2005)
3-bed 8-step	FP, F, CoD, LEE, HPP or HR-IP, N, CnD, LEE	AC	1.5	15	17	99.8	34	331	Na et al., (2001)
3-bed 7-step	FP, F, LEE, HR-IP, N, CnD, LEE	AC	2.0	20	13	99	55	156	Na et al., (2002)
3-bed 8-step	FP, F, LEE, HPP, HR-IP, N, CnD, LEE	13X	1.5	30	13	99.5	69	228	Choi et al., (2003)
3-bed 8-step	FP, F, CoD, FR, N, HR-IP, CnD, N	AC	1.1	16.6	16	99	50	610	Chue et al., (2005)
4-bed 4-step	LPP, F+R, HR, CnD	AC	1.2	12	17	99.9+	68	33	Kikkinides et al., (1993)
4-bed 8-step	LPP, N, F, HR, LEE, CnD, LR, LEE	13X	1.1	11	13	64	80	120	Takamura et al., (2001)
3-bed 5-step	FP, F, HR, CnD, LR	13X	1.1	17.2	10	83	54	338	Park et al., (2002)
2-bed 6-step	LEE, FP, F, LEE, CnD, LR	13X	1.1	17.2	10	82	57	477	Park et al., (2002)
2-bed 4-step	HPP, FP, CoD, CnD	13X	5.5	110	20	48	94	426	Chou and Chen (2004)
2-bed 5-step	LPP, FP, F, CoD, CnD	13X	5.5	110	20	43	88	426	Chou and Chen (2004)
3-bed 4-step	LPP, F, CnD, LR	13X	1.5	30	20	58	75	273	Chou and Chen (2004)
3-bed 6-step	LPP, FP, F, HR, CoD, CnD	13X	1.5	30	20	63	70	273	Chou and Chen (2004)

* CnD = countercurrent depressurization; CoD = cocurrent depressurization; FP = feed pressurization; F = high pressure feed; HPP = heavy product pressurization; HR = heavy reflux; IP = intermediate pressure; LEE = light end equalization; LPP = light product pressurization; LR = light reflux; N = null or delay; R = recycle

Two other studies looked at using the conventional 4-step stripping PSA cycles with light reflux to concentrate CO_2 from exhaust gases, one as a 2-bed process with feed pressurization (Gomes and Yee, 2002), and the other one as a 1-bed process with light product pressurization (Ko et al., 2003). Neither study attained high purities or high recoveries of CO_2, because as stated earlier, the enrichment of the heavy component, i.e., CO_2, would be limited to the pressure ratio and usually be much lower than this value due to dilution with the light reflux gas. Gomes and Yee while processing 15.0 L STP/hr/kg of feed, used a pressure ratio of three, which limited their CO_2 enrichment to three or less, meaning they could never produce a heavy product stream containing more than 25 vol% CO_2, because their feed contained only 8.3 vol% CO_2. Although they did not report any CO_2 recoveries or purities, their results were probably much worse than this upper limit due to dilution of the heavy product with light reflux (Liu and Ritter, 1996 and Subramanian and Ritter, 1997). A similar limitation existed in the work by Ko et al. (2003), because they used a pressure ratio of around two and a feed concentration of 15 vol% CO_2. No matter the other conditions, with a simple 4-step stripping PSA cycle with only light reflux, they could never produce a heavy product containing more than 30 vol% CO_2; and they did not. For example, in their best case, they obtained a CO_2 purity of 24.4 vol% and a CO_2 recovery of 9.4% at a feed throughput of 17.1 L STP/hr/kg.

However, even when the pressure ratio did not limit the enrichment of the heavy component, the simple 4-step stripping PSA cycle with light reflux still could not produce a highly enriched heavy product due to dilution with light reflux. Park et al (2002) and Ko et al (2005) both showed this kind of behavior. For example, Park et al (2002) investigated a 2-bed 4-step stripping PSA cycle with light reflux using a vacuum swing cycle with a pressure ratio of 17.2 and with four steps of feed pressurization, feed, countercurrent depressurization and light reflux. For a feed throughput of 507 L STP/hr/kg, they obtained a CO_2 purity of 68 vol% and a CO_2 recovery of 50% while processing a feed containing 10 vol% CO_2. Similarly, Ko et al (2005) obtained a high CO_2 recovery of 97.5%, but a low CO_2 purity of only 56.4 vol% using the same four cycle steps while processing a feed containing 15 vol% CO_2 at a feed throughput of 908 L STP/hr/kg. In their 1-bed 4-step stripping PSA cycle with light reflux, the low pressure was set at essentially atmospheric pressure and the pressure ratio was 16. In both cases, even though theoretically the pressure ratio was more than enough to produce a heavy product steam containing 100 vol% CO_2, it did not happen most likely due to the significant dilution effect of light reflux.

In contrast to these stripping PSA cycles with light reflux, a few studies used far more complex PSA cycles that included in all cases a heavy reflux step to concentrate CO_2 from flue or stack gases, with much better results. For example, in a series of works (Na et al. 2001 and 2002, Choi et al., 2003), 3-bed 8-step and 3-bed 7-step PSA cycle configurations were studied. The 3-bed 8-step (Na et al., 2001) included feed pressurization, feed, cocurrent depressurization, light end equalization between two beds (two steps), heavy reflux, null (delay), and countercurrent depressurization steps, but no light reflux step. While processing a feed containing 17 vol% CO_2 at a feed throughput of 331 L STP/hr/kg, they achieved a high CO_2 purity of 99.8 vol%, but a rather low CO_2 recovery of 34%. The same group then studied a similar 3-bed 7-step PSA cycle configuration (Na et al., 2002) with no cocurrent depressurization step and with the heavy reflux step carried out at an intermediate pressure, and achieved a CO_2 purity of 99 vol% at a CO_2 recovery of 55%, with a feed throughput of 156 L

STP/hr/kg and a feed containing 13 vol% CO_2. Finally, with a 3-bed 8-step PSA cycle configuration (Choi et al., 2003) consisting of partial feed pressurization, feed, light end equalization, partial heavy product pressurization, heavy reflux at an intermediate pressure, null, countercurrent depressurization and pressure equalization steps, they achieved a CO_2 purity of 99.5 vol% at a CO_2 recovery of 69% while processing a feed containing 13 vol% CO_2 at a feed throughput of 228 L STP/hr/kg. These decent but somewhat varied process performances were most likely due to the inclusion of the heavy reflux step, but in this case with the heavy reflux gas necessarily obtained from one of the beds undergoing countercurrent depressurization because no light reflux step was used in any of these complex cycle sequences.

Similar stripping PSA cycles with heavy reflux were exploited by Yang and co-workers (Chue et al., 1995; Kikkinides and Yang, 1993). In one case (Chue et al., 1995), a 3-bed 7-step cycle configuration was able to produce a heavy product stream containing over 99 vol% CO_2 at CO_2 recoveries ranging from 50 to 70%, depending on the CO_2 concentration in the feed (16 and 26 vol% CO_2, respectively), while processing 610 L STP/hr/kg of feed, an impressive throughput of gas for a 2.5 cm diameter column. In this case, the cycle sequence included a cocurrent depressurization step and an intermediate pressure feed step, in addition to two heavy reflux steps, and feed pressurization, high pressure feed and countercurrent depressurization steps.

In the other case (Kikkinides and Yang, 1993), a 4-bed 4-step PSA cycle sequence was studied that utilized a light product pressurization step, a feed step that was blended with a recycle stream from a bed undergoing heavy reflux, a heavy reflux step, and a countercurrent depressurization step. This relatively simple vacuum swing cycle with no light reflux step, which meant that the heavy reflux gas necessarily came from the countercurrent depressurization gas, was able to produce a heavy product stream containing 99.997 vol% CO_2 at 68.4% CO_2 recovery and at a reasonable throughput of 33 L STP/hr/kg from a feed stream containing 17 vol% CO_2. There is no doubt that the heavy reflux step was instrumental in fostering the superior performance of this PSA cycle; however, it was somewhat surprising that such a high purity CO_2 at a reasonable recovery could be obtained with such a simple cycle sequence. One plausible explanation is associated with the way they ran the heavy reflux step. They allowed significant breakthrough of CO_2 from the light end of the column undergoing heavy reflux, with this effluent being recycled back and blended with the column undergoing the feed step. Hence, the column undergoing heavy reflux was filled up with so much of the heavy component that, by the end of the step, the light product effluent contained enough CO_2 to justify recycling it back to the feed, not only to minimize the loss of CO_2 in the light product, but also to ensure that the heavy product obtained during the subsequent countercurrent depressurization step was highly enriched in CO_2.

More complex stripping PSA cycle sequences that take advantage of both light and heavy reflux steps were explored by Takamura et al. (2001), Chou and Chen (2004), and Park et al. (2002), but only the works of Takamura et al. and Park et al. used both light and heavy reflux steps in the same cycle sequence (i.e, a true dual reflux process). For example, Takamura et al. (2001) studied a 4-bed 8-step dual reflux PSA cycle using light product pressurization, null, high pressure feed, heavy reflux, light end equalization, countercurrent depressurization, light reflux, and light end equalization steps. This rather complex stripping PSA cycle produced a heavy product stream containing only 64 vol% CO_2 at a CO_2 recovery of 80% but with a reasonably

high feed throughput of 120 L STP/hr/kg from a feed containing 13 vol% CO_2. In contrast, Park et al. (2002) used perhaps the simplest 3-bed 5-step stripping PSA cycle configuration with light reflux and heavy reflux (obtained from the countercurrent depressurization and light reflux purge steps) that included feed pressurization, feed, heavy reflux, countercurrent depressurization and light reflux. With the feed containing 10 vol% CO_2, a reasonably good performance was obtained corresponding to a CO_2 purity of 83 vol%, a CO_2 recovery of 54%, and a feed throughput of 338 L STP/hr/kg. It was surprising; however, that these rather complex dual reflux PSA cycles were seemingly limited in their performances, especially when considering the performance reported by Park et al. (2002) for a 2-bed 6-step stripping PSA cycle with light reflux and light end equalization steps. This modified Skarstrom cycle, consisting of light end equalization, feed pressurization, feed, light end equalization, countercurrent depressurization and light reflux steps, produced a CO_2 purity of 82 vol% at a CO_2 recovery of 57% and a feed throughput of 477 L STP/hr/kg. This surprisingly good performance they obtained from a stripping PSA cycle with only a light reflux step, apparently resulted from the simple addition of a light end equalization step, a somewhat remarkable and certainly unexpected outcome.

Chou and Chen (2004) on the other hand, studied 2-bed 4-step, 2-bed 5-step, 3-bed 4-step, and 3-bed 6-step PSA cycle configurations with the 2-bed cycles not using any reflux steps, and the 3-bed cycles using either a light or heavy reflux step, but not both in the same cycle sequence. For example, in their 2-bed 4-step PSA cycle configuration they used heavy product pressurization from vacuum to atmospheric pressure, feed pressurization up to the high pressure, cocurrent depressurization to atmospheric pressure, and countercurrent depressurization to vacuum, a very unusual PSA cycle, indeed. A more conventional PSA cycle consisting of light product pressurization, feed pressurization, feed, cocurrent depressurization and countercurrent depressurization steps was studied in a 2-bed 5-step PSA cycle configuration. In their 3-bed 4-step process, light product pressurization, feed, countercurrent depressurization and light reflux steps were employed. Finally, in their 3-bed 6-step PSA cycle configuration, they used light product pressurization followed by feed pressurization, feed, heavy reflux, cocurrent depressurization, and countercurrent depressurization steps. They showed that the 2-bed 4-step process with a feed throughput of 426 L STP/hr/kg could not enrich the CO_2 very much, with it being around 48 vol% from a feed containing 20 vol% CO_2; however, the recovery of CO_2 was quite high at around 94%. At the same feed throughput, the 2-bed 5-step process did even worse, with the CO_2 purity limited to 43 vol% at a CO_2 recovery of 88%. Not terribly surprising results when considering the fact that no reflux steps were implemented. They also showed that the 3-bed 6-step process with heavy reflux outperformed the 3-bed 4-step process with light reflux, with the best, but not stellar, performance corresponding to a CO_2 purity of around 63 vol% (compared to 58 vol%) but at a lower CO_2 recovery of 70% (compared to 75%) from a feed containing 20 vol% CO_2 being fed at a feed throughput of 273 L STP/hr/kg. Based on the arguments presented above, the heavy reflux cycle would certainly be expected to out perform all the other cycles they studied.

This fairly comprehensive, but certainly not exhaustive, review of some of the more relevant studies that have dealt with removing and concentrating CO_2 from flue and stack gases by various stripping PSA cycles is given here to illuminate a few key points about the ambiguity associated with choosing one PSA cycle over another one for a given application. Even after carefully examining the results from these studies summarized in Table 1, in most cases, it is still

not clear why the authors chose the cycles they did, and more importantly, why one PSA cycle outperformed another one, except when it was obvious that an inappropriate cycle was chosen, like when a no reflux cycle or a 4-step Skarstrom cycle was employed in an attempt to concentrate a heavy component. But even in the case where a stripping PSA cycle with light reflux was inappropriately chosen, this review showed that in some instances it still was able to outperform a stripping PSA cycle with heavy reflux, depending on many factors like the process conditions, cycle times, bed sizes, adsorbent CO_2 capacity, or even the addition of a light end equalization step (Park et al., 2002), which are all interrelated and which make PSA cycle configurations difficult to understand and interpret, even for one skilled in the art. Moreover, there are other motivations that foster studying a stripping PSA cycle with light reflux for concentrating a heavy component, even when it is understood that this may not be the best cycle in terms of CO_2 purity. One of the most important incentives is to avoid using an additional compressor for implementing a heavy reflux step.

2.3 Mathematical Model of PSA Process based on Numerical Analysis

The multicomponent PSA model used in this work is similar (but not identical) to that previously developed by Liu et al (1998). It includes the following assumptions: the ideal gas law applies, the heat of adsorption is independent of temperature and adsorbed phase loading, the heat capacity of the solid is constant, the heat transfer with the surroundings is described by an average heat transfer coefficient that is constant, heat effects due solely to the compression and expansion of the gas between the high and low pressures is ignored, the pressure drop within the column is considered negligible, and the linear driving force (LDF) mass transfer model is considered applicable. It is also assumed that as the loading increases in the pores of the adsorbent, the adsorbed phase occupies a small but increasing fraction of the volume of the pore φ, which changes the intraparticle void fraction χ according to

$$\varphi = \sum_{i=1}^{N} \frac{q_i \rho_p M_i}{\rho_{a,i}} \tag{1}$$

where the adsorbed phase density $\rho_{a,i}$ is assumed to have the same density of its corresponding liquid at its normal point.

For an *N* component gas mixture, the component mass balances are given by

$$\frac{\varepsilon + (1-\varepsilon)(\chi - \varphi)}{\varepsilon} \frac{\partial y_i}{\partial t} + u \frac{\partial y_i}{\partial z} - y_i \sum_{j=1}^{N} S_j + S_i = 0 \qquad i = 1, 2, \ldots, N\text{-}1 \tag{2}$$

where

$$S_i = \frac{1-\varepsilon}{\varepsilon} \frac{RT\rho_p}{P} \frac{\partial q_i}{\partial t} \qquad i = 1, 2, \ldots, N \tag{3}$$

and with the constraint that

$$\sum_{i=1}^{N} y_i = 1 \tag{4}$$

The $\frac{\partial q_i}{\partial t}$ term is based on the LDF approximation as

$$\frac{\partial q_i}{\partial t} = k_i\left(q_i^* - q_i\right) \qquad i = 1, 2, \ldots, N \tag{5}$$

After algebraic manipulation, the total mass balance can be expressed as

$$\frac{\partial u}{\partial z} - \frac{u}{T}\frac{\partial T}{\partial z} + \frac{\varepsilon + (1-\varepsilon)(\chi - \varphi)}{\varepsilon}\left(\frac{1}{P}\frac{\partial P}{\partial t} - \frac{1}{T}\frac{\partial T}{\partial t}\right) - \frac{(1-\varepsilon)}{\varepsilon}\frac{\partial \varphi}{\partial t} + \sum_{i=1}^{N} S_i = 0 \tag{6}$$

where

$$\frac{\partial \varphi}{\partial t} = \sum_{i=1}^{N} \frac{\frac{\partial q_i}{\partial t}\rho_p M_i}{\rho_{a,i}} \tag{7}$$

The energy balance is given by

$$\frac{\varepsilon + (1-\varepsilon)(\chi - \varphi)}{\varepsilon} C_{P,g}\frac{\partial T}{\partial t} + uC_{P,g}\frac{\partial T}{\partial z} + \frac{2h}{\varepsilon r_b}\frac{RT}{P}(T - T_0) +$$
$$\frac{1-\varepsilon}{\varepsilon}\frac{RT}{P}\rho_P \sum_{i=1}^{N}\left(C_{P,a,i}q_i\frac{\partial T}{\partial t} + \Delta H_i\frac{\partial q_i}{\partial t}\right) + \rho_p C_{P,p}\frac{1-\varepsilon}{\varepsilon}\frac{RT}{P}\frac{\partial T}{\partial t} = 0 \tag{8}$$

The heat capacity of the gas mixture $C_{P,g}$ is obtained from the component heat capacities $C_{P,g,i}$ according to

$$C_{P,g} = \sum_{i=1}^{N} y_i C_{P,g,i} \tag{9}$$

where

$$C_{P,g,i} = A_i + B_i T + C_i T^2 + D_i T^3 \tag{10}$$

The component adsorbed phase heat capacity $C_{P,a,i}$ is assumed to be equal to its gas phase heat capacity, so $C_{P,a,i} = C_{P,g,i}$.

The equilibrium amount adsorbed q_i^* from the gas phase is predicted by the Langmuir adsorption isotherm:

$$q_i^* = \frac{q_i^s b_i P y_i}{1 + \sum_{i=1}^{N} b_i P y_i} \tag{11}$$

where

$$q_i^s = q_{i,1}^s T + q_{i,2}^s \tag{12}$$

and

$$b_i = b_i^0 \exp\left(\frac{B_i^0}{T}\right) \tag{13}$$

However, only the adsorption of CO_2 is accounted for in this model. The adsorption of N_2 and H_2O are considered to be inert with the K-promoted hydrotalcite-like compound (HTlc) adsorbent.

The pressure history during a cycle is assumed to be a known. During the feed and heavy reflux steps the pressure is constant and set at P_H, and during the light reflux step the pressure is also constant and set at P_L. During the depressurization and pressurization steps, however, the pressure is assumed to change linearly with time, but with the constraint that the specified intermediate pressure (P_I) for cocurrent depressurization (CoD), the low pressure (P_L) for countercurrent depressurization (CnD) and the high pressure (P_H) for pressurization are always reached by the end of a pressure changing step. This linear function is given by:

$$P(t) = P_i - \frac{\left(P_i - P_f\right)}{t_s} t \tag{14}$$

For the light product pressurization (LPP) step, $P_i = P_L$ and $P_f = P_H$. For the CoD step, $P_i = P_H$ and $P_f = P_I$. For the CnD step, $P_f = P_L$, and $P_i = P_I$ for the cycles that incorporate a CoD step, or $P_i = P_H$ for the cycles that do not have a CoD step.

The initial and boundary conditions depend on the stripping PSA cycle configuration being studied. All simulations start from clean beds saturated with N_2; therefore, the initial conditions for all six stripping PSA cycles are:

F: at t = 0: $y_i = y_{N2} = 1.0$, $T = T_o$, $q_i = q_{N2}$, for all z

For all subsequent cycles, the initial and boundary conditions are taken from the final conditions existing in the bed and at its boundaries from the previous cycle. These initial and boundary conditions for each step in the 4-bed 4-step stripping PSA cycle with light reflux (LR) are:

F: at t = 0: $y_i = y_{i,LPP}$, $T = T_{LPP}$, $q_i = q_{i,LPP}$, for all z
at z = 0: $y_i = y_{i,f}$, $T = T_f$, $u = u_f$, for all t

CnD:	at t = 0:	$y_i = y_{i,F}$,	$T = T_F$,	$q_i = q_{i,F}$,	for all z
	at z = L:	$u = 0$,			for all t
LR:	at t = 0:	$y_i = y_{i,CnD}$,	$T = T_{CnD}$,	$q_i = q_{i,CnD}$,	for all z
	at z = L:	$y_i = y_{i,F}(t)$,	$T = T_F(t)$,	$u = u_{LR}$,	for all t
LPP:	at t = 0:	$y_i = y_{i,LR}$,	$T = T_{LR}$,	$q_i = q_{i,LR}$,	for all z
	at z = 0:	$u = 0$,			for all t

When the cocurrent depressurization (CoD) step is used with the 5-bed 5-step and 4-bed 5-step stripping PSA cycles with LR, the following initial and boundary conditions apply:

F:	at t = 0:	$y_i = y_{i,LPP}$,	$T = T_{LPP}$,	$q_i = q_{i,LPP}$,	for all z
	at z = 0:	$y_i = y_{i,f}$,	$T = T_f$,	$u = u_f$,	for all t
CoD:	at t = 0:	$y_i = y_{i,F}$,	$T = T_F$,	$q_i = q_{i,F}$,	for all z
	at z = 0:	$u = 0$,			for all t
CnD:	at t = 0:	$y_i = y_{i,CoD}$,	$T = T_{CoD}$,	$q_i = q_{i,CoD}$,	for all z
	at z = L:	$u = 0$,			for all t
LR:	at t = 0:	$y_i = y_{i,CnD}$,	$T = T_{CnD}$,	$q_i = q_{i,CnD}$,	for all z
	at z = L:	$y_i = y_{i,F}(t)$,	$T = T_F(t)$,	$u = u_{LR}$,	for all t
LPP:	at t = 0:	$y_i = y_{i,LR}$,	$T = T_{LR}$,	$q_i = q_{i,LR}$,	for all z
	at z = 0:	$u = 0$,			for all t

The 5-bed 5-step stripping PSA cycle with LR and heavy reflux (HR) from countercurrent depressurization (CnD) has the following initial and boundary conditions:

F:	at t = 0:	$y_i = y_{i,LPP}$,	$T = T_{LPP}$,	$q_i = q_{i,LPP}$,	for all z
	at z = 0:	$y_i = y_{i,f}$,	$T = T_f$,	$u = u_f$,	for all t
HR:	at t = 0:	$y_i = y_{i,F}$,	$T = T_F$,	$q_i = q_{i,F}$,	for all z
	at z = 0:	$y_i = y_{i,CnD}(t)$,	$T = T_{CnD}(t)$,	$u = u_{HR}$,	for all t
CnD:	at t = 0:	$y_i = y_{i,HR}$,	$T = T_{HR}$,	$q_i = q_{i,HR}$,	for all z
	at z = L:	$u = 0$,			for all t
LR:	at t = 0:	$y_i = y_{i,CnD}$,	$T = T_{CnD}$,	$q_i = q_{i,CnD}$,	for all z
	at z = L:	$y_i = y_{i,F}(t)$,	$T = T_F(t)$,	$u = u_{LR}$,	for all t
LPP:	at t = 0:	$y_i = y_{i,LR}$,	$T = T_{LR}$,	$q_i = q_{i,LR}$,	for all z
	at z = 0:	$u = 0$,			for all t

The initial and boundary conditions for the 5-bed 5-step stripping PSA cycle with LR and HR from LR purge are:

F:	at t = 0:	$y_i = y_{i,LPP}$,	$T = T_{LPP}$,	$q_i = q_{i,LPP}$,	for all z
	at z = 0:	$y_i = y_{i,f}$,	$T = T_f$,	$u = u_f$,	for all t
HR:	at t = 0:	$y_i = y_{i,F}$,	$T = T_F$,	$q_i = q_{i,F}$,	for all z
	at z = 0:	$y_i = y_{i,LR}(t)$,	$T = T_{LR}(t)$,	$u = u_{HR}$,	for all t
CnD:	at t = 0:	$y_i = y_{i,HR}$,	$T = T_{HR}$,	$q_i = q_{i,HR}$,	for all z
	at z = L:	$u = 0$,			for all t
LR:	at t = 0:	$y_i = y_{i,CnD}$,	$T = T_{CnD}$,	$q_i = q_{i,CnD}$,	for all z
	at z = L:	$y_i = y_{i,F}(t)$,	$T = T_F(t)$,	$u = u_{LR}$,	for all t

LPP:	at t = 0:	$y_i = y_{i,LR}$,	$T = T_{LR}$,	$q_i = q_{i,LR}$,	for all z
	at z = 0:	$u = 0$,			for all t

Finally, the 4-bed 4-step stripping PSA cycle with HR from countercurrent depressurization (CnD) has the following initial and boundary conditions:

F:	at t = 0:	$y_i = y_{i,LPP}$,	$T = T_{LPP}$,	$q_i = q_{i,LPP}$,	for all z
	at z = 0:	$y_i = y_{i,f}$,	$T = T_f$,	$u = u_f$,	for all t
HR:	at t = 0:	$y_i = y_{i,F}$,	$T = T_F$,	$q_i = q_{i,F}$,	for all z
	at z = 0:	$y_i = y_{i,CnD}(t)$,	$T = T_{CnD}(t)$,	$u = u_{HR}$,	for all t
CnD:	at t = 0:	$y_i = y_{i,HR}$,	$T = T_{HR}$,	$q_i = q_{i,HR}$,	for all z
	at z = L:	$u = 0$,			for all t
LPP:	at t = 0:	$y_i = y_{i,CnD}$,	$T = T_{CnD}$,	$q_i = q_{i,CnD}$,	for all z
	at z = 0:	$u = 0$,			for all t

Using the in-house developed cyclic adsorption process simulator, each simulation of a single bed was carried out step by step and cycle by cycle until the periodic state was reached. The periodic state was defined as that state wherein none of the dependent variables changed from cycle to cycle within a set tolerance. Periodic behavior was typically achieved for each set of PSA process conditions and cycle configuration after carrying out 100 to 500 cycles. The periodic state process performance of all the PSA cycles analyzed was judged by the CO_2 recovery (R), CO_2 purity ($y_{CO2,HP}$) or CO_2 enrichment (E), and feed throughput (θ). R was defined as the number of moles of CO_2 leaving the bed during the steps where heavy product was withdrawn from the system divided by the number of moles of CO_2 entering the bed in the feed. $y_{CO2,HP}$ was defined as the average mole fraction of CO_2 leaving the bed during the steps where heavy product was withdrawn from the system. θ was defined as the total amount of feed fed to the process during one complete cycle divided by the total cycle time and the mass of adsorbent in all the columns.

2.4 Simple 4-Bed 4-Step Skarstrom PSA Cycle

The rigorous pressure swing adsorption (PSA) process simulator was used to study a new, high temperature PSA cycle, based on the use of a K-promoted hydrotalcite-like compound (HTlc) adsorbent and a simple, 4-step, Skarstrom-type, vacuum swing cycle designed to process a typical stack gas effluent at 575 K containing (in vol%) 15 % CO_2, 75% N_2 and 10% H_2O. The effects of the purge-to-feed ratio (γ), cycle step time (t_s) (with all four steps of equal time), and pressure ratio (π_T) on the process performance was studied in terms of the CO_2 recovery (R) and enrichment (E) at a constant throughput θ of 14.4 L STP/hr/ kg. The process parameters and conditions used in this mathematical model are shown in Table 2. The bench-scale column dimensions and corresponding heat transfer coefficient were taken from an experimental setup described by Liu et al. (1998). The mass transfer coefficients for CO_2 in this HTlc adsorbent were estimated by Ding and Alpay (2001). Figure 1 shows the experimental adsorption isotherm data for CO_2 on a K-promoted HTlc at four different temperatures (Ding and Alpay, 2000, 2001). These data were fitted to a temperature dependent Langmuir isotherm model shown in the figure. The isosteric heat of adsorption, ΔH_i, was estimated from the temperature dependence of the isotherm parameter, b_i. N_2 and H_2O were considered to be inert for this HTlc adsorbent.

Table 2. Bed characteristics, adsorbent properties, transport properties, and operating parameters investigated.

Bed Length (L)	0.2724 m
Bed Radius (r_b)	0.0387 m
Bed Porosity (ε)	0.48
Particle Radius (r_p)	0.001375 m
Particle Density (ρ_p)	1563 kg/m^3
Particle Heat Capacity ($C_{P,p}$)	0.850 kJ/kg/K
Isosteric Heat of Adsorption (ΔH_i)	2.22 kcal/mol
Heat Transfer Coefficient (h)	0.00067 kW/m^2/K
Mass Transfer Coefficient: ads (k_a), des (k_d)	0.0058 s^{-1}, 0.0006 s^{-1}
High Pressure (P_H)	137.9 kPa
Pressure Ratio ($\pi_T = P_H/P_L$)	4, 6, 8, 10, 12
Feed Flow Rate (V_f)	1.0 L STP/min
Feed Mole Fractions: CO_2, N_2, and H_2O	0.15, 0.75 and 0.10
Throughput (θ)	14.4 L STP/hr/kg
Feed Temperature (T_f)	575 K
Wall Temperature (T_o)	575 K
Purge to Feed Ratio (γ)	0.50, 0.75, 1.00, 1.25, 1.50
Cycle Step Time (t_s)	100 s, 200 s, 300 s, 400 s, 500 s
Total Cycle Time (t_c)	400 s, 800 s, 1200 s, 1600 s, 2000 s

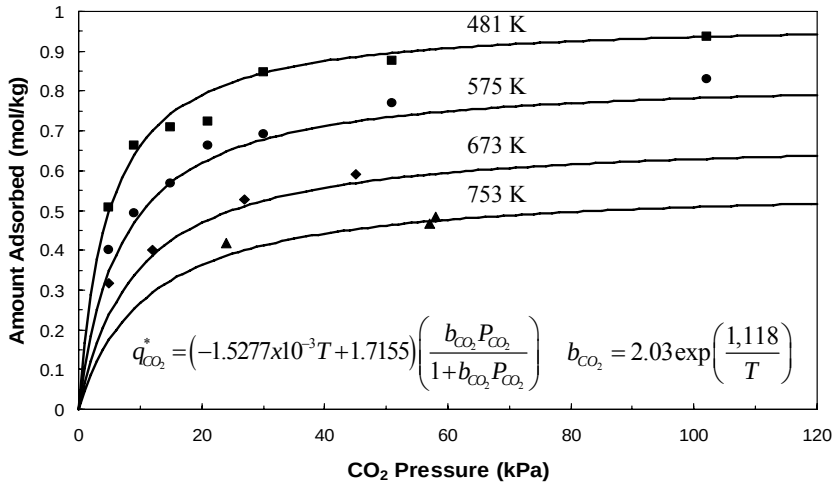

Figure 1. CO_2 adsorption isotherms for K-promoted HTlc (Ding and Alpay , 2000; 2001). Symbols: experiment; lines: model.

The PSA cycle consisted of four interconnected beds each undergoing four cycle steps in tandem. The four steps were high-pressure (P_H) adsorption with feed gas (step II) just above atmospheric pressure, countercurrent blowdown (evacuation) from P_H to a lower (vacuum) pressure (P_L) (step III), countercurrent low-pressure desorption with light product purge under

vacuum (step IV), and repressurization from P_L to P_H (step I) with light product gas. The heavy product (CO_2) was enriched and recovered in steps III and IV, whereas the inert light product (mainly N_2 and H_2O) was recovered in step II. The purge and pressurization gases used in steps IV and I came directly from the other bed as the light product of step II, retained their time-dependent composition and temperature.

Using 125 simulations, the effects of the purge-to-feed ratio (γ), cycle step time (t_s) (with all four steps of equal time), and pressure ratio (π_T) on the process performance was studied in terms of the CO_2 recovery (R) and enrichment (E) at a constant throughput θ of 14.4 L STP/hr/kg. At each of five pressure ratios, five cycle step times and five purge to feed ratios were investigated. The base case conditions for the purge to feed ratio (γ), cycle step time (t_s), and pressure ratio ($\pi_T = P_H/P_L$) are underlined in Table 2. With the feed flow rate (V_f) fixed at 1.0 L STP/min, γ was changed by changing the purge flow rate; and with P_H fixed at 137.9 kPa, π_T was changed by changing P_L. All simulations were started from a clean bed containing only inert gas and carried out until the periodic state was reached. The results from 15 simulations carried out at the base case conditions (i.e., $\gamma = 0.75$, $t_s = 300$ s and $\pi_T = 8$ for the base case, non-varying parameters) are shown in Figure 2. Qualitatively similar trends were observed for conditions outside of the base case conditions (not shown).

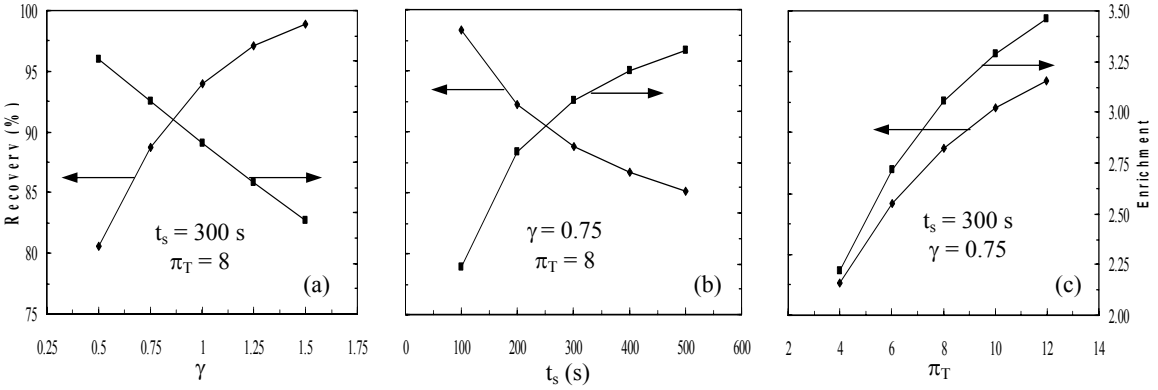

Figure 2. Effect of the (a) purge to feed ratio (γ), (b) cycle step time (t_i), and (c) pressure ratio (π_T) on the process performance in terms of the CO_2 recovery (R) and CO_2 enrichment (E). Base case conditions used for the non-varying parameters. The throughput θ = 14.4 L STP/hr/kg.

Figure 2a shows the effect of γ on R and E with $\pi_T = 8$ and $t_s = 300$ s. R increased, but E decreased, as γ increased. Since the purge gas was taken from the light product gas and used to sweep the low pressure column during the countercurrent purge step, more CO_2 left the column as enriched product. Also, the light product purge regenerated the adsorbent; thus, the adsorbent was able to adsorb more CO_2 in the subsequent adsorption step, thereby allowing less CO_2 to breakthrough into the light product. Both caused R to increase with increasing γ. However, since more of the light product was returned to the low pressure column as purge with increasing γ, it diluted the CO_2 in the heavy product, which caused E to decrease with increasing γ.

Figure 2b shows the effect of t_s on R and E with $\pi_T = 8$ and $\gamma = 0.75$. R decreased, but E increased, as t_s increased. Since CO_2 entered the column during the feed step, more CO_2 entered

the system as t_s increased; thus, it was more likely for CO_2 to breakthrough into the light product, which decreased R with increasing t_s. However, as more CO_2 entered the system, more CO_2 was adsorbed by the hydrotalcite; hence, more CO_2 desorbed during the blowdown and low pressure purge steps and exited the system in the enriched product gas, which caused E to increase with increasing t_s.

Figure 2c shows the effect of π_T on R and E with t_s = 300 s and γ = 0.75. Both R and E increased with increasing π_T. Since t_s and P_H were fixed, the amount of CO_2 entering the system during the feed step was also fixed, as was the periodic state loading of CO_2 on the HTlc at the end of the feed step. Hence, the observed increases in R and E with increasing π_T were actually caused by P_L decreasing, i.e., a deeper vacuum was being applied to the system, which had two effects. For a fixed γ (i.e., the ratio of the purge gas to feed gas velocities), a lower P_L meant less purge gas was used to clean the bed, which caused R to increase. The use of less purge gas also resulted in less dilution of the heavy product, which caused E to increase. In effect, the working capacity of the adsorbent increased, because larger pressure swings allowed for a greater change in the loading, as gleaned from the large slope changes in the low pressure regions of the hydrotalcite isotherms shown in Figure 1.

The results in Figure 2, not surprisingly, implied that a compromise exists between the CO_2 recovery and enrichment. In other words, the set of PSA process conditions that simultaneously maximizes both recovery (R) and enrichment (E) is not necessarily the same set of conditions that maximizes R or E independently. The results in Figure 3, which show the effect of the purge to feed ratio (γ) and cycle step time (t_s) on the (a) CO_2 recovery (R) and (b) CO_2 enrichment (E) for 25 simulations carried out at a pressure ratio π_T = 8 and throughput θ = 14.4 L STP/hr/kg, in terms of 3-D contour plots tend to reveal the conditions that produce this optimum behavior better than simple 2-D plots (Figure 2). The results in Figure 3a clearly show that R increased monotonically with increasing γ and decreasing t_s with R = 100% for numerous sets of conditions. In contrast, the results in Figure 3b reveal much more complex behavior: E increased monotonically with increasing γ, but only at the lower values of t_s; it clearly went through a maximum at the higher values of t_s. Moreover, at the lower values of γ, E decreased with decreasing t_s, whereas at the higher values of γ, E increased with increasing t_s. Nevertheless, it is clear that a set of γ and t_s exists that maximizes both R and E, an effect that could not be ascertained from Figure 2.

The results in Figure 3 provide a convenient, but somewhat limited methodology, to evaluate the simulations, because only a fraction of them can be plotted. The results from all 125 simulations are easily evaluated, however, by constructing a plot or R versus E, as shown in Figure 4. Performance curves are shown for a feed flow rate of 1.0 L STP/min (i.e., θ = 14.4 L STP/hr/kg). Each line corresponds to five runs with t_s increasing from right to left. Each family of lines correspond to a constant γ with π_T increasing as their fan spreads from left to right. From this graph, it is easy to pinpoint the conditions that maximize both R and E. In this case, an E = 3.89 at R = 86.8% was obtained with γ = 0.5, t_s = 500 s and π_T = 12, which correspond to the smallest γ, longest t_s and highest π_T investigated, possibly an expected outcome with a bit of hindsight. The conditions that optimized E or R independently clearly were not the same, but could readily be identified from such a plot. For example, the best CO_2 enrichment dropped to E

= 2.79 to achieve an R = 99.99%, but now with γ = 1.5, t_s = 400 s and π_T = 12. Since all 125 simulations were obtained at the same throughput θ, other θs will shift these lines accordingly.

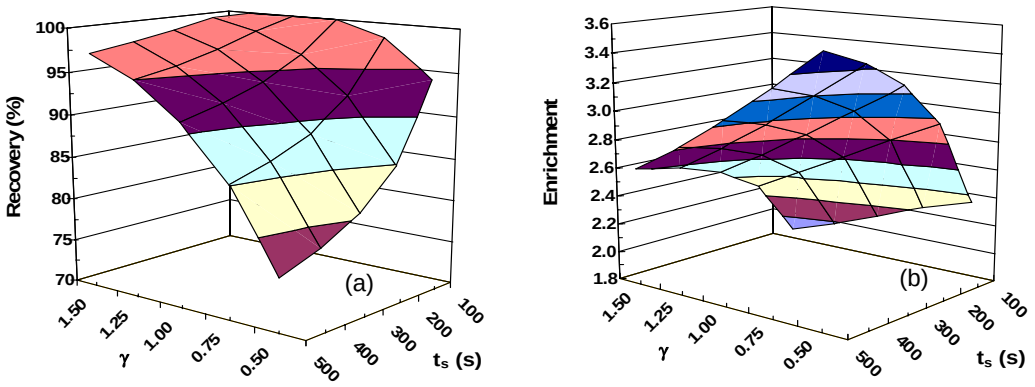

Figure 3. Effect of the purge to feed ratio (γ) and cycle step time (t_s) on the process performance in terms of the (a) CO_2 recovery (R) and (b) CO_2 enrichment (E). Results from 25 simulations are shown with π_T = 8 and θ = 14.4 L STP/hr/kg.

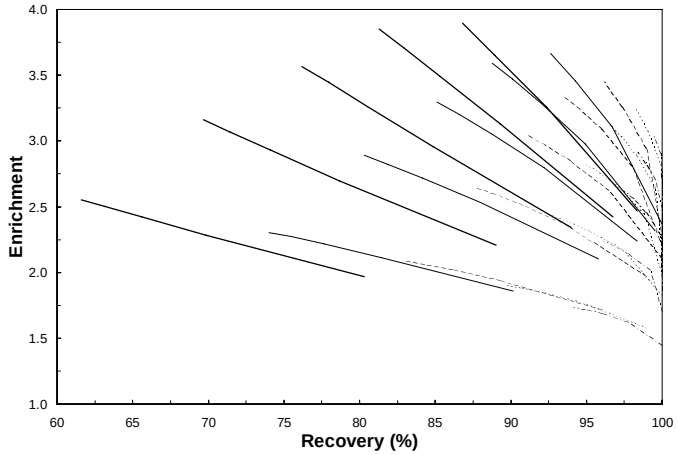

Figure 4. Performance curves for a feed flow rate of 1.0 L STP/min (θ = 14.4 L STP/hr/kg) and purge to feed ratios (γ) of 0.50 (bold line), 0.75 (thin line), 1.00 (dashed line), 1.25 (dotted line), and 1.5 (dot-and-dash). Each line corresponds to five runs with t_s increasing from right to left. Each family of lines of constant γ corresponds to π_T increasing as their fan spreads from left to right.

The results from 125 simulations, carried out at five different purge-to-feed ratios, cycle step times and pressure ratios showed that R increased with increasing γ and π_T and decreasing t_s, while E increased with increasing t_s and π_T and decreasing γ. The highest E of 3.9 was obtained at R = 87% with γ = 0.5, π_T = 12 and t_s = 500 s, apparent optimum conditions for both R and E. In contrast, at R = 100% the highest E of 2.8 was obtained at γ = 1.5, π_T = 12 and t_s = 500 s, apparent optimum conditions for R but not E. Different feed flow rates, i.e., different θs, will result in different sets of optimum possible better conditions. Hence, these results were very encouraging and showed the potential of a high temperature PSA cycle for CO_2 capture.

2.5 More Complex PSA Cycles With and Without a HR Step

The above mentioned results focused on a simple 4-step Skarstrom cycle. The goal now was to see how the use of cocurrent depressurization and heavy reflux steps would change the process performance. Based on the arguments given above and the results reviewed from the literature (Table 1), the effect of these steps seemed to be significant. However, the extent of the improvement certainly cannot be predicted *a priori*, and it is not clear *a priori* how to cast these cycle steps into effective light, heavy and dual reflux PSA cycle configurations. Therefore, one of the objectives of this work was to carry out a systematic study to explore the advantages and disadvantages associated with adding a cocurrent depressurization step or a heavy reflux step to the simple 4-bed 4-step stripping PSA cycle with and/or without light reflux for concentrating the heavy component in a feed stream.

In addition to the four basic PSA steps studied previously, a cocurrent depressurization step or a high pressure heavy reflux step were added to the stripping PSA cycle to create multiple versions of 4-bed 4-step, 4-bed 5-step, and 5-bed 5-step stripping PSA cycle configurations. The process performances obtained from the different PSA cycle configurations, based on results obtained from more than a thousand simulations carried out systematically over a broad range of process conditions using a cyclic adsorption process simulator, were compared and contrasted to each other. The effectiveness of the cocurrent depressurization step and especially the heavy and dual (light and heavy) reflux steps for concentrating the heavy component in a feed stream were demonstrated.

More than a thousand simulations of six different stripping PSA cycle configurations were carried out using the in-house developed cyclic adsorption process simulator. These six stripping PSA cycle configurations are shown in Figure 5. Table 3 indicates the range of performances achieved in terms of feed throughput, CO_2 purity and CO_2 recovery for a given PSA cycle configuration and the range of process conditions studied. Table 4 provides a summary of the best performances achieved, based on the highest CO_2 purity obtained for a given PSA cycle configuration and set of corresponding process conditions. Figures 6 to 11 present a systematic account of the PSA process performances of these various stripping PSA cycles in terms of CO_2 purity versus CO_2 recovery plots. These performance plots are a convenient way to represent performance data over a wide range of conditions, because they make it easy to observe and interpret trends and pinpoint conditions for best performances. The discussion begins with the more common stripping PSA cycle configurations and ends with the less common ones. It is noteworthy that although only simulation results are presented and discussed below, the mathematical model used to obtain these results has been validated against extensive butane-nitrogen-activated carbon PSA experiments carried out by Ritter and co-workers (Liu et. al., 1996, 1998 and 1999), and CO_2-nitrogen-K-promoted HTlc breakthrough experiments carried out by Ding and Alpay (2000) (results not shown).

2.5.1 4-Bed 4-Step Stripping PSA Cycle with Light Reflux

The vacuum swing version of the 4-bed 4-step stripping PSA cycle with light reflux (LR) studied here, one of the most popular PSA cycles, consisted of four interconnected beds each undergoing in succession four cycle steps of equal duration, as shown in Figure 5a. The four

steps were high pressure (P_H) adsorption with feed gas (F) just above atmospheric pressure, countercurrent depressurization (CnD) from P_H to a lower (vacuum) pressure (P_L), countercurrent low-pressure desorption with light product purge as light reflux (LR), and light product pressurization (LPP) from P_L to P_H. The heavy product (CO_2) was enriched and recovered during the CnD and LR steps, whereas the inert light product (mainly N_2 and H_2O) was recovered during the feed step. The problem with this popular stripping PSA cycle with light reflux for enriching the heavy component is that the enrichment is limited by the pressure ratio and rarely approaches it due to significant dilution of the heavy product stream during the LR step (Subramanian and Ritter, 1997).

Table 3. Range of performances achieved in terms of feed throughput, and CO_2 purity and CO_2 recovery for a given stripping PSA cycle configuration and the range of process conditions studied.

Stripping PSA Cycle Configuration	Feed Throughput Range (L STP/hr/kg)	CO_2 Purity* (%)	CO_2 Recovery* (%)	Number of Simulations
4-Bed 4-Step Cycle with LR	7.2 – 43.2	17.5 – 62.7 (100) (75.3) [7.2] [21.6]	37.6 – 100 (31.7) (50.6) [43.2] [7.2]	450
4-Bed 5-Step Cycle with LR and CoD and CnD ($t_{co} = t_{cn} = 0.5t_s$; P_I = 101.3 kPa)	14.4	33.0 – 64.6 (73.9) (85.0) [14.4] [14.4]	59.4 – 95.4 (39.5) (43.1) [14.4] [14.4]	15
5-Bed 5-Step Cycle with LR and Co and CnD ($t_{co} = t_{cn} = t_s$; P_I = 101.3 kPa)	11.5	33.4 – 65.0 (75.5) (86.7) [11.5] [11.5]	59.4 – 97.3 (39.5) (43.4) [11.5] [11.5]	15
4-Bed 5-Step Cycle with LR and CoD and CnD ($t_{co} = t_{cn} = 0.5t_s$; P_I = 68.9 kPa)	14.4	37.7 – 68.2 (68.5) (84.2) [14.4] [14.4]	58.1 – 93.2 (41.1) (51.1) [14.4] [14.4]	15
5-Bed 5-Step Cycle with LR and HR from CnD**	5.8 – 17.3	27.5 – 72.2 (100) (82.2) [5.8] [11.5]	49.4 – 100 (38.9) (57.9) [17.3] [5.8]	180
5-Bed Cycle with LR and HR from LR Purge**	5.8 – 34.6	25.4 – 75.5 (100) (48.8) [5.8] [23.1]	14.8 – 100 (40.8) (47.8) [34.6] [5.8]	360
4-Bed 4-Step Cycle with HR from CnD	7.2 – 21.6	24.4 – 82.7 (59.6) (17.4) [7.2] [14.4]	1.7 – 95.2 (35.9) (30.1) [21.6] [7.2]	225

* The values in parentheses correspond to the CO_2 recovery achieved for the highest and lowest CO_2 purity, and the CO_2 purity achieved for the highest and lowest CO_2 recovery. The values in brackets correspond to the feed throughput achieved for the highest and lowest CO_2 purity, and the feed throughput achieved for the highest and lowest CO_2 recovery.

** The values for the highest and lowest CO_2 recovery and CO_2 purity are based on results with R_R = 0.2 to 0.8. The results for R_R = 0.0 correspond to those obtained for the 4-bed 4-step cycle with LR.

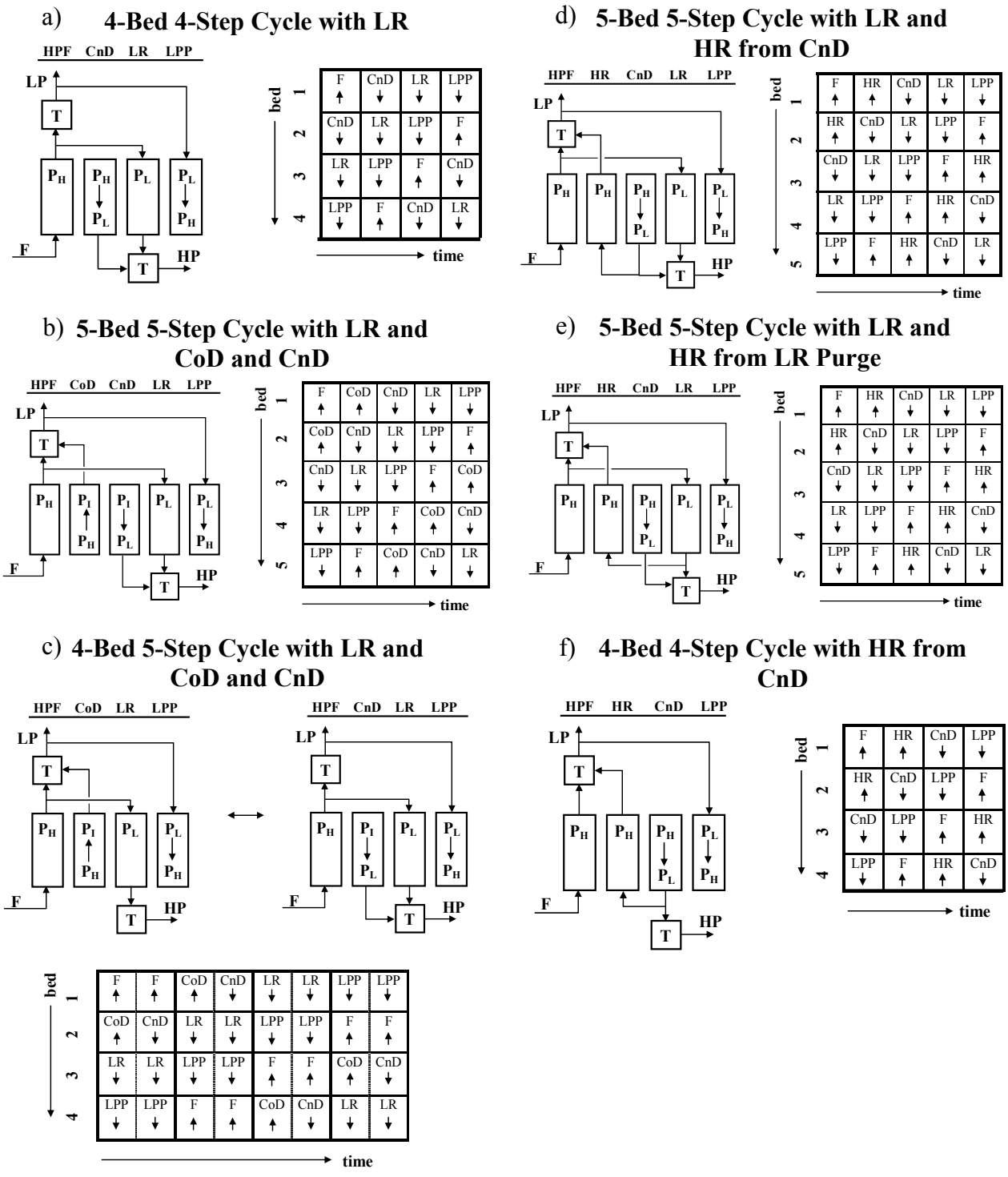

Figure 5. Schematics of the six different stripping PSA cycle configurations analyzed for high temperature CO_2 capture and concentration with the CO_2 selective K-promoted HTlc adsorbent. F = feed; CoD = cocurrent depressurization; CnD = countercurrent depressurization; LR = light reflux; HR = heavy reflux; LPP = light product pressurization; P_L = low pressure; P_H = high pressure; P_I = intermediate pressure; LP = light product; HP = heavy product; T = tank.

Four hundred fifty simulations of this cycle were carried out with the feed throughput ranging from 7.2 to 43.2 L STP/kg/hr (Tables 3 and 4). The effect of the feed throughput (θ) on the process performance of this cycle is shown collectively in Figures 6a to 6f with θ respectively varying from 7.2 to 43.2 L STP/kg/hr. Within each figure three cycle step times, five pressure ratios, and five light product purge to feed ratios were also investigated, with their respective effects on the process performance easily observed.

Table 4. Best performance achieved based on highest CO_2 purity obtained for a given stripping PSA cycle configuration and set of corresponding conditions.

Stripping PSA Cycle Configuration	Feed Throughput (L STP/hr/kg)[A]	Pressure Ratio[B]	Light Product Purge to Feed Ratio	Heavy Product Recycle Ratio	Cycle Time[C] (s)	CO_2 Purity (%)	CO_2 Recovery (%)
4-Bed 4-Step Cycle with LR	21.6 (1.5)	12	0.5	---	2000	62.7	75.3
4-Bed 5-Step Cycle with LR and CoD and CnD ($t_{co} = t_{cn} = 0.5t_s$; P_I = 101.3 kPa)	14.4 (1.0)	12	0.5	---	2000	64.6	85.0
5-Bed 5-Step Cycle with LR and Co and CnD ($t_{co} = t_{cn} = t_s$; P_I = 101.3 kPa)	11.2 (1.0)	12	0.5	---	2500	65.0	86.7
4-Bed 5-Step Cycle with LR and CoD and CnD ($t_{co} = t_{cn} = 0.5t_s$; P_I = 68.9 kPa)	14.4 (1.0)	12	0.5	---	2000	68.2	84.2
5-Bed 5-Step Cycle with LR and HR from CnD	11.5 (1.0)	12	0.5	0.8	2500	72.2	82.2
5-Bed Cycle with LR and HR from LR Purge	23.1 (2.0)	12	0.5	0.8	2500	75.5	48.8
4-Bed 4-Step Cycle with HR from CnD	14.4 (1.0)	12	0.5	0.8	2000	82.7	17.4

[A] Values in parentheses correspond to the feed flow rate Q_F in L STP/min.
[B] P_H = 137.9 kPa
[C] All step times t_s were equal in length except for the 4-bed 5-step stripping PSA cycle with LR and CoD and CnD where $t_{co} = t_{cn} = 0.5t_s$.

Any of the figures in Figure 6 show that the CO_2 recovery (R) decreased, but the CO_2 purity increased as the cycle step time t_s (or, equivalently, the total cycle time t_c) increased. Since CO_2 entered the column during the feed step, more CO_2 entered the system as t_s increased; thus, it was more likely for CO_2 to breakthrough into the light product, which decreased R with increasing t_s. However, as more CO_2 entered the system, more CO_2 was adsorbed by the hydrotalcite; hence, more CO_2 desorbed during the countercurrent depressurization and low pressure purge steps and exited the system in the enriched product gas, which caused the CO_2

purity to increase with increasing t_s.

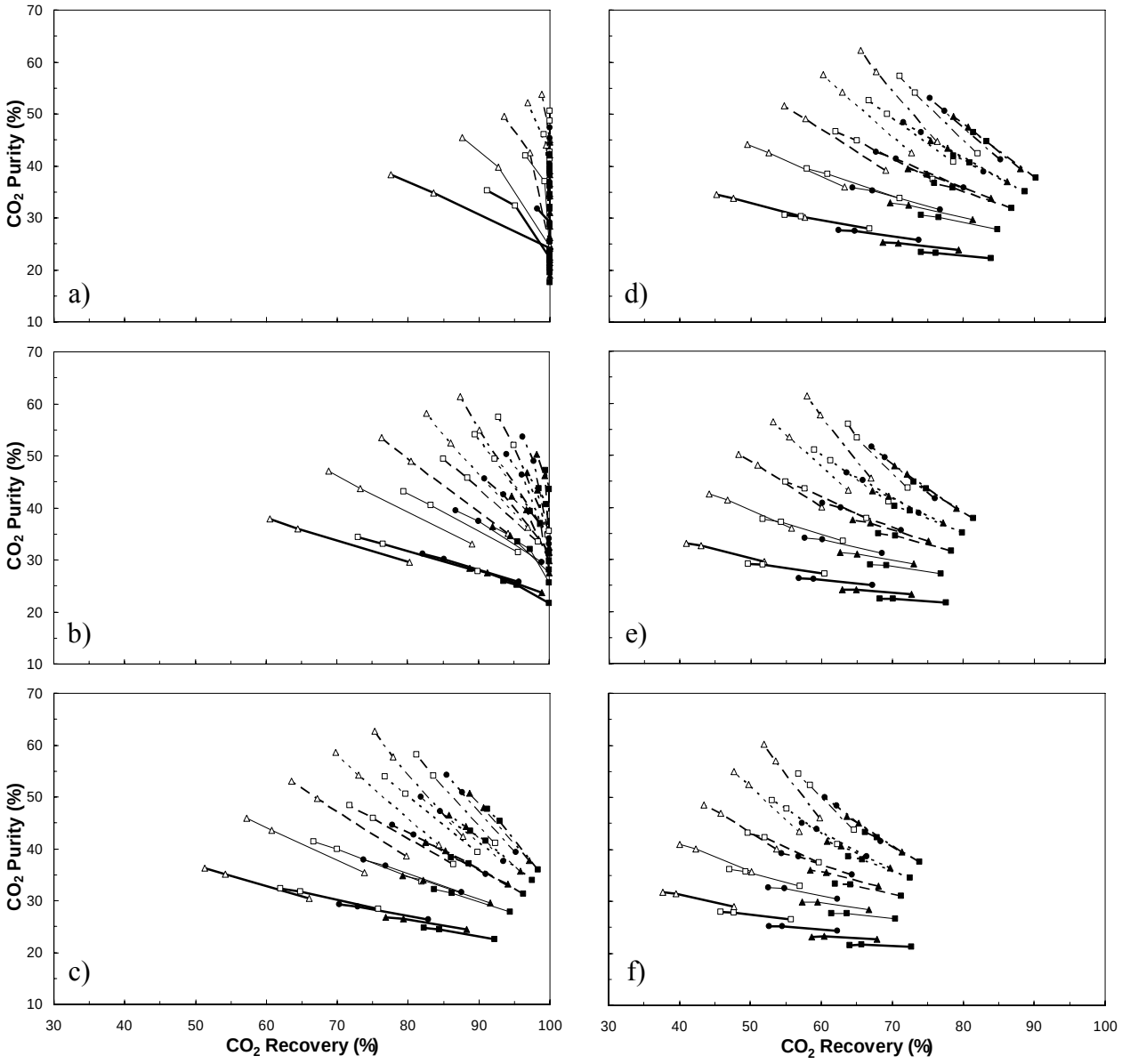

Figure 6. Comparison of performance curves for the 4-bed 4-step stripping PSA cycle with light reflux for θ or Q_F (in parentheses) = a) 7.2 (0.5), b) 14.4 (1.0), c) 21.6 (1.5), d) 28.8 (2.0), e) 36.0 (2.5), and f) 43.2 (3.0) L STP/hr/kg (L STP/min). Each line corresponds to three runs with t_s increasing from right to left (t_s = 100, 300 and 500 s). Lines: bold – π_T = 4; thin – π_T = 6; dashed – π_T = 8; dotted – π_T = 10; dot-and-dash – π_T = 12. Symbols: filled squares – γ = 1.50; filled triangles – γ = 1.25; filled circles – γ = 1.00; empty squares – γ = 0.75; empty triangles – γ = 0.50.

It is also observed from any of the figures in Figure 6 that the CO_2 recovery (R) and the

CO_2 purity both increased with an increase in the high to low pressure ratio π_T. Since t_s and P_H were fixed, the amount of CO_2 entering the system during the feed step was also fixed. Hence, the observed increases in the CO_2 recovery and the CO_2 purity with increasing π_T were actually caused by P_L decreasing, i.e., a deeper vacuum was being applied to the system. For a fixed γ (i.e., the ratio of the light product purge gas to feed gas velocities), a lower P_L meant less purge gas was used to clean the bed, which resulted in less dilution of the heavy product, which in turn caused the CO_2 purity to increase with increasing π_T. The working capacity of the adsorbent also increased, because larger pressure swings allowed for a greater change in the loading between the adsorption and desorption steps, as gleaned from the large slope changes in the low pressure regions of the CO_2 adsorption isotherms shown in Figure 1. This increased working capacity manifested as less breakthrough of CO_2 into the light product, which in turn caused R to increase with increasing π_T.

The figures in Figure 6 also reveal that the CO_2 recovery (R) increased but the CO_2 purity decreased as the light product purge to feed ratio (γ) increased. Since the purge gas was taken from the light product gas and used to sweep the low pressure column during the countercurrent purge step, more CO_2 left the column as enriched product. Also, the light product purge regenerated the adsorbent; thus, the adsorbent was able to adsorb more CO_2 in the subsequent adsorption step, thereby allowing less CO_2 to breakthrough into the light product. Both caused R to increase with increasing γ. However, since more of the light product was returned to the low pressure column as purge with increasing γ, it diluted the CO_2 in the heavy product, which caused the CO_2 purity to decrease with increasing γ.

A comparison of the results in Figures 6a to 6f reveals the effect of increasing the feed throughput θ (Figures 6a to 6f), which corresponds to an increase in the feed flow Q_F, on the CO_2 purity and the CO_2 recovery. These CO_2 purity versus CO_2 recovery plots show very clearly the conditions where a CO_2 recovery of 100% was achieved over a broad range of θ up to 14.4 L STP/hr/kg (Figures 6a and 6b). This was due to the column being long enough to avoid breakthrough of CO_2 into the light product stream under these conditions. However, for higher θ, breakthrough of CO_2 into the light product stream was eminent and the CO_2 recovery systematically decreased as θ increased, as noticed by comparing the results in Figures 6c to 6f. In contrast to the effect of θ on R, the CO_2 purity went through a maximum with increasing θ. Clearly, as θ increased, more CO_2 was fed to the column which in turn caused more CO_2 to be adsorbed by the hydrotalcite; hence, more CO_2 desorbed during the countercurrent depressurization and light reflux steps and exited the system in the enriched product gas, which caused the CO_2 purity to increase with increasing θ, but only up to a certain θ. Beyond this θ, the CO_2 purity began to decrease, because an increase in θ corresponded to an increase in the feed flow rate or feed velocity, which corresponded to an increase in the purge flow rate or purge velocity (i.e., the amount of light product gas used as light reflux) for a given γ. Since more and more of the light product was returned to the low pressure column as purge with increasing θ, the CO_2 in the heavy product stream became more and more diluted, which caused the CO_2 purity to eventually decrease with increasing θ.

In summary, the results in Table 3 and Figure 6 show clearly that at a CO_2 recovery of 100% the maximum CO_2 purity was limited to 50.6 vol% for this typical 4-bed 4-step stripping

PSA cycle with LR, with θ = 7.2 L STP/hr/kg, γ = 0.75, t_s = 500 s and π = 12. However, these were not the conditions that maximized the CO_2 purity. The results in Tables 3 and 4 and Figure 6 show that the maximum CO_2 purity obtained with this cycle was 62.7 vol% with the CO_2 recovery now limited to 75.3% for θ = 21.6 L STP/hr/kg, γ = 0.50, t_s = 500 s and π = 12.

Based on these results for this 4-bed 4-step stripping PSA cycle with light reflux, it became glaringly obvious that it was not possible to even approach a CO_2 purity of 100 vol% with this cycle, irrespective of the recovery. Hence, this cycle was modified in an attempt to improve the purity without diminishing the throughput and recovery. Five modifications of this stripping PSA cycle were studied to try to achieve this goal. The results are provided below.

2.5.2 5-Bed 5-Step and 4-Bed 5-Step Stripping PSA Cycles with LR, CoD and CnD

One way to increase the purity obtained from the 4-bed 4-step stripping PSA cycle with light reflux (LR) is to include a cocurrent depressurization (CoD) step along with the countercurrent depressurization (CnD) step, as shown in Figures 5b and 5c. During this CoD step the pressure in the column decreases from the high pressure (P_H) to some intermediate pressure (P_I) while still producing a light product gas, as explained earlier. However, depending on the P_I attained during CoD, some of the heavy component may be lost in the light product stream causing the CO_2 recovery to decrease. Also, to avoid significant loss of the heavy product in the light product stream, typically the cycle time or the feed flow rate must be decreased with the inclusion of a CoD step with both diminishing the feed throughput.

Forty-five simulations were run to investigate the effect of the CoD step: 15 simulations in a 4-bed 5-step configuration (Figure 5c) with P_I = 101.3 kPa and the CoD and CnD each consuming half of the cycle step time allotted for the other steps, 15 simulations in a 5-bed 5-step configuration (Figure 5b) with P_I = 101.3 kPa and the CoD and CnD each having the same cycle step time allotted for the other steps, and 15 simulations in a 4-bed 5-step configuration (Figure 5c) with P_I = 68.9 kPa and the CoD and CnD each consuming half of the cycle step time allotted for the other steps.

Two feed throughputs, θ = 14.4 and 11.5 L STP/kg/hr, corresponding to the same feed flow rate Q_F = 1.0 L STP/min, were studied with these stripping PSA cycles. The lower value of θ corresponds to the effect of adding the fifth bed to the cycle configuration to allow for all five steps to be carried out with the same cycle step time. Figure 7 reveals the effect of adding the CoD step to both 4-bed 5-step and 5-bed 5-step configurations (Figures 5c and 5b, respectively) with P_I = 101.3 kPa by comparing the performances of these PSA cycles to those obtained from the 4-bed 4-step stripping PSA cycle with LR and no CoD step (Figure 5a). Figure 8 shows the effect of changing P_I from 101.3 to 68.9 kPa in the 4-bed 5-step stripping PSA cycle with LR and CoD and CnD (Figures 5c). Within each figure, five pressure ratios (π_T) and three cycle step times (t_c) were investigated, with the light product purge to feed ratio γ = 0.5. Since the parametric effects of both π_T and t_c on the PSA process performance, i.e., the CO_2 purity and the CO_2 recovery, were the same as those just discussed with the 4-bed 4-step stripping PSA cycle with LR, along with their interpretation, they are not repeated here.

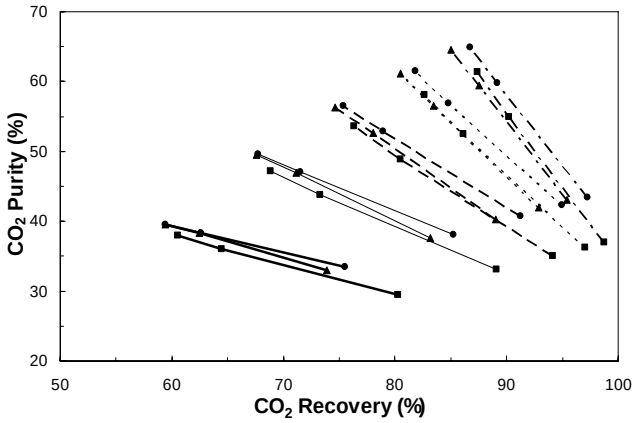

Figure 7. Comparison of performance curves for the 4-bed 4-step, 4-bed 5-step and 5-bed 5-step stripping PSA cycles with LR, and with and without CoD and CnD for $\gamma = 0.5$. θ or Q_F (in parentheses) = 14.4 L STP/hr/kg (1.0 L STP/min) for the 4-bed 4-step LR cycle, θ or Q_F (in parentheses) = 14.4 L STP/hr/kg (1.0 L STP/min) and $P_I = 101.3$ kPa for the 4-bed 5-step LR with CoD and CnD ($t_{co} = t_{cn} = 0.5t_s$), and θ or Q_F (in parentheses) = 11.5 L STP/hr/kg (1.0 L STP/min) and $P_I = 101.3$ kPa for the 5-bed 5-step LR with CoD and CnD ($t_{co} = t_{cn} = t_s$). Each line corresponds to three runs with t_s increasing from right to left (t_s = 100, 300 and 500 s). Lines: bold – $\pi_T = 4$; thin – $\pi_T = 6$; dashed – $\pi_T = 8$; dotted – $\pi_T = 10$; dot-and-dash – $\pi_T = 12$. Symbols: filled squares – 4-bed 4-step LR; filled triangles – 5-bed 5-step LR with CoD and CnD; filled circles – 4-bed 5-step LR with CoD and CnD.

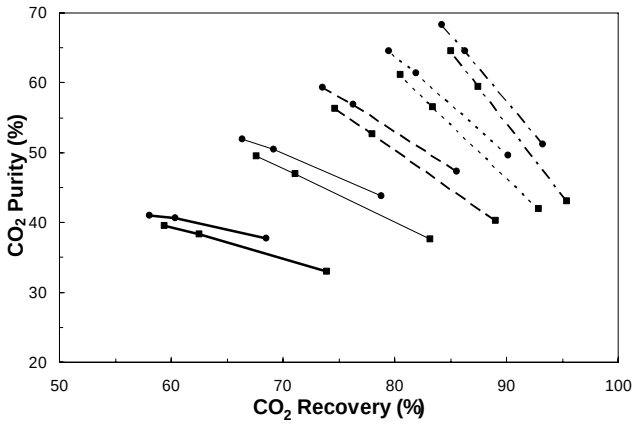

Figure 8. Comparison of performance curves with different intermediate pressures (P_I) for the 4-bed 5-step stripping PSA cycles with LR and CoD and CnD for $\gamma = 0.5$ and θ or Q_F (in parentheses) = 14.4 L STP/hr/kg (1.0 L STP/min). Each line corresponds to three runs with t_s increasing from right to left (t_s = 100, 300 and 500 s). Lines: bold – $\pi_T = 4$; thin – $\pi_T = 6$; dashed – $\pi_T = 8$; dotted – $\pi_T = 10$; dot-and-dash – $\pi_T = 12$. Symbols: filled triangles – P_I = 101.3 kPa; filled circles – P_I = 68.9 kPa.

The comparison between the original 4-bed 4-step stripping PSA cycle with LR, the 5-bed 5-step stripping PSA cycle with LR and CoD and CnD, and the 4-bed 5-step stripping PSA cycle with LR and CoD and CnD shown in Figure 7 reveals marginal but always positive effects of adding a CoD step, at least in terms of CO_2 purity. Essentially only a slight increase in the CO_2 purity resulted but always with a corresponding decrease in the CO_2 recovery, especially for the shorter cycle times, when adding the CoD step as a fifth step with its step time equal to all the other step times (5-bed configuration). However, in this case, the performance in terms of feed throughput actually decreased due to the addition of the fifth bed with all the other process conditions being held constant. In contrast, the change in performance, in terms of CO_2 purity and CO_2 recovery, was always slightly better when adding the CoD step as a fifth step with its step time equal to the CnD step time and half of that of the other step times (4-bed configuration). For example, for a given set of process conditions, the CO_2 recovery and the CO_2 purity both always increased and in this case at the same feed throughput. An explanation that anticipated these effects of adding a CoD step on the process performance was given previously. To further this explanation, one plausible reason for the only marginal effects observed here on the process performance when including a CoD step is associated with the value of P_I not being low enough to foster significant desorption of the heavy component during this step, especially with P_H limited in this case to being only slightly greater than atmospheric pressure.

Hence, an important variable when including a CoD step in a 4-bed stripping PSA cycle with LR is the intermediate pressure P_I. If P_I is too high, then the feed throughput is diminished and the CO_2 recovery is lost without a significant gain in the CO_2 purity. If P_I is too low, then the feed throughput is diminished with a corresponding large decrease in the CO_2 recovery but with a possible significant gain in the CO_2 purity. The most important point is that P_I should correspond to a steep region of the heavy component adsorption isotherm to foster significant desorption during the CoD step.

Fifteen simulations were carried out with P_I set at a lower intermediate pressure of 68.9 kPa. Figure 8 shows the effect of operating at this lower P_I by comparing the same 4-bed 5-step stripping PSA cycle with LR and CoD and CnD, but with different intermediate pressures of 101.3 and 68.9 kPa. In all cases, as expected and just explained, the lower P_I caused the process performance to improve in terms of the CO_2 purity; but this improvement came at the expense of decreasing the CO_2 recovery. For example, with $\gamma = 0.5$, $t_s = 500$ s and $\pi_T = 12$, the CO_2 purity increased from 64.6 to 68.2 vol% while R decreased from 85.0 to 84.2%. This marginal improvement also came at the expense of having to use a vacuum pump to draw gas from the light product end of the column to attain a $P_I = 68.9$ kPa.

In summary, the results in Table 3 show that for the 4-bed 5-step stripping PSA cycle with LR and CoD ($P_I = 101.3$ kPa) and CnD, at a CO_2 recovery of 95.4% the maximum CO_2 purity was limited to 43.1 vol% with $\theta = 14.4$ L STP/hr/kg, $\gamma = 0.50$, $t_s = 100$ s and $\pi = 12$. However, these were not the conditions that maximized the CO_2 purity. The results in Tables 3 and 4 and Figure 7 show that the maximum CO_2 purity obtained with this cycle was 64.6 vol% with the CO_2 recovery now limited to 85.0% for $\theta = 14.4$ L STP/hr/kg, $\gamma = 0.50$, $t_s = 500$ s and $\pi = 12$. In contrast, for the 5-bed 5-step stripping PSA cycle with LR and CoD ($P_I = 101.3$ kPa) and CnD, for the conditions studied, a CO_2 recovery of 100% was also not obtainable; it was

limited to 97.3% for θ = 11.5 L STP/hr/kg, γ = 0.50, t_s = 100 s and π = 12, with the maximum CO_2 purity limited to 43.4 vol%. However, these were not the conditions that resulted in a maximum CO_2 purity. These conditions were θ = 11.5 L STP/hr/kg, γ = 0.50, t_s = 500 s and π = 12, which resulted in a CO_2 purity of 65.0 vol% and a CO_2 recovery of 86.7%. Finally, for this 4-bed 5-step stripping PSA cycle with LR and CoD (P_I = 68.9 kPa) and CnD, at 93.2% CO_2 recovery the maximum CO_2 purity was now limited to 51.1 vol%, with θ = 14.4 L STP/hr/kg, γ = 1.25, t_s = 100 s and π = 12. However, these were not the conditions that maximized the CO_2 purity. The maximum CO_2 purity obtained with this cycle was 68.2 vol% with the CO_2 recovery limited to 84.2% for θ = 14.4 L STP/hr/kg, γ = 0.50, t_s = 500 s and π = 12, which was the best performance among all the cycles with a CoD step.

Hence, although a CoD step is utilized in many industrial PSA processes, for this particular PSA process, with its feed (high) pressure being limited (at least for now) to pressures only slightly above atmospheric pressure, based on the results obtained from these three stripping PSA cycles with a CoD step, this step does not appear to be a viable option for improving the performance of this particular high temperature PSA process much beyond that which can be achieved with the 4-bed 4-step stripping PSA cycle with LR and only a CnD step. Therefore, the CoD step was not investigated any further. Instead a heavy reflux (HR) step was added to the traditional 4-bed 4-step stripping PSA cycle with LR, either as an additional step or as a replacement for the LR step. These novel HR cycles are discussed below.

2.5.3 4-Bed 4-Step and 5-Bed 5-Step Stripping PSA Cycles with LR and or HR

Another way to improve the heavy product purity is to include a heavy reflux (HR) or cocurrent high pressure purge or rinse step, as shown in Figures 5d, 5e and 5f. This step takes a portion of the heavy product gas from the low pressure column during the countercurrent depressurization (CnD) step, the light reflux (LR) step or both steps, and uses it as high pressure purge or heavy reflux in the high pressure column following the feed step, as explained earlier. A HR step can be used in conjunction with a LR step, being in reality a dual reflux stripping PSA cycle, or it can be used without a LR step, being simply a HR stripping PSA cycle. However, like with the addition of a CoD step, to avoid significant loss of the heavy product in the light product stream, typically the cycle time or the feed flow rate must be decreased with the inclusion of a HR step with both diminishing the feed throughput. Also, the addition of a HR step usually requires an additional compressor to take the low pressure gas coming from the CnD and/or LR steps and compress it to the high pressure before being fed to the high pressure column.

Seven hundred sixty-five simulations were carried out to investigate various stripping PSA cycles with HR: 180 simulations in a 5-bed 5-step configuration (Figure 5d) with the HR gas coming from the CnD step (i.e., a dual reflux cycle), 360 simulations in a 5-bed 5-step configuration (Figure 5e) with the HR gas coming from the LR purge step instead of the CnD step (still a dual reflux cycle), and 225 simulations in a 4-bed 4-step configuration (Figure 5f) with the HR gas coming from the CnD step but now with no LR step.

Feed throughputs ranging from 5.8 to 34.6 L STP/kg/hr were studied with these stripping PSA cycles with HR (Tables 3 and 4). Figures 9a to 9c collectively show the effect of the feed

throughput varying from 5.8 to 17.3 L STP/hr/kg for the 5-bed 5-step stripping PSA cycle with LR and HR from CnD. Figures 10a to 10f collectively show the effect of the feed throughput varying from 5.8 to 34.6 L STP/hr/kg for the 5-bed 5-step stripping PSA cycle with LR and HR from LR purge. Figures 11a to 11c collectively show the effect of the feed throughput varying from 7.2 to 21.6 L STP/hr/kg for the 4-bed 4-step stripping PSA cycle with HR from CnD. Within each of these figures five different recycle ratios (R_R) varying from 0.0 to 0.8 were investigated, with the R_R defined as the fraction of gas coming from CnD or LR step that is recycled as HR. Note that the performance of a PSA cycle with $R_R = 0.0$ corresponds to that of the equivalent PSA cycle with one less bed and without a HR step. Within each of these figures five pressure ratios (π_T) and three cycle step times (t_c) were also investigated, with the light product purge to feed ratio $\gamma = 0.5$ for the two HR cycles that also have a LR step. Since the parametric effects of both π_T and t_c on the CO_2 purity and the CO_2 recovery, and their corresponding interpretation, were the same as those discussed with the 4-bed 4-step stripping PSA cycle with LR, they are not repeated here. Moreover, with the effects of θ on the process performance of these HR PSA cycles (including the interpretation of its effects) being essentially the same as those reported earlier for the 4-bed 4-step stripping PSA cycle with LR, with the CO_2 recovery from these HR PSA cycles always decreasing with increasing θ, and with the CO_2 purity either consistently increasing or going through a maximum with increasing θ, no further discussion on these trends is given here.

The results in Figures 9 to 11 collectively show that the HR step does indeed increase the CO_2 purity as the R_R increases, irrespective of the particular HR cycle sequence. Clearly, as more CO_2 entered the column during the HR step, more CO_2 was adsorbed by the K-promoted HTlc, leading to a higher CO_2 purity in the heavy product during the subsequent CnD and LR (i.e., desorption) steps. However, as more CO_2 entered the column during the HR step, the breakthrough of CO_2 in the light product gas increased, causing a substantial decrease in the CO_2 recovery as R_R increased.

For example, the results in Figure 9 for the 5-bed 5-step stripping PSA cycle with LR and HR from CnD show that the CO_2 purity increases from 62.7 to 70.2 vol% while the CO_2 recovery decreases from 75.3% to 69.0% with the R_R increasing from 0.0 to 0.8 and with θ = 17.3 L STP/hr/kg, $\gamma = 0.5$, $t_s = 500$ s and $\pi_T = 12$. It must be emphasized, however, that the changes in the process performance with an increase in the R_R were not as much as initially expected for this HR cycle. The reason for this subtle and highly diminished effect of the HR step was due to the fact that the HR gas was taken from the CnD step. The flow rate and hence total amount of the depressurization gas available for HR was quite small, which necessarily limited the amount of gas that could be used as HR to enrich the heavy product. In fact, the depressurization flow rate was approximately three to four times less than the LR flow rate, perhaps due to mass transfer limitations (recall that k_d is ten times less than k_a, and both are rather small; refer to Table 2). With this in mind, the effect of the HR step on the process performance was expected to be much more pronounced when the HR gas was obtained from the LR purge step instead of the CnD step. These results are shown in Figure 10.

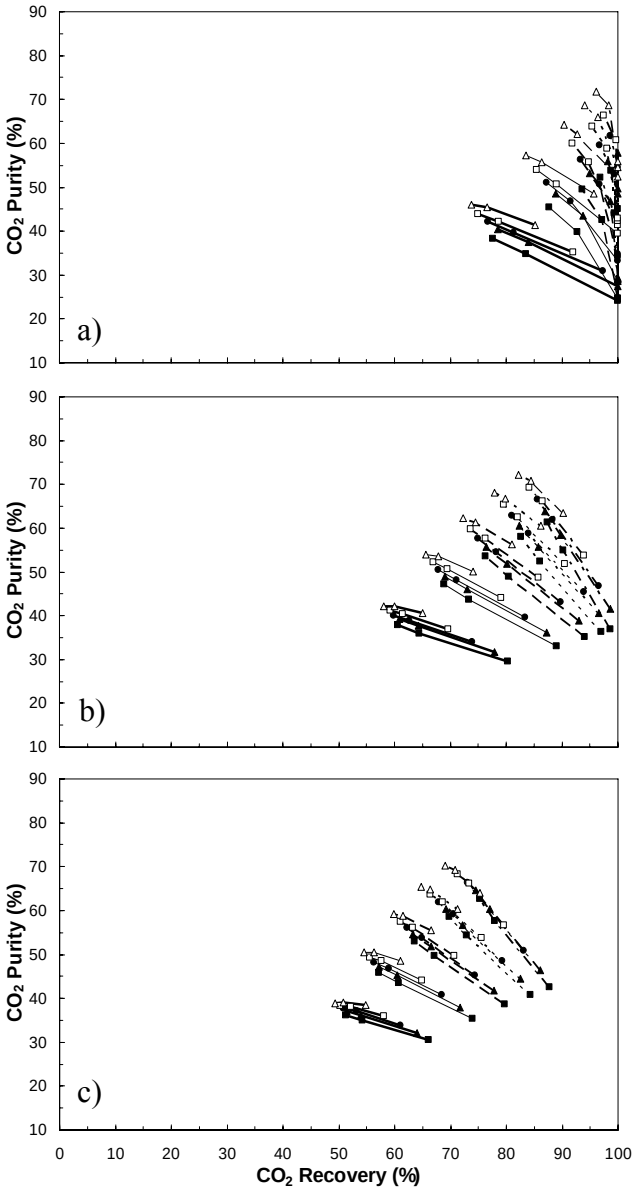

Figure 9. Comparison of performance curves for the 5-bed 5-step stripping PSA cycle with LR and HR from depressurization for $\gamma = 0.5$ and θ or Q_F (in parentheses) = a) 5.8 (0.5), b) 11.5 (1.0), and c) 17.3 (1.5) L STP/hr/kg (L STP/min). Each line corresponds to three runs with t_s increasing from right to left (t_s = 100, 300 and 500 s). Lines: bold – $\pi_T = 4$; thin – $\pi_T = 6$; dashed – $\pi_T = 8$; dotted – $\pi_T = 10$; dot-and-dash – $\pi_T = 12$. Symbols: filled squares – $R_R = 0.0$; filled triangles – $R_R = 0.2$; filled circles – $R_R = 0.4$; empty squares – $R_R = 0.6$; empty triangles – $R_R = 0.8$. For $R_R = 0.0$, the performance corresponds to that of a 4-bed 4-step stripping PSA cycle with LR at the same Q_F but with θ increased by the ratio 5:4.

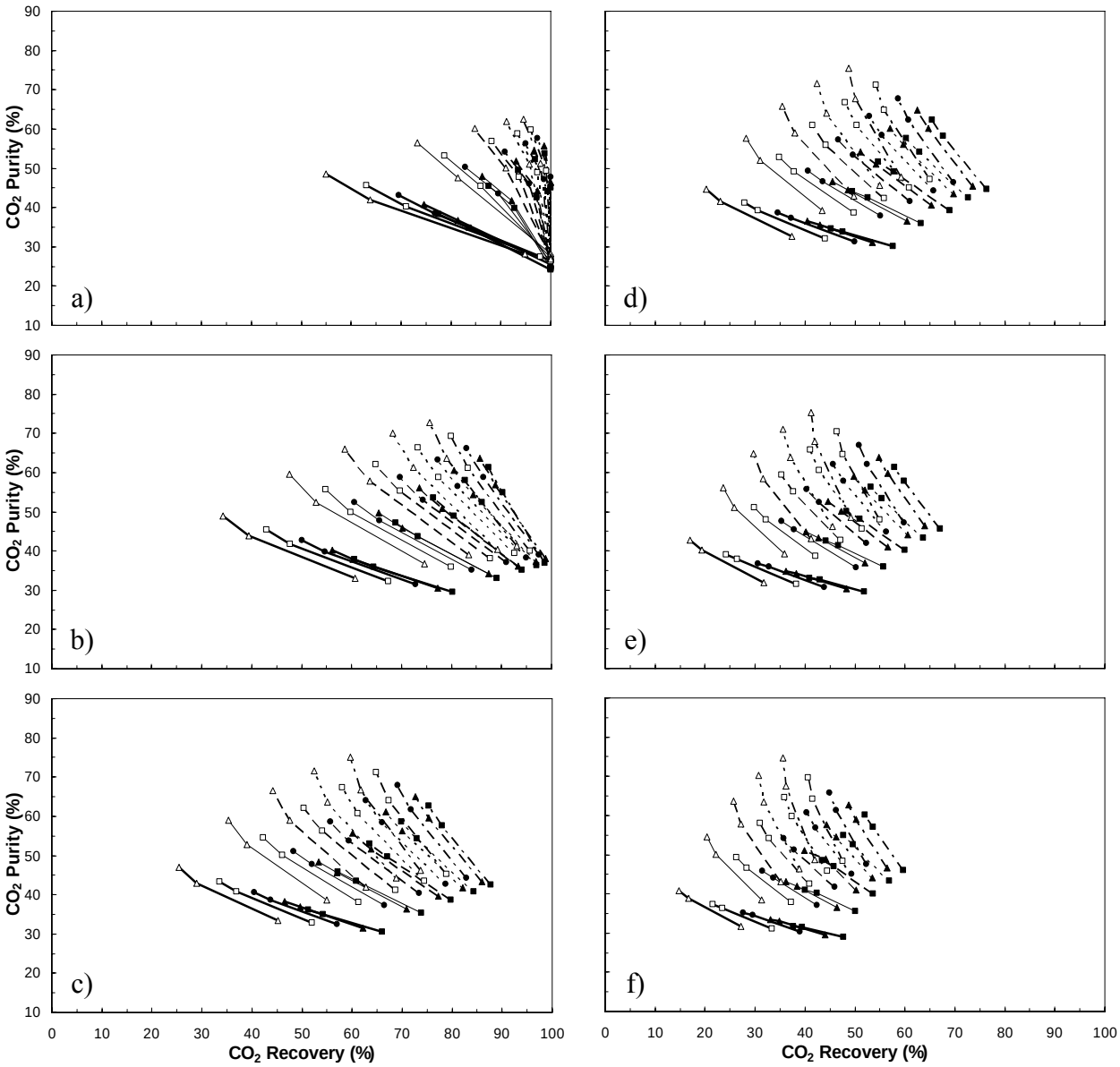

Figure 10. Comparison of performance curves for the 5-bed 5-step stripping PSA cycle with LR and HR from purge for $\gamma = 0.5$ and θ or Q_F (in parentheses) = a) 5.8 (0.5), b) 11.5 (1.0), c) 17.3 (1.5), d) 23.1 (2.0), e) 28.8 (2.5), and f) 34.6 (3.0) L STP/hr/kg (L STP/min). Each line corresponds to three runs with t_s increasing from right to left (t_s = 100, 300 and 500 s). Lines: bold – $\pi_T = 4$; thin – $\pi_T = 6$; dashed – $\pi_T = 8$; dotted – $\pi_T = 10$; dot-and-dash – $\pi_T = 12$. Symbols: filled squares – $R_R = 0.0$; filled triangles – $R_R = 0.2$; filled circles – $R_R = 0.4$; empty squares – $R_R = 0.6$; empty triangles – $R_R = 0.8$. For $R_R = 0.0$, the performance corresponds to that of a 4-bed 4-step stripping PSA cycle with LR at the same Q_F but with θ increased by the ratio 5:4.

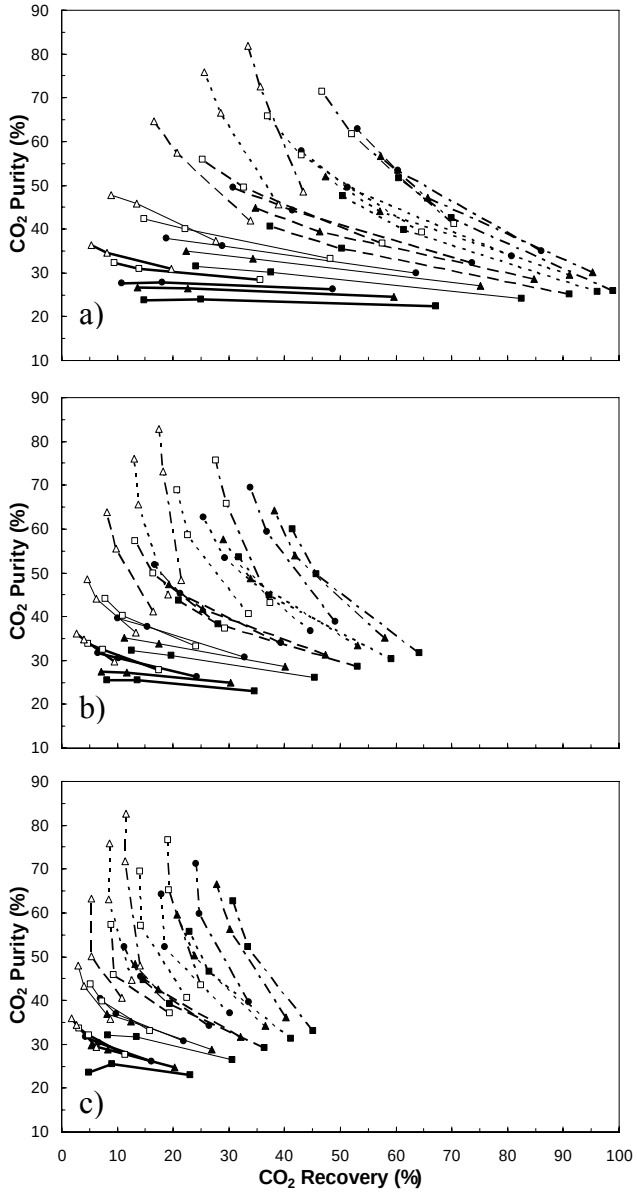

Figure 11. Comparison of performance curves for the 4-bed 4-step stripping PSA cycle with HR from depressurization for θ or Q_F (in parentheses) = a) 7.2 (0.5), b) 14.4 (1.0), and c) 21.6 (1.5) L STP/hr/kg (L STP/min). Each line corresponds to three runs with t_s increasing from right to left (t_s = 100, 300 and 500 s). Lines: bold – π_T = 4; thin – π_T = 6; dashed – π_T = 8; dotted – π_T = 10; dot-and-dash – π_T = 12. Symbols: filled triangles – R_R = 0.2; filled circles – R_R = 0.4; empty squares – R_R = 0.6; empty triangles – R_R = 0.8.

The results in Figure 10 for the 5-bed 5-step stripping PSA cycle with LR and HR from LR purge show a dramatic and positive effect of the R_R on the process performance in terms of

the CO_2 purity but at the expense of significantly decreasing the CO_2 recovery. For example, the CO_2 purity increases from 62.7 to 75.0 vol% while the CO_2 recovery decreases from 75.3 to 59.7% with the R_R increasing from 0.0 to 0.8 and with θ = 17.3 L STP/hr/kg, γ = 0.5, t_s = 500 s and π_T = 12. This is in stark contrast to the effects of the HR step shown in Figure 9. As just alluded to, the marked increase in CO_2 purity that resulted from the 5-bed 5-step stripping PSA cycle with LR and HR from LR purge, as compared to the same stripping PSA cycle with LR and HR from CnD, was caused by the larger purge flow rate compared to the depressurization flow rate that allowed more CO_2 to enter the high pressure column. In fact, the 5-bed 5-step stripping PSA cycle with LR and HR from LR purge produced the best process performance among all the dual reflux cycles, at least in terms of CO_2 purity (75.5 vol%) with a reasonable feed throughput (23.1 L STP/kg/hr) but unfortunately with a rather low CO_2 recovery (48.8 %).

The final stripping PSA cycle evaluated in this study was a 4-bed 4-step stripping PSA cycle with HR from CnD (because no LR step was included). This cycle was worth evaluating because by eliminating the LR step only 4 beds were needed and more importantly dilution of the heavy product gas would possibly be minimized. The results are shown in Figure 11 for three feed throughputs ranging from 7.2 to 21.6 L STP/kg/hr. In general, a comparison of Figures 9 and 11 reveals that under similar conditions, elimination of the LR step resulted in moderate increases in the CO_2 purity but marked decreases in the CO_2 recovery. The CO_2 purity increased because there was no LR step to dilute the heavy product or the heavy reflux. The CO_2 recovery was greatly reduced because without LR it was very difficult to effect substantial regeneration of the adsorbent during the cycle, again possibly due to mass transfer limitations. Since the adsorbent was not very well regenerated, breakthrough of CO_2 into the light product gas was more prevalent thereby reducing the CO_2 recovery. For example, for θ = 17.3 L STP/hr/kg, R_R = 0.8, γ = 0.5, t_s = 500 s and π_T = 12, the CO_2 purity and the CO_2 recovery for the 5-bed 5-step process (Figure 9) were respectively 70.2 vol% and 69.0%, while they were 82.6 vol% and 11.5% for the 4-bed 4-step process (Figure 11). The best performance for this 4-bed 4-step stripping PSA cycle with HR from CnD in terms of CO_2 purity was the best of all the HR PSA cycles studied, with a CO_2 purity of 82.7 vol% at a CO_2 recovery of only 17.4% and a throughput of only 14.4 L STP/kg/hr (Table 4).

Summarizing, the results in Table 3 and Figure 9 show that for the 5-bed 5-step stripping PSA cycle with LR and HR from CnD, the maximum CO_2 recovery was 100% at a CO_2 purity of 57.9 vol%, with θ = 5.8 L STP/hr/kg, γ = 0.50, t_s = 500 s, π = 12 and R_R = 0.2. However, these were not the conditions that maximized the CO_2 purity. The results in Tables 3 and 4 and Figure 9 show that the maximum CO_2 purity obtained with this cycle was 72.2 vol% with the CO_2 recovery limited to 82.2% for θ = 11.5 L STP/hr/kg, γ = 0.50, t_s = 500 s, π = 12 and R_R = 0.8. In contrast, Table 3 and Figure 10 show that for the 5-bed 5-step stripping PSA cycle with LR and HR from LR purge, the CO_2 recovery was 100% at a maximum CO_2 purity of 47.8 vol% with θ = 5.8 L STP/hr/kg, γ = 0.50, t_s = 300 s, π = 12 and R_R = 0.4. However, the conditions that resulted in the maximum CO_2 purity of 75.5 vol% at a CO_2 recovery of 48.8% were different, with θ = 23.1 L STP/hr/kg, γ = 0.50, t_s = 500 s, π = 12 and R_R = 0.8 (Tables 3 and 4, and Figure 10). Finally, the results in Table 3 and Figure 11 show that for the 5-bed 5-step stripping PSA cycle with HR from CnD, 100% recovery of CO_2 was not obtainable under the conditions studied; in this case, with θ = 5.8 L STP/hr/kg, γ = 0.50, t_s = 100 s, π = 12 and R_R = 0.2, the maximum CO_2 recovery was limited to 95.2%, which resulted in a CO_2 purity of 30.1vol%. The

conditions that resulted in a maximum CO_2 purity of 82.7 vol% were different, with θ = 14.4 L STP/hr/kg, γ = 0.50, t_s = 500 s, π = 12 and R_R = 0.8, but this limited the CO_2 recovery to 17.4% (Tables 3 and 4, and Figure 11).

It is important to remark that, in terms of CO_2 purity, these performances were, in some cases, similar to those listed in Table 1 for the stripping PSA cycles utilizing HR, however, in other cases, a significant disparity existed between them, with the CO_2 purity never exceeding 85 vol% in this study compared to 99.9+ vol% reported in the literature. Possible reasons for these performance differences include slight cycle step variations, such as unequal step times and heavy component recycle or recovery during the heavy reflux step, and adsorbent properties, such as mass and heat transfer effects.

2.5.4 Effects of Mass Transfer on the PSA Process Performance

The results discussed in the previous section showed that the three stripping PSA cycles with a heavy reflux (HR) step outperformed the three stripping PSA cycles without a HR step, with the 5-bed 5-step stripping PSA cycle with light reflux (LR) and HR from LR purge (i.e., a dual reflux cycle) and the 4-bed 4-step stripping PSA cycle with HR from countercurrent depressurization (CnD) providing the best process performances. With the best performance defined in terms of CO_2 purity, the 5-bed process produced a CO_2 purity of 75.5 vol%, a CO_2 recovery of 48.8%, and a feed throughput of 23.1 L STP/hr/kg. In contrast, the 4-bed process produced a higher CO_2 purity of 82.7 vol%, a lower CO_2 recovery of 17.4%, and a lower feed throughput of 14.4 L STP/hr/kg. No matter the CO_2 recovery or feed throughput, this showed that it was not possible to obtain a higher CO_2 purity with any of the six cycles. Yet, a CO_2 purity approaching 100% with a reasonable recovery and feed throughput is desirable for CO_2 sequestration or sale.

However, the values of two key parameters utilized in the PSA process simulator were uncertain. These were the adsorption (k_a) and desorption (k_d) mass transfer coefficients for CO_2 in the K-promoted HTlc. The values of k_a and k_d used in all the previous studies of this system by the authors were those reported by Ding and Alpay (2001) i.e., 0.0058 s^{-1} for adsorption and 0.0006 s^{-1} for desorption. Ding and Alpay (2001) also stated that similar adsorption and desorption mass transfer coefficients would be attained if the surface diffusion was negligible to the overall flux. In contrast, Hufton et al. (1999) showed very steep breakthrough curves and an elution curve predicted by equilibrium theory, with both indicating very fast mass transfer. Soares et al.(2004) very recently reported mass transfer coefficients as high as 0.0153 s^{-1} for CO_2 release from a HTlc.

The objective of this analysis was to report the effects of adsorption and desorption mass transfer coefficients of CO_2 in a K-promoted HTlc on the PSA process performance. To meet this objective, PSA process simulations were carried out over a wide range of conditions to compare the results obtained from the original adsorption and desorption mass transfer coefficients of CO_2 in the K-promoted HTlc with those obtained from their magnitudes increased by factors of five and ten. Simulations were also carried out to determine the effect of equal adsorption and desorption mass transfer coefficients, with the desorption mass transfer coefficient increased and set equal to the original adsorption mass transfer coefficient and also

with both of them increased by a factor of five.

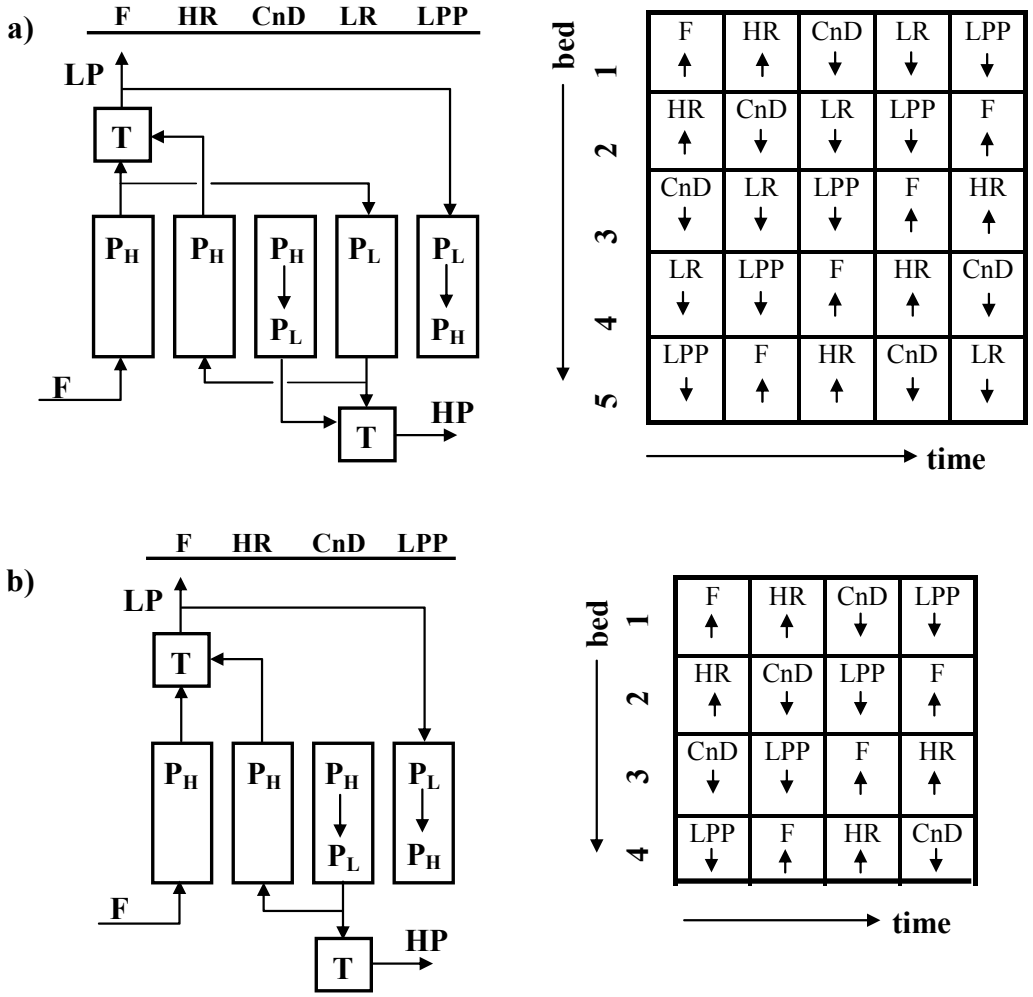

Figure 12. Schematic diagrams and cycle sequencing of a) the 5-bed 5-step stripping PSA cycle with LR and HR from LR purge and b) the 4-bed 4-step stripping PSA cycle with HR from CnD. F = feed; CnD = countercurrent depressurization; LR = light reflux; HR = heavy reflux; LPP = light product pressurization; P_L = low pressure; P_H = high pressure; LP = light product; HP=heavy product; T=tank.

The schematic diagrams of a 5-bed 5-step stripping PSA cycle with LR and HR from LR purge and a 4-bed 4-step stripping PSA cycle with HR from CnD studied for this analysis, along with their cycle sequencing, are depicted in Figure 12. The former cycle consisted of the following five cycle steps: feed (F), heavy reflux (HR), countercurrent depressurization (CnD), light reflux (LR) and light product pressurization (LPP). The latter cycle consisted of the following four cycle steps: feed (F), heavy reflux (HR), countercurrent depressurization (CnD) and light product pressurization (LPP). The F step was carried out cocurrently at just above atmospheric pressure (P_H). This step was followed by the HR or high pressure rinse step, which was also carried out cocurrently at P_H. The HR gas was obtained from the column undergoing the

LR step for the 5-bed 5-step process and from the column undergoing the CnD step for the 4-bed 4-step process. The CnD step was carried out next, which entailed evacuating the column countercurrently to decrease its pressure from P_H to the low pressure (P_L). For the 5-bed 5-step process, the LR step followed and was carried out countercurrently at P_L, with the purge gas obtained from the light product of the column undergoing the F step. The 4-bed 4-step process did not have a LR step. The final step in each cycle sequence was the LPP step, which was carried out countercurrently to increase the pressure in the bed from P_L to P_H. The LPP gas was obtained from the light products (mainly N_2 and H_2O) produced from the beds undergoing the F and HR steps. It was delivered to the column at ambient temperature and at the average composition of the two light product streams after blending. The heavy product (CO_2) was enriched and recovered during the CnD and LR steps.

The adsorption and desorption mass transfer coefficients (k_a and k_d) for CO_2 on the K-promoted HTlc used for all the results discussed in the previous sections were 0.0058 s^{-1} and 0.0006 s^{-1}, respectively. Since an uncertainty existed in those base case values, the values of k_a and k_d were increased by factors of five and ten. The desorption mass transfer coefficient was also set equal to the adsorption mass transfer coefficient, and this value was also increased by a factor of five.

Hundreds of simulations of the two PSA cycles with a HR step (Figure 12) were carried out using the cyclic adsorption process simulator to study mass transfer effects. In all of the simulations, like before, the mole fractions of CO_2, N_2 and H_2O in the feed were fixed at 0.15, 0.75 and 0.10, respectively. The rest of the process parameters were kept the same as depicted in Table 2. Figures 13 to 18 display the effects of systematic changes in the adsorption and desorption mass transfer coefficients on the process performances of the 5-bed and 4-bed stripping PSA cycles in terms of CO_2 purity versus CO_2 recovery plots. The high to low pressure ratio (P_H/P_L), the cycle time (t_c), and the heavy product reflux ratio (R_R) were varied in some of these plots, while the light product purge to feed ratio (γ) was always fixed. In every simulation, the duration of each cycle step was the same, which made the feed throughput smaller for the 5-bed process compared to the 4-bed process at the same feed flow rate, because of the additional step. R_R was defined as the fraction of gas coming from CnD or LR step that was recycled as HR, whereas γ was defined in the usual way as the ratio of the LR purge gas to feed gas velocities.

The effect of increasing the base case adsorption and desorption mass transfer coefficients both by a factor of five on the process performance is shown in Figure 13 for a range of cycle times (t_s), high to low pressure ratios (π_T), and feed throughputs (θ) at a fixed light product purge to feed ratio ($\gamma = 0.5$) and heavy product recycle ratio ($R_R = 0.8$). The higher mass transfer coefficients always improved the process performance by increasing both the CO_2 recovery and the CO_2 purity. For example, the best process performance that resulted with the original mass transfer coefficients corresponded to a CO_2 purity of 75.5%, a CO_2 recovery of 48.8% at a throughput of 23.1 L STP/hr/kg. For the same set of conditions, when the adsorption and desorption mass transfer coefficients were both increased by a factor of five, the CO_2 purity increased to 84.5% and the CO_2 recovery increased to 92.1%. Clearly, the mass transfer coefficients had a marked effect on the process performance.

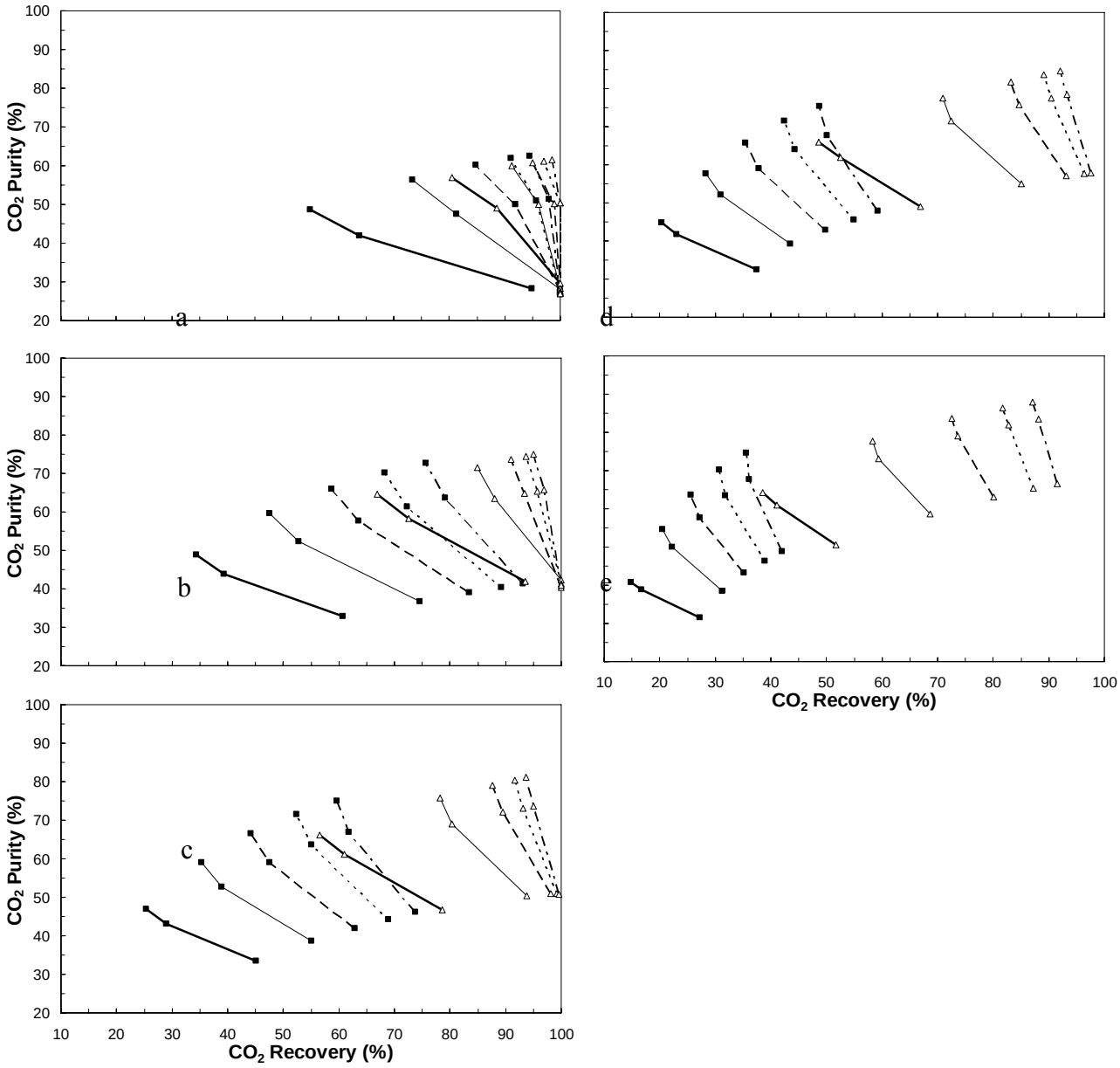

Figure 13. Comparison of the performance curves obtained from the 5-bed 5-step stripping PSA cycle with LR and HR from LR purge for the base case mass transfer coefficients (k_a = 0.0058 s^{-1} and k_d = 0.0006 s^{-1}) and five times those values (k_a = 0.029 s^{-1} and k_d = 0.003 s^{-1}). γ = 0.5, R_R = 0.8 and θ or Q_F (in parentheses) = a) 5.8 (0.50), b) 11.5 (1.00), c) 17.3 (1.50), d) 23.1 (2.00), and e) 34.6 (3.00) L STP/hr/kg (L STP/min). Each line corresponds to three runs with t_s increasing from right to left (t_s = 100, 300, and 500 s). Lines: bold – π_T = 4; thin – π_T = 6; dashed – π_T = 8; dotted – π_T = 10; dot-and-dash – π_T = 12. Symbols: filled squares – base case mass transfer coefficients; empty triangles – five times the base case mass transfer coefficients.

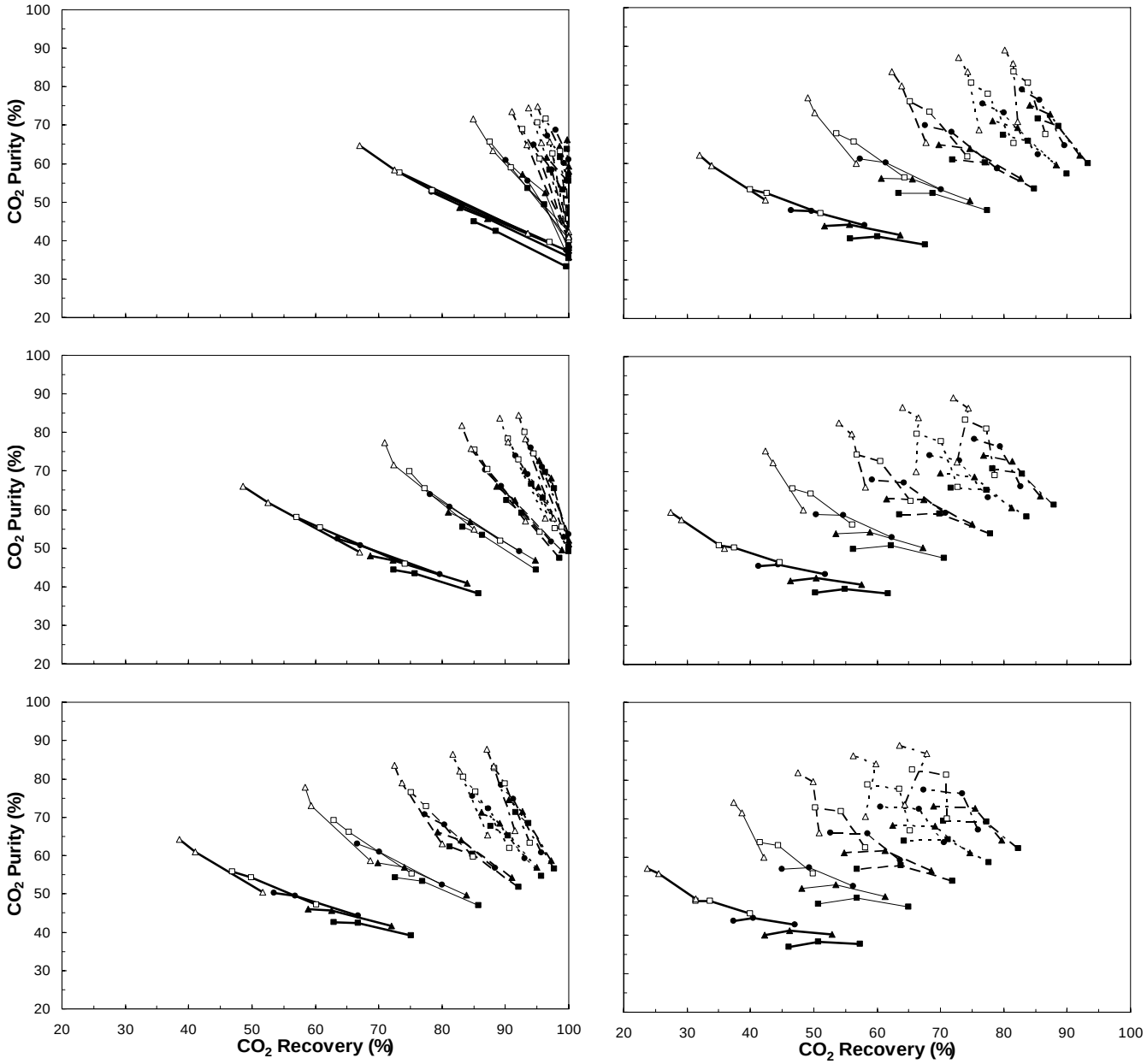

Figure 14. Comparison of the performance curves obtained from the 5-bed 5-step stripping PSA cycle with LR and HR from LR purge for the case with the five times higher mass transfer coefficients (k_a = 0.029 s^{-1} and k_d = 0.003 s^{-1}). γ = 0.5 and θ or Q_F (in parentheses) = a) 11.5 (1.00), b) 23.1 (2.00), c) 34.6 (3.00), d) 46.1 (4.00), e) 57.6 (5.00), and f) 69.2 (6.00) L STP/hr/kg (L STP/min). Each line corresponds to three runs with t_s increasing from right to left (t_s = 100, 300, and 500 s). Lines: bold – π_T = 4; thin – π_T = 6; dashed – π_T = 8; dotted – π_T = 10; dot-and-dash – π_T = 12. Symbols: filled squares – R_R = 0.0; filled triangles – R_R = 0.2; filled circles – R_R = 0.4; empty squares – R_R = 0.6; empty triangles – R_R = 0.8. For R_R = 0.0, the performance corresponds to that of a 4-bed 4-step stripping PSA cycle with LR at the same Q_F but with θ increased by the ratio 5:4.

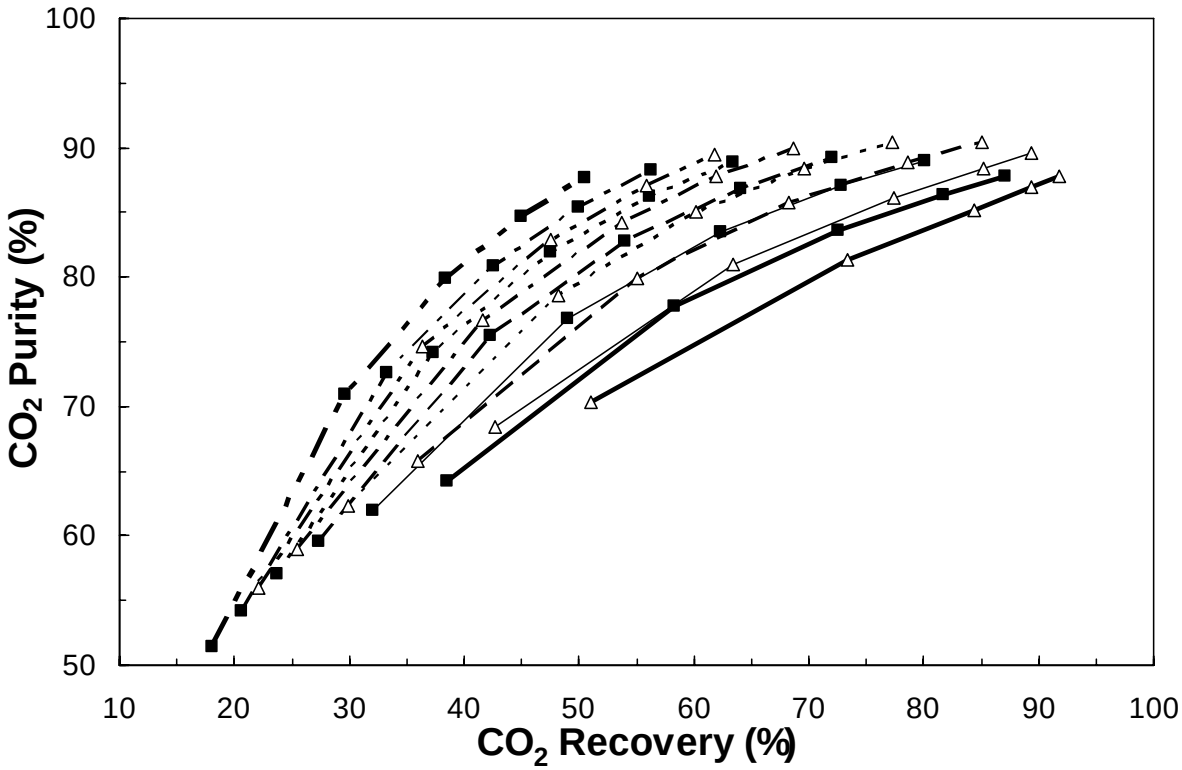

Figure 15. Comparison of the performance curves obtained from the 5-bed 5-step stripping PSA cycle with LR and HR from LR purge for the cases with five (k_a = 0.029 s^{-1} and k_d = 0.003 s^{-1}) and ten (k_a = 0.058 s^{-1} and k_d = 0.006 s^{-1}) times higher mass transfer coefficients. γ = 0.5, R_R = 0.8, and t_s = 500 s. Each line corresponds to five runs with π_T increasing from left to right (π_T = 4, 6, 8, 10, and 12). Lines: bold – θ or Q_F (in parentheses) = 34.6 (3.00); thin – θ or Q_F (in parentheses) = 46.1 (4.00); dashed – θ or Q_F (in parentheses) = 57.6 (5.00); dotted – θ or Q_F (in parentheses) = 69.2 (6.00); dot-and-dash – θ or Q_F (in parentheses) = 80.7 (7.00); dot-dot-dash – θ or Q_F (in parentheses) = 92.2 (8.00) L STP/hr/kg (L STP/min). Symbols: filled squares – five times the base case mass transfer coefficients (k_a = 0.029 s^{-1} and k_d = 0.003 s^{-1}); empty triangles – ten times the base case mass transfer coefficients (k_a = 0.058 s^{-1} and k_d = 0.006 s^{-1}).

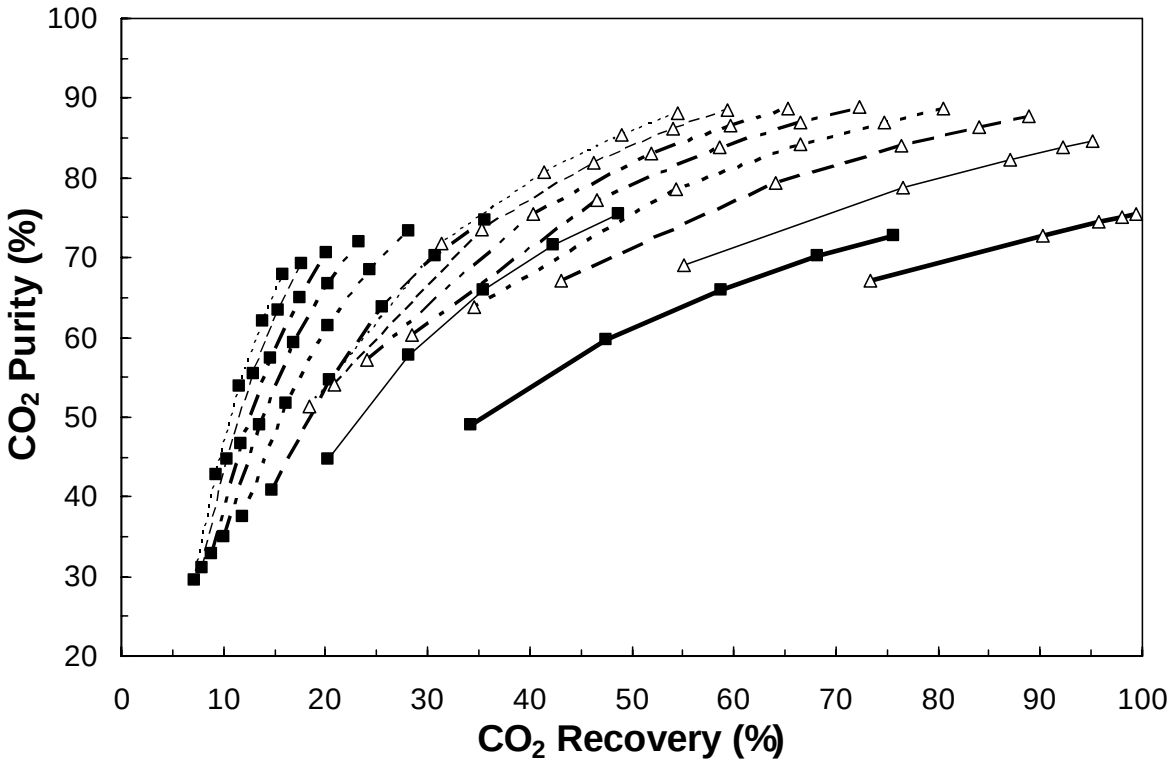

Figure 16. Comparison of the performance curves obtained from the 5-bed 5-step stripping PSA cycle with LR and HR from LR purge for the cases with original (k_a = 0.0058 s^{-1} and k_d = 0.0006 s^{-1}) and equal (k_a = 0.0058 s^{-1} and k_d = 0.0058 s^{-1}) mass transfer coefficients. γ = 0.5, R_R = 0.8, and t_s = 500 s. Each line corresponds to five runs with π_T increasing from left to right (π_T = 4, 6, 8, 10, and 12). Lines: bold – θ or Q_F (in parentheses) = 34.6 (3.00); thin – θ or Q_F (in parentheses) = 46.1 (4.00); dashed – θ or Q_F (in parentheses) = 57.6 (5.00); dotted – θ or Q_F (in parentheses) = 69.2 (6.00); dot-and-dash – θ or Q_F (in parentheses) = 80.7 (7.00); dot-dot-dash – θ or Q_F (in parentheses) = 92.2 (8.00) L STP/hr/kg (L STP/min). Symbols: filled squares – base case mass transfer coefficients (k_a = 0.0058 s^{-1} and k_d = 0.0006 s^{-1}); empty triangles – equal mass transfer coefficients (k_a = 0.0058 s^{-1} and k_d = 0.0058 s^{-1}).

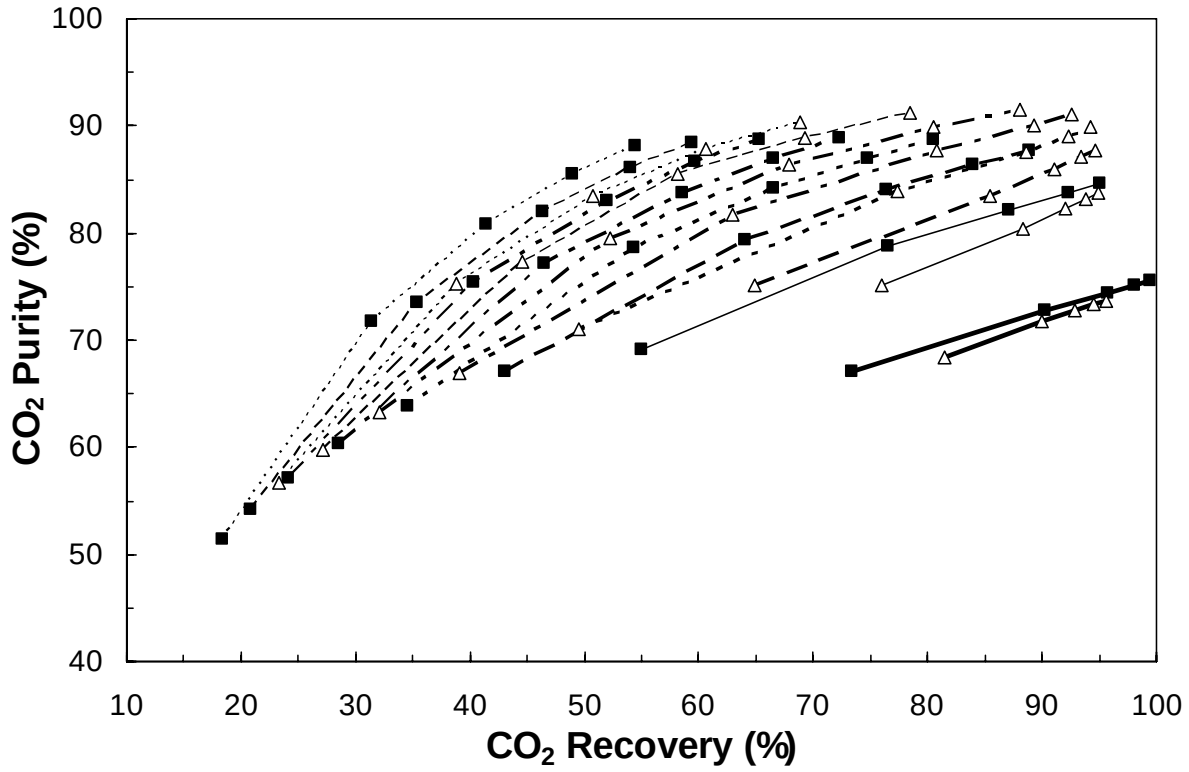

Figure 17. Comparison of the performance curves obtained from the 5-bed 5-step stripping PSA cycle with LR and HR from LR purge for the cases with equal (k_a = 0.0058 s^{-1} and k_d = 0.0058 s^{-1}) and five times higher and equal (k_a = 0.029 s^{-1} and k_d = 0.029 s^{-1}) mass transfer coefficients. γ = 0.5, R_R = 0.8, and t_s = 500 s. Each line corresponds to five runs with π_T increasing from left to right (π_T = 4, 6, 8, 10, and 12). Lines: bold – θ or Q_F (in parentheses) = 34.6 (3.00); thin – θ or Q_F (in parentheses) = 46.1 (4.00); dashed – θ or Q_F (in parentheses) = 57.6 (5.00); dotted – θ or Q_F (in parentheses) = 69.2 (6.00); dot-and-dash – θ or Q_F (in parentheses) = 80.7 (7.00); dot-dot-dash – θ or Q_F (in parentheses) = 92.2 (8.00) L STP/hr/kg (L STP/min). Symbols: filled squares – equal mass transfer coefficients (k_a = 0.0058 s^{-1} and k_d = 0.0058 s^{-1}); empty triangles – five times and equal mass transfer coefficients (k_a = 0.029 s^{-1} and k_d = 0.029 s^{-1}).

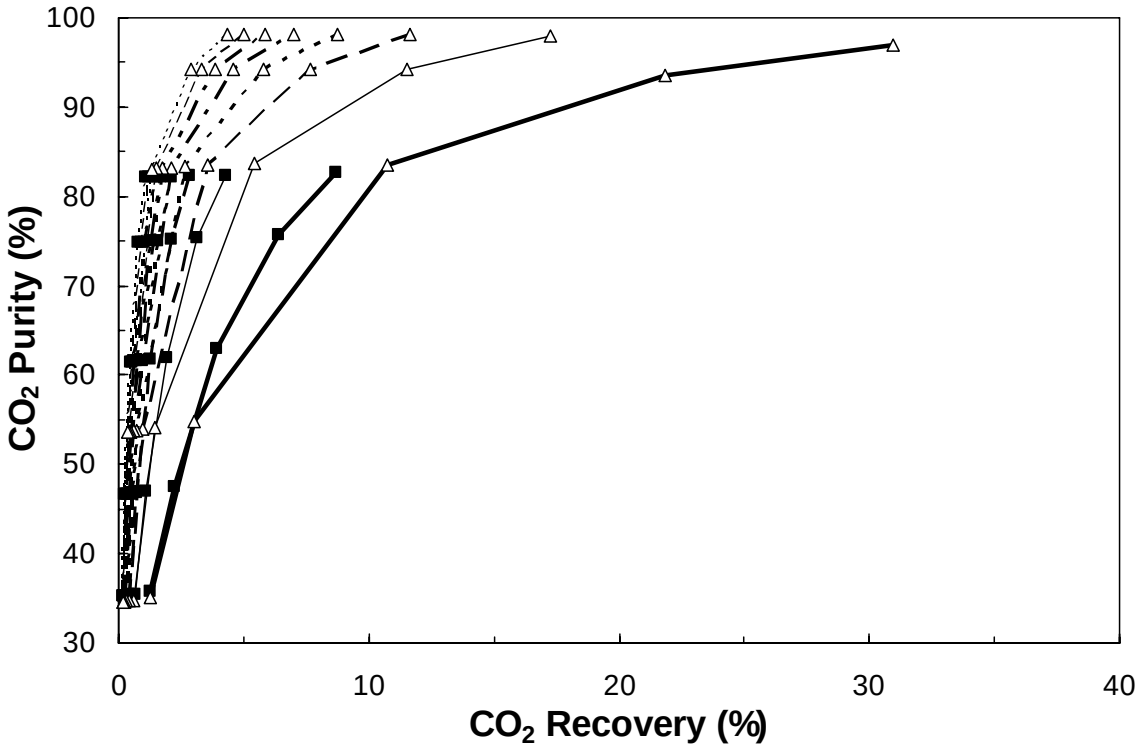

Figure 18. Comparison of the performance curves obtained from the 4-bed 4-step stripping PSA cycle with HR from CnD for the cases with original (k_a = 0.0058 s^{-1} and k_d = 0.0006 s^{-1}) and five times higher (k_a = 0.029 s^{-1} and k_d = 0.003 s^{-1}) mass transfer coefficients. γ = 0.5, R_R = 0.8, and t_s = 500 s. Each line corresponds to five runs with π_T increasing from left to right (π_T = 4, 6, 8, 10, and 12). Lines: bold – θ or Q_F (in parentheses) = 28.8 (2.00); thin – θ or Q_F (in parentheses) = 57.6 (4.00); dashed – θ or Q_F (in parentheses) = 86.4 (6.00); dotted – θ or Q_F (in parentheses) = 115.3 (8.00); dot-and-dash – θ or Q_F (in parentheses) = 144.1 (10.00); dot-dot-dash – θ or Q_F (in parentheses) = 172.9 (12.00); thin dashed– θ or Q_F (in parentheses) = 201.7 (14.00); thin dashed – θ or Q_F (in parentheses) = 230.5 (16.00) L STP/hr/kg (L STP/min). Symbols: filled squares – base case mass transfer coefficients (k_a = 0.0058 s^{-1} and k_d = 0.0006 s^{-1}); empty triangles – five times the base case mass transfer coefficients (k_a = 0.029 s^{-1} and k_d = 0.003 s^{-1}).

The higher k_a increased the rate of adsorption of CO_2 into the K-promoted HTlc, which, in turn, produced a sharper or smaller mass transfer zone. Consequently, less CO_2 broke through into the light product during the F and HR steps, resulting in an increase in the CO_2 recovery. Similarly, the higher k_d increased the rate of desorption of CO_2 out of the K-promoted HTlc, which, in turn, allowed more CO_2 to desorb during the CnD and LR steps. Accordingly, less inert gas was present to dilute the heavy product, resulting in an increase in the CO_2 purity.

Figure 14 shows a series of runs performed with the five times higher mass transfer coefficients with throughputs (θ) ranging from 11.5 to 69.2 L STP/hr/kg. Within each panel three cycle step times (t_s), five high to low pressure ratios (π_T), and five heavy product recycle ratios (R_R) were also investigated. The best process performance corresponded to a CO_2 purity of 89.2% and a CO_2 recovery of 72.0% at θ = 576 L STP/hr/kg, π_T = 12, γ = 0.5, R_R = 0.8 and t_s = 500 s.

The effect of increasing the adsorption and desorption mass transfer coefficients by factors of ten on the process performance is shown in Figure 15 for a range of high to low pressure ratios (π_T) and feed throughputs (θ) at a fixed light product purge to feed ratio ($\gamma = 0.5$), heavy product recycle ratio ($R_R = 0.8$), and cycle step time ($t_s = 500$ s). These higher mass transfer coefficients again improved the process performance by increasing both the CO_2 recovery and the CO_2 purity. The best process performance corresponded to a CO_2 purity of 90.5% and a CO_2 recovery of 85.0% at $\theta = 57.6$ L STP/hr/kg, $\pi_T = 12$, $\gamma = 0.5$, $R_R = 0.8$ and $t_s = 500$ s. This was the first time a CO_2 purity greater than 90% was attained based on literally thousands of simulations done in this work and the work shown in previous sections. Achieving a CO_2 purity over 90% makes this process much more attractive for flue gas treatment.

Figure 16 shows the effect of increasing the desorption mass transfer coefficient by setting it equal to the original adsorption mass transfer coefficient ($k_a = k_d = 0.0058$ s^{-1}) for a range of high to low pressure ratios (π_T) and feed throughputs (θ) at a fixed light product purge to feed ratio ($\gamma = 0.5$), heavy product recycle ratio ($R_R = 0.8$), and cycle step time ($t_s = 500$ s). The larger desorption mass transfer coefficient improved both the CO_2 recovery and CO_2 purity. As mentioned earlier, the higher k_d increased the rate of desorption of CO_2 out of the HTlc, which, in turn, allowed more CO_2 to desorb during the CnD and LR steps. Accordingly, less inert gas was present to dilute the heavy product, resulting in an increase in the CO_2 purity. Furthermore, the higher k_d also regenerated the adsorbent more; thus, more CO_2 was adsorbed during the F and HR steps of the next cycle, thereby improving the CO_2 recovery. The best process performance corresponded to a CO_2 purity of 88.9% and a CO_2 recovery of 72.3% at $\theta = 57.6$ L STP/hr/kg, $\pi_T = 12$, $\gamma = 0.5$, $R_R = 0.8$ and $t_s = 500$ s. This performance was similar to the best performance for the situation where both mass transfer coefficients were increased by a factor of five, which suggested that the desorption mass transfer coefficient was very important to the process performance and that the process performance with the original mass transfer coefficients was desorption limited.

The effect of increasing the equal mass transfer coefficients by a factor of five is shown in Figure 17 for a range of high to low pressure ratios (π_T) and feed throughputs (θ) at a fixed light product purge to feed ratio ($\gamma = 0.5$), heavy product recycle ratio ($R_R = 0.8$), and cycle step time ($t_s = 500$ s). This higher mass transfer coefficient also improved both the CO_2 recovery and CO_2 purity. The best process performance obtained a CO_2 purity of 91.5% and a CO_2 recovery of 88.0% at $\theta = 57.6$ L STP/hr/kg, $\pi_T = 12$, $\gamma = 0.5$, $R_R = 0.8$ and $t_s = 500$ s. Among the results discussed so far in terms of both CO_2 purity and CO_2 recovery, these results represented the best performance based on literally thousands of simulations that have been carried out by the authors. The feed throughput was also quite reasonable. These results also revealed the importance of gaining a better understanding of the CO_2 uptake and release mechanisms in K-promoted HTlc.

Several simulations were also carried out to study the effect increasing the mass transfer coefficients by a factor of five for the 4-bed process for a range of high to low pressure ratios (π_T) and feed throughputs (θ) at a fixed light product purge to feed ratio ($\gamma = 0.5$), heavy product recycle ratio ($R_R = 0.8$), and cycle step time ($t_s = 500$ s). The results are shown in Figure 18. The CO_2 purity improved, but the CO_2 recovery decreased at the best performance. The best process performance corresponded to a CO_2 purity of 98.1%, which improved from 82.7%, and a

CO_2 recovery of 5.0%, which fell from 17.4%, at $\pi_T = 12$, $\gamma = 0.5$, $R_R = 0.8$ and $t_s = 500$ s. Although the recovery was quite low, one notable improvement was in the feed throughput, which increased from 14.4 L STP/hr/kg to 201.7 L STP/hr/kg. At this high of a feed throughput, it might be economical to employ such a process to recover at least some of the CO_2 from a stack gas at high purity.

2.5.5 PSA Cycles with Feed+Recycle (F+R) Step or Recovery step (REC)

The prime objective of this work was to expound on the previous studies discussed above by evaluating nine stripping PSA cycle configurations, all with a heavy reflux (HR) step, some with a light reflux (LR) step, and some with a recovery (REC) or feed plus recycle (F+R) step, for concentrating CO_2. The specific objectives were to introduce two additional cycle steps that have been used in the literature with stripping PSA cycles that have a HR step. These cycle steps are called the recovery (Chue et al., 1995) and recycle (Kikkinides et al., 1993) steps. The next objective was to introduce a novel way of operating the LR step in conjunction with a HR cycle. The final objective was to carry out a comprehensive evaluation of the performance of nine uniquely different stripping PSA cycles with HR, i.e., the three HR cycles mentioned above with and without the recovery or recycle step added. Simulations of these nine HR cycles were carried out using an in-house developed cyclic adsorption process simulator. Part I of this work is limited to evaluating the performance of these cycles; Part II of this work is dedicated to providing a detailed explanation of the trends (Mehrotra et al., 2007).

Based on the above discussion, it is clear that the operation of the HR step in a PSA cycle depends on the other steps in the cycle schedule. The HR gas can be obtained from the depressurization step and/or the low pressure light reflux purge step, depending on whether this latter step is included in the PSA cycle. If it is included, then the PSA cycle is actually a dual reflux cycle with both light and heavy reflux steps.

The light gas effluent coming from the column undergoing the HR step can be managed in several ways. In most cases there are three choices. It can be taken as part of the light product. But, operating the cycle in this manner may limit the recovery of the heavy component, as some of it can be lost in this light product. Instead, it can also be recycled back into the process for subsequent recovery as heavy product. There are two ways to recycle this light gas effluent back into the process. The first way is to simply blend this light gas effluent with the feed gas during the feed step (Kikkinides et al., 1993). This approach does not add another step to the cycle and is referred to here as the feed plus recycle (F+R) step. The second way is to feed this light gas effluent to the heavy end of another column in between the feed and heavy reflux steps (Chue et al., 1995). This approach adds another step to the cycle and is referred to here as the recovery (REC) step.

A recovery or recycle step was added to each of the three stripping PSA cycles with HR that were studied previously (Figures 5, 12). In this way, nine different stripping PSA cycles with HR were formulated: a 5-bed 5-step stripping PSA cycle with LR and HR from CnD, alone and with the addition of a REC or F+R step; a 5-bed 5-step stripping PSA cycle with LR and HR from LR purge, alone and with the addition of a REC or F+R step; and a 4-bed 4-step stripping PSA cycle with HR from CnD, alone and with the addition of a REC or F+R step. The

schematics and cycle sequencing of these nine stripping PSA cycles with HR are displayed in Figures 19, 20 and 21, respectively.

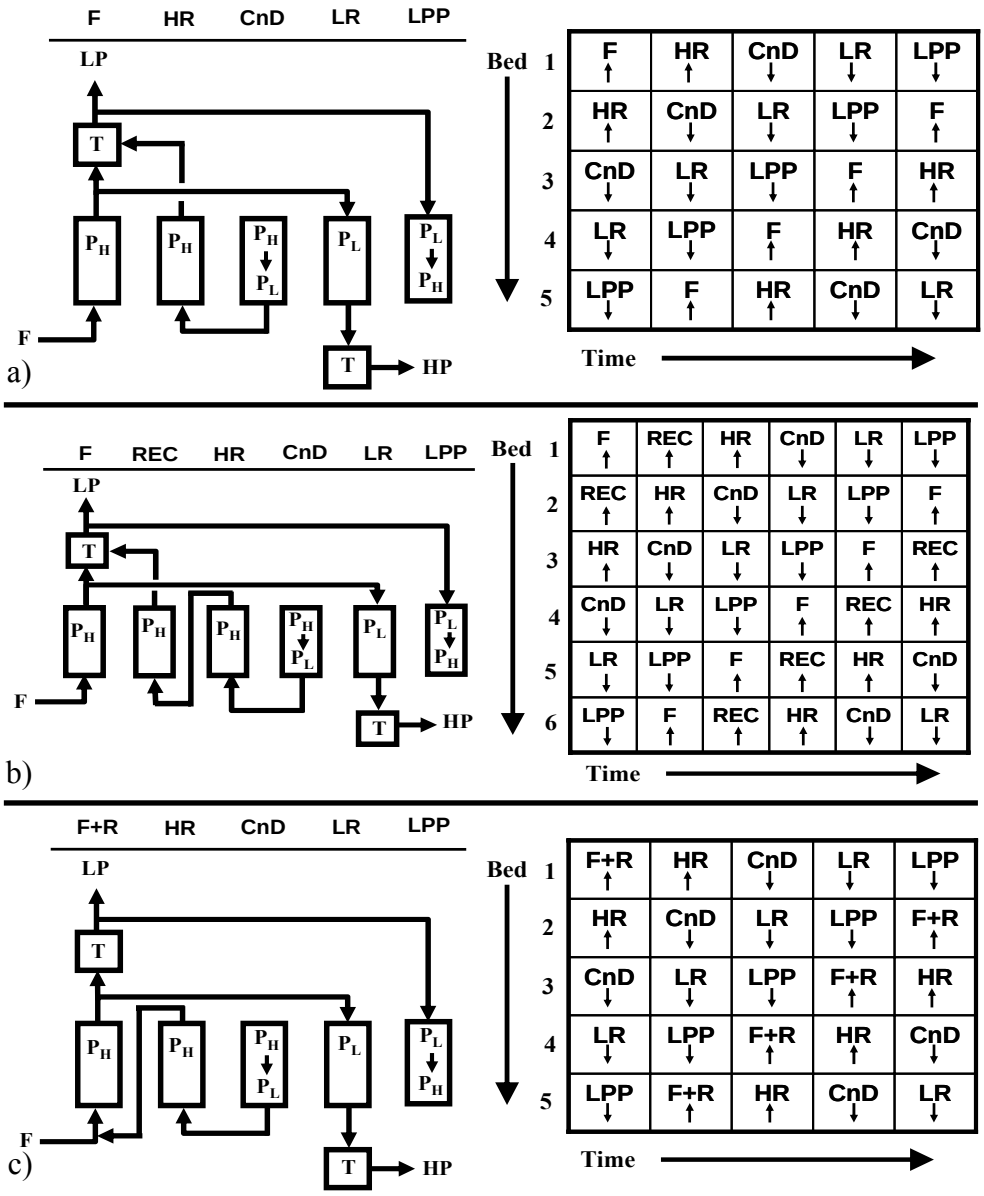

Figure 19. Schematics and cycle sequencing of various heavy reflux PSA cycles analyzed for high temperature CO_2 capture and concentration with the CO_2 selective K-promoted HTlc adsorbent: a) 5-bed 5-step stripping PSA cycle with LR and HR from CnD, b) 6-bed 6-step stripping PSA cycle with LR, HR from CnD and REC and c) 5-bed 5-step stripping PSA cycle with LR, HR from CnD and R to F. F = feed; CnD = countercurrent depressurization; LR = light reflux; HR = heavy reflux; LPP = light product pressurization; REC = recovery; R = recycle; P_L = low pressure; P_H = high pressure; LP = light product; HP = heavy product; T = tank.

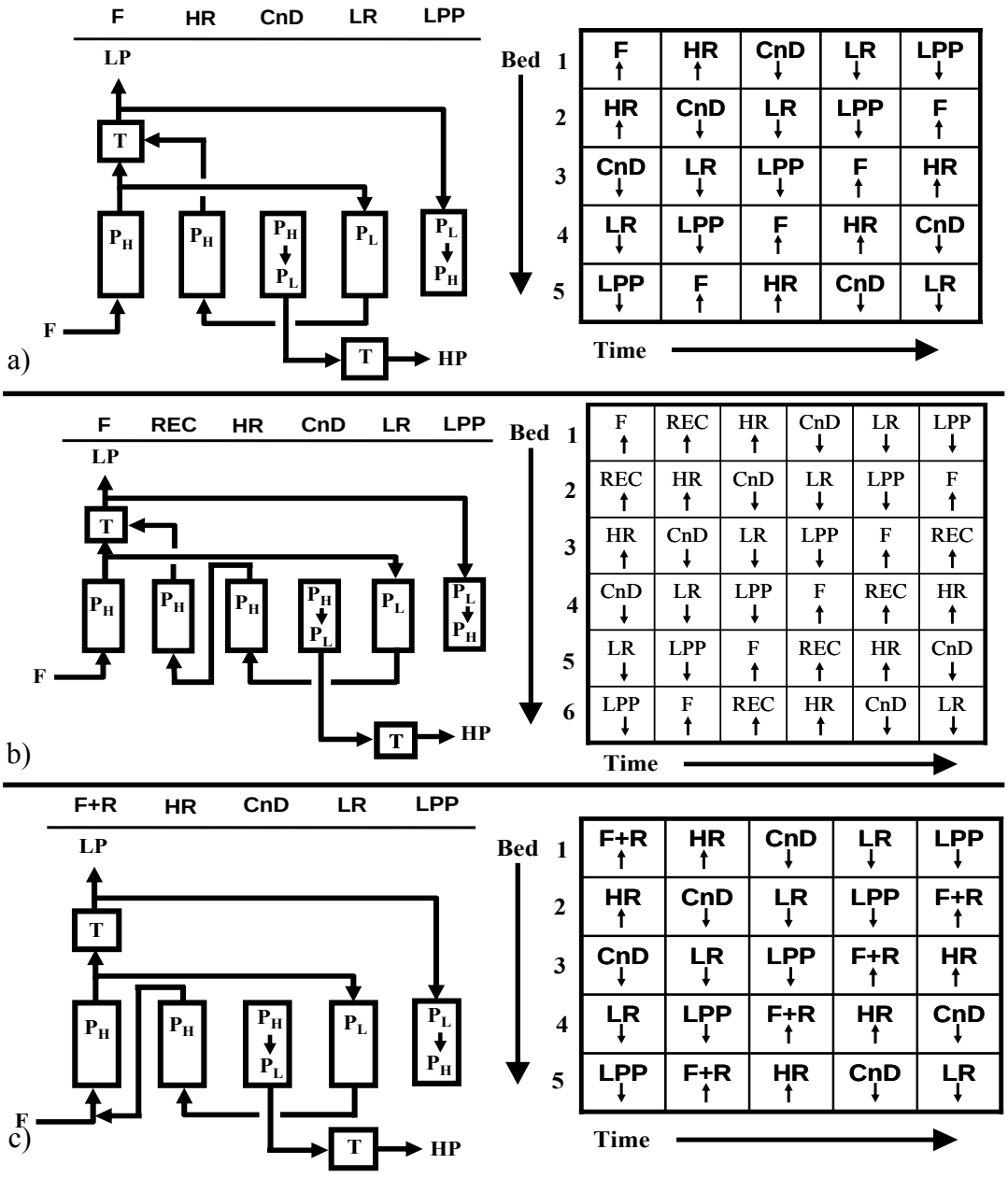

Figure 20. Schematics and cycle sequencing of various heavy reflux PSA cycles analyzed for high temperature CO_2 capture and concentration with the CO_2 selective K-promoted HTlc adsorbent: a) 5-bed 5-step stripping PSA cycle with LR and HR from LR purge, b) 6-bed 6-step stripping PSA cycle with LR, HR from LR purge and REC and c) 5-bed 5-step stripping PSA cycle with LR, HR from LR purge and R to F. F = feed; CnD = countercurrent depressurization; LR = light reflux; HR = heavy reflux; LPP = light product pressurization; REC = recovery; R = recycle; P_L = low pressure; P_H = high pressure; LP = light product; HP = heavy product; T = tank.

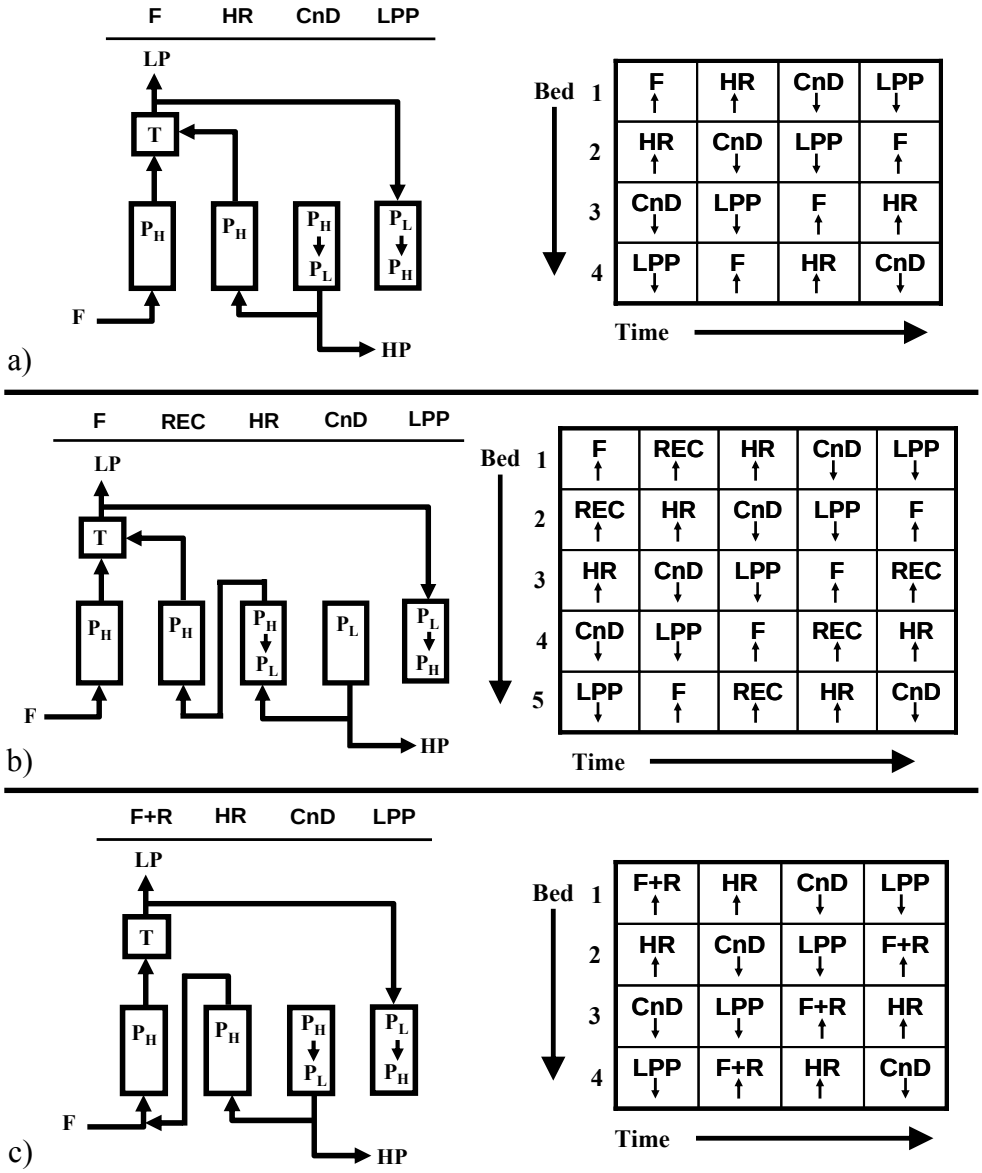

Figure 21. Schematics and cycle sequencing of various heavy reflux PSA cycles analyzed for high temperature CO_2 capture and concentration with the CO_2 selective K-promoted HTlc adsorbent: a) 4-bed 4-step stripping PSA cycle with HR from CnD, b) 5-bed 5-step stripping PSA cycle with HR from CnD and REC and c) 4-bed 4-step stripping PSA cycle with HR from CnD and R to F. F = feed; CnD = countercurrent depressurization; HR = heavy reflux; LPP = light product pressurization; REC = recovery; R = recycle; P_L = low pressure; P_H = high pressure; LP = light product; HP = heavy product.

The stripping PSA cycle in Figure 19a contained the following steps: high pressure (P_H) adsorption with feed (F) just above atmospheric pressure, cocurrent high-pressure adsorption with heavy product purge as heavy reflux (HR), countercurrent depressurization (CnD) from P_H to a lower (vacuum) pressure (P_L), countercurrent low-pressure desorption with light product

purge as light reflux (LR), and light product pressurization (LPP) from P_L to P_H. All of the effluent from the CnD step was recompressed to P_H and used as the feed to the column undergoing the HR step. All of the effluent from the LR step was recovered as heavy product. The recovery (REC) step was added to this cycle by taking the light product effluent from the column undergoing the HR step, which was essentially at the feed pressure, and sending it to the column that just finished the feed step, as shown in Figure 19b. The feed plus recycle (F+R) step was added to this cycle by taking the light product effluent from the column undergoing the HR step, which was essentially at the feed pressure, blending it with feed gas, and sending this blended gas to the column undergoing the feed plus recycle step, as shown in Figure 19c.

The cycles shown in Figures 20a, 20b and 20c were the same as those in Figures 19a, 19b and 19c, except for the cycle step that was used to produce the HR gas. In this case, all of the effluent from the LR step (in lieu of the CnD step) was recompressed to P_H and used as the feed to the column undergoing the HR step. All of the effluent from the CnD step (in lieu of the LR step) was recovered as heavy product.

The cycles in Figures 21a, 22b and 23c were the same as those in Figures 19a, 19b and 19c, or Figures 20a, 20b and 20c, except that none of these cycles had a light reflux step. This meant that some specified fraction of the effluent from the CnD step was recompressed to P_H and used as the feed to the column undergoing the HR step. The remaining fraction of the effluent from the CnD step was recovered as heavy product.

In all cases, the heavy product (mainly CO_2) was enriched and recovered during the CnD or LR step, and the light product (mainly N_2 and H_2O) was recovered during the F, HR, REC and/or F+R steps. The purge or pressurization gases used during the LR or LPP step came directly from the light effluent end of the bed undergoing the F or F+R step. The heavy reflux gas used during the HR step came directly from the heavy effluent end of the bed undergoing either the CnD or LR step. The recovery gas used during the REC step was obtained from the light effluent end of the bed undergoing the HR step. The recycle gas that was blended with the feed and used during the F+R step came from the light effluent end of the bed undergoing the HR step. In every case these recycled column effluents retained their time-dependent composition and temperature.

The bed characteristics, gas phase species, and K-promoted HTlc adsorbent transport and thermodynamic properties used in the mathematical model are shown in Table 5. Data (Ding and Alpay, 2000, 2001) for CO_2 adsorption on the K-promoted HTlc adsorbent were fitted to a temperature dependent Langmuir isotherm model. The isosteric heat of adsorption (ΔH_i) was estimated from the temperature dependence of the isotherm parameter b_i.

The values for adsorption and desorption mass transfer coefficients shown in Table 5 are five times higher that those used in the three previous studies discussed above, which were taken from the work of Ding and Alpay (2001). The other components in the system, namely N_2 and H_2O, were considered to be inert with this adsorbent (Ding and Alpay, 2000). Therefore, their adsorption isotherm parameters, mass transfer coefficients and adsorbed phase heat capacities were set to zero. The gas phase properties for N_2 and H_2O, such as their gas phase heat capacities, were accounted for in the model.

Table 5. Bed characteristics, gas phase species, and K-promoted HTlc adsorbent transport and thermodynamic properties.

Bed, K-Promoted HTlc Adsorbent, and Process Characteristics

Bed Length (L)	0.2724 m
Bed Radius (r_b)	0.0387 m
Bed Porosity (ε)	0.48
Adsorbent Particle Porosity (χ)	0.0
Fraction of χ Occupied by Adsorbed Phase (φ)	0.0
Adsorbent Particle Density (ρ_p)	1563 kg/m^3
Adsorbent Particle Heat Capacity ($C_{P,p}$)	0.850 kJ/kg/K
CO_2-HTlc Isosteric Heat of Adsorption (ΔH_i)	9.29 kJ/mol
Heat Transfer Coefficient (h)	0.00067 kW/m^2/K
CO_2-HTlc Mass Transfer Coefficient: ads (k_a), des (k_d)	0.029 s^{-1}, 0.003 s^{-1}
Feed Mole Fractions: CO_2, N_2, and H_2O	0.15, 0.75 and 0.10
Feed (T_f) and Wall Temperature (T_o)	575 K
High Pressure (P_H) (absolute)	139.7 kPa
Low Pressure (P_L) (absolute)	11.64 kPa
P_H/P_L	12.0

Adsorption Isotherm Model and Parameters for CO_2 on K-Promoted HTlc

$$q^* = \frac{q^s bPy}{1+bPy} \text{ where } q^s = q_1^s T + q_2^s \text{ and } b = b^0 \exp\left(\frac{B^0}{T}\right)$$

q_1^s (mol/kg/K)	-1.5277E-3
q_2^s (mol/kg)	1.7155
b^0 (kPa^{-1})	0.0203
B^0 (K)	1118.1

Gas (and Adsorbed) Phase Heat Capacity Model and Coefficients for CO_2, N_2 and H_2O

$$C_{P,g} = \sum_{i=1}^{N} y_i C_{P,g,i} \text{ where } C_{P,g,i} = A_i + B_i T + C_i T^2 + D_i T^3$$

A_i for CO_2, N_2, and H_2O (kJ/mol/K)	1.9795E-2, 3.1123E-2, 3.2221E-2
B_i for CO_2, N_2, and H_2O (kJ/mol/K^2)	7.3437E-5, -1.3553E-5, 1.9217E-6
C_i for CO_2, N_2, and H_2O (kJ/mol/K^3)	-5.6019E-8, 2.6772E-8, 1.0548E-8
D_i for CO_2, N_2, and H_2O (kJ/mol/K^4)	1.7153E-11, 1.1671E-11, -3.5930E-12

The column radius (r_b) and length (L), and the corresponding heat transfer coefficient (h) were adopted from an experimental setup described by Liu et al. (1998). The values are given in Table 5. The reason why these bed dimensions were chosen for this and all previous studies was because Liu et al. (1998) actually measured the heat transfer coefficient for a bed with these dimensions. In fact, it is noteworthy that although only simulation results are presented and discussed below, the mathematical model used to obtain these results has been validated against extensive butane-nitrogen-activated carbon PSA experiments carried out by Liu et al. (1999), and CO_2-nitrogen-K-promoted HTlc breakthrough experiments carried out by Ding and Alpay (2001) (results not shown).

The rigorous PSA process simulator utilized in this study was the same as that developed and presented in previous sections. It suffices to state that the model accounts for heat and mass transfer effects, velocity variation in the bed, and fully integrates the pressure changing steps. The only changes to that model were the boundary conditions for the recovery (REC) and feed plus recycle (F+R) steps when used.

The initial and boundary conditions affected by the REC step were:

REC:	at t = 0:	$y_i = y_{i,F}$,	$T = T_F$,	$q_i = q_{i,F}$,	for all z
	at z = 0:	$y_i = y_{i,HR}(t)$,	$T = T_{HR}(t)$,	$u = u_{REC}$,	for all t
HR:	at t = 0:	$y_i = y_{i,REC}$,	$T = T_{REC}$,	$q_i = q_{i,REC}$,	for all z
	at z = 0:	$y_i = y_{i,CnD}(t)$ or $y_i = y_{i,LR}(t)$,	$T = T_{CnD}(t)$ or $T = T_{LR}(t)$,	$u = u_{REC}$,	for all t

The initial and boundary conditions affected by the F+R step were:

F+R:	at t = 0:	$y_i = y_{i,LPP}$,	$T = T_{LPP}$,	$q_i = q_{i,LPP}$,	for all z
	at z = 0:	$y_i = y_{i,F+R}(t)$,	$T = T_f$,	$u = u_{F+R}$,	for all t
HR:	at t = 0:	$y_i = y_{i,REC}$,	$T = T_{REC}$,	$q_i = q_{i,REC}$,	for all z
	at z = 0:	$y_i = y_{i,CnD}(t)$ or $y_i = y_{i,LR}(t)$,	$T = T_{CnD}(t)$ or $T = T_{LR}(t)$,	$u = u_{REC}$,	for all t

Note that the temperature and gas phase mole fraction boundary conditions for the heavy reflux (HR) step depended on whether the gas came from the countercurrent depressurization (CnD) or light reflux (LR) step. Also, $y_{i,F+R}(t)$ is the average, time-dependent concentration obtained by blending the feed with the effluent from the HR step, as given by:

$$y_{i,F+R}(t) = \frac{y_{i,f} \cdot Q_f + y_{i,HR}(t) \cdot Q_{HR}(t)}{Q_f + Q_{HR}(t)} \tag{15}$$

Over three hundred simulations of the nine different stripping PSA cycle configurations with HR were carried out to the periodic state using the in-house developed cyclic adsorption process simulator. All nine cycle configurations are shown in Figures 19 to 21. Table 5 shows the bed characteristics, gas phase species, and K-promoted HTlc adsorbent transport and thermodynamic properties. Table 5 also shows the parameters that were held constant in all cases, like the feed and wall temperatures (575 K), and the high to low pressure ratio (P_H/P_L =

12). Table 6 indicates the ranges of process conditions studied and corresponding performances achieved in terms of feed throughput, CO_2 purity, and CO_2 recovery for each of the nine PSA cycle configurations. Table 7 provides a summary of the best process performances achieved, based on the highest CO_2 purity obtained for a given PSA cycle configuration and set of corresponding process conditions. Figures 22 to 27 present a systematic account of the performances of these nine stripping PSA cycles with HR in terms of CO_2 purity versus CO_2 recovery plots. However, the discussions below are limited to evaluating only the performance of each HR PSA cycle. Detailed explanations of the observed and sometimes very subtle trends are provided in Part II of this study (Mehrotra et al., 2007).

2.5.6 Stripping PSA Cycles with LR and HR from CnD, with and without a REC or F+R Step

The 5-bed 5-step stripping PSA cycle with light reflux (LR) and heavy reflux (HR) from countercurrent depressurization (CnD) consisted of five interconnected beds each undergoing in succession five cycle steps of equal duration, as shown in Figure 19a. The heavy product (CO_2) was recovered only during the LR step, as all of the effluent from the CnD step was recycled to the HR step, i.e., the recycle ratio was equal to one (R_R = 1.0) in this case. This mode of operation contrasted with previous studies of this cycle (discussed above), wherein the heavy product was recovered not only during the LR step, but also during the CnD step with R_R varying from 0.2 to 0.8. In those studies, the CO_2 purity always increased with increasing R_R , which is why R_R = 1.0 was always used in this study.

Thirty-six different cases were simulated over the range of parameters listed in Table 6. Three light product purge to feed ratios (γ), three cycle step times (t_s), and four feed throughputs (θ) were investigated. Note that the largest value of γ investigated here of 0.5 was the only value investigated in the previous work (discussed above), because it was concluded that the CO_2 purity always increased with decreasing γ. The notion here was to determine if using a very small value of γ, like γ = 0.02, could further improve the purity. A purge to feed ratio of this magnitude, in conjunction with a HR cycle, has not been discussed in the literature. The effects of γ, t_s, and θ on the process performance are shown collectively in Figure 22.

The CO_2 purity always decreased with increasing γ, t_s and θ, whereas recovery decreased with decreasing γ, and increasing t_s and θ. The best performance based on purity was a CO_2 purity of 98.7% and a CO_2 recovery of 98.7%, with γ = 0.02, t_s = 100 s and θ = 5.8 L STP/hr/kg. Note the small γ that was responsible for this very positive performance. The best result based on recovery was a CO_2 purity of 78.7% and a CO_2 recovery of 99.9%, with γ = 0.50, t_s = 100 s and θ = 5.8 L STP/hr/kg. In this case, the larger γ improved the recovery, but only slightly and at the expense of decreasing the purity. Clearly, this HR PSA cycle is best suited for producing CO_2 at both high purities and high recoveries, but at relatively lower feed throughputs. These results are summarized and compared to all the other HR PSA cycles in Tables 6 and 7.

Table 6. Range of process conditions studied and corresponding performances achieved in terms of feed throughput, and CO_2 purity and CO_2 recovery for each of the six stripping PSA cycle configurations.

Stripping PSA Cycle Configuration[A]	Feed Throughput (L STP/hr/kg)	Cycle Time[B] (s)	Heavy Product Recycle Ratio[C]	CO_2 Purity[D] (%)	CO_2 Recovery[D] (%)
5-Bed 5-Step Cycle with LR and HR from CnD (Figure 19a)	5.8 – 57.6	500 – 2500	1.0	70.8 – 98.7 (63.5) (98.7) [57.6] [5.8]	26.7 – 99.9 (96.4) (78.7) [57.6] [5.8]
6-Bed 6-Step Cycle with LR, HR from CnD and REC (Figure 19b)	4.8 – 48.0	600 – 3000	1.0	70.8 – 98.6 (63.6) (91.3) [48.0] [4.8]	26.7 – 98.9 (96.4) (78.6) [48.0] [4.8]
5-Bed 5-Step Cycle with LR, HR from CnD and F+R (Figure 19c)	5.8 – 57.6	500 – 2500	1.0	71.0 – 98.6 (63.1) (91.8) [57.6] [5.8]	26.4 – 99.5 (96.5) (78.7) [57.6] [5.8]
5-Bed 5-Step Cycle with LR and HR from LR purge (Figure 20a)	5.8 – 57.6	500 – 2500	1.0	25.5 – 96.6 (98.5) (71.1) [5.8] [57.6]	43.6 – 99.9 (91.6) (42.2) [57.6] [11.5]
6-Bed 6-Step Cycle with LR, HR from LR purge and REC (Figure 20b)	4.8 – 48.0	600 – 3000	1.0	25.4 – 96.5 (98.1) (71.1) [4.8] [48.0]	43.6 – 99.5 (91.6) (42.1) [48.0] [9.6]
5-Bed 5-Step Cycle with LR, HR from LR purge and F+R (Figure 20c)	5.8 – 57.6	500 – 2500	1.0	25.6 – 96.5 (98.6) (71.0) [5.8] [57.6]	43.6 – 99.3 (91.6) (52.0) [57.6] [5.8]
4-Bed 4-Step Cycle with HR from CnD (Figure 21a)	7.2 – 72.0	400 – 2000	0.2 – 0.8	30.3 – 99.2 (100) (15.0) [7.2] [72.0]	12.6 – 100 (76.5) (37.1) [72.0] [7.2]
5-Bed 5-Step Cycle with HR from CnD and REC (Figure 21b)	5.8 – 57.6	500 - 2500	0.2 – 0.8	30.0 – 99.1 (98.9) (15.0) [5.8] [57.6]	12.4 – 99.3 (75.8) (30.1) [57.6] [5.8]
4-Bed 4-Step Cycle with HR from CnD and F+R (Figure 21c)	7.2 – 72.0	400 – 2000	0.2 – 0.8	31.3 – 99.2 (99.3) (15.2) [7.2] [72.0]	12.5 – 99.0 (76.4) (30.0) [72.0] [7.2]

[A] The cycle configuration corresponds to the figure number shown in parentheses.
[B] All step times t_s were equal in length.
[C] The light product purge to feed ratio always ranges from 0.02 – 0.50.
[D] The values in parentheses correspond to the CO_2 recovery achieved for the highest and lowest CO_2 purity (column 5), and the CO_2 purity achieved for the highest and lowest CO_2 recovery (column 6). The values in brackets correspond to the feed throughput (L STP/hr/kg) achieved for the highest and lowest CO_2 purity (column 5), and the feed throughput achieved for the highest and lowest CO_2 recovery (column 6).

Table 7. Best performance achieved based on highest CO_2 purity obtained for a given stripping PSA cycle configuration and set of corresponding conditions.

Stripping PSA Cycle Configuration[A]	Feed Throughput (L STP/hr/kg)[B]	Light Product Purge to Feed Ratio	Heavy Product Recycle Ratio	Cycle Time[C] (s)	CO_2 Purity (%)	CO_2 Recovery (%)
5-Bed 5-Step Cycle with LR and HR from CnD (Figure 19a)	5.8 (0.5)	0.02	1.0	500	98.7	98.7
6-Bed 6-Step Cycle with LR, HR from CnD and REC (Figure 19b)	4.8 (0.5)	0.02	1.0	600	98.6	91.3
5-Bed 5-Step Cycle with LR, HR from CnD and F+R (Figure 19c)	5.8 (0.5)	0.02	1.0	500	98.6	91.8
5-Bed 5-Step Cycle with LR and HR from LR purge (Figure 20a)	57.6 (5.0)	0.50	1.0	2500	96.6	71.1
6-Bed 6-Step Cycle with LR, HR from LR purge and REC (Figure 20b)	48.0 (5.0)	0.50	1.0	3000	96.5	71.1
5-Bed 5-Step Cycle with LR, HR from LR purge and F+R (Figure 20c)	57.6 (5.0)	0.50	1.0	2500	96.5	71.0
4-Bed 4-Step Cycle with HR from CnD (Figure 21a)	72.0 (5.0)	---	0.8	2000	99.2	15.2
5-Bed 5-Step Cycle with HR from CnD and REC (Figure 21b)	57.6 (5.0)	---	0.8	2500	99.1	15.0
4-Bed 4-Step Cycle with HR from CnD and F+R (Figure 21c)	72.0 (5.0)	---	0.8	2000	99.2	15.2

[A] The cycle configuration corresponds to the figure number shown in parentheses.
[B] Values in parentheses correspond to the feed flow rate Q_F in L STP/min.
[C] All step times t_s were equal in length.

REC and F+R steps were also added to this 5-bed 5-step stripping PSA cycle with LR and HR from CnD, as shown in Figures 19b and 19c, respectively. Simulations of these cycle variations were carried out with the same range of γ, t_s and θ. For the conditions studied and except at the lowest θ, if the results from these new cycle variations were plotted in Figure 22, along with the curves for the same cycle without these steps, all the curves would essentially

overlap each other (not shown). Hence, not only were the effects of γ, t_s and θ on the process performance approximately the same for such conditions, but also the effect of adding a REC or F+R step were surprisingly nil. The slight differences that did occur between these cycles at the lowest θ are shown in Figure 23. Clearly, the addition of a REC or F+R step had a similar effect on the process performance with both of them lowering it compared to the cycle without them. The effect of these steps was expected to be much more pronounced. It was also expected to be favorable, not unfavorable.

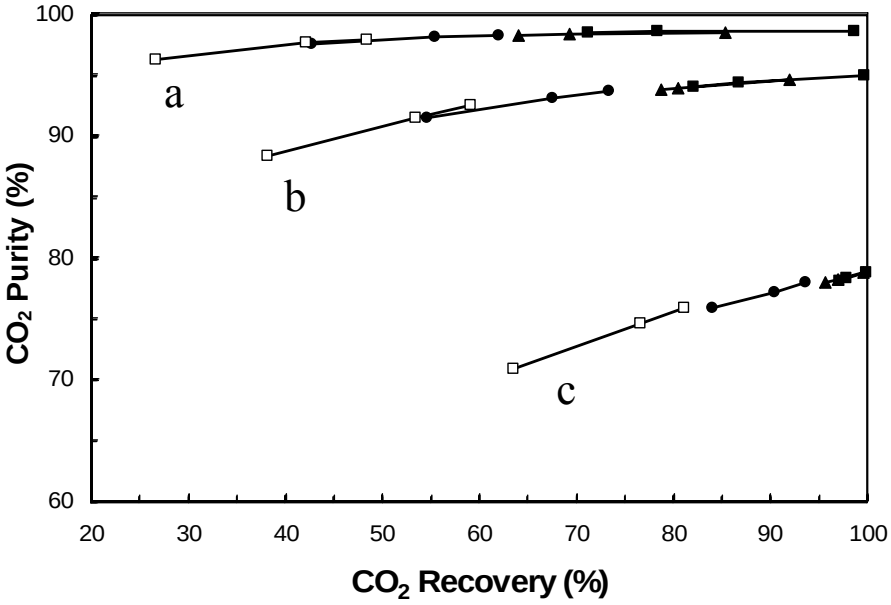

Figure 22. Performance curves from the 5-bed 5-step stripping PSA cycle with LR and HR from CnD (Figure 1a) for γ = a) 0.02, b) 0.10, and c) 0.50. Each line corresponds to three runs with t_s increasing from right to left (t_s = 100, 300, and 500 s). Symbols: filled squares – θ = 5.8 (Q_F = 0.5); filled triangles – θ = 11.5 (Q_F = 1.0); filled circles – θ = 34.6 (Q_F = 3.0); empty squares – θ = 57.6 (Q_F = 5.0). The performance curves from the corresponding stripping PSA cycle with LR, HR from CnD, and with REC or F+R were essentially the same (not shown).

2.5.7 Stripping PSA Cycles with LR and HR from LR Purge, with and without a REC or F+R Step

The 5-bed 5-step stripping PSA cycle with LR and HR from LR purge consisted of five interconnected beds each undergoing in succession five cycle steps of equal duration, as shown in Figure 20a. The only difference between this cycle and the one discussed in Figure 19a was that the heavy product was recovered only during the CnD step and all the effluent from the LR step was recycled to the HR step. Just the opposite was done in the cycle in Figure 19a. Again, the recycle ratio was equal to one (R_R = 1.0).

Thirty six different cases were simulated over the range of parameters listed in Table 6.

Three light product purge to feed ratios (γ), three cycle step times (t_s), and four feed throughputs (θ) were investigated. The effects of γ, t_s, and θ on the process performance are shown collectively in Figures 24a to 24c.

The CO_2 purity increased with increasing γ, t_s and θ, and the CO_2 recovery decreased with decreasing γ and increasing θ. However, the effect of t_s on the CO_2 recovery was much more complex and depended on the values of both γ and θ, in some cases exhibiting a maximum as t_s increased. The best performance based on purity was a CO_2 purity of 96.6% and a CO_2 recovery of 71.1%, with $\gamma = 0.50$, $t_s = 500$ s and $\theta = 57.6$ L STP/hr/kg. The best performance based on recovery was a CO_2 purity of 42.2% and a CO_2 recovery of 99.9%, with $\gamma = 0.50$, $t_s = 100$ s and $\theta = 11.5$ L STP/hr/kg. Note that the larger γ produced the best performances for this cycle, a result that contrasted starkly with the previous cycle and indicated that the origin of the HR gas makes a significant difference. Clearly, this cycle is useful for producing CO_2 at both high purities and high feed throughputs, but at relatively lower recoveries compared to the HR PSA cycle with HR from CnD. These results are summarized and compared to all the other HR PSA cycles in Tables 6 and 7.

REC and F+R steps were also added to this 5-bed 5-step stripping PSA cycle with LR and HR from LR purge, as shown in Figures 20b and 20c, respectively. Simulations of these cycle variations were carried out with the same range of γ, t_s and θ. Again, for all the conditions studied and except at the lowest θ, the addition of a REC or F+R step to this cycle had hardly any effect on its process performance. Hence, most of results would essentially overlap each other if plotted in Figure 24. The differences that did appear between these cycles at the lowest θ are shown in Figure 25. The trends were the same as those in Figure 23, but with even less pronounced but always unfavorable effects. These results were again very subtle and unexpected. Part II of this work provides an explanation (Mehrotra et al., 2007).

2.5.8 Stripping PSA Cycles with HR from CnD, with and without a REC or F+R Step

The 4-bed 4-step stripping PSA cycle with HR from CnD consisted of four interconnected beds each undergoing in succession four cycle steps of equal duration, as shown in Figure 21a. The difference between this cycle and all the previous cycles was the elimination of the LR step. Hence, the heavy product was necessarily recovered during the CnD step, with a fraction of the effluent from this step being recycled to the HR step. This mode of operation was similar to that used in the previous studies of this cycle (discussed above), wherein the recycle ratio R_R was varied from 0.2 to 0.8. The light product was still recovered during the F and HR steps.

Forty-eight cases were simulated over the range of parameters listed in Table 6. Four heavy product recycle ratios (R_R), three cycle step times (t_s), and four feed throughputs (θ) were investigated. The effects of R_R, t_s, and θ on the process performance are shown collectively in Figures 26a to 26d.

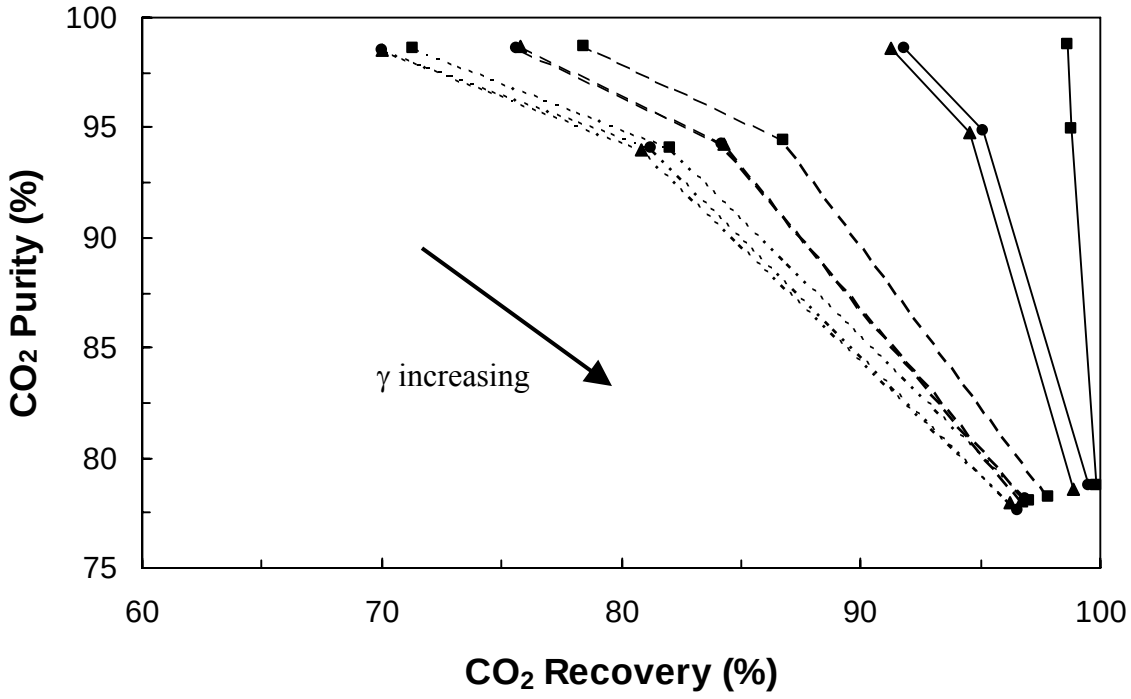

Figure 23. Performance curves comparing the results from the three stripping PSA cycles with LR and HR from CnD with and without REC or F+R steps and for Q_F = 0.5 L STP/min. Lines: solid – t_s = 100 s; dashed – t_s = 300 s; dotted – t_s = 500 s. Symbols: squares – 5-bed 5-step stripping PSA cycle with LR and HR from CnD (θ = 5.8 L STP/hr/kg); triangles – 6-bed 6-step stripping PSA cycle with LR, HR from CnD and REC (θ = 4.8 L STP/hr/kg); circles – 5-bed 5-step stripping PSA cycle with LR, HR from CnD and F+R (θ = 5.8 L STP/hr/kg).

The CO_2 purity always increased as R_R, t_s and θ increased. The CO_2 recovery always decreased with increasing R_R and θ. However, the effect of t_s on the CO_2 recovery was again much more complex and depended on the values of both R_R and θ, in some cases exhibiting a maximum as t_s increased. These trends are similar to the ones in Figure 24, suggesting that the process performance depends strongly on the step from which the HR gas is obtained. The best performance based on purity was a CO_2 purity of 99.2% and a CO_2 recovery of 15.2%, with R_R = 0.8, t_s = 500 s and θ = 72.0 L STP/hr/kg. The best performance based on recovery was a CO_2 purity of 37.1% and a CO_2 recovery of 100.0%, with R_R = 0.4, t_s = 100 s and θ = 7.2 L STP/hr/kg. Compared to the two HR cycles with a LR step, the results of this performance evaluation clearly revealed that the CO_2 recoveries of this cycle would always be much lower than the corresponding cycles with a LR step, no matter the process conditions. These results thus exposed the importance of the LR step to the process performance of these particular HR cycles for this application. These results are summarized and compared to all the other HR PSA cycles in Tables 6 and 7.

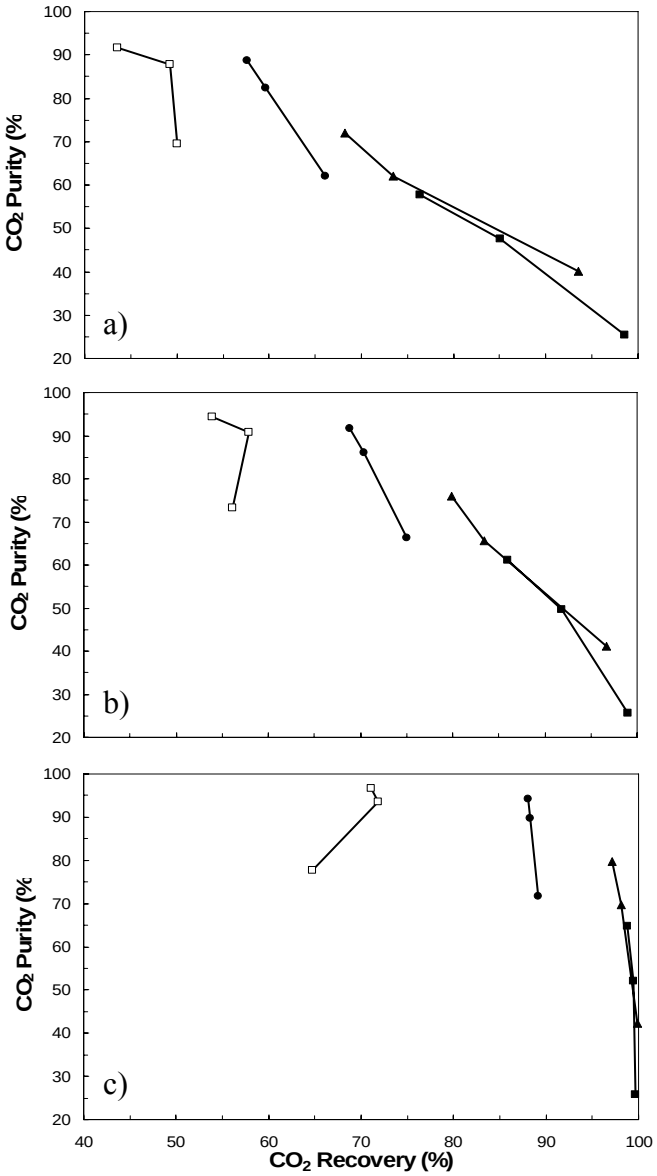

Figure 24. Performance curves from the 5-bed 5-step stripping PSA cycle with LR and HR from LR purge (Figure 2a) for γ = a) 0.02, b) 0.10, and c) 0.50. Each line corresponds to three runs with t_s increasing from right to left (t_s = 100, 300, and 500 s). Symbols: filled squares – θ = 5.8 (Q_F = 0.5); filled triangles – θ = 11.5 (Q_F = 1.0); filled circles – θ = 34.6 (Q_F = 3.0); empty squares – θ = 57.6 (Q_F = 5.0). The performance curves from the corresponding stripping PSA cycle with LR, HR from CnD, and with REC or F+R were essentially the same (not shown).

REC and F+R steps were also added to this 4-bed 4-step stripping PSA cycle with HR from CnD, as shown in Figures 21b and 21c, respectively. Simulations of these cycle variations were carried out with the same range of R_R, t_s and θ. Again, for the conditions studied and except for the lowest θ, the addition of REC and F+R steps to this cycle did not have much effect on its process performance. Hence, most of results would essentially overlap each other if plotted in Figure 26. The differences that did appear between these cycles at the lowest θ are shown in Figure 27. The trends were the same as those in Figures 23 and 25, but with some quite

pronounced but always unfavorable effects, especially for the shortest cycle step time.

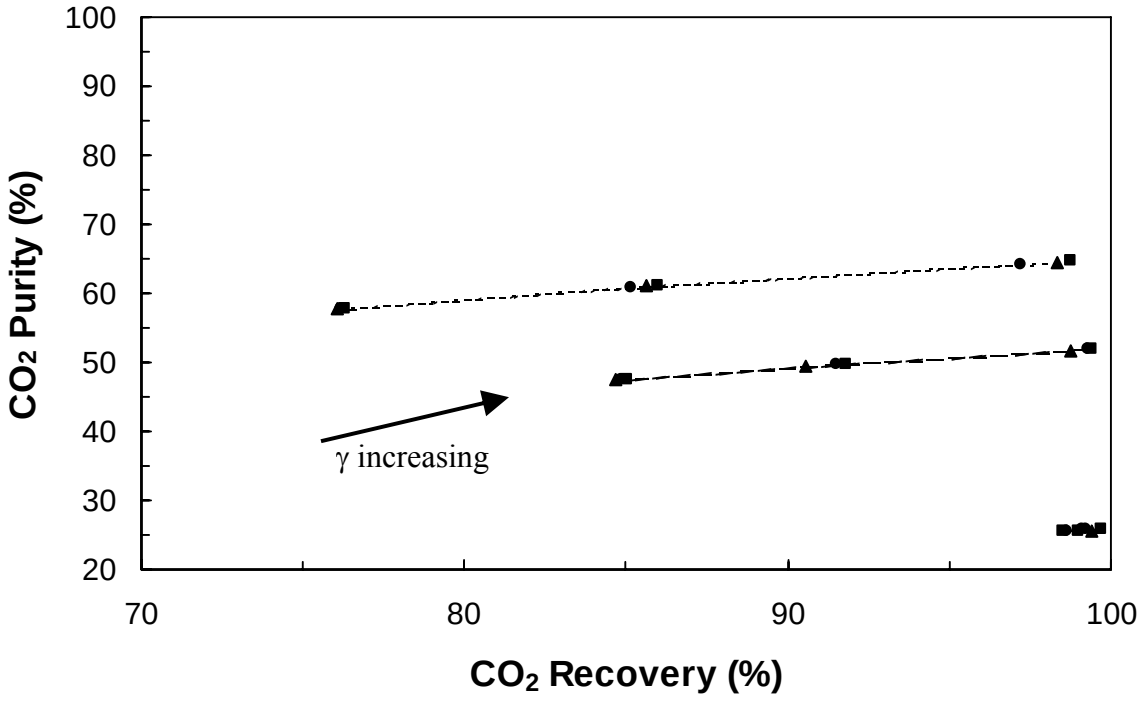

Figure 25. Performance curves comparing the results from the three stripping PSA cycles with LR and HR from LR purge with and without REC or F+R steps and for Q_F = 0.5 L STP/min. Lines: solid (lowest curve) – t_s = 100 s; dashed (middle curve) – t_s = 300 s; dotted (upper curve) – t_s = 500 s. Symbols: squares – 5-bed 5-step stripping PSA cycle with LR and HR from LR purge (θ = 5.8 L STP/hr/kg); triangles – 6-bed 6-step stripping PSA cycle with LR, HR from LR purge and REC (θ = 4.8 L STP/hr/kg); circles – 5-bed 5-step stripping PSA cycle with LR, HR from LR purge and F+R (θ = 5.8 L STP/hr/kg).

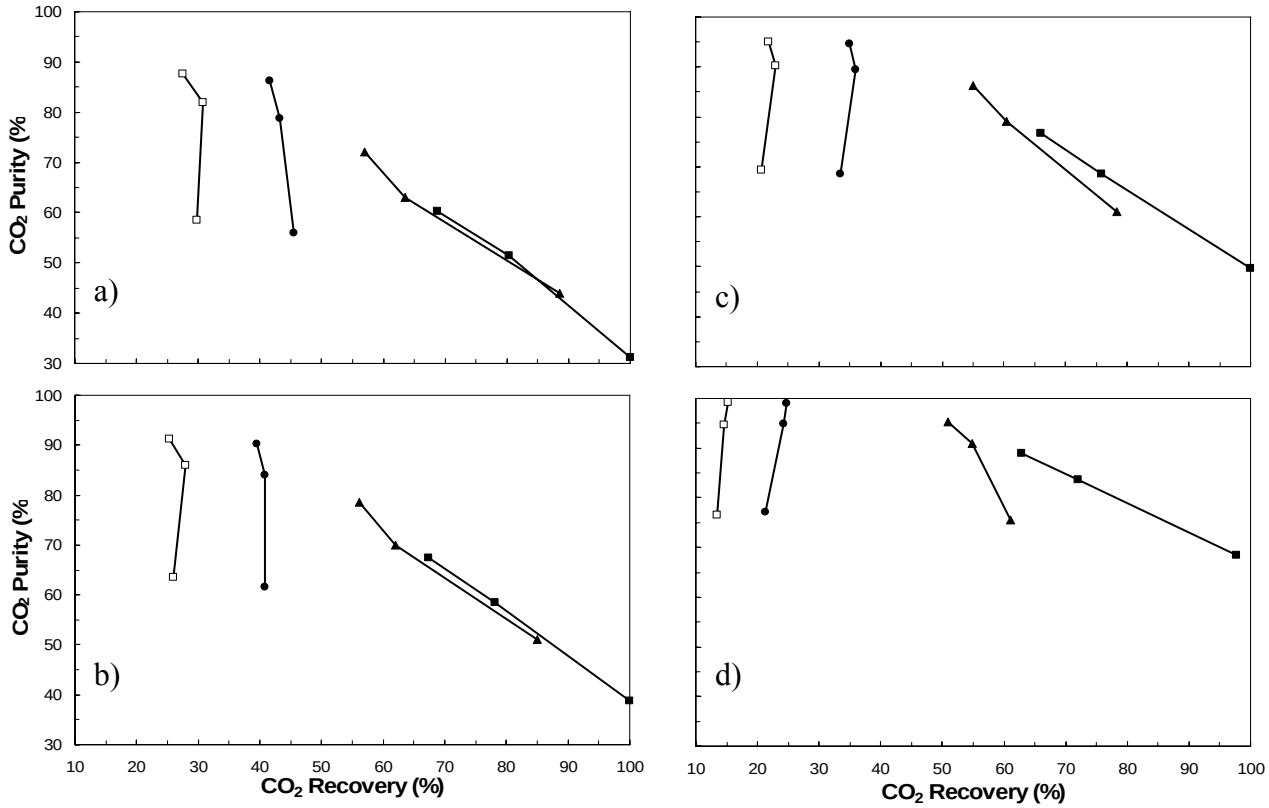

Figure 26. Performance curves from the 4-bed 4-step stripping PSA cycle with HR from CnD (Figure 3a) for R_R = a) 0.2, b) 0.4, c) 0.6 and d) 0.8. Each line corresponds to three runs with t_s increasing from bottom to top (t_s = 100, 300, and 500 s). Symbols: filled squares – θ = 7.2 (Q_F = 0.5); filled triangles – θ = 14.4 (Q_F = 1.0); filled circles – θ = 28.8 (Q_F = 2.0); empty squares – θ = 43.2 (Q_F = 3.0); empty triangles – θ = 57.6 (Q_F = 4.0); empty circles – θ = 72.0 L STP/hr/kg (Q_F = 5.0 L STP/min). The performance curves from the corresponding stripping PSA cycle with HR from CnD, and with REC or F+R were essentially the same (not shown).

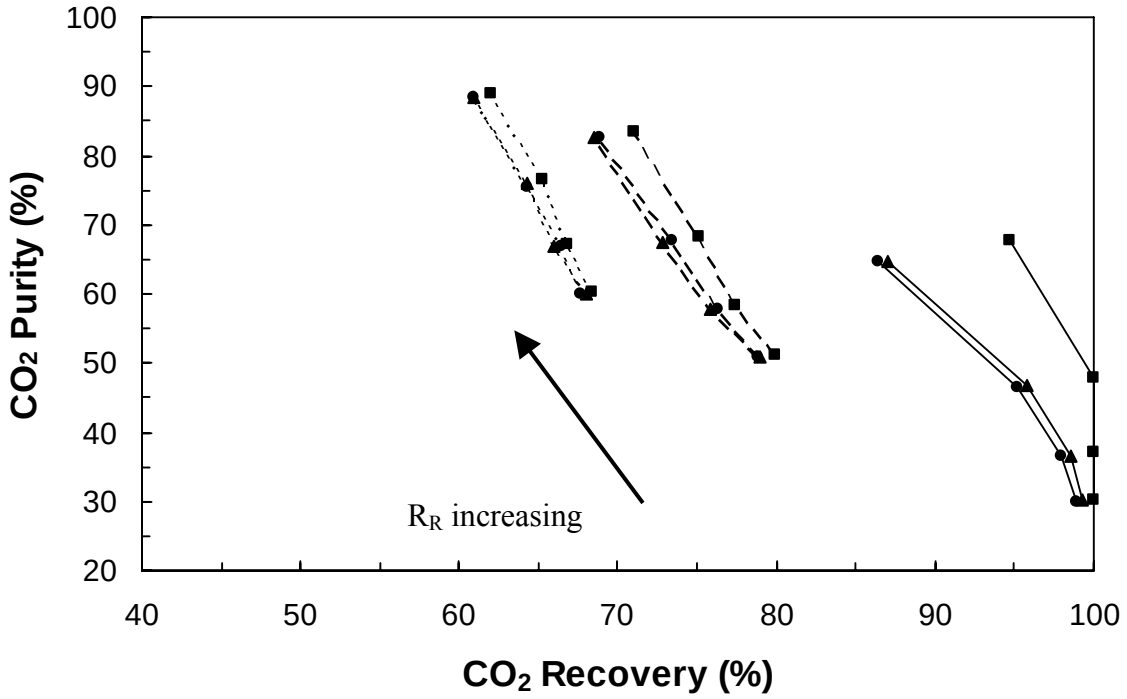

Figure 27. Performance curves comparing the results from the three stripping PSA cycles with HR from CnD with and without REC or F+R steps and for Q_F = 0.5 L STP/min. Lines: solid – t_s = 100 s; dashed – t_s = 300 s; dotted – t_s = 500 s. Symbols: squares – 4-bed 4-step stripping PSA cycle with HR from CnD (θ = 7.2 L STP/hr/kg); triangles – 5-bed 5-step stripping PSA cycle with HR from CnD and REC (θ = 5.8 L STP/hr/kg); circles – 4-bed 4-step stripping PSA cycle with HR from CnD and F+R (θ = 7.2 L STP/hr/kg).

Overall, this study revealed that changes in a HR cycle configuration that were initially thought to be only very slight turned out to have a marked effect on the process performance. For example, the biggest impact on the performance manifested when a LR step was added to the HR cycle, making it a dual reflux cycle. In turn, this made the performance depend very strongly on which step was used to produce the HR gas (or equivalently the heavy product gas). Significant and unexpected differences in the performances were obtained when the HR gas was obtained from the CnD step compared to the LR purge step, which meant that the heavy product gas was respectively produced from the LR purge and CnD steps. Conversely, changes in a HR cycle configuration that were initially thought to be very significant turned out to have only a minimal impact on its performance. For example, the addition of a REC or F+R step to a HR cycle was expected to improve the CO_2 recovery, but the impact turned out to be rather insignificant or even negative.

2.6 Conclusions

First, a simple, 4-step, Skarstrom-type, vacuum swing cycle designed to process a typical stack gas effluent at 575 K containing (in vol%) 15 % CO_2, 75% N_2 and 10% H_2O was studied.

The effects of the purge-to-feed ratio (γ), cycle step time (t_s) (with all four steps of equal time), and pressure ratio (π_T) on the process performance was studied in terms of the CO_2 recovery (R) and enrichment (E) at a constant throughput θ of 14.4 L STP/hr/ kg. The results from 125 simulations, carried out at five different purge-to-feed ratios, cycle step times and pressure ratios showed that R increased with increasing γ and π_T and decreasing t_s, while E increased with increasing t_s and π_T and decreasing γ. The highest E of 3.9 was obtained at R = 87% with $\gamma = 0.5$, $\pi_T = 12$ and $t_s = 500$ s, apparent optimum conditions for both R and E. In contrast, at R = 100% the highest E of 2.8 was obtained at $\gamma = 1.5$, $\pi_T = 12$ and $t_s = 500$ s, apparent optimum conditions for R but not E. Different feed flow rates, i.e., different θs, will result in different sets of optimum possible better conditions. Hence, these results are very encouraging and show the potential of a high temperature PSA cycle for CO_2 capture.

Second, the cyclic adsorption process simulator was used to carry out more than a thousand simulations to study six different high temperature stripping pressure swing adsorption (PSA) cycles over a wide range of process conditions for concentrating CO_2 from a stack gas effluent using a K-promoted HTlc adsorbent. These cycles included a 4-bed 4-step stripping PSA cycle with light reflux (LR), a 5-bed 5-step stripping PSA cycle with LR and cocurrent depressurization (CoD) and countercurrent depressurization (CnD), a 4-bed 5-step stripping PSA cycle with LR and CoD and CnD, a 5-bed 5-step stripping PSA cycle with LR and heavy reflux (HR) from CnD, a 5-bed 5-step stripping PSA cycle with LR and HR from LR purge, and a 4-bed 4-step stripping PSA cycle with HR from CnD. Not only were the effects of the light product purge to feed ratio (γ), the cycle step time (t_s), the high to low pressure ratio (π_T) and the heavy product recycle ratio (R_R) on the process performance revealed and interpreted in terms of their effects on the CO_2 recovery (R), CO_2 purity in the heavy product stream, and feed throughput (θ), but also the effects of different PSA cycle configurations on the process performance were also examined under similar process conditions.

The best PSA cycle depended on which process performance indicator (i.e., the CO_2 purity, the CO_2 recovery or the feed throughput) was considered to be the most important; in this case, the CO_2 purity was chosen to minimize downstream processing. The results of this study showed that the three stripping PSA cycles with a HR step outperformed the three stripping PSA cycles without a HR step, with the dual reflux (LR and HR) stripping PSA process configuration providing the best performance. In terms of CO_2 purity, the 4-bed 4-step stripping PSA cycle with HR from the CnD step performed the best, resulting in a CO_2 purity of 82.7 vol%, a CO_2 recovery of 17.4%, and a feed throughput of 14.4 L STP/hr/kg. The next best PSA cycle was the dual reflux, 5-bed 5-step stripping PSA cycle with LR and HR from LR purge, with a CO_2 purity of 75.5 vol%, a CO_2 recovery of 48.8%, and a feed throughput of 23.1 L STP/hr/kg. The third best PSA cycle performance was exhibited by the 5-bed 5-step stripping PSA cycle with LR and HR from the CnD step (CO_2 purity of 72.2 vol%, CO_2 recovery of 82.2% and low feed throughput of 11.5 L STP/hr/kg).

In contrast to the three HR cycles, the stripping PSA cycles with LR and with or without a CoD step all exhibited similar but somewhat diminished process performances compared to their HR counterparts. For example, the 4-bed 4-step stripping PSA cycle with LR exhibited a less impressive but nevertheless respectable process performance in terms of all three process performance indicators (CO_2 purity of 62.7 vol%, CO_2 recovery of 75.3% and feed throughput of

21.6 L STP/hr/kg).

An unexpected result was the disappointing improvement in the performance of the 4-bed 4-step stripping PSA cycle with LR after adding a CoD step, making it either a 4-bed 5-step stripping PSA cycle (CO_2 purity of 64.6 vol%, CO_2 recovery of 85.0%, and feed throughput of 14.4 L STP/hr/kg), or a 5-bed 5-step (CO_2 purity of 65.0 vol%, CO_2 recovery of 86.7%, and feed throughput of 11.5 L STP/hr/kg) stripping PSA cycle. The inclusion of a CoD step only had a significant but negative effect on the CO_2 recovery, not the CO_2 purity, even when the intermediate CoD pressure was reduced from 101.3 kPa to below atmospheric pressure down to 68.9 kPa (CO_2 purity of 68.2%, CO_2 recovery of 84.2%, and feed throughput of 14.4 L STP/hr/kg). The most important point was that the two intermediate pressures apparently did not correspond to a steep region of the heavy component adsorption isotherm; hence, significant desorption did not take place during the CoD step.

Overall, this second study further substantiated the feasibility of a high temperature stripping PSA cycle for CO_2 capture and concentration from flue gas using an HTlc adsorbent, it disclosed the importance of the PSA cycle configuration to the process performance by gaining an understanding of and appreciation for the use of heavy reflux, and it exposed the rigor involved in determining the best PSA cycle sequence for a given application. Although no attempt was made here to optimize the process performance in terms of the PSA cycle configuration or process conditions, the broad ranges of the process conditions studied in this work for each of the different stripping PSA cycle configurations, made it possible to encompass and essentially reveal the optimum performances of each of these PSA cycles. The question that remains is how to further improve the best performing PSA cycles for CO_2 capture and concentration with a K-promoted HTlc adsorbent, in terms of increasing the CO_2 purity, the CO_2 recovery and the feed throughput through innovative PSA cycle design? To this end, stripping or even enriching PSA cycle configurations with unequal step times and novel light effluent recovery schemes during the HR steps are being explored.

Next, very promising heavy and dual reflux pressure swing adsorption (PSA) cycles, that are being studied for the capture and concentration of CO_2 from flue gases at high temperature (575 K) using a K-promoted hydrotalcite (HTlc), were analyzed under periodic state conditions to determine the effects of the adsorption (k_a) and desorption (k_d) mass transfer coefficients of CO_2 in the K-promoted HTlc on the process performance. Both, a 5-bed 5-step stripping PSA cycle with light reflux (LR) and heavy reflux (HR) from LR purge and a 4-bed 4-step stripping PSA cycle with HR from countercurrent depressurization were studied using a vacuum swing cycle with the high pressure fixed at 137.9 kPa and the feed set at 15 vol% CO_2, 75 vol% N_2 and 10 vol% H_2O. The process performance was judged in terms of the CO_2 purity, CO_2 recovery and feed throughput. Literally hundreds (640) of simulations of these two PSA cycles were carried out over a wide range of process conditions using a cyclic adsorption process simulator, with the values of k_a and k_d changed to reflect reasonable and accepted values in the literature.

For the 5-bed process, increasing the original base case values of k_a (= 0.0058 s^{-1}) and k_d (= 0.0006 s^{-1}) both by a factor of five led to significant increases in both the CO_2 purity and the CO_2 recovery. In the best case, a CO_2 purity of nearly 90% at a relatively high CO_2 recovery of 72.0% and reasonable feed throughput of 57.6 L STP/hr/kg were achieved. Increasing these base

case mass transfer coefficients both by a factor of ten led to even more significant increases in both the CO_2 purity and the CO_2 recovery. In the best case, a CO_2 purity of greater than 90% was achieved for the first time at a high CO_2 recovery of 85.0% and reasonable feed throughput of 57.6 L STP/hr/kg.

Equal mass transfer coefficients for adsorption and desorption also led to significant increases in both the CO_2 purity and the CO_2 recovery. When both mass transfer coefficients were set equal to the original adsorption mass transfer coefficient in the 5-bed process, the best performance achieved had a CO_2 purity of 88.9% with a CO_2 recovery of 72.3% at a reasonable feed throughput of 57.6 L STP/hr/kg. Increasing this mass transfer coefficient by a factor of five then led to a CO_2 purity of 91.5% and a CO_2 recovery of 88.0% at a feed throughput of 57.6 L STP/hr/kg. These results showed that the overall performance of this PSA process was perhaps limited by the rate of desorption of the CO_2 from the K-promoted HTlc.

The 4-bed process produced the highest CO_2 purity so far, based literally on thousands of simulations of this high temperature CO_2 recovery process. However, the CO_2 recovery was quite low in this HR only PSA cycle, compared to the 5-bed process that had both LR and HR steps. For this 4-bed process, increasing the original k_a and k_d both by factors of five led to a sizable increase in the CO_2 purity, with the best performance providing a very high CO_2 purity of 98.1%. But, the corresponding CO_2 recovery decreased substantially down to only 5.0%. Nevertheless, the corresponding feed throughput increased from 14.4 L STP/hr/kg to 201.7 L STP/hr/kg, a significant change.

Overall, the results from this third work continued to show that a high temperature PSA process might be feasible for the capture and concentration of CO_2 from flue gases using a K-promoted HTlc. For the simulations carried out with the faster, but reasonable, uptake and release rates of CO_2 in the K-promoted HTlc, CO_2 purities of greater than 90%, even up to 98%, were achieved for the first time with this high temperature PSA process. Very high feed throughputs were also achieved for the first time, exceeding 200 L STP/hr/kg. From a CO_2 sequestration or sale perspective, at these high CO_2 purities and feed throughputs, it might be economical to employ such a PSA process to recover at least some of the CO_2 from a stack gas, even though the CO_2 recovery might be low.

In a final study nine different stripping PSA cycle configurations with HR were studied for concentrating CO_2 from stack and flue gas at high temperature using a K-promoted HTlc. The best performing cycle based on overall performance was the 5-bed 5-step stripping PSA cycle with LR and HR from CnD. The CO_2 purity was 98.7% and the CO_2 recovery was 98.7%, with $\gamma = 0.02$, $t_s = 100$ s and $\theta = 5.8$ L STP/hr/kg. This was a very exciting result, as the CO_2 purity and recovery were both very high. This very much improved performance was caused by the use of a very small γ ($\gamma = 0.02$). One of the drawbacks of this cycle configuration was the corresponding low feed throughput. Hence, this cycle was good at producing CO_2 at high purities and recoveries, but at lower feed throughputs. When adding either a REC or F+R step to this cycle, nearly identical performances were obtained, especially at the higher feed throughputs. At the lowest feed throughput studied, the differences that did manifest surprisingly were always unfavorable, with lower process performances resulting in both cases.

The next best performing cycle based on overall performance was the 5-bed 5-step stripping PSA cycle with LR and HR from LR purge. This cycle was able to produce a heavy product with a CO_2 purity of 96.5% and a CO_2 recovery of 71.1%, with $\gamma = 0.50$, $t_s = 500$ s and $\theta = 57.6$ L STP/hr/kg. Even though this cycle configuration did not provide as high of a CO_2 purity or CO_2 recovery as the other cycle with HR from CnD, it was very encouraging because the feed throughput was ten times higher, which corresponded to ten times smaller columns. This much improved performance was caused by the use of a relatively larger γ ($\gamma = 0.5$). Hence, this cycle was good at producing CO_2 at high purities and feed throughputs, but at lower recoveries. The addition of a REC or F+R step to this cycle was similar to the previous case, with the process performance never improving.

The worst performing cycle based on recovery was the 4-bed 4-step stripping PSA cycle with HR from CnD. Although it was able to produce a heavy product with a high CO_2 purity of 99.2%, the CO_2 recovery was only 15.2%, with $R_R = 0.8$, $t_s = 500$ s and $\theta = 72.0$ L STP/hr/kg. This much diminished performance surprisingly was caused by the absence of a LR step in this HR cycle. Hence, this cycle was good at producing CO_2 at very low recoveries, but at high purities and feed throughputs. The addition of a REC or F+R step to this cycle was similar to the previous two cases.

Overall, this last study revealed that changes in a HR cycle configuration that were initially thought to be only very slight turned out to have a marked effect on the process performance. For example, the biggest impact on the performance manifested when a LR step was added to the HR cycle, making it a dual reflux cycle. In turn, this made the performance depend very strongly on which step was used to produce the HR gas (or equivalently the heavy product gas). Significant and unexpected differences in the performances were obtained when the HR gas was obtained from the CnD step compared to the LR purge step, which meant that the heavy product gas was respectively produced from the LR purge and CnD steps. Conversely, changes in a HR cycle configuration that were initially thought to be very significant turned out to have only a minimal impact on its performance. For example, the addition of a REC or F+R step to a HR cycle was expected to improve the CO_2 recovery, but the impact turned out to be rather insignificant or even negative. These marked and sometimes subtle effects on the performance of a HR cycle were not expected.

3.0 Graphical Approach for Complex PSA Cycle Scheduling

3.1 Introduction, Literature Review and Objectives

There are just six basic cycle steps associated with any PSA process (Ruthven et al., 1994). These are the feed, rinse (or heavy reflux), co-current or counter-current depressurization, purge (or light reflux), pressure equalization, and repressurization steps. However, since a typical PSA process has multiple beds operating simultaneously and every bed following the same set of cycle steps in order, these six different cycle steps can be scheduled in many different ways. This gives rise to a multitude of different cycle configurations, including cycles that have beds interacting with each other.

In fact, each one of the six basic cycle steps can be coupled to another cycle step, which

necessarily results in pairs of beds being periodically linked during operation of a PSA process. The most obvious step is the pressure equalization step. In this case, two beds are interconnected to allow their pressures to equalize. The gas used for purge can also come from a bed under going either the feed step or the co-current depressurization step (Ruthven et al., 1994). Similarly, the gas used for rinse can come from a bed undergoing either the counter-current depressurization step or purge step. Finally, the gas used for repressurization can come from a bed undergoing the feed step (Ruthven et al., 1994).

In addition, each one of the six basic cycle steps does not always operate for the same length of time, unless it is coupled to another step. These two features, i.e., unequal step time cycles and coupled steps, naturally give rise to numerous constraints that must be met when developing a cycle step schedule for a PSA process. For instance, the operation of two beds undergoing equalization steps must have these steps initiate and terminate at the same time. Likewise, if light product from the feed step is used for repressurization, the length of the pressurization step must be less than or equal to that of the feed step. Clearly, the scheduling of complex PSA cycles is a daunting task, with a paucity of information available in the literature.

Chiang presented an arithmetic approach for scheduling rather simple PSA cycles. However, his analysis did not consider the possibility of idle steps being included in the cycle schedule. An idle step is one where the bed is isolated from the rest of the PSA process for a certain amount of time by closing all of the valves leading to it. It sometimes has to be incorporated to make a set of interacting steps line up properly in the schedule. From Chiang's work, the total idle time for a particular bed can be obtained, but not the positions where the idle steps are to be placed and their respective durations.

Smith and Westerberg (1990) approached this problem from a different perspective. Their idea was to model and solve a set of equations and constraints, considering it as an optimization problem. However, the models became very complicated as the number of beds or constraints increased, due to a corresponding increase in the number of interactions. Understanding and solving such a system of equations and constraints can become an overwhelming and time consuming task, especially for complex, multi-bed, multi-step, PSA systems.

Another objective of this work was to introduce a comparatively simple, graphical approach for complex PSA cycle scheduling. The mechanics of this new methodology are described using a generic example of a PSA cycle schedule. Then, the graphical approach was used to obtain the cycle schedules of several PSA cycles taken from the patent literature, including those with multi-beds, multi-steps, multi-couplings and multi-idle steps. Strengths and weaknesses of this new graphical approach for complex PSA cycle scheduling are discussed in the upcoming sections.

Cycle Sequence: F→E1D→E2D→E3D→CoD→DoD→CnD→LR→E4R→E3R→E2R→E1R→FR

Time →

Bed ↓	**A**	**B**	**C**	**D**	**E**	**F**	**G**	**H**	**I**	**J**	**K**	**L**	**M**	**N**	**O**	**P**	**Q**	**R**	**S**	**T**	**U**	**V**	**W**	**X**
1	CoD		DoD	CnD	LR		E4R	E3R	I	E2R	I	I	E1R	FR			F				E1D	E2D	I	E3D
2	E1D	E2D	I	E3D	CoD		DoD	CnD	LR		E4R	E3R	I	E2R	I	I	E1R	FR			F			
3	F				E1D	E2D	I	E3D		CoD	DoD	CnD	LR		E4R	E3R	I	E2R	I	I	E1R	FR		
4	E1R	FR			F				E1D	E2D	I	E3D		CoD	DoD	CnD	LR		E4R	E3R	I	E2R	I	I
5	I	E2R	I	I	E1R	FR			F				E1D	E2D	I	E3D	CoD		DoD	CnD	LR		E4R	E3R
6	LR		E4R	E3R	I	E2R	I	I	E1R	FR			F				E1D	E2D	I	E3D	CoD		DoD	CnD

Figure 28. PSA cycle schedule of a six-bed thirteen-step process, depicting the primary set (each lighter shaded row of cells), the beginning unit step and ending unit step in the primary set (darker shaded cells), the primary diagonal (all lighter shaded cells), and the unit block (cells contained within the thick black rectangle).

3.2 PSA Cycle Schedule Grid

Figure 28 shows a typical PSA cycle schedule or grid of a PSA system (Xu and Weist, 2002). It consists of six beds and thirteen steps, including four equalization steps and four idle (I) steps. The sequence of the thirteen cycle steps (excluding the I steps) goes as follows:

1. feed (F) at high pressure, where a bed receives gas in its heavy end from the feed source while producing light product from its light end;
2. first pressure equalization step (E1D), where a bed provides gas from its light end to the light end of a bed undergoing pressure equalization (E1R);
3. second pressure equalization step (E2D), where a bed provides gas from its light end to the light end of a bed undergoing pressure equalization (E2R);
4. third pressure equalization step (E3D), where a bed provides gas from its light end to the light end of a bed undergoing pressure equalization (E3R);
5. co-current depressurization (CoD), where a bed provides purge gas from its light end to the light end of a bed undergoing light reflux (LR);
6. dual ended depressurization (DoD), where a bed is depressurized from both the light and heavy ends, with the gas exiting its light end being provided to the light end of a bed receiving pressure equalization (E4R) and the gas exiting its heavy end being taken as heavy product;
7. counter-current depressurization (CnD), where a bed is depressurized through its heavy end to provide most of the heavy product;
8. light reflux (LR), where a bed receives purge gas in its light end from the light end of a bed undergoing co-current depressurization (CoD);
9. fourth pressure equalization step (E4R), where a bed receives gas in its light end from the light end of a bed undergoing dual ended depressurization (DoD);
10. third pressure equalization step (E3R), where a bed receives gas in its light end from the light end of a bed undergoing pressure equalization (E3D);
11. second pressure equalization step (E2R), where a bed receives gas in its light end from the light end of a bed undergoing pressure equalization (E2D);
12. first pressure equalization step (E1R), where a bed receives gas in its light end from the light end of a bed undergoing pressure equalization (E1D); and
13. feed repressurization (FR), where a bed receives gas in its heavy end from the feed source.

In the corresponding grid, all six beds are placed along the vertical direction, whereas time is placed along the horizontal direction. The twenty-four columns in the grid, i.e., A through X along the horizontal direction, represent unit time steps or time steps of identical length. A row of the grid represents all the different cycle steps a given bed undergoes over the entire cycle, whereas a column of the grid represents which cycle step is being run by which bed at a particular unit time step. The total cycle time is the sum of all the individual unit time steps of a particular row. The intersection of a row and a column of the grid is a unit cell and is the smallest repeating element of the grid.

A unit cell is denoted by its row and column position in the grid. For example, unit cell D-4 contains the step which runs in bed 4 during unit time step D (i.e., FR). For a particular bed,

one unit cell corresponds to the minimum time of operation of any cycle step. In other words, a unit cell can be occupied by only one cycle step. In addition, the total length of an individual cycle step is always a multiple of the unit time step. For instance, in Figure 28, the CnD step occupies one unit time step, and the F step occupies four unit time steps.

The lighter shaded cells in Figure 28 represent one of many primary diagonals that can be identified in this grid. As shown later, the primary diagonal is the fundamental element that is required for the formation of any grid. Notice that the primary diagonal consists of the same repeating blocks (for every bed) placed diagonally along the grid. Each repeating block is denoted as a primary set. In this case, a primary set is six unit cells long and consists of cycle steps CoD, DoD, CnD, and LR. As there are six beds, six primary sets are arranged diagonally along the grid. The primary sets can be arranged diagonally in different ways, which gives rise to many other solutions or schedules other than the one shown in Figure 28. Such possibilities are discussed in detail in the next section.

Every primary set has two key elements, i.e., the beginning unit step, which is the first unit time step in the set, and the ending unit step, which is the last unit time step in the set. For example, the beginning unit and ending unit steps for the primary sets in rows three and four are indicated in Figure 28 by the darker shaded cells. The ending unit step of the first row must also be aligned properly with the beginning unit step of the second row and so on in subsequent rows to initiate and complete the formation of the primary diagonal and thus the primary grid. There are three possibilities. First, these two steps can be aligned vertically with one unit time step overlapping. Second, the beginning unit step can be shifted to the left from this vertical position with multiple unit time steps overlapping. For example, the schedule in Figure 28 has its primary sets shifted to the left from the vertical position by one unit cell. Third, the beginning unit step can be shifted to the right by multiple unit time steps with no unit time steps overlapping. This choice may or may not be arbitrary, depending on the imposed constraints, as illustrated later by example.

Since every bed operates identically in a PSA process, the same cycle steps are run by successive beds after a fixed interval of time. This means that the same operation in one bed is repeated in another bed after this interval, the duration of which constitutes a unit block. A thick solid line enclosing unit step times A through D represents one unit block for the cycle shown in Figure 28. Notice that within the unit block, all the steps in the schedule are being run by one of the six beds. The unit block occurs again during unit step times E through H. In the same way, the total cycle time is made up of six consecutive unit blocks, and this number must match the total number of beds.

3.3 PSA Cycle Schedule Methodology

This graphical scheduling methodology is divided into two parts. In the first part, the goal is to build the primary grid. A primary grid is formed when the array of a given number of rows (i.e., beds) and a given number of columns (i.e., unit time steps) is determined. In the second part, the final cycle schedule is built around the primary grid by filling in the rest of the remaining empty unit cells. During this second part, the number of idle steps (if any), their duration, and relative location within the grid is determined.

In part one, two pieces of information about the PSA cycle must be decided *a priori* to start building a grid. First, the individual cycle steps of the cycle must be chosen from the six basic steps, along with their sequence of operation. Second, the number of beds must be chosen. Consider the hypothetical PSA cycle shown in Figure 29, where the number of beds is chosen to be three and the sequence of cycle steps is defined generically by I through V. Figure 29a shows an empty grid with three rows (equivalent to the total number of beds) and multiple vertical columns (representing different unit time steps). At this point, the total number of unit time steps or the total cycle time has not been determined. In other words, the grid is free to expand or contract horizontally.

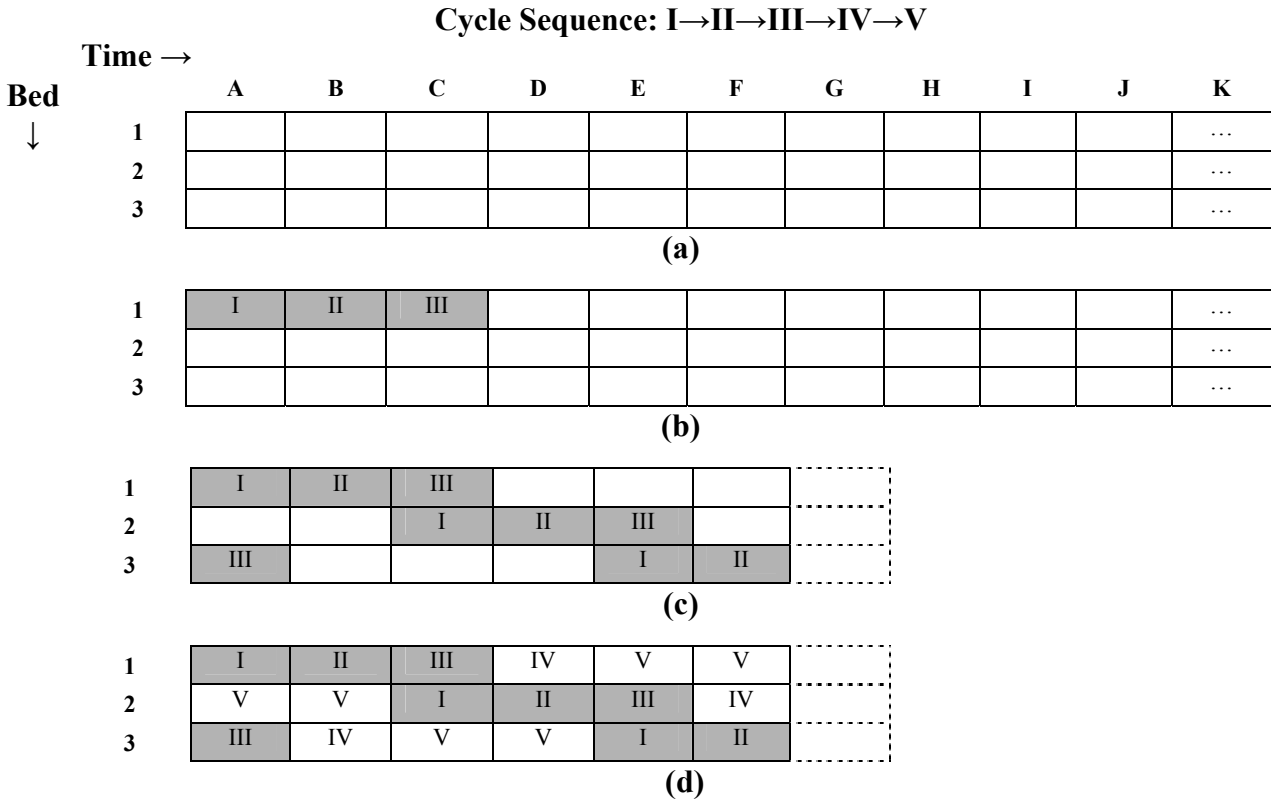

Figure 29. Construction of a PSA cycle schedule for a three-bed five-step process: a) initial empty grid; b) grid from (a) showing primary set (shaded cells); c) grid from (b) showing primary set added to every row, forming the primary diagonal and primary grid (shaded cells); and d) grid from (c) showing all cycle steps added, forming a cycle schedule.

Typically, for any PSA cycle schedule a few constraints must be satisfied. For instance, in the sequence shown in Figure 28, the gas from the CoD step is used to purge the bed undergoing the LR step. Thus, these two steps are coupled, so they must initiate and terminate at the same time. In the schedule shown in Figure 29, the same is assumed for steps I and III. In other words, at a given unit time step, at least two different beds must have these steps operating simultaneously. Although there is usually more than one constraint that must be satisfied in a PSA cycle, like that shown in Figure 28, only one constraint (if any) should be selected for the formation of the primary grid, because it allows for more flexibility in part two, i.e., during grid

filling. Heuristic: choose the constraint associated with a coupled set of steps that has the least number of cycle steps in between them.

The next stage of part one involves the formation of the primary set. The length of the primary set is chosen arbitrarily, while keeping the above heuristic in mind. At this point, it must be decided whether all the cycle steps in the primary set are the same duration, with each one being only one unit time step long, or whether one or more of the cycle steps occupies more than one unit time step. The beginning unit and ending unit steps of the primary grid are then identified, with the caveat that these steps can only be one unit time step long, even if the cycle step they belong to is more than one unit time step.

In this example, to build the primary set, one of the two coupled cycle steps, i.e., I or III, must be chosen to begin the set, while the other must be chosen to end it. Since, the cycle steps always run in order, step I can be chosen as either the beginning unit step or the ending unit step, and the same holds true for step III. Hence, a primary set can be formed in two ways. For the cycle sequence shown in Figure 29, the two possible primary sets are [I, II, and III] and [III, IV, V, I], with the shorter one preferred because it also allows for more flexibility with placement of the remaining steps during grid filling, especially if any one of the remaining steps is expected to be longer than one unit cell, like a feed step. Constructing a primary set with more cycle steps requires the lengths of the intermediate steps to be decided *a priori*, which for certain cases thwarts the possibility of considering other options that a smaller primary set may allow. Heuristic: choose the primary set with the least number of cycle steps.

Based on the above heuristic, the first primary set is placed in the first row of the grid in Figure 29b in unit cells A-1, B-1, and C-1. This makes step I the beginning unit step and step III the ending unit step. For the particular case shown in Figure 29, the total length of the primary set is based on the stipulation that the lengths of steps I, II and III are equal and that they each occupy only one unit time step. Thus, the primary set shown in Figure 29 is three unit time steps long.

The next stage of part one is to take the primary set that has been established for bed 1 in row one and place it in consecutive rows by aligning it in such a way that it forms the primary diagonal along the grid. Recall that this diagonal arrangement with the primary set to form the primary diagonal can be done in three ways. The ending unit step in row one can align vertically with the beginning unit step in row two, or the beginning unit step can be shifted to the left or to the right of this position. For the schedule in Figure 28, the shift in the alignment from the vertical position is to the left by one unit time step, logically resulting in overlap of the LR and CoD steps, which are each two unit time steps long and coupled. In contrast, for the example in Figure 29, the simplest case is considered, where the ending unit step in row one (step III) and the beginning unit step in row two (step I) overlap and each cycle step happens to be only one unit time step long (Figure 29c). In other words, these two steps are vertically aligned. The primary diagonal is thus formed by placing the primary set in each consecutive row with the proper alignment of the ending unit step and beginning unit step until the last row is reached. Heuristic: consider the simplest alignment first; shifts to the left second, especially if they make a coupled set of steps that each occupy more than one unit cell to be completely aligned; and shifts to the right last, if grid expansion is deemed necessary.

Observe that while proceeding down the primary diagonal, unit cell F-3 is occupied by step II. If step III is aligned along its side in unit cell G-3 like in the rest of the rows, then there is no corresponding step III for step I of bed 1 in A-1. Hence, step III must be placed in A-3 to complete the primary grid. This primary grid is unique to the specified cycle step sequence, number of beds, and primary set.

The importance of forming the primary grid, i.e., the primary diagonal from the primary set cannot be overstated. It fixes the length of the grid horizontally, which, in turn, fixes the number of unit time steps in the grid and thus the total cycle time. In the example in Figure 29, the diagonal arrangement makes sure that steps I and III are always coupled, as seen in Figure 29c at unit times A, C and E. Moreover, as mentioned above, the primary grid can be formed in different ways. For example, if steps I and III are coupled for only part of the time, then they do not need to be the same duration. In other words, an equally valid primary set is [I, I, II, II, II, II, and III], which occupies seven unit time steps. This primary set stipulates that steps I and III are coupled during only one of the unit time steps, the duration of step I is two times this unit time step, and the duration of step II is four times this unit time step. Another equally valid primary set is [I, I, II, III and III], which occupies five unit time steps. Steps I and III are still coupled for the entire time, but their duration is twice that of step II. Heuristic: choose to have a cycle step in a primary set that occupies more than one unit cell only if that step is known to be longer than a cycle step that occupies a single unit cell.

With respect to primary set alignment, there is no limit to the number of unit time step shifts that can be taken to the right, as the total number of unit time steps in the grid has not been determined. However, there is a limit to the number of unit time step shifts that can be taken to the left. This limit is reached when the two primary sets become completely aligned in two consecutive rows. The PSA cycle schedule that forms for such a situation corresponds to one where all the beds operate independent of each other with no coupled steps possible. This is not a very useful PSA cycle schedule. However, one shift to the left less may result in a viable PSA cycle schedule.

In addition, the total unit time steps in the primary grid increases with an increase in the number of right shifts and it decreases with an increase in the number of left shifts. These may be positive or negative attributes and may even lead to nonsensical solutions or schedules, depending on the number of beds, particular cycle sequence, and relative time of the shortest cycle step to that of the longest cycle step. Clearly, some trial and error is involved with the choice of the primary set and its alignment to form the corresponding primary grid, where experience with PSA cycles is paramount to minimizing the number of options to consider.

In part two, the final PSA cycle schedule is built around the primary grid by filling in the rest of the remaining empty unit cells using intuition, experience, and also some trail and error. Notice that for the primary grid in Figure 29c, there are three empty unit cells (for each row) in which the two remaining cycle steps must be placed. Clearly, there are two possible ways to do this ([IV, IV, V] and [IV, V, V]), with each resulting in a unique solution or cycle schedule. Heuristic: if you have coupled cycle steps to deal with during part two, choose to add each set of coupled steps one at a time in such a way that it minimizes the number of idle steps. This

heuristic becomes clear later in an example.

By assuming that no additional constraints need to be satisfied in this example, one possible cycle schedule of many is shown in Figure 29d. In this case, step V takes up two unit step times and step IV takes up only one unit step time. More illustrations of the versatility afforded in part two are provided in the *Applications* section, where this methodology is used to obtain actual PSA cycle schedules from the literature.

In closing this section, it is noteworthy that the methodology presented so far is very restrictive due to the constraints imposed by the coupled cycle steps. However, a completely general methodology is also possible that relaxes all constraints during the formation of the primary grid in part one. This relaxation allows for the most flexibility in deriving uniquely different PSA cycle schedules. Any constraints are then handled one at a time in a logical fashion during the filling of the grid in part two. One of the applications addressed later illustrates this more general approach to primary grid formation and solution or schedule refinement.

3.4 PSA Cycle Schedule Applications

To illustrate how to apply this new graphical approach to an actual PSA cycle schedule, a relatively simple two-bed four-step Skarstrom PSA cycle is analyzed first (Skarstrom, 1960). In this example, every bed undergoes the same following steps: feed (F) at high pressure, countercurrent depressurization (CnD) from high pressure to a low pressure, light reflux purge (LR) at low pressure, and light product pressurization (LPP) from low to high pressure. For this configuration, gas leaving the light end of the bed undergoing the F step is provided as purge to the light end of the bed undergoing the LR step and is also used to pressurize the bed during LPP. Hence, two constraints must be considered while forming such a cycle schedule. These are coupling of F with LR, and F with LPP. Also, if a buffer tank is not to be used, the length of the LPP and LR steps must be less than or equal to the F step.

One possible grid is depicted in Figure 30a. The F, CnD and LR steps are arbitrarily chosen to constitute the primary set. F is the beginning unit step while LR is the ending unit step, with their durations the same and each equal to one unit time step. The simplest alignment is also selected in this case to satisfy one of the constraints mentioned above on coupled steps. So, the ending unit step of the primary set in the first row is vertically aligned with the beginning unit step of the primary set in the second row, which is shown in Figure 30a. This particular primary grid leaves one unit cell (darker shaded cell) for LPP to be placed in. There is only one solution for this situation, i.e., the equal step time cycle schedule shown in Figure 30b. However, notice that the F step is not continuous, which may not be acceptable depending on the application.

One of the primary goals in designing a PSA process is to maximize the feed throughput, which can be accomplished by feeding longer or by feeding multiple beds at the same time. To increase the feed time of this two-bed four-step PSA process, the grid needs to be expanded horizontally. Clearly, this is not possible with the primary set used in Figure 30. Figure 31a shows a primary set where the F step occupies two unit cells and the CnD and LR steps take one unit cell each. The formation of the primary grid is again based on vertical alignment, which also satisfies one of the constraints on the coupled steps. But now the grid size is six unit time steps

(Figure 31a) instead of five (Figure 30), which makes two unit cells (darker shaded cells in Figure 31a) available for the placement of LPP and/or the F step. The only solution which can accommodate continuous feed for a two-bed four-step cycle arranged in six unit cells is shown in Figure 31b. In other words, for the feed to be continuous, it must occupy three of the six unit cells. This leaves only three unit cells for the remaining three steps; hence, there is only one solution for this case.

Cycle Sequence: F→CnD→LR→LPP

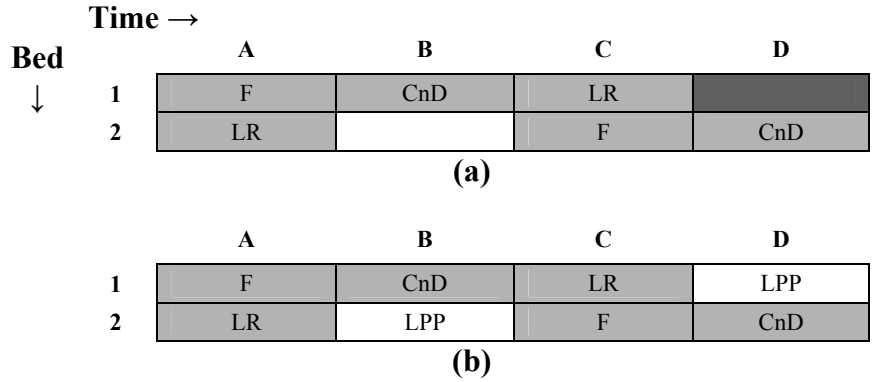

Figure 30. Construction of a PSA cycle schedule for a two-bed four-step process: a) grid showing primary set, primary diagonal and primary grid (lighter shaded cells), and empty cells for filling with remaining cycle steps (darker shaded cells); and b) grid from (a) showing all cycle steps added, forming an equal step time cycle schedule.

Cycle Sequence: F→CnD→LR→LPP

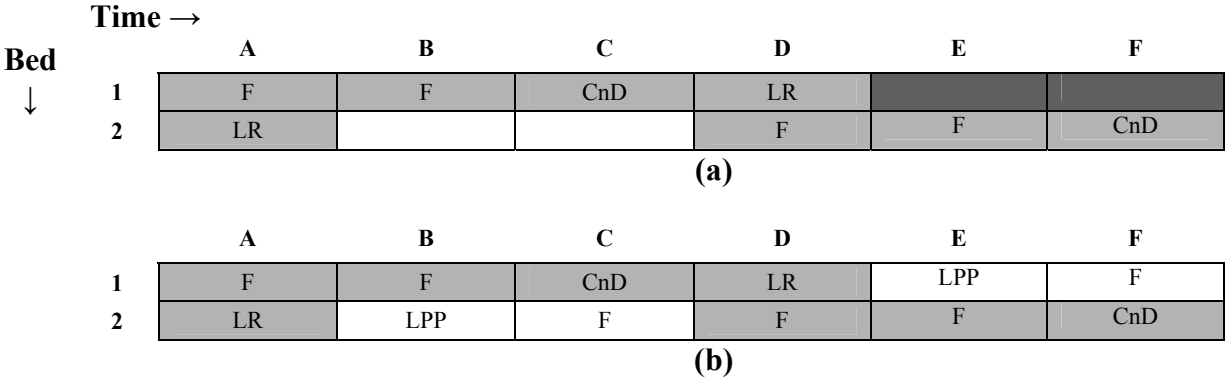

Figure 31. Construction of a PSA cycle schedule for a two-bed four-step process: a) grid showing primary set, primary diagonal and primary grid (lighter shaded cells) with more intermediate steps between the beginning unit step (F) and ending unit step (LPP) and with empty cells for filling with remaining cycle steps (darker shaded cells); and b) grid from (a) showing all cycle steps added, forming the final cycle schedule.

All the two-bed four-step cycles discussed so far were based on coupling the F and LR steps. The primary set and consecutively the primary diagonal can also be formed by considering

the other constraint instead, i.e., by coupling the F and LPP steps together. For this particular case, choosing LPP to be the beginning unit step and F to be the ending unit step results in a primary grid where no space is left for the rest of the cycle steps. However, this might not be true when the number of beds is more than two. Alternatively, the primary set can be constructed with F being the beginning unit step and LPP being the ending unit step, as shown in Figure 32a. This is an interesting case where all the cycle steps in the sequence are used to form the primary grid. For this case, the only solution with continuous feed is shown in Figure 32b. Notice that this solution is the same as that shown in Figure 31b. This implies that the same solution might be obtained even when starting from a different primary set.

Figures 33a, 33b and 33c show an example where the primary grid can be expanded even further. The expansion results from using different relative lengths of any of the steps including the beginning unit step, ending unit step and any intermediate steps. For example, intermediate steps occupy three unit cells in Figure 33a (B-1 to D-1 in bed 1), four unit cells in Figure 33b (B-1 to E-1 in bed 1), and five unit cells in Figure 33c (B-1 to F-1 in bed 1). Notice that the length of the feed step is the same in all three cases (50% relative to the total cycle time); but, the relative lengths of the other steps constituting the sequence are different. Such a procedure can prove to be very useful while exploring different PSA cycles for a specific application. Also, the grid shown in Figure 33c is exactly the same as that in Figure 31b i.e., if the duration of every unit cell of Figure 31b is doubled, Figure 33c is obtained. This demonstrates that if every unit cell in a particular grid is expanded by a constant factor, like 2, 3 or 4, then it results in the same grid (provided they both represent the same total cycle time).

Cycle Sequence: F→CnD→LR→LPP

Time →

Bed ↓

	A	B	C	D	E	F
1	F	CnD	LR	LPP		
2	LPP			F	CnD	LR

(a)

	A	B	C	D	E	F
1	F	CnD	LR	LPP	F	F
2	LPP	F	F	F	CnD	LR

(b)

Figure 32. Construction of a PSA cycle schedule for a two-bed four-step process: a) grid showing primary set, primary diagonal and primary grid (lighter shaded cells) formed with F and LPP being coupled and empty cells for filling with remaining cycle steps (darker shaded cells); and b) grid from (a) showing all cycle steps added, forming the final cycle schedule.

Cycle Sequence: F→CnD→LR→LPP

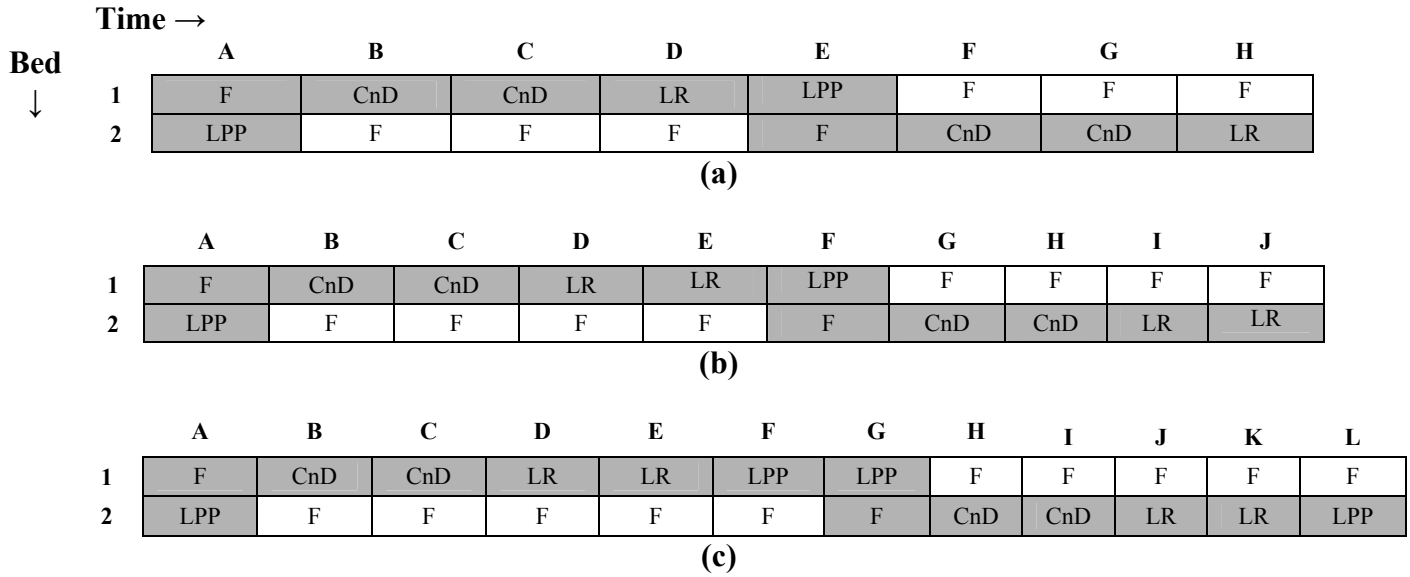

Figure 33. Construction of PSA cycle schedules for a two-bed four-step process showing the importance of grid expansion: a) grid showing primary set, primary diagonal and primary grid (shaded cells) formed with F and LPP being coupled, intermediate steps occupying three unit cells, and the entire grid formed with eight unit time steps; b) intermediate steps occupying four unit cells and entire grid formed with ten unit time steps; c) intermediate steps occupying five unit cells and entire grid formed with twelve unit time steps.

It is noteworthy that a variation of the two-bed four-step PSA cycle schedules depicted in Figures 31 to 33 are used commercially in gasoline vapor recovery units (Dinsmore and Young, 1984). All of these cycle schedules have one bed being fed while the other bed is undergoing CnD, LR and LPP. In this way the feed is continuous to the PSA unit, as required when recovering gasoline vapor from large tank filling operations.

These concepts can be implemented and extended easily for a larger number of beds. Figures 34a and 34b show two primary grids for a three-bed four-step PSA cycle with F and LR coupled in one case, and F and LPP coupled in the other case. Based on the heuristics and procedure discussed above, the rest of the unit cells can be filled in easily, resulting in the cycle schedules shown in Figures 34c, 34d and 34e. In Figure 34c, two LPP steps and one F step are chosen to fill in the grid, with the only other option being LR, LPP and F. The schedule in Figure 34d is unique because two beds are being fed simultaneously at all times. With the F steps occupying 33.3% and 66.7% of the total cycle time in Figures 34c and 34d, respectively, it is interesting that the feed throughput can be doubled simply by choosing a different coupled step to form the primary step and the primary diagonal. Other options are possible, like that shown in Figure 34e.

Cycle Sequence: F→CnD→LR→LPP

Time →

Bed ↓

	A	B	C	D	E	F
1	F	CnD	LR			
2			F	CnD	LR	
3	LR				F	CnD

(a)

	A	B	C	D	E	F	G	H	I
1	F	CnD	LR	LPP					
2				F	CnD	LR	LPP		
3	LPP						F	CnD	LR

(b)

	A	B	C	D	E	F
1	F	CnD	LR	LPP	LPP	F
2	LPP	F	F	CnD	LR	LPP
3	LR	LPP	LPP	F	F	CnD

(c)

	A	B	C	D	E	F	G	H	I
1	F	CnD	LR	LPP	F	F	F	F	F
2	F	F	F	F	CnD	LR	LPP	F	F
3	LPP	F	F	F	F	F	F	CnD	LR

(d)

	A	B	C	D	E	F	G	H	I
1	F	CnD	LR	LPP	LPP	LPP	I	F	F
2	I	F	F	F	CnD	LR	LPP	LPP	LPP
3	LPP	LPP	LPP	I	F	F	F	CnD	LR

(e)

Figure 34. Construction of a PSA cycle schedule for a three-bed four-step process: a) and b) grid showing primary set, primary diagonal and primary grid (lighter shaded cells), and empty cells for filling with remaining cycle steps (darker shaded cells) with F and LR and F and LPP forming the coupled steps; c) grid from (a) showing all cycle steps added, forming a cycle schedule; d) grid from (b) showing all cycle steps added, forming a cycle schedule where two beds are being fed simultaneously at any instant; e) grid from (b) showing all cycle steps added, forming a cycle schedule with one idle step.

This cycle schedule has an idle (I) step after the LPP step and before the F step. Sometimes it may be necessary to accommodate an I step in the final cycle schedule for two reasons. First, an I step can be used to align the various coupled steps in different beds (as shown in later examples), and second, for a particular bed, an I step can be used to shorten an individual cycle step (if needed). In the grid shown in Figure 34e, placing the I step in between the F and

LPP steps causes the length of both these steps to be equal. Placing F in G-1 results in a variable feed cycle (where one bed is being fed sometimes and two beds are being fed other times), whereas placing LPP there makes the LPP step longer than the F step, which is impossible without a buffer tank.

As discussed earlier, it is not always necessary for the ending unit step to align vertically with the beginning unit step of consecutive beds to form the primary grid. Consider the primary set shown in Figure 34b, where F, CnD, LR and LPP occupy one unit cell each and the ending unit step (LPP) of any one bed is aligned vertically with the beginning unit step (F) of another bed. If this alignment is broken, the ending unit step of a particular bed can be displaced one (or more) position(s) either to the left or to the right relative to the ending unit step of another bed. These cases are depicted in Figures 35. Compared to Figure 34b, Figure 35a shows the primary grid with the alignment shifted one position to the left. Following the same logic from previous examples, the primary grid can be completed, resulting in Figure 35b. This is the only possible solution. Figure 35c shows the grid with the alignment shifted one position to the right. Notice in this case, none of the coupled steps are aligned along the primary diagonal, which means care must be taken to ensure alignment of coupled steps when filling in the grid. One possible solution is shown in Figure 35d. In this case two columns are again being fed simultaneously at all times. Other solutions are possible, but they allow only one bed to be fed at a time and involve one or two LPP steps and numerous I steps.

As realized from the PSA cycle schedule shown in Figure 28, pressure equalization steps are quite common in the PSA patent literature and used commercially not only to save on operating costs (intuitive) but also to improve the performance (Ruthven et. al., 1994). The next example is more complicated in that it adds two pressure equalization steps to a four-bed PSA cycle. One such way is presented below, based on the following nine-step cycle sequence:

1. high pressure feed (F), provides light product;
2. first pressure equalization (E1D), coupled with E1R;
3. co-current depressurization (CoD), coupled with light reflux (LR) purge;
4. second pressure equalization (E2D), coupled with E2R;
5. counter-current depressurization (CnD), provides heavy product;
6. light reflux (LR) purge, coupled with CoD;
7. second pressure equalization (E2R), coupled with E2D;
8. first pressure equalization (E1R), coupled with E1D; and
9. light product pressurization (LPP), coupled with F.

Figure 36a shows the resulting primary grid. Clearly, CoD, E2D, CnD and LR form the primary set (shaded cells in every row) with the alignment being vertical. CoD and LR steps are two unit time steps long, whereas E2D and CnD are each a unit time step long. In addition, CoD and LR are the beginning unit step and ending unit step, respectively. These are logical choices, especially since they satisfy one constraint on step coupling, i.e., CoD and LR are coupled. The darker shaded cells C-3 and C-4 depict the possible places that E2R (corresponding to E2D in C-1) can occupy. C-2 is eliminated because placing E2R in it leaves no space for other steps between E2R and CoD, and placing E2R in C-3 results in four I steps between LR and E2R (occupying O-3 to B-3). Figure 36b shows E2R placed in C-4. As every bed follows the same

sequence of steps, E2R is further placed in G-1, K-2 and O-3. Notice that for the steps shown in Figure 36b, the grid is completely balanced. In other words, the coupled steps are properly aligned. Figure 36c shows E1R being placed next to E2R in all the beds. The darker shaded cells show two possible places where E1D can be placed (corresponding to E1R in D-4). D-2 is the logical choice as placing E1D in D-3 results in four I steps (in cells F-3 to H-3) between E1D and CoD. The result is the grid depicted in Figure 36d. Observe that for every bed, seven unit cells are occupied by the LPP and F steps (combined). To have continuous feed, LPP must occupy three unit cells, whereas F must occupy four unit cells. This results in the grid shown in Figure 36e, which is the same as proposed by Cassidy and Holmes (1984).

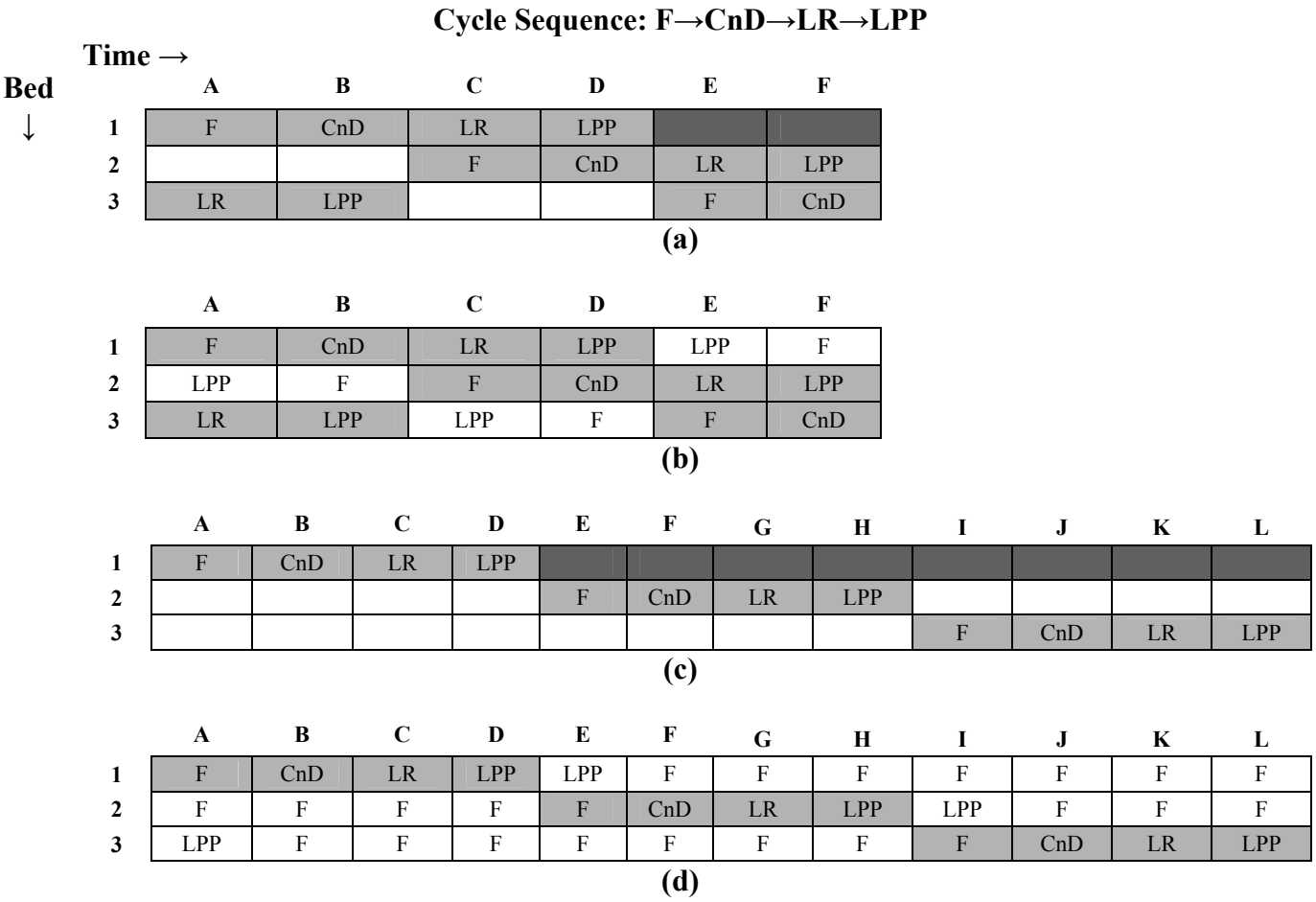

Figure 35. Construction of PSA cycle schedules for a three-bed four-step process showing the relative importance of aligning primary sets in different beds: a) grid showing primary set, primary diagonal and primary grid (lighter shaded cells), and empty cells for filling with remaining cycle steps (darker shaded cells) with the beginning unit step (F) aligned one unit time step to the left relative to the end step (LPP) in consecutive beds; b) grid from (a) showing all cycle steps added, forming a cycle schedule; c) grid showing primary set, primary diagonal and primary grid (lighter shaded cells), and empty cells for filling with remaining cycle steps (darker shaded cells) with the beginning unit step (F) aligned one unit time step to the right relative to the end step (LPP) in consecutive beds; d) grid from (c) showing all cycle steps added, forming a cycle schedule.

At this point it is probably becoming obvious that there are many ways to configure PSA cycles. Next consider a five-bed eleven-step cycle based on the following sequence:

1. high pressure feed (F), provides light product;
2. first pressure equalization (E1D), coupled with E1R;
3. second pressure equalization (E2D), coupled with E2R;
4. co-current depressurization (CoD), coupled with light reflux (LR) purge;
5. third pressure equalization (E3D), coupled with E3R;
6. counter-current depressurization (CnD), provides heavy product;
7. light reflux (LR) purge, coupled with CoD;
8. third pressure equalization (E3R), coupled with E3D;
9. second pressure equalization (E2R), coupled with E2D;
10. first pressure equalization (E1R), coupled with E1D; and
11. feed repressurization (FR).

Figure 37a shows the resulting primary grid. Clearly, CoD, E3D, CnD and LR form the primary set, the duration of each step is equal to the unit time step, CoD and LR are the beginning unit step and ending unit step, and the alignment is vertical. These are logical choices, especially since they satisfy one constraint on step coupling, i.e., CoD and LR are coupled. The darker shaded cells B-4 and B-5 depict the possible places that E3R (corresponding to E3D in B-1) can occupy. B-2 and B-3 are eliminated because placing E3R in them leaves no space for other steps between E3R and CoD. Also, E3R in B-4 requires I steps in three unit cells (N-4, O-4 and A-4), resulting in a shorter F step. Hence, E3R occupying B-5 is the logical choice. This result is shown in Figure 37b.

The darker shaded cells in Figure 37b represent two choices where E1D can be placed corresponding to E1R in A-4. When E1D occupies A-3, only one unit cell (O-3) becomes available for the F step, thereby lowering the feed throughput considerably. Contrarily, Figure 37c shows E1D in A-2, and depending on the length of E1D, two solutions are possible. These are shown in Figures 37d and 37e. The grid in Figure 37d is the same as that shown by Chiang (1988). Note that these grids can be configured in many ways, resulting in many solutions, depending upon the relative lengths of FR and F.

The next example illustrates how to form the primary grid with overlap of the unit cells during left shifting alignment of the primary sets. Consider the same sequence of steps for the six-bed system shown in Figure 28. The not so obvious choice for the primary set is CoD, DoD, CnD, and LR. The durations of the CoD and LR steps are each twice the unit time step, with the other two steps having durations equal to the unit time step. The beginning unit step and ending unit step are associated with the first unit time step occupied by CoD and the second unit time step occupied by LR. The alignment is such that the beginning unit step in row two is shifted one unit time step to the left from the vertical alignment position. This alignment choice puts the coupled CoD and LR steps in complete alignment with each other. The resulting primary grid is given in Figure 38a. Observe that because the CoD and LR steps occupy two unit cells each, the primary grid expands to twenty-four columns (A through X). It is worth insisting that the decision to start with longer CoD and LR steps to expand the grid horizontally depends on the relative gain in the feed time without compromising the process performance. However, this can

be judged only after solutions are obtained.

Cycle Sequence: F→E1D→CoD→E2D→CnD→LR→E2R→E1R→LPP

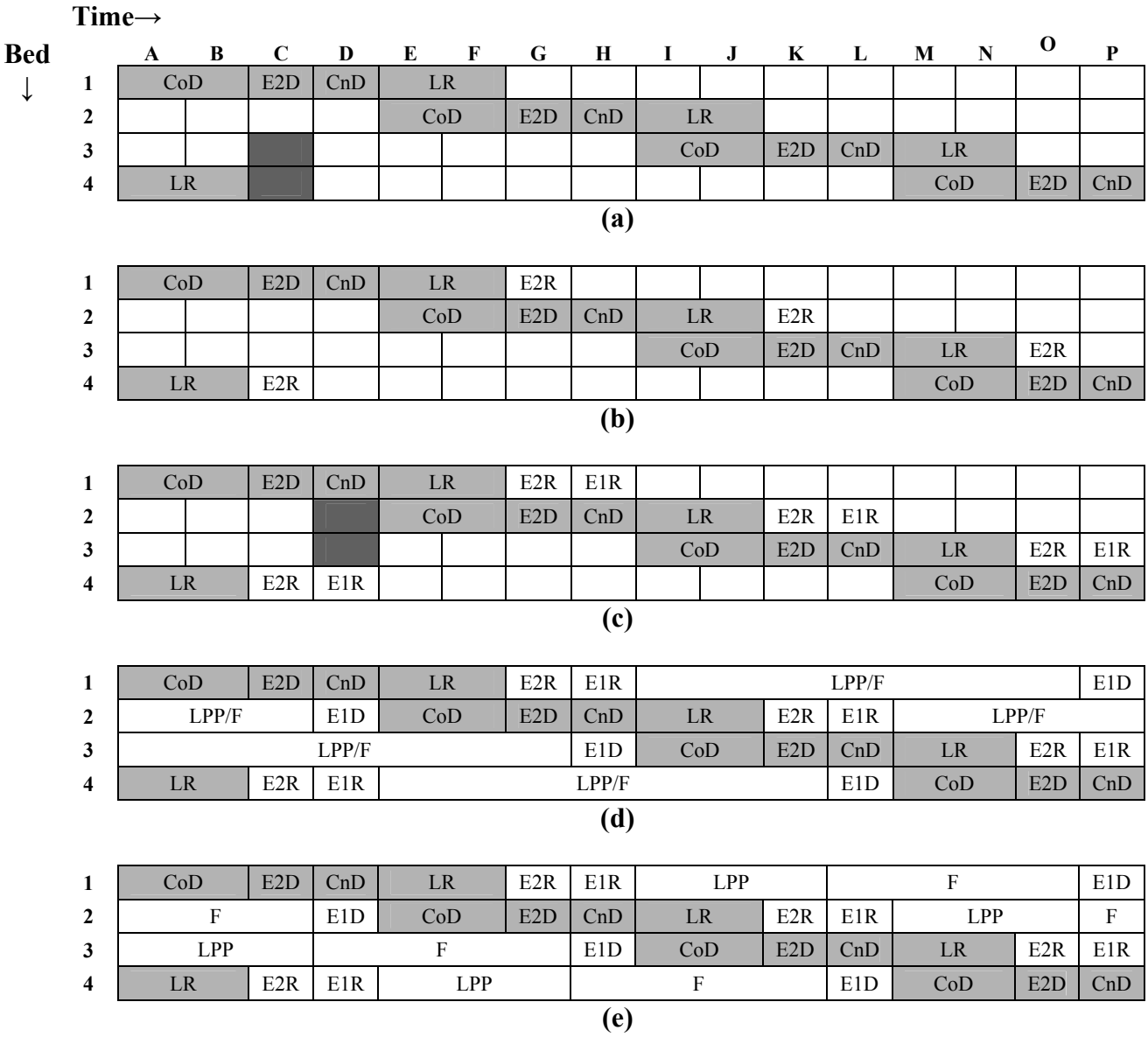

Figure 36. Construction of a PSA cycle schedule for a four-bed nine-step process with two equalization steps: a) grid showing primary set, primary diagonal and primary grid (lighter shaded cells); b) and c) showing placement of two equalization steps; d) and e) grids from (b) and (c) showing all cycle steps added, forming two cycle schedules.

Cycle Sequence: F→E1D→E2D→CoD→E3D→CnD→LR→E3R→E2R→E1R→FR

Time →

Bed ↓

	A	B	C	D	E	F	G	H	I	J	K	L	M	N	O
1	CoD	E3D	CnD	LR											
2				CoD	E3D	CnD	LR								
3							CoD	E3D	CnD	LR					
4										CoD	E3D	CnD	LR		
5	LR												CoD	E3D	CnD

(a)

1	CoD	E3D	CnD	LR	E3R	E2R	E1R								
2				CoD	E3D	CnD	LR	E3R	E2R	E1R					
3							CoD	E3D	CnD	LR	E3R	E2R	E1R		
4	E1R									CoD	E3D	CnD	LR	E3R	E2R
5	LR	E3R	E2R	E1R									CoD	E3D	CnD

(b)

1	CoD	E3D	CnD	LR	E3R	E2R	E1R								E2D
2	E1D		E2D	CoD	E3D	CnD	LR	E3R	E2R	E1R					
3						E2D	CoD	E3D	CnD	LR	E3R	E2R	E1R		
4	E1R								E2D	CoD	E3D	CnD	LR	E3R	E2R
5	LR	E3R	E2R	E1R								E2D	CoD	E3D	CnD

(c)

1	CoD	E3D	CnD	LR	E3R	E2R	E1R			FR/F				E1D		E2D	
2	E1D		E2D	CoD	E3D	CnD	LR	E3R	E2R	E1R		FR/F					
3	FR/F			E1D		E2D	CoD	E3D	CnD	LR	E3R	E2R	E1R			FR/F	
4	E1R		FR/F			E1D		E2D	CoD	E3D	CnD	LR	E3R	E2R			
5	LR	E3R	E2R	E1R		FR/F				E1D		E2D	CoD	E3D	CnD		

(d)

1	CoD	E3D	CnD	LR	E3R	E2R	E1R	FR/F					E1D	I	E2D
2	E1D	I	E2D	CoD	E3D	CnD	LR	E3R	E2R	E1R	FR/F				
3	FR/F			E1D	I	E2D	CoD	E3D	CnD	LR	E3R	E2R	E1R	FR/F	
4	E1R	FR/F				E1D	I	E2D	CoD	E3D	CnD	LR	E3R	E2R	
5	LR	E3R	E2R	E1R	FR/F					E1D	I	E2D	CoD	E3D	CnD

(e)

Figure 37. Construction of a PSA cycle schedule for a five-bed eleven-step process with three equalization steps: a) grid showing primary set, primary diagonal and primary grid (lighter shaded cells), and two empty cells for filling with remaining cycle steps (darker shaded cells); b) grid from (a) showing new cycle steps added and two new empty cells for filling with remaining cycle steps (darker shaded cells); c) grid from (b) showing more cycle steps added and two new empty cells for filling with remaining cycle steps (darker shaded cells); d) grid from (c) showing all cycle steps added, forming a cycle schedule; and e) grid from (a) showing all cycle steps added, but forming an alternative cycle schedule than that in (d), because the cycle steps are added differently than in (b) and (c).

Since E4R follows LR and E3D precedes CoD, they each occupy only one unit time step, resulting in the grid in Figure 38b. This makes steps DoD and E4R overlap in consecutive beds, as required since they are coupled (see Figure 28 and the *Cycle Schedule Grid* section). The darker shaded cells show the possible places where E3R can be placed corresponding to E3D in D-2. E3R cannot occupy D-3 as this leaves no space for the six steps in between E3R and E3D. Also, E3R in D-4 gives a solution where the equalization steps do not align. So, the only two places that E3R can occupy are D-5 or D-6. By observation, D-5 is not the preferred choice, as it forces four I steps in between E4R and E3R, leaving little room for the feed step. This leaves D-6 as the place to put E3R. This arrangement is shown in Figure 38c, with equalization steps E1D, E2D and E3D also added and placed together. The darker shaded cells represent the two places that E2R can occupy in unit time step W. To minimize the idle steps, E2R is placed in W-4. The resulting cycle schedule is shown in Figure 38d. Seven unit cells are now available for any combination of the FR and F steps, with longer feed times usually preferred.

A different schedule is obtained if equalization steps E4R, E3R and E2R instead of equalization steps E1D, E2D and E3D are placed together in the primary grid shown in Figure 38c. This grid is shown in Figure 39a. Again, to minimize the number of I steps in the solution, E1R (corresponding to E1D in H-4) is placed in H-6. The resulting cycle schedule is shown in Figure 39b. However, if an I step is placed *a priori* between E3R and E2R after the formation of the primary grid (Figure 38a) and the same procedure discussed above is followed, then the cycle schedule depicted in Figure 39c results. This cycle schedule has been reported by Xu et al (2002). Note that the lengths of the different cycle steps in Figure 39c are exactly the same as those in Figure 38d. The only difference between the two solutions is the position of the four I steps; thus, in essence, they are the same cycle schedule, if the position of the idle step has no effect on the process performance. Clearly, this comparison shows the utility of the graphical scheduling methodology, as it can be used in a logical fashion to obtain cycle schedules that have been obtained perhaps by less rational approaches.

The last example takes the nine-bed eleven-step PSA cycle sequence shown in Figure 40 and illustrates the situation when the primary grid is comprised of uncoupled cycle steps. The nomenclature for the various steps is the same as that for the configurations in Figure 38. Unlike all the previous cycle sequences, the primary set E1D, E2D and E3D has no coupled steps, with the beginning unit step as E1D, the ending unit step as E3D, and the alignment being vertical. It is worth pointing out that aligning E1D and E2D makes the grid too small, and other combinations may result in the grid being too wide, thereby reducing the equalization times compared to the total cycle time. This grid is also based on the initial stipulation that the E3D and E1D equalization steps operate for the same duration. This is a reasonable assumption for equalization steps.

The darker shaded cells in Figure 40a show the possible places where E1R can be placed in a unit step time A. E1R and E1D are separated by two steps, FR and F. So, to increase the feed throughput, it is desirable to put E1R in A-6, which, in turn, leaves nine unit cells (B-6 to J-6) in which the FR and F steps can be distributed. As a consequence, the depressurization and LR steps are comparatively shortened, which may be undesirable. To avoid such a scenario, E1R is placed in A-5, which produces the grid shown in Figure 40b. This grid is now balanced for the first equalization steps.

Cycle Sequence: F→E1D→E2D→E3D→CoD→DoD→CnD→LR→E4R→E3R→E2R→E1R→FR

Time→

Bed ↓

	A	B	C	D	E	F	G	H	I	J	K	L	M	N	O	P	Q	R	S	T	U	V	W	X
1	CoD		DoD	CnD	LR																			
2					CoD		DoD	CnD	LR															
3									CoD		DoD	CnD	LR											
4													CoD		DoD	CnD	LR							
5																	CoD		DoD	CnD	LR			
6	LR																				CoD		DoD	CnD

(a)

	A	B	C	D	E	F	G	H	I	J	K	L	M	N	O	P	Q	R	S	T	U	V	W	X
1	CoD		DoD	CnD	LR		E4R																	E3D
2				E3D	CoD		DoD	CnD	LR		E4R													
3								E3D	CoD		DoD	CnD	LR		E4R									
4												E3D	CoD		DoD	CnD	LR		E4R					
5																E3D	CoD		DoD	CnD	LR		E4R	
6	LR		E4R																	E3D	CoD		DoD	CnD

(b)

	A	B	C	D	E	F	G	H	I	J	K	L	M	N	O	P	Q	R	S	T	U	V	W	X
1	CoD		DoD	CnD	LR		E4R	E3R														E1D	E2D	E3D
2		E1D	E2D	E3D	CoD		DoD	CnD	LR		E4R	E3R												
3						E1D	E2D	E3D	CoD		DoD	CnD	LR		E4R	E3R								
4										E1D	E2D	E3D	CoD		DoD	CnD	LR		E4R	E3R				
5														E1D	E2D	E3D	CoD		DoD	CnD	LR		E4R	E3R
6	LR		E4R	E3R														E1D	E2D	E3D	CoD		DoD	CnD

(c)

	A	B	C	D	E	F	G	H	I	J	K	L	M	N	O	P	Q	R	S	T	U	V	W	X
1	CoD		DoD	CnD	LR		E4R	E3R	I	I	E2R	I	I	E1R	FR/F							E1D	E2D	E3D
2	F	E1D	E2D	E3D	CoD		DoD	CnD	LR		E4R	E3R	I	I	E2R	I	I	E1R	FR/F					
3	FR/F					E1D	E2D	E3D	CoD		DoD	CnD	LR		E4R	E3R	I	I	E2R	I	I	E1R	FR/F	
4	I	E1R	FR/F							E1D	E2D	E3D	CoD		DoD	CnD	LR		E4R	E3R	I	I	E2R	I
5	I	I	E2R	I	I	E1R	FR/F							E1D	E2D	E3D	CoD		DoD	CnD	LR		E4R	E3R
6	LR		E4R	E3R	I	I	E2R	I	I	E1R	FR/F							E1D	E2D	E3D	CoD		DoD	CnD

(d)

Figure 38. Construction of a PSA cycle schedule for a six-bed thirteen-step process with four equalization steps: a) grid showing primary set, primary diagonal and primary grid (shaded cells); b) grid from (a) showing new cycle steps added and two empty cells for filling with remaining cycle steps (darker shaded cells); c) grid from (b) showing more cycle steps added and two new empty cells for filling with remaining cycle steps (darker shaded cells); and d) grid from (c) showing all cycle steps added, forming a cycle schedule.

Cycle Sequence: F→E1D→E2D→E3D→CoD→DoD→CnD→LR→E4R→E3R→E2R→E1R→FR

Time→

Bed ↓

	A	B	C	D	E	F	G	H	I	J	K	L	M	N	O	P	Q	R	S	T	U	V
1	CoD	DoD	CnD	LR	E4R	E3R	E2R											E1D	E2D	I	I	E3D
2	E2D	I	E3D	CoD	DoD	CnD	LR		E4R	E3R	E2R											E1D
3			E1D	E2D	I	I	E3D	CoD		DoD	CnD	LR		E4R	E3R	E2R						
4							E1D	E2D	I	I	E3D	CoD		DoD	CnD	LR		E4R	E3R	E2R		
5	E2R										E1D	E2D	I	I	E3D	CoD		DoD	CnD	LR	E4R	E3R
6	LR		E4R	E3R	E2R										E1D	E2D	I	I	E3D	CoD	DoD	CnD

(a)

1	CoD	DoD	CnD	LR	E4R	E3R	E2R	I	I	E1R	FR/F							E1D	E2D	I	I	E3D
2	E2D	I	I	E3D	CoD	DoD	CnD	LR		E4R	E3R	E2R	I	I	E1R	FR/F						E1D
3	FR/F		E1D	E2D	I	I	E3D	CoD		DoD	CnD	LR		E4R	E3R	E2R	I	I	E1R	FR/F		
4	FR/F						E1D	E2D	I	I	E3D	CoD		DoD	CnD	LR		E4R	E3R	E2R	I	I	E1R
5	E2R	I	I	E1R	FR/F					E1D	E2D	I	I	E3D	CoD		DoD	CnD	LR		E4R	E3R
6	LR		E4R	E3R	E2R	I	I	E1R	FR/F					E1D	E2D	I	I	E3D	CoD		DoD	CnD

(b)

1	CoD		DoD	CnD	LR		E4R	E3R	I	E2R	I	I	E1R	FR/F						E1D	E2D	I	I	E3D
2	E1D	E2D	I	E3D	CoD		DoD	CnD	LR		E4R	E3R	I	E2R	I	I	E1R	FR/F						
3	FR/F				E1D	E2D	I	E3D	CoD		DoD	CnD	LR		E4R	E3R	I	E2R	I	I	E1R	FR/F		
4	E1R	FR/F							E1D	E2D	I	E3D	CoD		DoD	CnD	LR		E4R	E3R	I	E2R	I	I
5	I	E2R	I	I	E1R	FR/F							E1D	E2D	I	E3D	CoD		DoD	CnD	LR		E4R	E3R
6	LR		E4R	E3R	I	E2R	I	I	E1R	FR/F							E1D	E2D	I	E3D	CoD		DoD	CnD

(c)

Figure 39. Construction of a PSA cycle schedule for a six-bed thirteen-step process with four equalization steps: a) grid from Figure 38a showing a different placement of cycle steps than in Figure 38b or 38c; b) grid from (a) showing all cycle steps added, but forming an alternative cycle schedule than that in Figure 38d; and c) grid from Figure 38a showing all cycle steps added, but forming another alternative cycle schedule than those in Figure 38d and (b).

To couple the third equalization steps, E3R (corresponding to E3D in A-9) can occupy either A-6 or A-7. When E3R is placed in A-6, the grid shown in Figure 40c is reached. This grid provides multiple solutions depending on the lengths of the CoD, CnD, LR, FR, and F steps. As the CoD and LR steps are coupled, the two combinations possible for CoD, CnD, and LR are (2, 1, 2) and (1, 3, 1). Similarly, for FR and F, the possibilities include (1, 6), (2, 5), (3, 4), (4, 3), (5, 2) and (6, 1). When the CoD, CnD, and LR steps are distributed as (2, 1, 2), and the FR and F steps are distributed as (1, 6), the solution shown in Figure 40d is realized. This cycle schedule has been reported by Fuderer (1976). On the other hand, when E3R occupies A-7 in Figure 40b, the cycle schedule depicted in Figure 40e is reached. Here, the lengths of the FR and F steps remain the same as the previous schedules, but the depressurization and LR steps are shortened. It is clear that there are many possible cycle schedules for this nine-bed eleven step PSA cycle, some desirable and some not.

It must be emphasized that the intent behind the development of this approach was to provide a simple set of rules from which a PSA cycle schedule can be built. It was never the intent to provide an optimum schedule for a given PSA cycle. Thus, although this graphical approach cannot be used to indicate the total number of permutations from a given set of cycle steps, their sequence and number of beds, and although it cannot be used to indicate which one is better, it can be employed in a very straightforward fashion to determine cycle schedules for virtually any PSA process that can be conceived. To determine the best cycle schedule from the multitude of possibilities that typically result, significant experience, sound intuition, and a good PSA process simulator are needed.

3.5 Conclusions

A simple graphical approach to scheduling complex pressure swing adsorption (PSA) cycles was introduced. This new methodology involves *a priori* specifying the cycle steps, their sequence, and the number of beds, and then following a systematic procedure that requires filling in a 2-D grid based on a few simple rules, some heuristics, some experience, and possibly a trial and error approach. The outcome from a single graphical analysis is a grid comprised of columns that represent the total cycle time, rows that represent the total number of beds, and cells that represent the duration of each cycle step, i.e., a complete cycle schedule. This cycle schedule is usually one of many possible cycle schedules that can be obtained for the chosen set of cycle steps, their sequence, and number of beds.

This new graphical approach was tested successfully against several PSA cycle schedules taken from the literature, including a two-bed four-step Skarstrom cycle, a four-bed nine-step process with two equalization steps, a nine-bed eleven-step process with three pressure equalization steps, and a six-bed thirteen-step process with four pressure equalization steps and four idle steps. The results revealed the existence of numerous cycle schedules for each of those bed and cycle step combinations. Hence, many possible cycle schedules were easily derived for any number of beds involving multiple constraints with numerous bed interactions through the application of this graphical approach.

Cycle Sequence: F→E1D→E2D→E3D→CoD →CnD→LR→E3R→E2R→E1R→FR

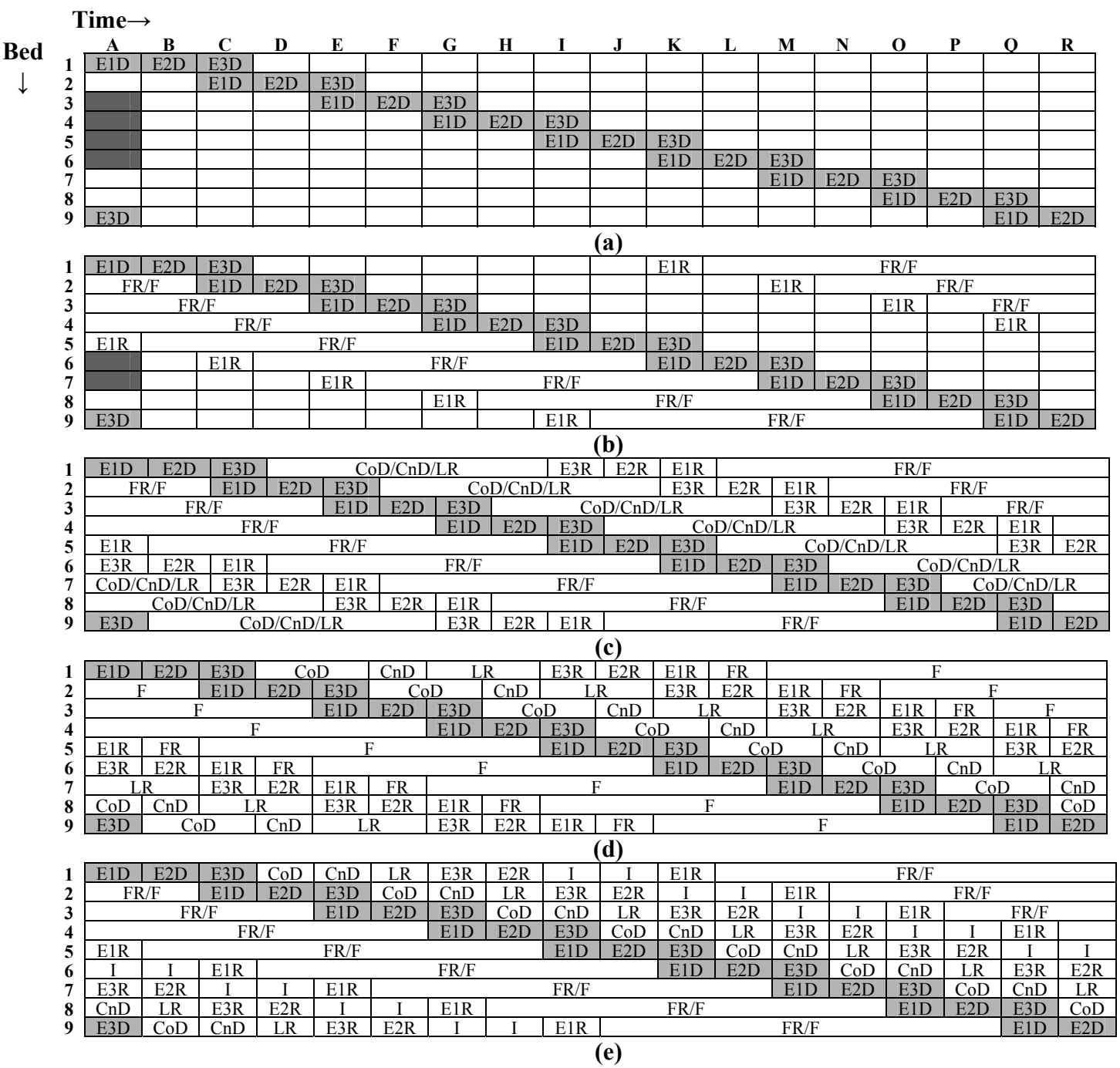

Figure 40. Construction of a PSA cycle schedule for a nine-bed eleven-step process with three equalization steps: a) grid showing primary set, primary diagonal and primary grid (lighter shaded cells), and three empty cells for filling with remaining cycle steps (darker shaded cells); b) grid from (a) showing new cycle steps added and two new empty cells for filling with remaining cycle steps (darker shaded cells); c) grid from (b) showing all cycle steps added, forming a cycle schedule; d) grid from (a) showing all cycle steps added, but forming an alternative cycle schedule than that in (c); and e) grid from (b) showing all cycle steps added, but forming another alternative cycle schedule than those in (c) and (d).

It must be emphasized that the intent behind the development of this approach was to provide a simple set of rules from which a PSA cycle schedule can be built. It was never the intent to provide an optimum schedule for a given PSA cycle. Thus, although this graphical approach cannot be used to indicate the total number of permutations from a given set of cycle steps, their sequence and number of beds, and although it cannot be used to indicate which one is better, it can be employed in a very straightforward fashion to determine cycle schedules for virtually any PSA process that can be conceived. To determine the best cycle schedule from the multitude of possibilities that typically result, significant experience, sound intuition, and a good PSA process simulator are needed.

4.0 Study of PSA Cycles for CO_2 Capture by Equilibrium Theory Analysis

4.1 Introduction, Literature review and Objectives

Pressure swing adsorption (PSA) has earned widespread acceptance and is being used extensively for gas purification and separation (Ruthven et al., 1994). Most of the PSA cycles practiced industrially and studied in the literature have been designed to purify the light component from bulk gas steams. Very little work has been done where the heavy component is the product of interest. The concept of heavy reflux (HR) has been used over the years to obtain high purities of the heavy species. Ruthven et al (1994) provides some insight on HR cycles being employed for CO_2 sequestration. The HR step normally follows the feed step and obtains its feed gas from the blowdown step and/or the purge step (if employed). Thus, the feed to a HR column is rich in the heavy component. Incorporating this step increases the loading of the heavy species in the bed which in turn results in high purities. When a particular cycle configuration employs both the HR and the LR purge steps, the cycle is also called as a dual reflux (DR) PSA cycle. Previous work on equilibrium theory and the analytical solutions obtained for the different models haven't considered the use of this HR step.

Mathematical models for PSA cycles can be classified into two groups, namely, equilibrium and non-equilibrium models. Non-equilibrium models consider the effects of heat and mass transfer within the beds and can be solved numerically for both linear and non-linear isotherms. However, when there is sufficiently fast mass transfer, the use of local equilibrium assumption is appropriate. Analytical solutions could be obtained for such systems which represent the upper limit of the separation possible.

Shendalman and Mitchell (1972) first came up with analytical solutions to a local equilibrium model for purification of a trace component from an inert gas. Their work was later extended to study a four step PSA cycle by Knaebel and Hill (1985). They found that pressurization with light product was more efficient than feed pressurization. Thus, the solutions presented in this paper consider light product pressurization alone. Also, complete purge of the column before pressurization is not always necessary, especially at high feed concentrations. A study by Matz and Knaebel (1988) showed improved recoveries with incomplete purge. However, their cycle configuration did not consider a heavy reflux step and the focus was mainly on the light component. Rousar and Ditl (1993) found optimum purge conditions for a four bed PSA cycle, but the study considered the concentration wave to have travelled the entire bed length at the end of the feed step. Such conditions are rarely achieved in practice. In addition,

none of these studies considered operation of the HR step in their cycle schedule. Although equilibrium theory neglects the effects of mass and heat transfer inside PSA beds which might not be true for real systems, it does provide quick estimates of the effects of various parameters on the process performance and provide ball park estimates of their ranges.

Thus, another objective of this work was to analyze a five-bed, five-step dual reflux (DR) stripping PSA cycle based on isothermal, linear isotherm equilibrium theory developed by Knaebel and Hill (1985). Analytical expressions derived were used to study the effect of different parameters on the process performance of the system. For a binary feed mixture, these expressions showed the effect of light product volumetric purge to feed ratio, selectivity, feed concentration, pressure ratio and throughput on the purities and recoveries of both components. In particular, the effect of incompletely purging the LR column was studied. The analysis revealed the ability of this stripping PSA cycle to produce pure heavy component with high recoveries. Also, this cycle configuration can be used to produce two pure products with 100% recovery of each species under certain conditions.

4.2 PSA Cycle Description

The five bed stripping PSA cycle studied in this analysis is shown in Figure 41. Reynolds et al. (2007) presented simulation results of this cycle configuration and found it to be useful for obtaining very high purities and recoveries of the heavy component. Each bed undergoes the following five steps in sequence: (1) feed (F) at high pressure (P_H), (2) heavy reflux (HR) or rinse also at P_H, (3) countercurrent depressurization (CnD) from P_H to the low pressure (P_L), (4) light reflux (LR) purge at P_L and (5) light product pressurization (LPP) from P_L to P_H. In this cycle configuration, all the gas exiting the column undergoing CnD is recycled back to the column undergoing HR. Hence, the heavy product is obtained solely from the LR step. Also, a portion of the light gas leaving the column undergoing feed is used to purge and pressurize the columns undergoing LR and LPP, respectively.

A shock wave of concentration y_F develops during the feed step, but is never allowed to breakthrough the light end of the column. This ensures that pure light gas is used to purge and pressurize the columns. Also, pure heavy gas exits the column undergoing CnD and thus enters the column undergoing HR. This causes another shock wave of concentration $y = 1$ to form behind the feed concentration shock front. During the HR step, the smaller shock wave ($y = y_F$) is forced to exit the bed completely and, as a consequence, the entire column is saturated with the heavy component at the end of this step. Doing so ensures that there is no light product left in the bed at the end of CnD, which allows pure heavy product to be obtained for a determinable period of time during the subsequent LR step.

A simple dispersed wave forms during the LR step, because this column just finished CnD and thus contains a higher concentration of the heavy species than in the light gas used as purge (y = 0) to this column during LR. Since the aim of this study is to maximize the recovery and purity of the heavy component, process conditions are chosen such that this dispersed wave either just reaches the end of the bed which ensures the production of a pure heavy product, or is allowed to breakthrough which causes the heavy product to be less than pure.

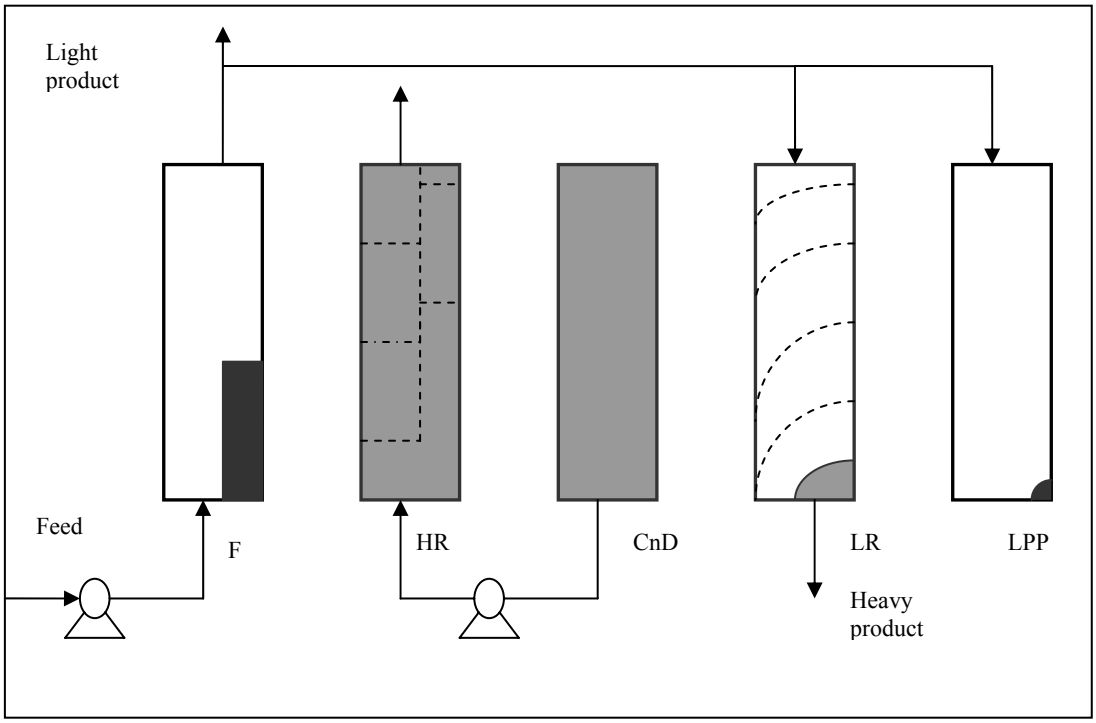

Figure 41. Schematic of a five-bed, five-step stripping PSA cycle with LR and HR from CnD; F = feed; HR = heavy reflux; CnD = countercurrent depressurization; LR = light reflux; LPP = light product pressurization

A simple modification to the above cycle is also possible, which gives rise to the perfect separation of both species, i.e., the separation of species A and B into two 100% pure products with 100% recovery of each species When the smaller shock wave ($y = y_F$) reaches z = L and starts to breakthrough the light end of the HR column, this exit gas is used to purge the LR column. This slight modification allows all of the heavy species to be recovered and thus prevents it from otherwise being lost in the light product during the HR step as a result of breakthrough. However, another restriction needs to be imposed. The purge to feed ratio must be chosen so that the dispersed wave that forms during the LR step just reaches the end of the bed. This ensures that no light species ends up in the heavy product. With these two changes, the perfect separation of species A and B can be achieved.

4.3 Mathematical Model of a PSA Process based on Equilibrium Theory Analysis

The following equilibrium theory analysis is based on the approach presented by Knaebel and Hill (1985). The system is assumed to operate under isothermal conditions and at pressures where the ideal gas law applies. Also, the effects of dispersion, mass transfer, and non-ideal flow are not considered. Species A represents the heavy component and species B represents the light component. Species A and the total mole balance equations are, respectively, given by:

$$\varepsilon\left(\frac{\partial P_A}{\partial t}+\frac{\partial uP_A}{\partial z}\right)+RT\left(1-\varepsilon\right)\frac{\partial n_A}{\partial t}=0 \tag{16}$$

$$\varepsilon\left(\frac{\partial P}{\partial t}+\frac{\partial uP}{\partial z}\right)+RT\left(1-\varepsilon\right)\frac{\partial n}{\partial t}=0 \tag{17}$$

$$P=P_A+P_B \tag{18}$$

$$n=n_A+n_{\mathbf{B}} \tag{19}$$

where P is the total pressure, P_i is the partial pressure of component i, u is the interstitial velocity, ε is the interstitial void fraction, n_i is the number of moles of species i adsorbed on the solid per unit column volume, and n is the total moles adsorbed on the solid per unit column volume. When the isotherms are linear,

$$n_i=\frac{k_iP_i}{RT} \quad ; \text{i = A or B} \tag{20}$$

where $\frac{k_i}{RT}$ is the slope of the isotherm and k_i is the dimensionless Henry's law constant. Parameter β represents the degree of selectivity of the adsorbent towards the two species. Defining β_i in the same fashion as Knaebel and Hill (1985) gives:

$$\beta_i=\frac{1}{1+\frac{(1-\varepsilon)k_i}{\varepsilon}} \quad ; \text{i = A or B} \tag{21}$$

$$\beta=\frac{\beta_A}{\beta_B} \tag{22}$$

By assuming no pressure drop in the column, the interstitial velocity u can be calculated from (Knaebel and Hill, 1985):

$$u=\frac{-L}{\beta_B\left[1+(\beta-1)y\right]}\frac{1}{P}\frac{dP}{dt} \tag{23}$$

Eq (23) is valid for the pressure varying steps such as countercurrent depressurization and pressurization. Knaebel and Hill (1985) also showed that

$$\frac{u_p}{u_q}=\frac{1+(\beta-1)y_q}{1+(\beta-1)y_p} \tag{24}$$

where p and q are two different points in the bed. Eq (24) is valid for constant the pressure steps such as feed, heavy reflux and light reflux. For these steps the shock velocity is evaluated from (Knaebel and Hill, 1985):

$$u_s = \frac{\beta_A u_1}{1+(\beta-1)y_2} = \frac{\beta_A u_2}{1+(\beta-1)y_1} \tag{25}$$

Subscripts 1 and 2 denote points immediately in front of and behind the shock wave.

4.3.1 Step-Wise Mole Balances

The above relations are now combined with mass balances over each step. In the relations that follow, the total moles entering and exiting the beds are tracked along with the internal flows within each bed. It is assumed that the system has already reached periodic state.

Feed Step Analysis: The total moles that enter the column undergoing feed are given by:

$$\mathrm{N_{F(in)}} = \int_0^{\Delta t} \mathrm{u_F}\ \varepsilon\ \mathrm{A_{cs}}\ \frac{\mathrm{P_H}}{\mathrm{RT}}\,\mathrm{dt} = \pi\phi\Delta\tau \tag{26}$$

where π is the pressure ratio ($\pi = \frac{P_H}{P_L}$), $\phi = \frac{\varepsilon A_{cs} L P_L}{RT\beta_A}$ and $\Delta\tau = \frac{u_F \beta_A \Delta t}{L}$. u_F is the feed interstitial velocity and A_{cs} is the bed cross sectional area. This entire analysis considers no breakthrough during the feed step; hence, by using Eq (24), u_F can be related to the interstitial velocity at the bed exit, i.e., $u_{F(out)}$. Thus, the total moles that exit the column undergoing feed are given by:

$$N_{F(out)} = \int_0^{\Delta t} u_{F(out)} \varepsilon A_{cs} \frac{P_H}{RT} dt = \pi\ \phi\Delta\tau\left(1+(\beta-1)y_f\right) \tag{27}$$

Heavy Reflux Step Analysis: In a similar way, the total moles that enter the column undergoing HR are expressed as:

$$N_{HR(in)} = \int_0^{\Delta t} u_R \varepsilon A_{cs} \frac{P_H}{RT} dt = \frac{u_R \pi\phi\Delta\tau}{u_F} \tag{28}$$

u_R is the interstitial velocity at the entrance of the HR bed. Note that since the gas to the HR column is assumed to be at the feed pressure, a compressor is needed to pressurize the gas from P_L to P_H and in this way u_R remains constant over the entire step time. The integral used to calculate the total moles that exit the column undergoing HR needs to be split in two parts. This is because it takes time t_1 for the shock front corresponding to $y = y_F$ to reach the end of the

bed during which pure light product comes out of the column. Hence, from t_1 to Δt (step time), the mole fraction of the gas that exits the column undergoing HR is $y = y_f$, and

$$N_{HR(out)} = \int_0^{t_1} u_1 \varepsilon A_{cs} \frac{P_H}{RT} dt + \int_{t_1}^{\Delta t} u_2 \varepsilon A_{cs} \frac{P_H}{RT} dt = \phi \Delta\tau \pi t_1^* \frac{u_R}{u_F} \beta + \phi\pi(1 - t_1^*) \frac{u_R}{u_F} \frac{\Delta\tau\beta}{1 + (\beta - 1) y_F} \tag{29}$$

t_1 is the time taken by the smaller shock wave front to reach the end of the bed. t_1^* is the dimensionless time ($t_1^* = \frac{t_1}{\Delta t}$) where Δt is the step time. Eq (29) can also be written more conveniently as $N_{HR(out)} = N_{HR(1)} + N_{HR(2)}$, where $N_{HR(1)}$ and $N_{HR(2)}$ are the first and the second terms in Eq (29), respectively.

Pressure Changing Step Analyses: The pressure changing steps are countercurrent depressurization and light product pressurization. The moles that enter the column undergoing countercurrent depressurization step are given by:

$$N_{CnD} = \int_0^{\Delta t} u_{CnD} \varepsilon A_{cs} \frac{P}{RT} dt = \phi(\pi - 1) \tag{30}$$

Similarly, the moles that enter the column undergoing pressurization are:

$$N_{\Pr ess} = \int_0^{\Delta t} u_{press} \varepsilon A_{cs} \frac{P}{RT} dt = \phi\beta(\pi - 1) \tag{31}$$

u_{CnD} and u_{press} are calculated from Eq (23), and the limits of the integral now change from P_H to P_L, as the time derivative term cancels.

Light Reflux Step Analysis: Since pure light gas is fed to the column undergoing LR, the total moles that enter it during the LR step are expressed as:

$$N_{Purge(in)} = \int_0^{\Delta t} u_{purge(in)} \varepsilon A_{cs} \frac{P_L}{RT} dt = \gamma\phi\Delta\tau \tag{32}$$

In the above integral, γ is the light product purge to feed ratio ($\gamma = \frac{u_{purge(in)}}{u_{F(in)}}$). Similarly, the total moles of A that exit the column undergoing LR are:

$$N_{purge(out)} = \int_0^{\Delta t} u_{purge(out)} \varepsilon A_{cs} \frac{P_L}{RT} dt = \frac{\phi\Delta\tau\gamma}{1 + (\beta - 1)\overline{y_P}} \tag{33}$$

As before, $u_{purge(out)}$ is evaluated from Eq (24) and $\overline{y_P}$ is the average mole fraction of the gas leaving the column undergoing LR. The value of $\overline{y_P}$ depends on the position of the spreading wave at the end of this step. Since the bed is saturated with heavy product at the end of the countercurrent depressurization, the gas phase mole fraction at the outlet of the column undergoing LR (y_P) is unity until the time it takes for the wave to reach the end of the bed. Once this wave starts to breakthrough, y_P gradually decreases.

4.3.2 Shock Wave Analyses

Since the entire heavy product from the depressurization step is recycled back to the HR step, $N_{HR(in)} = N_{CnD}$, which reduces to:

$$\frac{u_R}{u_F} = \frac{\pi - 1}{\pi \Delta \tau} \tag{34}$$

When pure heavy product exits the column undergoing countercurrent depressurization and enters the column undergoing HR, a shock wave corresponding to y =1 forms at the feed end of the bed. The velocity of this shock can be calculated from Eq (25). In this model, the process parameters are maintained so that at the end of the HR step, the smaller shock wave corresponding to $y = y_F$ completely exits the bed and the bigger shock corresponding to $y = 1$ covers the entire bed without breaking through it. In other words, $y = 1$ travels distance L in time Δt.

So, using Eq (25), the interstitial velocity at the entrance to the column undergoing HR is:

$$u_R = \frac{L(1 + (\beta - 1) y_F)}{\beta_A \Delta t} \tag{35}$$

Substituting Eq (35) into Eq (34), an expression for the pressure ratio is obtained as:

$$\pi = \frac{1}{y_F (1 - \beta)} \tag{36}$$

By performing an overall component balance on component A, i.e.,

$$N_{F(in)} y_F = N_{HR(2)} y_F + N_{purge(out)} \tag{37}$$

and by substituting Eqs (26), (29) and (33) into Eq (37), and also by using Eqs (34) and (36), the following expression is obtained:

$$\Delta \tau = \beta \ (1 - t_1^*) + \frac{\gamma \Delta \tau \overline{y_P} (1 - \beta)}{1 + (\beta - 1) \overline{y_P}} \tag{38}$$

Now, the following relations relate internal flows within the beds with the external overall mass balance. The moles of A in the solid and gas phases at the end of countercurrent depressurization is $\varepsilon A_{cs} L \frac{P_L}{RT} + (1-\varepsilon) A_{cs} L k_A \frac{P_L}{RT}$. Further simplification of this expression reduces it to ϕ. The moles of A at the end of the feed step are given by:

$$\phi - N_{purge(out)} + N_{feed(in)} y_F$$

The moles of A in the bed at the end of feed can also be calculated from:

$$\varepsilon A_{cs} x \frac{P_H y_F}{RT} + (1-\varepsilon) A_{cs} x k_A \frac{P_H y_F}{RT} = (1-\alpha)\phi \pi y_F \tag{40}$$

where x is the position of the shock wave corresponding to $y = y_F$ in the bed at the end of the feed step and $\alpha = 1 - \frac{x}{L}$. Equating Eqs (39) and (40) and also using the relation for the pressure ratio from Eq (36), the fraction of the bed not occupied by the feed concentration wave is:

$$\alpha = \beta + \frac{\gamma \Delta\tau \overline{y_P}(1-\beta)}{1+(\beta-1)\overline{y_P}} - \Delta\tau \tag{41}$$

As discussed before, t_1^* is the dimensionless time it takes for the smaller shock wave corresponding to $y = y_F$ to breakthrough during the HR step. This wave travels a distance αL in time t_1 to reach the end of the bed. Its velocity is calculated by simultaneously solving Eqs (24) and (25), which leads to,

$$t_1^* = \frac{\alpha}{\beta} \tag{42}$$

Substituting Eq (41) into Eq (42) gives t_1^* as:

$$t_1^* = 1 + \frac{\Delta\tau}{\beta}\left(\frac{\gamma \overline{y_P}(1-\beta)}{(1+(\beta-1)\overline{y_P})} - 1\right) \tag{43}$$

The overall mass balance on the system also results in Eq (43) (Not shown). This shows that the internal flows align perfectly with the external mole balance.

4.3.3 Simple Wave Analyses

Knaebel and Hill (1985) showed that the velocity of concentration y moving through the bed is

$$u_y = \frac{dz}{dt} = \frac{\beta_A u}{1+(\beta-1)y} \tag{44}$$

where u is the interstitial velocity at a particular position in the bed. Using Eq (9), u can be expressed as a function of y during the purge step as:

$$u = \frac{\gamma u_F}{1+(\beta-1)y} \tag{45}$$

Substituting Eq (45) into Eq (44) leads to,

$$u_y = \frac{\beta_A \gamma u_F}{(1+(\beta-1)y)^2} \tag{46}$$

i.e., the velocity of a particular concentration y as it travels through the bed.

Let concentration y = 1 travel a distance ψL during time Δt, where $\psi \geq 1$ and is the fraction of the bed covered by this concentration front. Hence, $\psi \geq 1$ means that the dispersed wave is either just at the end of the bed or has broken through it. By incorporating the above into Eq (46), the velocity of the y = 1 concentration front is obtained which, in turn, provides an expression for the purge to feed ratio, i.e.,

$$u_{y=1} = \frac{\psi L}{\Delta t} = \frac{\beta_A \gamma u_F}{\beta^2} \Rightarrow \gamma = \frac{\psi \beta^2}{\Delta \tau} \tag{47}$$

In addition, let t_2 be the time it takes for the dispersed wave to reach the end of the bed and $t_2^* = \frac{t_2}{\Delta t}$ be the corresponding dimensionless time. In symbolic form, for $\psi \geq 1$, $t_2^* \leq 1$. So, $u_{y=1} = \frac{L}{t_2}$ and substituting this in Eq (47) gives:

$$t_2^* = \frac{1}{\psi} \tag{48}$$

Eq (46) can also be used to calculate the conditions required to achieve complete cleanup. In that case, the concentration front for y = 0 travels the entire length of the bed in time Δt. So,

$$u_{y=0} = \beta_A \gamma u_F = \frac{L}{\Delta t} \Rightarrow \Delta \tau = \frac{1}{\gamma} \tag{49}$$

Eq (49) gives the maximum purge to feed ratio required for completely cleaning the bed. In the same way, the concentration at z = L, denoted here by $y_{P(f)}$, varies with time and can be expressed as:

$$u_{P(f)} = \frac{\beta_A \gamma u_F}{(1+(\beta-1)y_{P(f)})^2} = \frac{L}{\Delta t} \Rightarrow y_{P(f)} = \frac{1-\sqrt{\gamma \Delta \tau}}{1-\beta} \tag{50}$$

To calculate the moles of species A that leaves the bed undergoing LR during time Δt,

$$N_{purge(A)} = \int_0^{t_2} \frac{\gamma u_F}{\beta} \varepsilon A_{cs} \frac{P_L}{RT} dt + \int_{t_2}^{\Delta t} \frac{\gamma u_F y}{1+(\beta-1)y} \varepsilon A_{cs} \frac{P_L}{RT} dt \tag{51}$$

The second integral in Eq (51) requires y as a function of t. So, using Eq (46), where u_y is replaced by $\frac{L}{t}$ and solving gives:

$$N_{purge(A)} = \frac{\phi \Delta \pi_2^* \gamma}{\beta} + (\beta-1)\phi[(\frac{1-\sqrt{\gamma \Delta \tau}}{1-\beta})^2 - 1] \tag{52}$$

$\overline{y_P}$ is evaluated by dividing Eq (52) by Eq (33). The average mole fraction of A leaving the column undergoing LR is:

$$\overline{y_P} = \frac{1-2\sqrt{\psi}+\psi\beta}{(1-2\sqrt{\psi})(1-\beta)} \tag{53}$$

4.3.4 Recoveries and Purities

The recovery of species A in the heavy product is defined as:

$$\Omega_A = \frac{N_{purge(A)}}{N_{F(in)} y_F} \tag{54}$$

Substituting Eqs (51) and (26) into Eq (54) gives:

$$\Omega_A = \frac{\beta(2\sqrt{\psi}-1-\beta\psi)}{\Delta \tau} \tag{55}$$

The purity of species A (Ξ_A) in the heavy product is evaluated from Eq (53). The recovery of species B in the heavy product is defined as:

$$\Omega_B = \frac{N_{F(out)} - N_{\text{Pr}ess} - N_{Purge(in)} + N_{HR(1)} + N_{HR(2)}(1-y_F)}{(1-y_F)N_{F(in)}} \tag{56}$$

Substituting Eqs (26), (27), (29), (31) and (32) into Eq (56), and by also using Eqs (34) and (36), gives Ω_B as:

$$\Omega_B = \frac{(\Theta - \pi y_F \beta) + t_1^* \beta(\pi y_F - 1)}{(1 - y_F)\pi\Delta\tau} \tag{57}$$

where $\Theta = \Delta\tau(\pi - \gamma - 1) + \beta$ and t_1^* can be evaluated from Eq (43).
The purity of species B in the light product is defined as:

$$\Xi_B = \frac{N_{F(out)} - N_{Press} - N_{Purge(in)} + N_{HR(1)} + N_{HR(2)}(1 - y_F)}{N_{F(out)} - N_{Press} - N_{Purge(in)} + N_{HR(out)}} \tag{58}$$

Using Eqs (27), (29), (31), (32), (34) and (36) in Eq (58) reduces it to:

$$\Xi_B = \frac{(\Theta - \pi y_F \beta) + t_1^* \beta(\pi y_F - 1)}{\Theta - t_1^* \beta} \tag{59}$$

It is important to note that the terms used in the expressions to calculate the purities and recoveries of both components may not be independent of each other. This is done to make the final forms of the expressions as simple as possible.

4.4 Analysis and Parametric Study

As can be seen from the expressions derived in the previous section, Ξ_A and Ω_A are dependent on $\beta, \Delta\tau$ and γ whereas Ξ_B and Ω_B are functions of $\beta, \Delta\tau, \gamma$ and y_F. In order understand how this cycle can be applied to a specific system, the H_2-CH_4 separation at 25°C on PCB activated carbon (Ritter and Yang, 1987) has been studied. The isotherms are shown in Figure 42. Process parameters used in this study are mentioned in Table 8. Notice that all the results shown in this section depict the 'range of solutions' obtained for the equations describing the system. In other words, in order to satisfy the boundary conditions at the end of feed and HR step, the cycle must operate only within specific values of $\gamma, \Delta\tau$ and y_F. Also, $\Delta\tau$ is a dimensionless parameter and is a function of feed throughput, step time, column length and heavy component selectivity. Hence $\Delta\tau$ could be used to study the effect of any one of these parameters, keeping the rest constant. However, this analysis considers $\Delta\tau$ to be a measure of feed throughput as maximizing this parameter is one of the major goals while designing any PSA system.

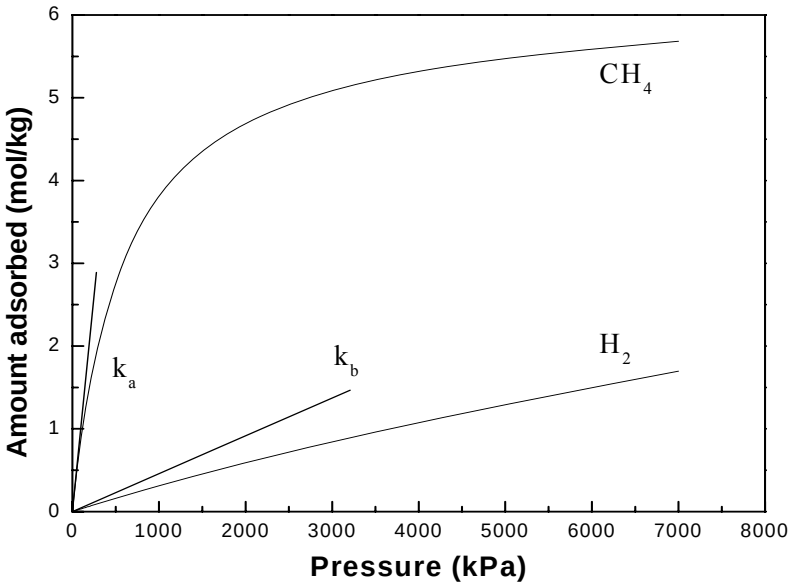

Figure 42. Adsorption isotherms for H_2 and CH_4 on PCB activated carbon at 25^0C (Ritter and Yang 1987)

Table 8. Process parameters, adsorbent and bed properties for Equilibrium theory analysis.

T	296	K
ε	0.4	
ρ_s	500	kg m^3
k_A	1.048e-08	kmol kg^{-1} Pa^{-1}
k_B	4.577e-10	kmol kg^{-1} Pa^{-1}
β_A	0.0492	
β_B	0.5420	
β	0.0907	

The effect of incomplete purge on the process performance is studied using the relations obtained in the previous section. In most industrial applications, the LR bed is not completely cleaned as this not only prevents further dilution of the heavy product but also helps maintain high recovery of the light component. Figures 43-45 depicts the variations in Ξ_A, Ξ_B, Ω_A and Ω_B for three different values of ψ. When $\psi = 1$, the dispersed wave is exactly at the end of the bed and hasn't broken through. Furthermore, Eq 49 shows that for complete cleanup, $\psi = \frac{1}{\beta^2}$ and hence for this specific system $\psi = 122.55$ would imply complete cleanup of the LR column. A third value of ψ in between the two extreme cases has been chosen for comparison. Figure 43a shows Ω_A decreasing with $\Delta\tau$ for these three different values of ψ. Here the constant ψ lines represent the range in which the cycle must operate in order to reach the same boundary conditions set at the end of each step. In order to understand the trends, consider a system where a constant feed mole fraction enters the system. According to Eq 32, the amount of light gas required as purge is given by $\gamma\phi\Delta\tau$. This is also equal to $\psi\beta^2\phi$ on using Eq 47. Thus for this system, the amount of pure light gas used to clean the bed is independent of throughput and along a constant ψ line in Figure 43a, $N_{purge(in)}$ remains constant. In addition, for this case the pressure ratio also remains same according to Eq 36. For any PSA cycle utilizing a purge step, the heavy component is desorbed from the bed in one or both of the following two ways. Either the operation has to be carried at a higher pressure ratio and/or more light gas is to be used to purge the LR column. Since both these factors remain constant along a constant ψ line, there is more breakthrough of A out of the HR column with increase in $\Delta\tau$, resulting in decrease of Ω_A. Moreover, the upper limit of Ω_A along each ψ line represents the case when both the shock waves ($y = y_F$ and $y = 1$) travelling in the HR step, reach the end of the bed simultaneously in Δt time. Thus, there is no loss of A from the light end of the system resulting in 100% recovery of the heavy component. Furthermore, higher throughput results in the concentration wave occupying a larger percentage of the feed bed and might causing it to breakthrough the light end of the column as can been seen from Eq 41 ($\alpha > 1$). Under such circumstances, one of the boundary conditions specified while solving the model will be violated. The lowermost point along the constant ψ line represents this case. Based on similar reasoning's, higher values of $\Delta\tau$ can be operated only at higher ψ because more light gas is needed to purge the bed in order to compensate the increase in adsorbent loadings due to higher throughputs.

Figure 43b depicts how Ξ_A varies with $\Delta\tau$ when the LR bed is purged to different extents. The dilution of heavy product on using more light gas is clearly evident from the three curves. The trends represent the range of $\Delta\tau$ within which the cycle must operate for a given ψ. Notice that the purities don't vary along a constant ψ line. This is because for two different $\Delta\tau$'s, same boundary conditions are obtained at the end of the HR step i.e. the entire bed is saturated with the heavy component. As a consequence, the purity of the heavy component will only depend on the extent to which the LR bed is purged or in other words the value of ψ determines Ξ_A and not $\Delta\tau$.

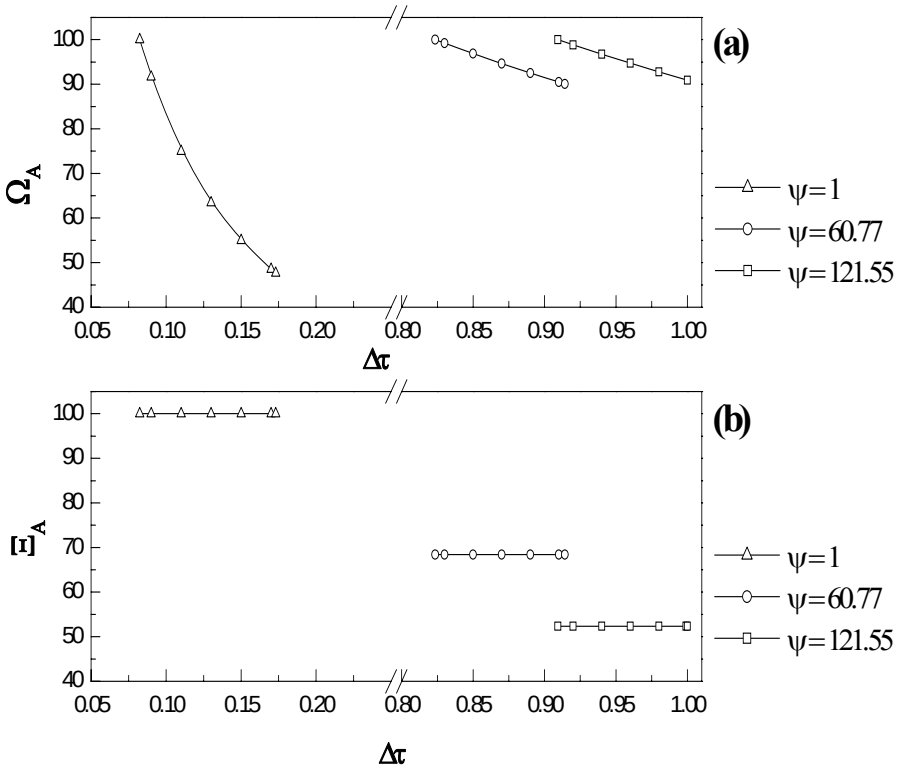

Figure 43. Performance curves showing the variation of recovery (Ω) and purity (Ξ) of the heavy component with $\Delta\tau$ at constant ψ

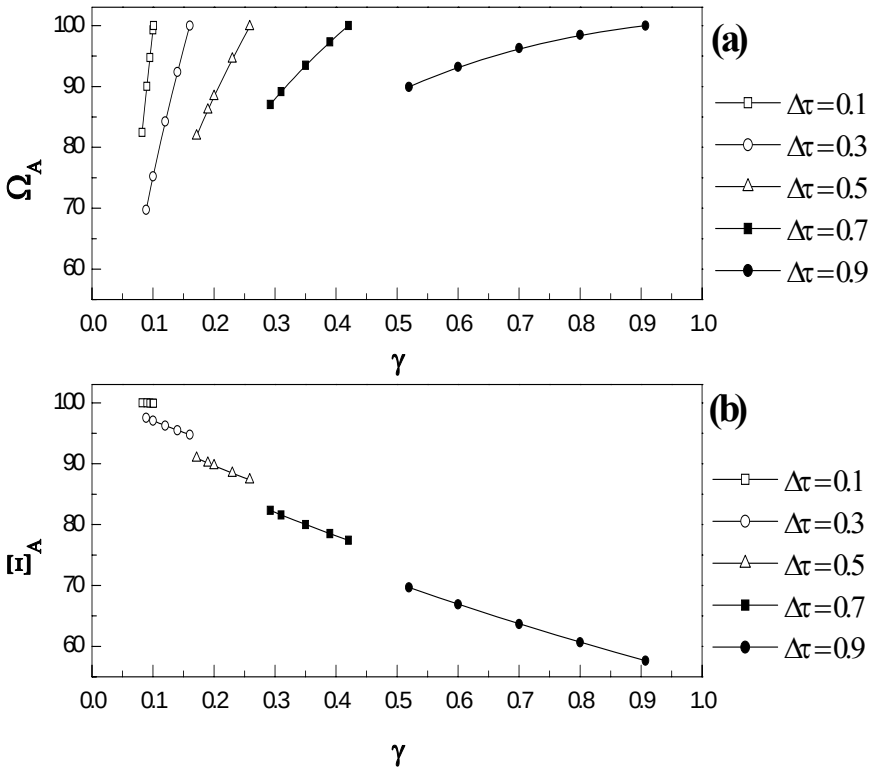

Figure 44. Effect of purge to feed ratio (γ) on the recovery (Ω) and purity (Ξ) of the heavy component at constant $\Delta\tau$.

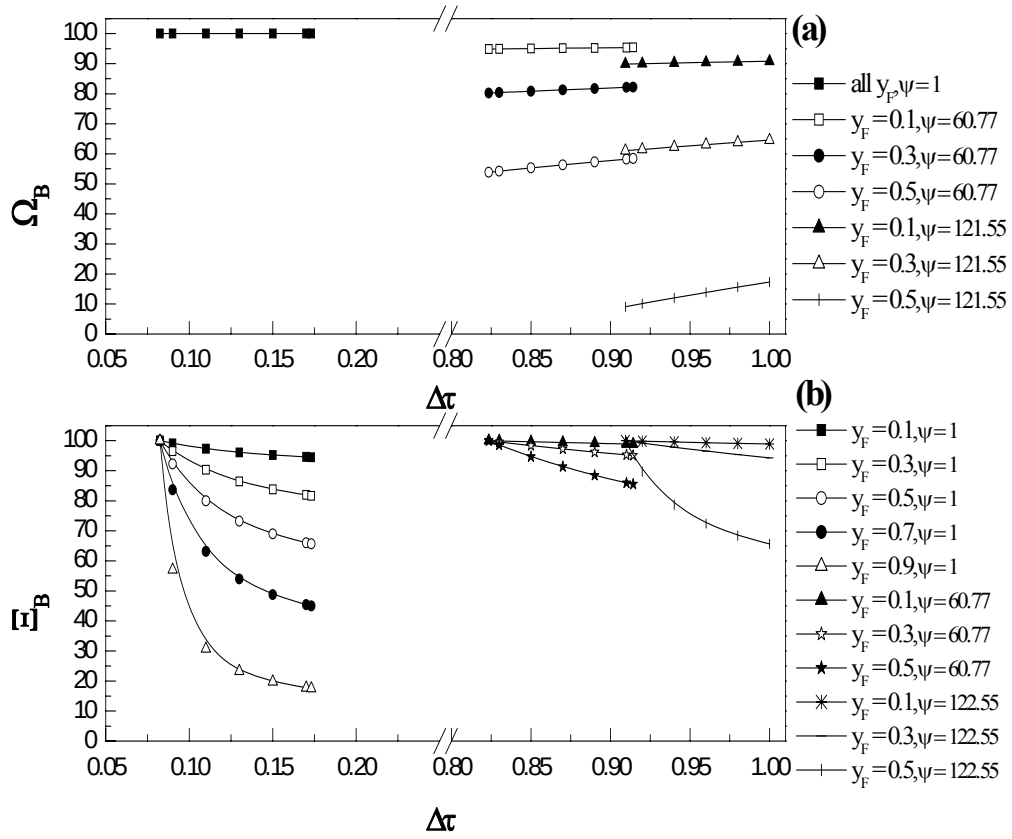

Figure 45. Effect of incomplete purge and $\Delta\tau$ on the recovery (Ω) and purity (Ξ) of the light component for different feed mole fractions.

It may seem surprising that the purities and the recoveries of the heavy component do not depend on y_F. From Eq 26 and Eq 36, the moles of A entering the system is $\frac{\phi\Delta\tau}{1-\beta}$, which is independent of y_F. As it can be seen, the increase in y_F is compensated by a decrease in π. Also, the amount of A that breaks through the HR step can be calculated from Eq 29 as $\phi\pi(1-t_1^*)\frac{u_R}{u_F}\frac{\Delta\tau\beta}{1+(\beta-1)y_F}y_F$. Using Eq 34, this reduces to $\frac{\phi(1-t_1^*)\beta}{1-\beta}$ which again is independent of y_F. So the same number of moles of species A that exit the HR column remain the same even with increasing y_F. This happens due to the fact that the pressure ratio decreases with increase in y_F and less and less heavy component exits the CnD bed. Since the only other column from where species A exits the system is from the LR bed, Ω_A is independent of y_F.

Another way to interpret the trends of Ξ_A, Ω_A is along constant $\Delta\tau$ lines at different purge to feed ratios as shown in Figure 44. Ω_A increases with increasing γ along a constant $\Delta\tau$ line as depicted in Figure 44a. This obvious result is because of the fact that purging the LR bed to a greater extent would result in less breakthrough during the HR step causing the recovery of the heavy component to increase. Since, γ and ψ are proportional to each other, the upper and

the lower limit of Ω_A along a constant $\Delta\tau$ line can be physically interpreted in a similar way as the effect of ψ was discussed above. The upper limit of all curves gives 100% recovery of A which means that at such values of γ, both the shock waves in the HR column reach the end of the bed simultaneously in time Δt. However, operating the cycle below this range of γ results in species A breaking through the light end of the feed column. Interestingly, Ω_A increases sharply with small changes in γ for lower values of $\Delta\tau$. This promising result shows that under such conditions, recovery of the heavy component can be improved dramatically only by using very small quantities of the light gas. Since, more γ signifies a higher ψ; this causes the purity of A to plummet with increasing purge to feed ratio as depicted by Figure 44b. For a constant value of $\Delta\tau$, increasing the value of γ beyond a certain point would result in cleaning the bed to an extent that the specified pressure ratio would not be enough to completely push the feed concentration shock wave out of the bed. On the other hand, if γ is too less the y_F shock front would breakthrough the feed column.

Figure 45 shows the changes in Ξ_B and Ω_B with increasing $\Delta\tau$. For any given y_F, Ω_B decreases with an increase in $\Delta\tau$ along a constant ψ line. As discussed before, with increasing throughput, the concentration wave occupies a larger portion of the feed bed. This implies that t_1^* i.e. the time it takes for the smaller shock wave to breakthrough during the HR step, will be smaller causing impure light product to exit the bed for a larger fraction of the total step time resulting in a decrease in Ξ_B. Based on similar grounds, a higher mole fraction shock wave exiting the HR bed would decrease the light product purity more severely. Note that in Figure 45, the curves for higher values of ψ do not cover the entire range of y_F. This can be understood by the following specific example. For a complete cleanup case ($\psi = 122.55$), the constraints for $\Delta\tau$ are given by Eq 55. For the maximum permissible $\Delta\tau$ of 1, the inequality $(1 - y_F) \geq y_F(\beta - 1)^2$ must be followed and thus $y_F \leq 0.5473$. Physically this implies that at constant throughput, the amount of light gas available for purge and pressurization becomes less and less with increasing y_F. As a result, beyond a certain feed mole fraction, there is not enough light gas to completely clean the bed. Thus, although the results for Ξ_A and Ω_A themselves do not depend on y_F but for higher feed mole fractions and under certain conditions (like the one discussed above), Ξ_B and Ω_B may not lie between 0 and 100%. Under such circumstances, the solutions of Ξ_A and Ω_A will occupy a part of the curves shown in this article.

The results show that this cycle configuration can be used to obtain high purities and high recoveries of the heavy and the light component only at low values of $\Delta\tau$. $\Delta\tau$ is directly proportional to feed throughput and step time but inversely proportional to the length of the column. Hence, in order to operate the cycle at low values of $\Delta\tau$ and still have a high feed throughput, a longer column and/or smaller step time is required. But, small step times are undesired as in such a scenario, mass transfer effects play a role and the local equilibrium assumption doesn't hold true. Thus, for this specific cycle, the idea of ultimate separation can only be realized at low feed throughputs. Observe that at higher values of $\Delta\tau$ and $y_F = 0.10$, a respectable 70% purity of heavy component can be achieved with 100% recovery along with 95% recovery, 100% purity of the light species. A moderate pressure ratio of 11 is necessary for

such a separation. Also, all the results show the use of γ less than one which is highly desired for making the process commercially viable.

4.5 Limiting Cases

The relations derived above can not only be used to determine the process performance for a given set of conditions, they can also be used to explore limiting cases. Four interesting cases are discussed below.

Case I: An extreme case is when the spreading wave that forms during the LR step reaches the end of the bed, but does not breakthrough it. This makes $\psi = 1$ and $\overline{y_P}$ =1. Under such conditions, Eq (47) reduces to:

$$\gamma = \frac{\beta^2}{\Delta\tau} \tag{60}$$

The pressure ratio remains the same as before and is given by Eq (36). Also, from Eq (55),

$$\Omega_A^* = \frac{\beta(1-\beta)}{\Delta\tau} \tag{61}$$

The purity of A is 100%, as $\overline{y_P}$ is 1. By using the relation for γ from Eq (60), Eq (43) becomes:

$$t_1^* = 2 - \beta - \frac{\Delta\tau}{\beta} \tag{62}$$

The recovery of B is 100%, as the heavy product leaving the bed undergoing LR is pure A. This can also be confirmed by substituting the above value of t_1^* in Eq (57). In a similar fashion, the purity of B is expressed as:

$$\Xi_B^* = \frac{\Delta\tau\pi(1-y) - \beta + \beta\pi y_F(1-\beta)}{\Delta\tau\pi - \beta} \tag{63}$$

Considering the fact that the values of t_1^*, Ξ_B^* and Ω_A^* all lie between 0 and 1, the range over which γ and $\Delta\tau$ must lie to maintain the boundary conditions in each column are given by:

$$\frac{\beta}{2-\beta} \le \gamma \le \frac{\beta}{1-\beta} \tag{64}$$

$$\beta(1-\beta) \le \Delta\tau \le (2-\beta)\beta \tag{65}$$

Case II: Another extreme case is when the dispersed wave that forms during the LR step is completely pushed out of the bed. The purge to feed ratio required to do so is given by Eq

(49). Also, the value of ψ is at its other extreme of $\frac{1}{\beta^2}$. Under such conditions complete cleanup of the column undergoing LR is achieved. Replacing these conditions in Eqs (53), (55), (57) and (59) allows the relations for the purities and recoveries of both components to be obtained as:

$$\Xi_A^1 = \frac{1}{2-\beta} \tag{66}$$

$$\Omega_A^1 = \frac{1-\beta}{\Delta\tau}$$

$$\Xi_B^1 = \frac{\Delta\tau(1-y_F) - y_F(\beta-1)^2}{\Delta\tau - y_F(\beta-1)(\beta-2)} \tag{68}$$

$$\Omega_B^1 = \frac{\Delta\tau(1-y_F) - y_F(\beta-1)^2}{\Delta\tau(1-y_F)} \tag{69}$$

Since all of the above terms lie between 0 and 1, two of the following three constraints must be satisfied:

$$\Delta\tau \geq \frac{y_F(\beta-1)^2}{1-y_F}, \Delta\tau \geq (1-\beta),\ (1-\beta) \leq \Delta\tau \leq 1 \tag{70}$$

Case III: Another unique situation is when the feed step is terminated just at the time when the feed concentration wave reaches the end of the bed but does not breakthrough it. This makes t_1^* = 0. In other words, the outlet concentration of the bed undergoing HR is always $y = y_F$. Again, for $\psi = 1$, Eq (62) gives:

$$\Delta\tau = \beta(2-\beta) \tag{71}$$

As a consequence, combining Eqs (60), (61) and (63) gives,

$$\gamma = \frac{\beta}{2-\beta} \tag{72}$$

$$\Omega_A^{II} = \frac{1-\beta}{2-\beta} \tag{73}$$

$$\Xi_B^{II} = 1 - \frac{y_F}{2-y_F-\beta(1-y_F)} \tag{74}$$

Note that the purity of A and recovery of B are both 100% for this case.

Case IV: The last extreme case is the perfect separation case, i.e., i.e., the case when 100% purity and 100% recovery of both species A and B is achieved. As mentioned earlier, breakthrough of species A during the feed step has not been considered in the entire analysis. So, a decrease in the recovery of species A can be caused only by its loss from column undergoing HR. However, when this impure light product from the HR step is utilized as purge gas for the column undergoing LR, all the heavy species in it is recovered.

As before, pure light gas exits the bed undergoing HR for time t_1, but then for the next time $\Delta t - t_1$, the concentration of the outlet gas is y_F. However, to keep the light end of the bed as free as possible of heavy species A, it is advantageous to switch the order of these purge gases and take the impure gas from the HR step and use it first to purge the LR column for time $\Delta t - t_1$ and then to use the pure light gas as purge for the LR column next for time t_1. A tank may be utilized for this purpose.

Interestingly, even though this approach changes the concentration at the inlet of the column undergoing LR, the value of the integral in Eq (32) remains the same. This is because a constant purge to feed ratio is maintained throughout, which is independent of the gas composition. However, there is a change in the total moles that exit the column undergoing LR. The expression in this case becomes:

$$N_{P(out)} = \int_0^{\Delta t - t_1} \frac{\gamma u_F (1 + (\beta - 1)\overline{y_{in}})}{\beta} \varepsilon A_{cs} \frac{P_L}{RT} dt + \int_{\Delta t - t_1}^{\Delta t} \frac{\gamma u_F}{\beta} \varepsilon A_{cs} \frac{P_L}{RT} dt \tag{75}$$

In Eq (75), $\overline{y_{in}}$ is the average composition of the gas entering the column undergoing LR during the first time $\Delta t - t_1$. Note that $\overline{y_{in}}$ is less than y_F because some of the pure light gas that exits the column undergoing feed is mixed with the impure light gas that exits the column undergoing HR to maintain a constant molar flow rate and γ at the entrance of the column undergoing LR. The interstitial velocities used in both the integrals in Eq (75) are calculated using Eq (24). Solving Eq (75) gives:

$$N_{P(out)} = \frac{\phi \Delta \tau \gamma}{\beta} (1 + (1 - t_1^*)(1 + (\beta - 1)\overline{y_{in}})) \tag{76}$$

Since there is no loss of species A from the feed or HR step, the moles of species A that enters the system in the feed should be equal to the moles of species A that leaves the system in the LR step for $\psi = 1$. Algebraic manipulation of Eq (76) thus leads to:

$$\gamma = \frac{\beta}{(1 - \beta)(1 + \overline{y_{in}}(\beta - 1)(1 - t_1^*))} \tag{77}$$

Also, a change in the concentration of the inlet gas during the LR step changes the

velocity of the dispersed wave that forms. Let u_1 and u_2 be the velocities of concentration $y = 1$ during this step. Now, if the wave travels a distance $\bar{x}$ during the first time $\Delta t - t_1$, upon solving Eqs (24) and (44) together gives:

$$u_1 = \frac{\bar{x}}{\Delta t - t_1} = \frac{\beta_A \gamma u_F (1 + (\beta - 1)\overline{y_{in}})}{\beta^2} \tag{78}$$

$$u_2 = \frac{\beta_A \gamma u_F}{\beta^2} = \frac{L - \bar{x}}{t_1} \tag{79}$$

Solving Eqs (77), (78) and (79) simultaneously gives,

$$\Delta\tau = \beta(1 - \beta) \tag{80}$$

Hence, for this particular cycle configuration, the throughput is only a function of the selectivity for a fixed cycle time and fixed column length.

Following the same procedure as discussed previously to derive the relations from the overall mass balance and the cyclic mass balance on the bed, the following range of γ is obtained,

$$\frac{\beta}{(1 - \beta)} \le \gamma \le \frac{1 + \beta}{1 - \beta} \tag{81}$$

In the above inequality, operating at the lowest value of γ results in both shock fronts, corresponding to $y = y_F$ and $y = 1$, reaching the end of the bed simultaneously in time Δt. In other words, there is no breakthrough of species A during this HR step. The relation for the pressure ratio remains the same as Eq (36). So, Eqs (36), (80) and (81) describe the range of operating conditions that result in the perfect separation of both components, i.e., 100% purity and 100% recovery of both species A and B.

However, the idealized model is very restricted and applicable to real systems only under certain conditions. Nonetheless, it provides an upper limit to the separation that can be achieved by employing such a heavy reflux cycle. Since, heat and mass transfer effects only ruin the process performance further; such an analysis not only provides a quick way to obtain the best possible separations but also fundamentally study the effect of different parameters on the process performance.

4.6 Conclusions

A PSA model based on equilibrium theory has been presented for a five-bed, five-step heavy reflux PSA cycle. It is based on isothermal, linear isotherm equilibrium theory analysis and is specifically targeted to obtain relatively pure heavy component at high recoveries from a

binary feed mixture. The analytical expressions are in terms of purities and recoveries of both species.

To demonstrate the commercial viability of such a heavy reflux PSA cycle, the expressions were applied to PCB activated carbon- H_2-CH_4 system at 25°C. In particular, the effect of incomplete purge on the process performance was studied. The results depict that 100% purity and recovery of both the species is attainable at low throughputs, even for very dilute feed streams. Operating the system at higher throughputs lowered the heavy component purity but still very high purities and recoveries of the light component were achieved. For example, partial purging of a system processing feed of mole fraction 0.10 and operating at high throughputs gave 70% purity, 100% recovery of the heavy component and 95% recovery, 100% purity of the light species.

However, the idealized model is very restricted and applicable to real systems only under certain conditions. Nonetheless, it provides an upper limit to the separation that can be achieved by employing such a heavy reflux cycle. Since, heat and mass transfer effects only ruin the process performance further; such an analysis not only provides a quick way to obtain the best possible separations but also fundamentally study the effect of different parameters on the process performance.

5.0 K-Promoted Hydrotalcite as a High Temperature Adsorbent for CO_2 Capture: Proposed CO_2 Interaction Mechanism

5.1 Introduction, Literature Review and Objectives

Of the various adsorption processes being proposed and explored for CO_2 capture and concentration, one of the more promising approaches considers the use of a pressure swing adsorption (PSA) process at high temperature (Reynolds et. al., 2005, 2006). This PSA process is based on the use of a K-promoted hydrotalcite-like compound (HTlc) that exhibits a reversible capacity for CO_2 at elevated temperatures (Nataraj et. al, 1998; Ding and Alpay, 2000 and 2001).

The uptake and release of CO_2 by HTlcs is described in the literature, for the most part, by a single mass transfer limited, equilibrium driven process that is akin to physical adsorption, but that occurs at high temperature (Reynolds et. al., 2005 and 2006; Ding and Alpay., 2000 and 2001; Hufton et. al, 1999; Sores et. al., 2002 and 2004). However, there is compelling evidence that points toward the actual mechanism being far more complex (Ding and Alpay., 2000 and 2001; Hufton et. al, 1999; Sores et. al., 2002 and 2004; Moreira et. al., 2006; Hutson et. al, 2004). For example, the rather slow formation of an irreversible solid phase in a K-promoted HTlc has been reported during repeated adsorption and desorption cycling with CO_2 (Hufton et. al., 1999). Consistent with this irreversible behavior, the desorption branches of several adsorption isotherms for CO_2 on HTlcs all exhibited significant hysteresis (Soares et. al., 2002). Irreversible adsorption has also been reported by Hutson et al (2004) during the initial exposure of various HTlcs to CO_2. Moreover, the diffusional time constants reported in the literature for CO_2 in various HTlcs range from being very slow (Ding and Alpay, 2000 and 2001) to being so fast that experimental results can be predicted by equilibrium theory (Hufton et.al., 1999. Are these apparent paradoxical results all manifestations of different aspects of the same

phenomenon?

The objective of this work was to answer the question posed above by explaining those behaviors in terms of a mechanism that involves both fast and slow CO_2 uptake and release processes that mimic these apparent equilibrium and irreversible processes, respectively. This mechanism was deduced from a series of non-equilibrium dynamic adsorption and desorption cycling experiments that clearly illuminated the fast and slow processes associated with the behavior of a K-promoted HTlc when exposed to CO_2 at various pressures and temperatures for finite periods of time. A reaction pathway was devised that describes the reversible adsorption and desorption behavior of CO_2 on a K-promoted HTlc with three simple reactions.

5.2 Adsorbent Preparation and Isotherm Measurement

An HTlc with molecular formula $[Mg_3Al(OH)_8]_2CO_3 \bullet nH_2O$ was prepared by a co-precipitation method (Nataraj et. al., 1998). While vigorously stirring, a solution of 41.7 ml of deionized water containing 0.75 mol $Mg(NO_3)_2 \bullet 6H_2O$ and 0.25 mol $Al(NO_3)_3 \bullet 9H_2O$ was added to a solution of 83.3 ml of deionized water containing 1.7 mol NaOH and 0.5 mol Na_2CO_3. The precipitate was separated from the slurry by vacuum filtration. The wet filter cake was washed with deionized water and vacuum filtered three times, dried overnight at 60 ^oC in a vacuum oven, crushed, and calcined in air at 400 ^oC for 4 hours.

A K-promoted HTlc with molecular formula $[Mg_3Al(OH)_8]_2CO_3 \bullet K_2CO_3 \bullet nH_2O$ was prepared using an incipient wetness procedure. To obtain an Al:K ratio of 1:1, a 0.33 M solution of K_2CO_3 was prepared in deionized water, and a pre-determined volume of it was added to the HTlc powder in three steps: 1) The solution was added drop wise to the powder until it appeared wet. 2) The wet powder was dried for 15 min in a vacuum oven at 60 ^oC. 3) Steps 1 and 2 were repeated until all the solution was added.

A 5000 torr MB 300 GHP VTI Integrated Microbalance system was utilized to measure the non-equilibrium dynamic adsorption and desorption isotherms of CO_2 on the K-promoted HTlc. For each isotherm, ~ 0.1 g of sample was loaded into the microbalance, evacuated to $1x10^{-5}$ torr, and activated in vacuum at 400 ^oC for 12 hours, as suggested elsewhere.[4] After activation, the temperature was changed to the isotherm temperature ($\pm$ 1 ^oC) for subsequent contact with CO_2.

A non-equilibrium dynamic adsorption and desorption isotherm at 250, 300, 350, 400, 450 or 500 ^oC was measured by taking differential pressure steps of 20 $\pm$ 5 torr between 30 and 300 torr and 50 $\pm$ 5 torr between 300 and 980 torr (29 steps up and 29 steps down), waiting 45 min at each step, and proceeding in that manner until periodic behavior was realized. This produced Langmuirian-shaped isotherms under non-equilibrium conditions. The absolute CO_2 capacity and the CO_2 working capacity on this K-promoted HTlc were extracted from these non-equilibrium isotherms.

5.3 Results and Discussion

The non-equilibrium dynamic adsorption and desorption isotherms at six temperatures for

CO_2 on a K-promoted HTlc are shown in Figure 46. Depending on the temperature, between 5 and 12 adsorption and desorption cycles were required in each case to attain periodic behavior. For the isotherms obtained at 400 ^oC and below, it was surmised that the continuously increasing absolute CO_2 capacity during the first cycle was due to slow adsorption kinetics with the CO_2 still driving toward an equilibrium state. After a relatively rapid period of adsorption that occurred within the first 90 min or so of exposure to CO_2, as indicated by the first few isothermal points, subsequent points along the non-equilibrium curve of the first adsorption cycle displayed a much more moderate slope that erroneously suggested a saturation limit was being approached and that was identified elsewhere (Sores et. al., 2002 and 2004, Yong et. al., 2001 and 2002, Moreira et. al., 2006) as a probable equilibrium state. But, this was not the case.

During the first desorption cycle that ensued after reaching 980 torr (the upper pressure limit), the weight of the sample kept increasing. For the 250 ^oC isotherm, for example, adsorption did not stop even after decreasing the CO_2 pressure back down to 65 torr, with this slow adsorption phenomenon persisting even after several additional cycles. However, as the absolute CO_2 capacity increased, desorption eventually superseded adsorption along the non-equilibrium desorption curves. This latter result became progressively more apparent in the isotherms obtained at the higher temperatures.

This behavior indicated that directly after activation and then after a rapid initial uptake of CO_2 at low pressures, the sample entered a region of slow adsorption kinetics. These kinetics were so slow that the sample kept gaining weight after each cycle, only to reach periodic behavior after several days of dynamic cycling. In fact, for the lower temperature isotherms (Figures 46a to 46c), after the first few isotherm points, the sample was still so distant from equilibrium that its absolute CO_2 capacity at that point increased 2 to 3 times as periodic behavior was reached.

The same phenomenon was presumably occurring with the isotherms obtained at 450 and 500 ^oC, except that in those two cases the absolute CO_2 capacity decreased with cycling. To understand this behavior, recall that this material was activated for 12 hr at 400 ^oC in vacuum. During this activation period (results not shown), the material decreased in mass by about 40%, rapidly at first and then more gradually as time passed, with no sign of it ever leveling off even after 12 hr. So, for the materials exposed to 450 and 500 ^oC, it was surmised that additional activation and associated weight loss occurred while the material was slowly being exposed to different pressures of CO_2. The net effect was a slightly decreasing absolute CO_2 capacity with cycling at 450 and 500 ^oC.

As periodic behavior was approached hysteresis loops also formed and remained intact during periodic cycling. The presence of a hysteresis loop in each isotherm indicated that although each isotherm was closer to equilibrium, the dynamics of both adsorption and desorption were still dominated by slow kinetics. It was believed, however, that given sufficient time the hysteresis loops would have merged into one single curve, i.e., the equilibrium isotherm.

It was also interesting that the first pressure step taken in all the experimental isotherms displayed in Figure 46, which was associated with a fast reversible phase, did not vary much with temperature. This indicated that this initial fast process was associated with a low heat of

adsorption. It was also surmised that the capacity associated with this initial phase was related to that predicted by Hufton et al (1999) using equilibrium theory.

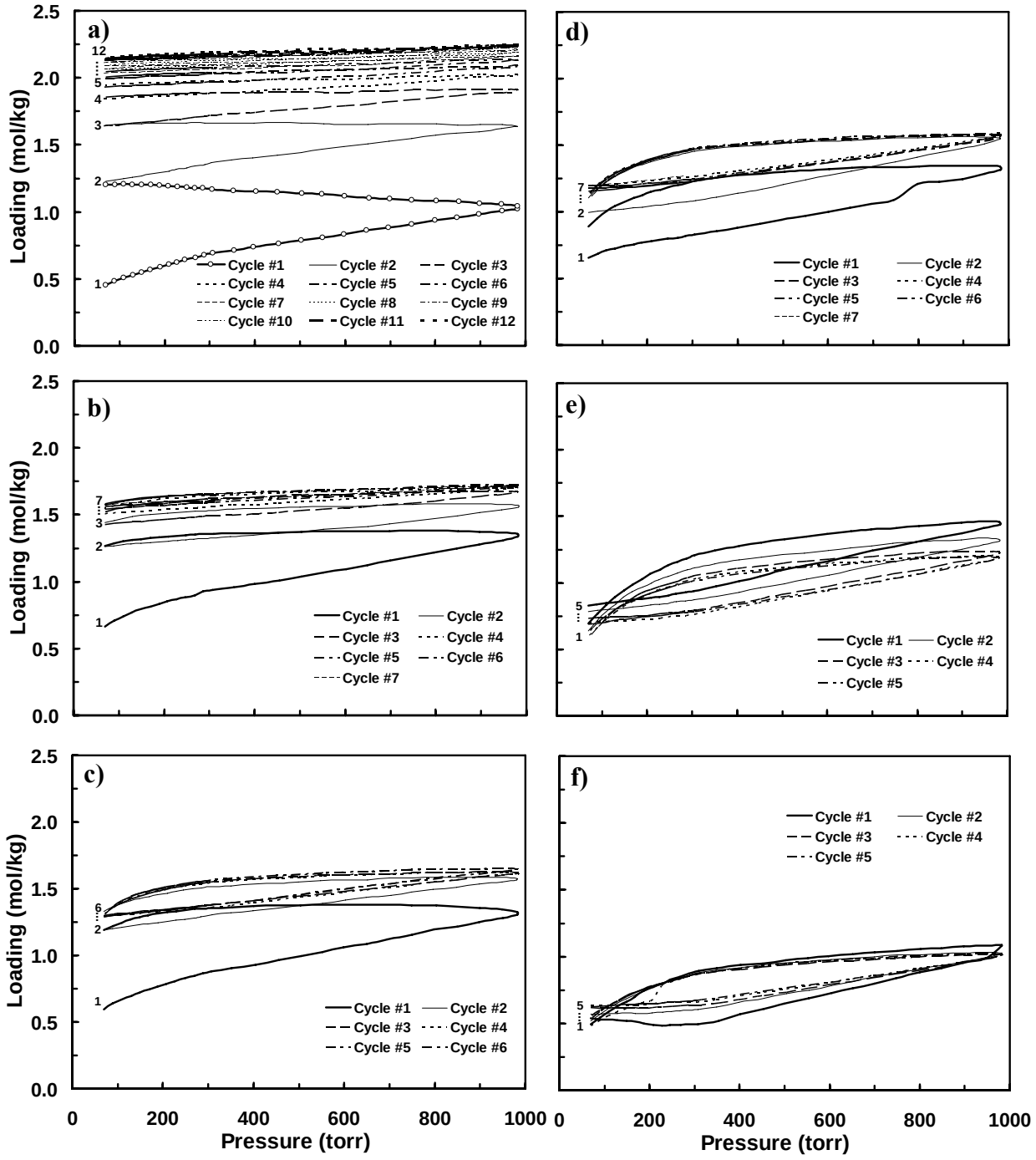

Figure 46. Non-equilibrium dynamic adsorption and desorption isotherms at a) 250 ^{o}C, b) 300 ^{o}C, c) 350 ^{o}C, d) 400 ^{o}C, e) 450 ^{o}C, and f) 500 ^{o}C for CO_2 on a K-promoted HTlc showing the attainment of periodic behavior. To facilitate a clear depiction of the cycles sample data points are shown by the open circles only for the first cycle at 250 ^{o}C, and only 27 adsorption steps and

27 desorption steps are shown for each cycle (those obtained at 30 and 50 torr are not shown).

Figure 47 shows the non-equilibrium dynamic adsorption and desorption isotherms at all six temperatures for CO_2 on K-promoted HTlc at the periodic state. The corresponding temperature dependence of the absolute CO_2 capacities on K-promoted HTlc obtained from these results at 980 torr is also shown in this figure. This capacity initially decreased with increasing temperature, reached a plateau at around 300 to 400 ^oC, and then decreased again with further increases in the temperature. This behavior was indicative of an exothermic adsorption process because of the increasing CO_2 capacity with decreasing temperature; and the plateau was perhaps caused by a phase transition occurring within the material with a critical temperature of about 500 ^oC. This absolute CO_2 capacity ranged from 1.02 mol/kg at 500 ^oC to 2.25 mol/kg at 250 ^oC.

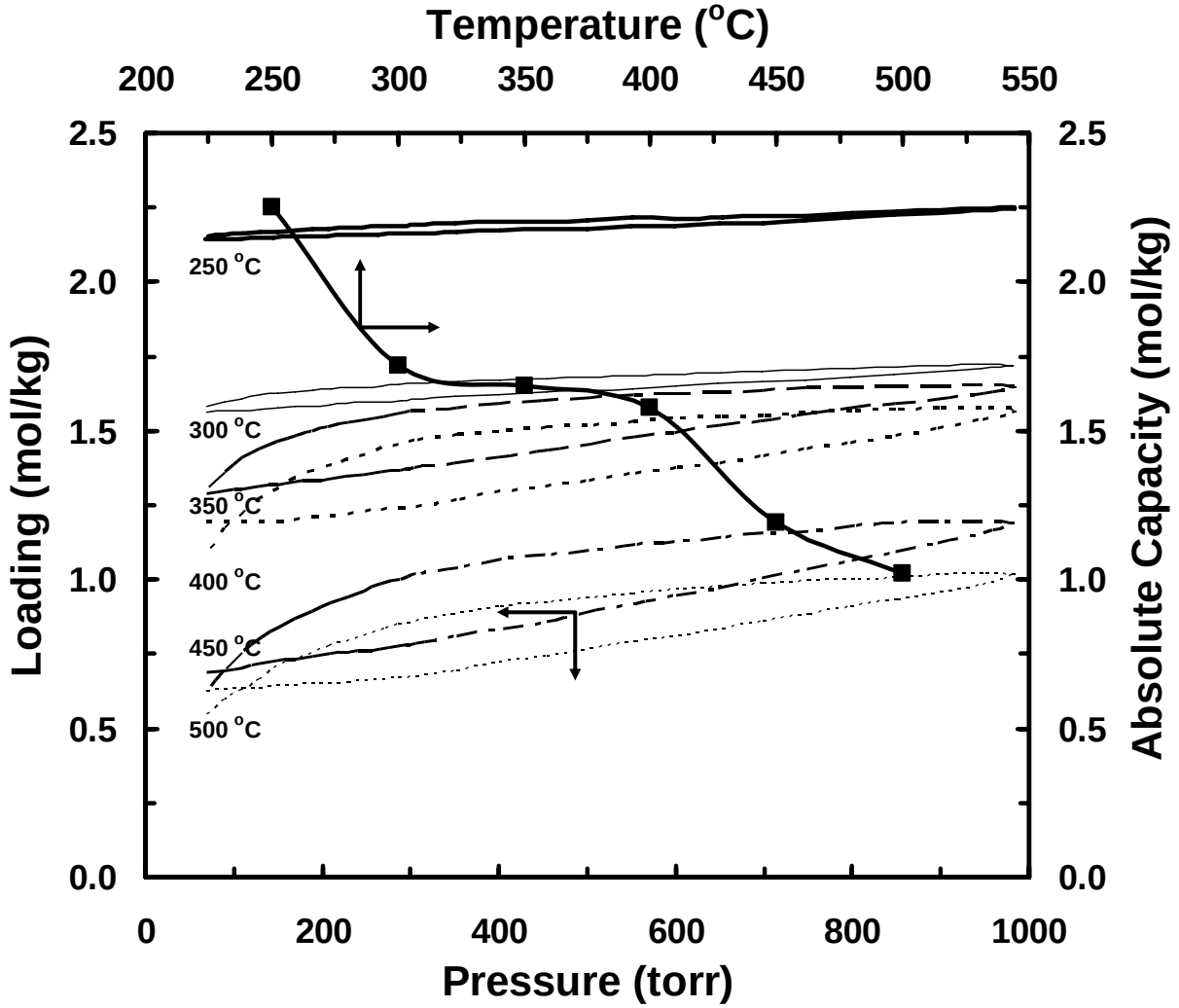

Figure 47. Dynamic non-equilibrium adsorption and desorption isotherms (thin lines) at 250, 300, 350, 400, 450 and 500 ^oC for CO_2 on a K-promoted HTlc at the periodic state; and non-equilibrium absolute capacity for CO_2 on a K-promoted HTlc (thick line) obtained from these results at 980 torr.

The results from Figure 47 are replotted in Figure 48 in terms of the CO_2 loading normalized to 0.0 mol/kg at 65 torr. In this depiction it was easier to observe not only the significant changes in the CO_2 loadings, but also the marked changes in the sizes of the hysteresis loops that occurred between 65 and 980 torr with temperature. The temperature dependence of the CO_2 working capacity is also shown in Figure 48, where the CO_2 working capacity of each isotherm was defined as the CO_2 loading change between 65 and 980 torr. The CO_2 working capacity exhibited a strong temperature dependence and a maximum of 0.55 mol/kg at around 450 ^oC. Below this temperature it decreased almost linearly down to 0.11 mol/kg at 250 ^oC, and above this temperature it also decreased down to 0.46 mol/kg at 500 ^oC. The larger hysteresis loops with increasing CO_2 working capacity were counterintuitive but consistent with faster desorption kinetics in the low pressure regions being offset by relatively slower desorption kinetics in the high pressure regions. These results perhaps indicated that two fundamentally different phenomena associated with two different interchangeable CO_2 phases were taking place within this K-promoted HTlc structure.

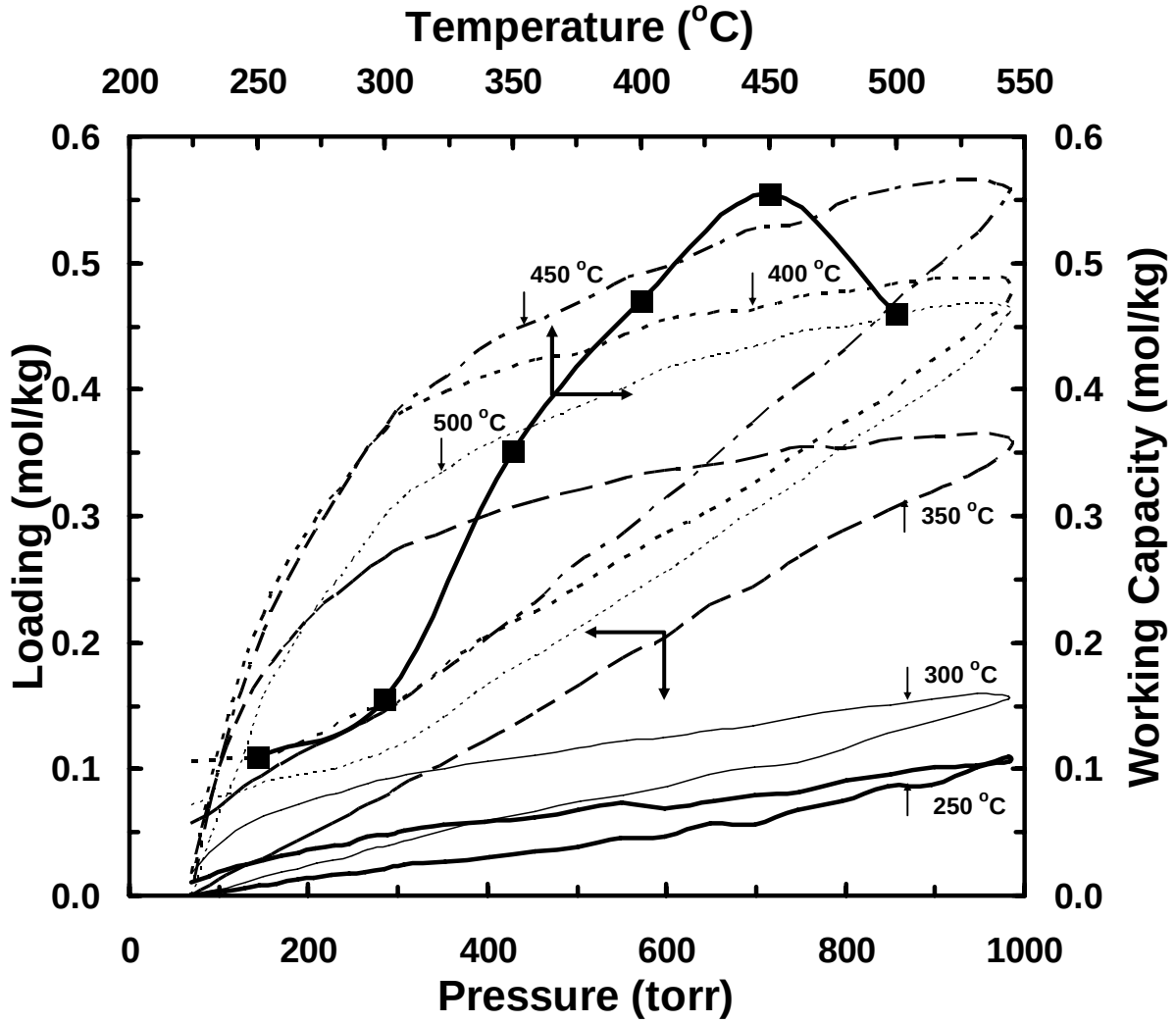

Figure 48. Non-equilibrium dynamic adsorption and desorption isotherms (thin lines) at 250, 300, 350, 400, 450 and 500 ^oC for CO_2 on a K-promoted HTlc at the periodic state, with each isotherm from Figure 2 normalized to zero CO_2 loading at 65 torr; and non-equilibrium dynamic

working capacity for CO_2 on a K-promoted HTlc (thick line) obtained from these results between 65 and 980 torr.

Based on the culmination of these findings, a reaction pathway was envisioned for the reversible uptake and release of CO_2 in K-promoted HTlc. This reaction pathway involved three reversible reactions with slow, intermediate and fast adsorption and desorption behavior, respectively. It also involved four different reaction sites, denoted by A, B, C, and E with reaction sites B, C and E being restricted to sharing a fixed total number of sites N_{total}. A pictorially representation of this reaction pathway is shown in Figure 49. The figure also shows one other reaction site, denoted by I, that represented the initial phase of the sample prior to activation. This reaction pathway is explained below.

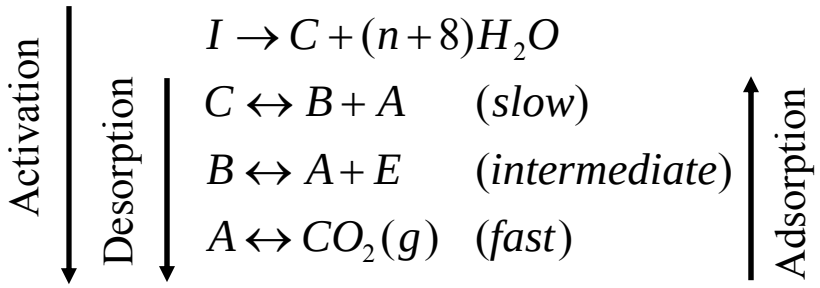

$$I \equiv \left[Mg_3Al(OH)_8\right]_2 (CO_3) \cdot K_2CO_3 \cdot nH_2O$$
$$A \equiv CO_2(ad)$$
$$E \equiv Mg_6Al_2K_2O_{10}$$
$$B \equiv Mg_6Al_2K_2O_9(CO_3)$$
$$C \equiv Mg_6Al_2K_2O_8(CO_3)_2$$
$$N_{total} = [E] + [B] + [C]$$
$$q = [A] + [B] + 2[C] - q_o$$
$$q_o = [B]_o + 2[C]_o$$

Figure 49. Proposed reaction pathway for the reversible adsorption and desorption of CO_2 on a K-promoted HTlc.

The decreasing absolute CO_2 capacity with increasing temperature (Figure 48) was consistent with an equilibrium driven, exothermic adsorption process (reaction) that represented the slow conversion of a high capacity, reversible, CO_2 phase identified as phase C. This slow reaction, the first of three reversible reactions involved in the proposed pathway, was most likely associated with the processes depicted in Figure 46 that exhibited the slowest adsorption and

desorption (or reaction) kinetics. It was envisioned that two other phases (A and B) were also involved in this slowest of processes, with the pertinent exothermic reaction identified as A+B $\leftrightarrow$ C. It was further assumed that two CO_2 molecules were associated with phase C, and that they equally distributed into phases A and B during the above reaction.

It was also envisioned that these two CO_2 molecules interacted with the K-promoted HTlc each in their own way, wherein, while still in phase C, they each originated from a different location within the structure of the K-promoted HTlc. In fact, it was highly probable that one of the CO_2 molecules originated from the potassium carbonate structure and the other one originated from the HTlc structure. It was further assumed that the CO_2 molecule originating from the potassium carbonate structure became the weakly chemisorbed CO_2 species (phase A) with limited diffusional mobility within the K-promoted HTlc, while the CO_2 molecule originating from the HTlc structure became the more strongly chemisorbed species (phase B) that remained tightly bound within the K-promoted HTlc.

The CO_2 working capacity that generally increased with increasing temperature, but that exhibited a maximum at high temperatures (Figure 47), was probably associated with the formation of phase B through the second of the three reversible reactions of the proposed pathway, with faster adsorption and desorption (reaction) kinetics than the first reaction. Two other phases were assumed to be involved in this process, i.e, phase A, which was already involved in the first reaction, and a phase identified as phase E that was devoid of CO_2 molecules. The pertinent exothermic reaction was identified as A+E $\leftrightarrow$ B. It was further assumed that the site associated with phase E corresponded to the original HTlc structure and thus the CO_2 molecule occupied the same site in both phases B and C. This assumption led to the total site restriction imposed on these three phases.

The maximum exhibited in the CO_2 working capacity in Figure 48 was consistent with the presumption that phase B was an intermediate species between the first and second reactions just described, i.e., A+B $\leftrightarrow$ C and A+E $\leftrightarrow$ B, and the fact that the first of these reactions was exothermic and very sensitive to temperature. Thus, the initial increase in capacity of phase B with increasing temperature (i.e., the CO_2 working capacity) was due to phase C losing capacity (or sites) that became available to phase B (as well as to phase E). The eventual loss of capacity of phase B with increasing temperature after reaching a maximum suggested that the second reaction A+E $\leftrightarrow$ B was also exothermic.

Finally, it was envisioned that the weakly bound chemisorbed layer of CO_2 (phase A) corresponded, in fact, to CO_2 molecules residing in the interstitial spaces within the K-promoted HTlc that were free to diffuse. This phase was associated with its own CO_2 capacity, and a fast and reversible adsorption reaction, i.e., $CO_2(g) \leftrightarrow$ A, which was identified as the third and final reversible reaction of the proposed pathway. As indicated earlier, phase A exhibited a very weak dependence on temperature. It also initiated and participated in the entire process and was responsible for the rapid adsorption and desorption kinetics in the low pressure regions. It was assumed that at equilibrium, the capacity of this layer depended on the partial pressure of CO_2.

In short, the proposed reaction pathway that describes the reversible uptake and release of CO_2 in a K-promoted HTlc is summarized as follows. The process starts with an activation step,

which is identical to a CO_2 release or desorption step with the exception that a dehydration process takes place first to eliminate the initial phase I. Once phase C is formed, which is the product created from the dehydration of phase I, the K-promoted HTlc undergoes a slow reaction described by $C \rightarrow A+B$, followed by an intermediate reaction described by $B \rightarrow A+E$ and finalized by a fast reaction described by $A \rightarrow CO_2(g)$. This sequence of reactions leads to a final state consisting of a mixture of phases E_o, C_o and B_o, as shown in Figure 50. The absence of phase A_o in the activated sample is the result of the fast kinetics of the third reversible reaction, i.e., $A \rightarrow CO_2(g)$. During this entire process, phases C, D and E constantly readjust to satisfy the restriction $E + C + B = N_{total}$ until they reach the final state previously indicated.

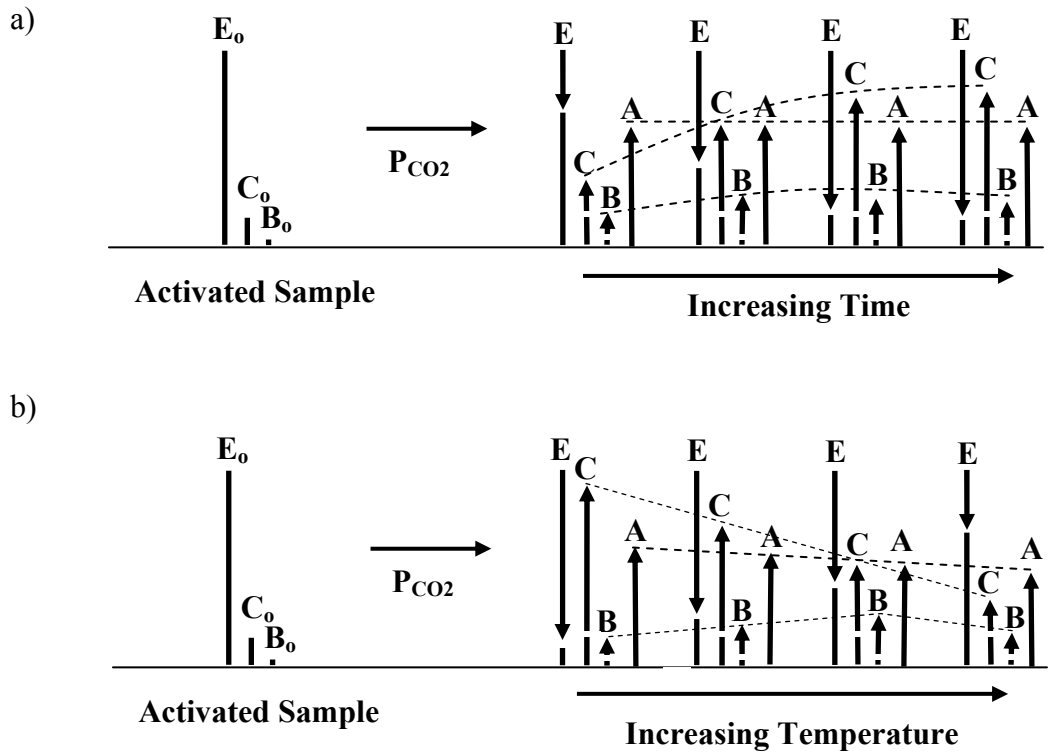

Figure 50. Loading transitions incurred during CO_2 uptake by all the different phases involved in the proposed reaction pathway of an activated sample: a) at increasing times and a fixed temperature, and b) at increasing temperatures and a fixed time. The sum of the loadings corresponding to B, C and E remains fixed and equal to N_{total}. The loading in phase A, which is nil in the activated sample and reaches equilibrium immediately, depends on the CO_2 partial pressure and decreases only slightly with temperature. Phase B may experience loading reversal in both situations.

Once the activation (or CO_2 release) step is finished, a partial pressure of CO_2 is imposed upon the sample to start the adsorption step. The diagrams on the right side of Figure 50 depict different states of the phases in a K-promoted HTlc during CO_2 uptake, by exposing the activated state shown on the left side to a fixed partial pressure of CO_2 under two different situations. In the first situation (Figure 50a), the diagrams depict from left to right the envisioned states within

the K-promoted HTlc after increasingly longer times of CO_2 exposure at a fixed temperature. In the second situation (Figure 50b), the diagrams depict from left to right the envisioned states within the K-promoted HTlc after increasingly higher temperatures at a fixed time of CO_2 exposure.

For the case where the temperature is fixed (Figure 50a), because of the fast reaction that converts CO_2 gas into phase A, the equilibrium for this phase, which depends only on the CO_2 pressure and temperature, is reached almost immediately. Consequently, all the diagrams in Figure 50a depict a loading of phase A that remains essentially fixed from the start. Moreover, at a fixed temperature (Figure 50a) and in excess of phase E, the loadings of phases B and C necessarily increase with time. For the large time scales depict in the figure, however, the faster converting phase B only adjusts based on the slow changes incurred by phase C. Depending on the loading of phase C, phase B may even experience a reversal during the process.

For the case where the temperature increases (Figure 50b), the weak dependence of phase A on temperature is represented in terms of a slight decay of the CO_2 loading with increasing temperature, while the changes incurred by phases B, C and E are still restricted by the total site condition. Moreover, at a fixed time (Figure 50b), the exothermic character of the slow reaction leading to phase C ($A+B \rightarrow C$) causes the loadings of this phase to decrease with increasing temperature, leaving more sites available for phases B and E. This result leads to phase B initially increasing with increasing temperature but then, in the excess of phase E, it again experiences a reversal due to the exothermic character of the reaction leading to phase B (i.e., $A+E \rightarrow B$)

In short, each isotherm exhibited the following characteristics: Depending on the temperature, it took between 5 and 12 adsorption and desorption cycles to attain periodic behavior. The approach to periodic behavior was associated with an initial non-equilibrium CO_2 capacity that exhibited substantial departure not only from equilibrium but also from the periodic absolute CO_2 adsorption capacity, with this departure being larger with decreasing temperature. A hysteresis loop formed between the non-equilibrium dynamic adsorption and desorption isotherms and remained intact at the periodic state.

These results were interpreted in terms of the uptake and release of CO_2 on K-promoted HTlc being associated with three temperature dependent, coupled, reversible and equilibrium driven reactions. The first reaction exhibited slow adsorption and desorption kinetics and a very high CO_2 capacity. The second reaction exhibited faster adsorption and desorption kinetics and an intermediate CO_2 capacity. The third reaction exhibited very rapid adsorption and desorption kinetics, with a slightly smaller CO_2 capacity. The third reaction also initiated the entire process by forming a chemisorbed layer of CO_2 within the K-promoted HTlc. This layer reversibly converted into a second phase through the second reaction, which reversibly converted into a third phase through the first reaction, with the weakly bound chemisorbed layer of CO_2 participating in both of these latter reactions.

5.4 Conclusions

A K-promoted HTlc was synthesized and tested to determine its reversible CO_2 capacity

between 250 and 500 ^{o}C. Non-equilibrium dynamic adsorption and desorption isotherms were measured between 65 and 980 torr using 20 and 50 torr steps and a 45 min duration between steps. The absolute CO_2 capacity on K-promoted HTlc increased with decreasing temperature, with CO_2 loadings of 2.25 and 1.02 mol/kg respectively at 250 and 500 ^{o}C and 980 torr. The CO_2 working capacity obtained between 65 and 980 torr exhibited a maximum at 450 ^{o}C, with a value of 0.55 mol/kg compared to 0.11 and 0.46 mol/kg at 250 and 500 ^{o}C, respectively.

Each isotherm exhibited the following characteristics: Depending on the temperature, it took between 5 and 12 adsorption and desorption cycles to attain periodic behavior. The approach to periodic behavior was associated with an initial non-equilibrium CO_2 capacity that exhibited substantial departure not only from equilibrium but also from the periodic absolute CO_2 adsorption capacity, with this departure being larger with decreasing temperature. A hysteresis loop formed between the non-equilibrium dynamic adsorption and desorption isotherms and remained intact at the periodic state.

These results were interpreted in terms of the uptake and release of CO_2 on K-promoted HTlc being associated with three temperature dependent, coupled, reversible and equilibrium driven reactions. The first reaction exhibited slow adsorption and desorption kinetics and a very high CO_2 capacity. The second reaction exhibited faster adsorption and desorption kinetics and an intermediate CO_2 capacity. The third reaction exhibited very rapid adsorption and desorption kinetics, with a slightly smaller CO_2 capacity. The third reaction also initiated the entire process by forming a chemisorbed layer of CO_2 within the K-promoted HTlc. This layer reversibly converted into a second phase through the second reaction, which reversibly converted into a third phase through the first reaction, with the weakly bound chemisorbed layer of CO_2 participating in both of these latter reactions.

6.0 K-Promoted Hydrotalcite as a High Temperature Adsorbent for CO_2 Capture: Proposed Non-Equilibrium Kinetic Model

6.1 Introduction, Literature review and Objectives

Hydrotalcite-like compounds (HTlcs) that exhibit a reversible capacity for CO_2 at elevated temperatures are being explored for the removal of CO_2 from equilibrium limited reactions (Nataraj et. al., 1998; Hufton et. al., 1999 and 2004; Ding and Alpay, 2000), and the capture and concentration of CO_2 from flue gas (Ding and Alpay, 2000; Yong et. al., 2000; Soares et. al., 2002 and 2004; Moreira et. al., 2006; Reynolds et. al., 2005 and 2006). Nevertheless, a paucity of literature is available on the adsorption properties of CO_2 on HTlcs (Nataraj et. al., 1998; Hufton et. al., 1999 and 2004; Hutson et. al., 2004; Ding and Alpay, 2000; Yong et. al., 2000 and 2002; Soares et. al., 2002 and 2004; Moreira et. al., 2006; Reynolds et. al., 2005 and 2006). A mechanism that clearly describes the reversible CO_2 uptake and release processes is also sorely lacking. Much of the literature that describes the reversible adsorption of CO_2 on HTlcs treats it as a high temperature, diffusion limited, equilibrium driven process that is akin to physical adsorption (Ding and Alpay, 2000 and 2001; Yong et. al., 2001; Soares et. al., 2002 and 2004; Moreira et. al., 2006; Reynolds et. al., 2005 and 2006). However, based on discrepancies in the values of the mass transfer coefficients of CO_2 in HTlcs reported in the literature (Hufton et. al., 1999; Ding and Alpay, 2000 and 2001; Yong et. al., 2001; Soares et. al.,

2002 and 2004; Moreira et. al., 2006) the actual mechanism appears to be much more complicated than this simple depiction.

For example, Ding and Alpay (2000) reported mass transfer coefficients for CO_2 in a K-promoted HTlc of 0.0058 s^{-1} for adsorption and 0.0006 s^{-1} for desorption. Those values both indicated the dominance of a slow diffusion or reaction limited process. In contrast, Hufton et al (1999) showed very steep breakthrough curves and an elution curve predicted by equilibrium theory for CO_2 in a K-promoted HTlc. Very fast mass transfer or reaction kinetics were indicated by those behaviors. Finally, Soares et al (2004) reported a mass transfer coefficient for CO_2 in HTlcs as high as 0.0153 s^{-1}. That value indicated a mass transfer or reaction limited process with CO_2 uptake and release rates lying somewhere in between those reported in the other studies. To further complicate matters, recent results (Moreira et. al., 2006) suggested that the reversible adsorption of CO_2 on HTlcs at elevated temperatures was a kinetically driven, non-equilibrium process that acquires the character of an equilibrium process only after extremely long times.

Ebner et al. (2006), showed that an initially fast adsorption or desorption phenomenon was followed by a state of extremely slow uptake or release of CO_2 that requires hours perhaps days to reach equilibrium. The CO_2 loadings at such an equilibrium state were also considerably different than those attained during the initial stages of adsorption or desorption. This kind of unusual behavior of CO_2 on HTlcs at elevated temperatures was consistent with the Langmuir-Hinshelwood type of kinetic model mentioned recently by Moreira et al (2006).

Therefore, the objective of this work was to report on the development of a non-equilibrium kinetic model that describes the reversible adsorption and desorption behavior of CO_2 on a K-promoted HTlc. This model combines adsorption, diffusion and reaction together with a Langmuir-Hinshelwood approach to describe the uptake and release processes of CO_2 on a K-promoted HTlc. Results are presented that convincingly reveal the adsorption and desorption behavior of CO_2 on a K-promoted HTlc to be associated with complex, highly coupled, completely reversible adsorption, diffusion and reaction phenomena.

6.2 Adsorbent Material Cycling

A Perkin Elmer TGA-7 thermogravimetric analyzer was used to measure the dynamic adsorption and desorption behavior of CO_2 on this K-promoted HTlc. A typical TGA run was carried out with a sample of K-promoted HTlc powder (~ 35 mg). This powder had a rather broad particle size distribution, with particle diameters ranging from 5 to 100 μm. First, the sample was activated at 400 ^oC for a specified length of time (8,12,16 or 20 h) in helium flowing at about 60 cm^3/min and 1 atm. At the end of the activation step, the temperature was maintained at 400 ^oC and the gas was switched from He to CO_2 (also flowing at about 60 cm^3/min and 1 atm) to initiate adsorption and begin the first half of an adsorption-desorption cycle. This adsorption half-step was continued for a specified length of time and then the gas was switched back to He to initiate desorption and finish the second half of the adsorption-desorption cycle. When the half cycle time was set at a very long time of 700 min, one adsorption-desorption cycle was carried out to allow the system to approach equilibrium at the end of the adsorption or desorption step. When the half cycle times were set at much shorter times of 15, 30, 45, 60 and

75 min, four adsorption-desorption cycles were carried to elucidate the dynamic behavior during cycling under more reasonable cycle times that were far away from equilibrium.

All of the CO_2 loadings on K-promoted HTlc were based on the weight of the sample at the end of the activation period. However, at the end of this period, the sample was not necessarily in an equilibrium state, it was still losing weight at a slow, but noticeably steady, rate without showing any sign of leveling off, and it still contained some undesorbed CO_2 (Ebner et. al., 2006). Because this slow activation (desorption) rate would have required inordinately long activation periods to reach a more activated, but not necessarily a completely activated state, the activation time was limited to durations between 8 and 20 hours.

6.3 Kinetic Model Development

It must be stated at the outset that the non-equilibrium kinetic model was developed through a painstaking effort that involved starting with the simplest formulation and adding complexity until a model was found that satisfactorily predicted the long cycle time experiment. Hence, this modeling effort began with a simple isothermal solid diffusion model, i.e., a linear driving force (LDF) approach. It failed to predict the long cycle time experiment, however. This isothermal model was extended to include both pore and surface diffusion, and pore and loading dependent surface diffusion phenomena with no avail. Film mass transfer outside the K-promoted HTlc particles was also added to all of these models. As expected, its effects were short lived and also did not play a role. These models were all evaluated again after a non-isothermal energy balance was included in the formulation with similar disappointing results. An isothermal solid diffusion model with one solid phase reaction also did not satisfactorily fit the long cycle time experiment. Finally, through careful examination of the behavior of the K-promoted HTlc when characterized in terms of non-equilibrium dynamic isotherms (Ebner et. al., 2006), and by taking into account the increasing level of complexity needed to fit the long cycle time experiment, it became apparent that one fast and two slow processes were taking place. Hence, an isothermal model with three reactions was devised. Two of the reactions were of the Langmuir-Hinshelwood type and one of them was a mass transfer limited (LDF) chemisorption process. This formulation is explained below.

Based on recent findings in the literature (Ebner et. al., 2006), and the painstaking modeling effort just described, the reaction pathway depicted in Figure 49 was envisioned for the reversible uptake and release of CO_2 in K-promoted HTlc. This reaction pathway involves three reversible reactions with slow, intermediate and fast adsorption and desorption behavior, respectively. It also involves four phases that participate in these reactions, each one represented by a reaction site and denoted by letters A, B and C and E. A possible chemical formulation for each of these phases is given in Figure 49. An irreversible step, consisting of dehydration and dehydroxilation, which transforms the inactive sites I into active sites C, is also presented in the figure. This irreversible step represents the activation step of the K-promoted HTlc sample, which occurs only once.

Reaction sites corresponding to phases C, B and E are assumed to be in the form of carbonates. Phases C, B, and E respectively represent sites where two, one and zero molecules of CO_2 can strongly and chemically bind to the structure of the K-promoted HTlc. These three sites combined also represent the total number of strong reaction sites available and is denoted by q_T.

In contrast, phase A represents a site that weakly binds CO_2 through a chemisorption mechanism. Phase A also actively participates in the formation of both phases B and C, and through a mass transfer-limited (i.e., diffusional) process in the rapid conversion between gaseous and chemisorbed CO_2.

The reaction pathway depicted in Figure 49 is defined such that all the reactions proceed from phases with higher to lower CO_2 contents, i.e., in the direction of CO_2 desorption or release. The first two reversible reactions represent the conversion of phase C into phase B and then the conversion of phase B into phase E, in each case giving up a CO_2 species to form phase A. The third reversible reaction represents the conversion of phase A into gaseous CO_2, which diffuses through the K-promoted HTlc particle according to the mass transfer limited LDF process.

The reversible, non-equilibrium, kinetic model consists of three overall differential equations that represent the mass balances for the three reversible phases C, B and A, and one algebraic equation that represents the mass balance restriction involving phases C, B, and E. These four relationships are written as follows:

$$\frac{dq_C}{dt} = -k_{1,f} q_C + k_{1,b} q_A q_B \tag{82}$$

$$\frac{dq_B}{dt} = k_{1,f} q_C - k_{1,b} q_A q_B - k_{2,f} q_B + k_{2,b} q_A q_E \tag{83}$$

$$\frac{dq_A}{dt} = k_m \left(q_{A,e} - q_A \right) + k_{1,f} q_C - k_{1,b} q_A q_B + k_{2,f} q_B - k_{2,b} q_A q_E \tag{84}$$

$$q_E \equiv q_T - q_B - q_C \tag{85}$$

q_A, q_B, q_C and q_E respectively represent the site concentrations of phases A, B, C and E, with CO_2-free K-promoted HTlc (i.e., $Mg_6Al_2K_2O_{10}$) as the basis. $k_{1,f}$ and $k_{1,b}$ represent the forward and backward rate constants for the first reversible reaction in Figure 49. $k_{2,f}$ and $k_{2,b}$ represent the forward and backward rate constants for the second reversible reaction in Figure 49. k_m represents the mass transfer coefficient for the process involving site A and gaseous CO_2 becoming chemisorbed within the particle. In this mass transfer process, the LDF is defined between q_A and $q_{A,e}$, where $q_{A,e}$ represents the value of q_A at equilibrium with T and P_{CO2}, which is an independent parameter. Depending on whether the sample is under adsorption ($q_{A,e} = q_{A,e,a} > q_A$) or desorption ($q_{A,e} = q_{A,e,d} < q_A$), the mass transfer coefficient k_m of this process takes on one of the following values:

$$k_m = \begin{cases} k_{m,a} & q_{A,e} = q_{A,e,a} > q_A \\ k_{m,d} & q_{A,e} = q_{A,e,d} < q_A \end{cases} \tag{86}$$

The adsorption and desorption mass transfer coefficients were allowed to be different to account for the possibility of a loading dependent mass transfer process. Finally, the CO_2 loading is readily defined in terms of q_A, q_B, and q_C as

$$q_{CO_2} \equiv \left(q_A - q_{A,o}\right) + \left(q_B - q_{B,o}\right) + 2\left(q_C - q_{C,o}\right) \tag{87}$$

where q_{Ao}, q_{Bo}, and q_{Co} respectively represent the site concentrations of phases A, B and C just after activation.

The CO_2 release and uptake model described by Equations 82 to 87 constitutes two kinetically slow Langmuir-Hinshelwood processes coupled with a fast mass transfer chemisorption process. This model has twelve parameters, namely $k_{m,a}$, $k_{m,d,}$ $k_{1,f}$, $k_{1,b}$, $k_{2,f}$, $k_{2,b}$, $q_{A,o}$, $q_{B,o}$, $q_{C,o}$, q_T, $q_{A,e,a}$ and $q_{A,e,d}$. However, values for three of these parameters (i.e., $q_{B,o}$, $q_{A,o}$ and $q_{A,e,d}$) are known implicitly from sound assumptions, and a value for one of them (i.e., q_T) can be calculated. The remaining eight parameters are fitting parameters. The methodology used to obtain values for all of these parameters is explained in detail below.

6.4 Interpretation of Experimental Data

All the experimental CO_2 loadings reported in Figures 51 to 53 are in terms of the CO_2-free K-promoted HTlc basis (i.e., $Mg_6Al_2K_2O_{10}$), according to

$$q_{CO_2,\text{exp}} = \frac{x - x_o}{x_o}\left(1 + q_{A,o} + q_{B,o} + 2q_{C,o}\right) \tag{88}$$

where x represents the experimental mass obtained from the TGA and x_o represents the value of x just after activation. Figure 51 displays the behavior of CO_2 in K-promoted HTlc at 400 ^oC during a single adsorption and desorption cycle with a 700 min half cycle time. Figure 51a displays the full 1,400 min cycle. Figures 51b and 51c respectively display only the first 20 min of the adsorption and desorption steps to exemplify the behavior at short times. Recall that the loadings displayed in Figure 51 were normalized relative to the weight of the sample at the end of the activation step, which as indicated earlier, was not necessarily at equilibrium and still contained some CO_2 in the sample. After reaching a CO_2 loading of q_{CO2} = 1.62 mol/kg at the end of the 700 min adsorption step, the sample returned to its original state with a $q_{CO2} \sim 0.0$ mol/kg after a 700 min desorption step (Figure 51a). This long cycle time experiment clearly demonstrated the complete reversibility of CO_2 in K-promoted HTlc.

Another interesting feature shown in Figure 51 was the steady rate (i.e, linear trend) exhibited by the CO_2 loading during the later stages of both the adsorption and desorption steps. In fact, for the desorption step, the trend was so steady that the CO_2 loading would have become negative if a longer time was allowed for desorption. A negative loading would correspond to the sample weighing less and being more activated than the reference state. Hence, this behavior was similar to that observed at the end of the activation step (results not shown), which was an important observation that indicated the sample was still far removed from equilibrium and that it was undergoing the same chemical transformation that was characterized by the same reversible but very slow kinetics in both cases. It was further surmised that the process responsible for this slow and steady behavior observed during the later stages of desorption was

also responsible for the slow and steady behavior observed during the later stages of adsorption, which defined the reversible nature of this particularly slow kinetic process.

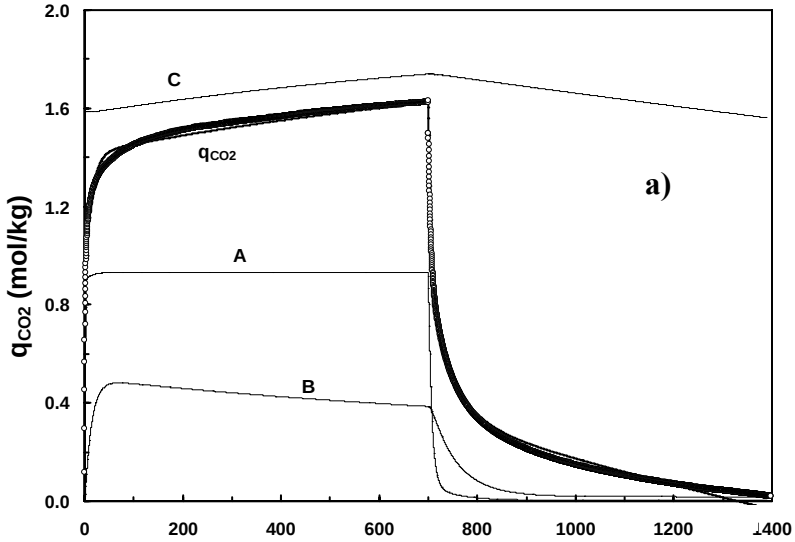

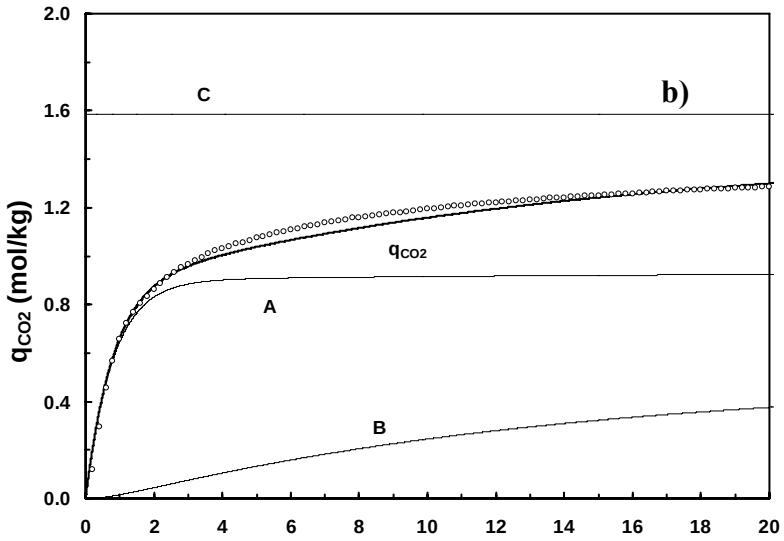

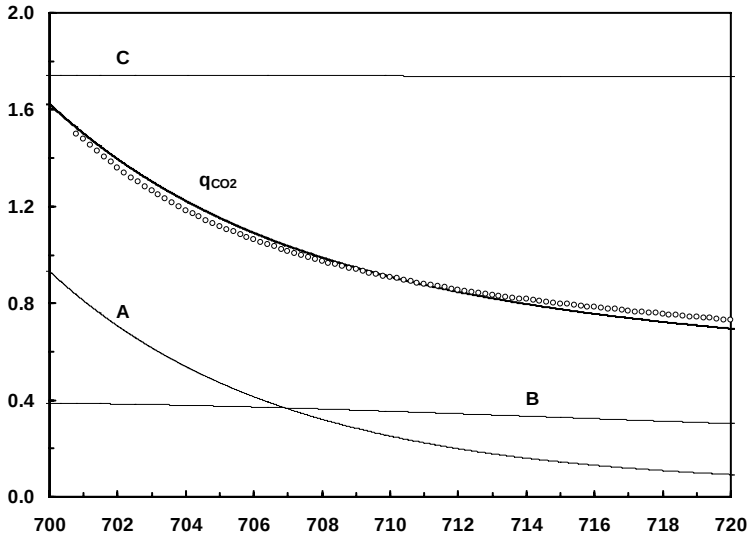

Figure 51. TGA experimental run (empty circles) and model fit (thick solid line labeled q_{CO2}) of the CO_2 loading in a K-promoted HTlc, and model predictions of the site concentrations of phases A, B and C (thin solid lines) during one CO_2 adsorption and desorption cycle with a 700 min half cycle time at 400 ^oC: a) complete 1,400 min adsorption and desorption cycle, b) first 20 min of the adsorption step, and c) first 20 min of the desorption step. This sample of K-promoted HTlc was activated in He at 400 ^oC for 12 hr.

This very slow kinetic behavior contrasted significantly with the very fast kinetic behavior observed during the early stages of both the adsorption and desorption steps, as highlighted in Figures 51b and 51c. This very fast process at short times indicated that the sample was undergoing an altogether different chemical transformation compared to the very slow process at long times. The large difference between the rates of adsorption and desorption were also very apparent during these early stages, with the former being about ten times faster than the latter. These rate differences were in good agreement with those reported by Ding and Alpay (2001) and signified that the sample was perhaps undergoing a loading dependent mass transfer process, where the CO_2 was only weakly adsorbed on the K-promoted HTlc.

However, neither the very fast nor the very slow kinetic processes could explain the adsorption and desorption behavior of CO_2 in K-promoted HTlc during the intermediate stages that ensued between 5 and 300 min of both the adsorption and desorption steps. It was surmised that the adsorption and desorption behavior of the sample during those stages were controlled by a third and altogether different mechanism than the previous two mechanisms. It was further assumed that this mechanism was probably similar in nature to the very slow kinetic process, but with somewhat faster kinetics. This intermediate behavior was consistent with the results reported in the previous section (Ebner et al., 2006).

It was becoming very clear that all three mechanisms collectively supported the existence of the four different phases identified in Figure 49 as phases A, B, C, and E. First, the slow process observed during the later stages of both the adsorption and desorption steps, as well as during the last moments of the activation step (not shown), described the slow and reversible

decomposition of phase C, which contained two CO_2 molecules, into an intermediate phase B, which contained only one CO_2 molecule, and phase A, which possessed a weakly bound CO_2 molecule. The CO_2 molecules in phases B and C were most likely in the form of carbonates, as depicted. The very fast process, on the other hand, was presumably due to phase A, which consisted of chemisorbed CO_2 molecules diffusing through the structure of the K-promoted HTlc and reversibly converting into gaseous CO_2 via a fast mass transfer limited process. Finally, the intermediate process observed during the intermediate stages of the adsorption and desorption steps (i.e., between 5 and 300 min) was probably associated with the reversible decomposition of phase B into phase A and a phase devoid of CO_2 molecules, i.e., phase E.

6.5 Model Calibration with Experimental Data

These three kinetic processes that vividly explained the uptake and release of CO_2 in K-promoted HTlc were illustrated mathematically by the reversible, non-equilibrium, kinetic model given by Eqs. 82 to 87. The excellent fit of this model to this long cycle time adsorption-desorption run over the entire 1,400 min duration of the experiment is also shown in Figure 51. The model was also used to predict the site concentrations of phases A, B and C throughout the experiment. These results are also plotted in Figure 51. The twelve model parameters that provided this excellent fit of the long cycle time TGA run and the corresponding predictions of the site concentration profiles were obtained as follows.

As stated above in the Kinetic Model Development section, four of the parameters were known *a priori*, which left only eight of them to be determined by fitting the model to experimental data. The first two known parameters were $q_{B,o}$ and $q_{A,o}$. It was easy to reason that at the end of the activation step only site C still contained some CO_2 molecules as a result of the extremely slow kinetics involved with the conversion this phase into phases B and A. In contrast, the much faster kinetics involved with the conversion of phase B into phase E and especially the conversion of phase A into gaseous CO_2 granted that $q_{B,o} = q_{A,o} = 0$ for all time ($t \geq 0$) after activation.

The third known parameter was $q_{A,e,d}$. For similar reasons as given for $q_{B,o}$ and $q_{A,o}$, it was easy to reason that the equilibrium condition for site A at the end of a desorption step was a vacant site free of CO_2 molecules. It then followed that $q_{A,e,d} = 0$ for all time ($t \geq 0$) after activation.

The fourth known parameter was q_T. This parameter was calculated from stoichiometry by first considering a fully activated form of K-promoted HTlc that contained no CO_2 molecules. This CO_2 free state corresponded to phase E with molecular formula $Mg_6Al_2K_2O_{10}$. The maximum number of CO_2 molecules that could be held by this K-promoted HTlc corresponded to phase C being completely filled with them, which was achieved by adding CO_2 molecules to phase E until phase C was completely saturated. This state corresponded to molecular formula $Mg_6Al_2K_2O_{10}(CO_3)_2$ and resulted in $q_T = 2.283$ mol/kg.

With four of the parameters known, the single cycle adsorption-desorption TGA run depicted in Figure 51 with a 700 min half cycle time was used to determine the remaining eight parameters in the model. This was accomplished in a sequential manner because, of the eight

parameters, three were associated with the formation of phase A (i.e., $k_{m,a}$, $k_{m,d,}$ and $q_{A,e,a}$), two were associated with the formation of phase B (i.e., $k_{1,f}$, and $k_{1,b}$), and three were associated with the formation of phase C (i.e., $k_{2,f}$, $k_{2,b}$, and $q_{C,o}$). In this way, these three sets of parameters were uniquely independent in that they defined the behavior of their respective reaction with little influence over the other reactions. The values of all twelve parameters are listed in Table 9.

The results in Figure 51 showed that there was very good agreement between the model and the experiments. For the adsorption step, only minor deviations between the model and the experiment resulted, with the largest, but still acceptable, difference occurring between times of 3 and 20 min, as shown in Figure 51b. The same was true for the desorption step, with the largest difference occurring at times greater than about 1,300 min, as shown in Figure 51a. Between times of 1,300 and 1,400 min, the model under predicted the experimental CO_2 loading and actually predicted slightly negative values of no more than -0.03 mol/kg. As explained earlier, these perfectly feasible negative values from the model indicated that the sample was losing more CO_2 than that corresponding to its loading just after activation. The very good agreement between the model and the experiments lent some credence to the magnitudes of the parameters obtained from the model. For example, from the values of the adsorption (1.218 min^{-1}) and desorption (0.140 min^{-1}) mass transfer coefficients, the model showed that the formation of phase A from gaseous CO_2 was a relatively fast process and that the reverse of this process was somewhat slower. This order of magnitude difference in the adsorption and desorption mass transfer coefficients was in agreement with that reported by Ding and Alpay (2001); however, their magnitudes were both larger and more similar to those reported by Soares et al. (2002). The resulting values of the rate constants for the slowest reaction, i.e., $k_{1,f}$ and $k_{1,b,}$ with respective values of 1.600×10^{-04} min^{-1} and 1.222×10^{-03} $kg^{-1}min^{-1}mol^{-1}$, corroborated that the dynamics of the reversible conversion of phase C into phases B and A was an extremely slow process that developed over a period of hundreds of hours. This result indicated that the sample would reach a true equilibrium state only after an exorbitantly long time. The model also predicted that phase B, with intermediate kinetic rate parameters of $2.192x10^{-02}$ min^{-1} and $5.793x10^{-02}$ $kg^{-1}min^{-1}mol^{-1}$ respectively for $k_{2,f}$ and $k_{2,b}$, barely existed after the first 400 minutes of desorption. This result verified the assumption made about $q_{B,o} = 0$ at the end of the activation period.

Parameter	Value	
$k_{m,a}$	1.218E 00	1/min
$k_{m,d}$	1.397E-01	1/min
$k_{1,f}$	1.600E-04	1/min
$k_{1,b}$	1.222E-03	kg/mol/min
$k_{2,f}$	2.192E-02	1/min
$k_{2,b}$	5.793E-02	kg/mol/min
$q_{A,e,a}$	0.932	mol/kg
$q_{A,e,d}$	0.000	mol/kg
q_T	2.283	mol/kg
$q_{A,o}$	0.000	mol/kg
$q_{B,o}$	0.000	mol/kg
$q_{C,o}$	1.587	mol/kg

Table 9. Assumed, calculated and fitted parameters used in the reversible, non-equilibrium, kinetic model that describe the adsorption and desorption behavior of CO_2 in a K-promoted HTlc at 400 ^oC.

The model predictions of the site concentrations of phases A, B and C shown in Figure 51 displayed trends that were consistent with three coupled reactions that have drastically different rate constants. For example, the model showed that during 700 min of adsorption and 700 min of desorption, the CO_2 loading in phase C changed only marginally due to its inherently slow kinetics. It exhibited only slight increases during adsorption and similarly slight decreases during desorption. In contrast, the model showed that phase A quickly saturated during the first 5 min of the adsorption step and nearly disappeared during the first 20 min of the desorption step. This trend was distinctly characteristic of the rapid adsorption and slightly slower desorption phenomena associated with this weakly chemisorbed phase of CO_2 in the K-promoted HTlc structure that was mass transfer limited in its conversion to gaseous CO_2. The intermediate rate process associated with the creation and extinction of phase B not surprisingly exhibited a maximum during the adsorption step, as it was being rapidly created from the conversion of phase A into phase B and slowly depleted from the subsequent conversion of phase B into phase C. During desorption, phase B essentially disappeared, but only long after phase A disappeared, due to the significant difference in their kinetic rate processes.

6.6 Model Validation with Experimental Data

Without any further adjustments, these twelve parameters were then used to further validate and evaluate the model by predicating the behavior of the 4-cycle adsorption-desorption TGA runs with half cycle times of 15, 30, 45, 60 and 75 min. The experimental and modeling results are shown in Figure 52 for each cycle time, along with the predictions of the site concentrations of phases A, B and C. All of the curves were characterized by a fast initial increase in the CO_2 loading that was consistent with the fast initial rate of adsorption in the long cycle time run shown in Figure 51. Due to the slower initial rate of desorption (compared to adsorption) that was associated with phase A, none of the samples returned to the reference state defined at the end of the activation step, i.e., $q_{CO2} = 0$ mol/kg. They did come increasingly closer to this state as the cycle time increased, however. With the longer cycle times increasingly giving more time for phase B to get involved in the CO_2 uptake and release processes, this result was understood to indicate that the forward and reverse reaction rates associated with phase B were similar in magnitude, compared to the order of magnitude slower desorption rate than adsorption rate associated with phase A.

The adsorption and desorption curves in Figure 52 all exhibited similar behaviors, not only from cycle to cycle and for the different cycle times, but also when compared to the long cycle time 1400 min curves shown in Figure 51. In particular, all the samples displayed the same behavior during the later stages of the adsorption and desorption steps, where the rate in all cases tended to approach a steady (i.e., linear) behavior, just like the curves in Figure 51. This result showed that, in all cases, an equilibrium state was once again far from being achieved. Nevertheless, the reversible nature of the adsorption and desorption behavior of CO_2 in K-promoted HTlc was quite apparent even from these short cycle time results. Indeed, if a longer time was provided for desorption, each sample would have returned to its reference state.

The results in Figure 52 also showed that the samples came very close to achieving periodic behavior just after the first cycle step (except for the sample cycled with a half cycle time of 15 min, which is explained later). Almost constant CO_2 working capacities were obtained from cycle to cycle that increased with increasing cycle time. Values of the CO_2 working capacities ranged between 0.58-0.62, 0.73-0.77, 0.85-0.87, 0.91-0.94, 0.99-1.05 mol/kg for respective half cycle times of 15, 30, 45, 60 and 65 min. These subtle experimental behaviors observed with cycling were also simulated fairly accurately with the model.

In all cases, the model provided excellent predictions of the first adsorption step. However, it exhibited some discrepancies for all subsequent adsorption and desorption steps, but only during the later stages of those steps. For example, the model over predicted the experimental working capacities by over predicting the CO_2 loadings during the adsorption steps and under predicting the CO_2 loadings during the desorption steps; but, it did predict the initial rates of adsorption and desorption in all cases, even after four cycles. These discrepancies were perhaps due to a somewhat large equilibrium loading of $q_{A,e,a}$ = 0.932 mol/kg for the adsorption step, which might have been a consequence of the oversimplified approach used to predict the mass transfer process between phase A and gaseous CO_2.

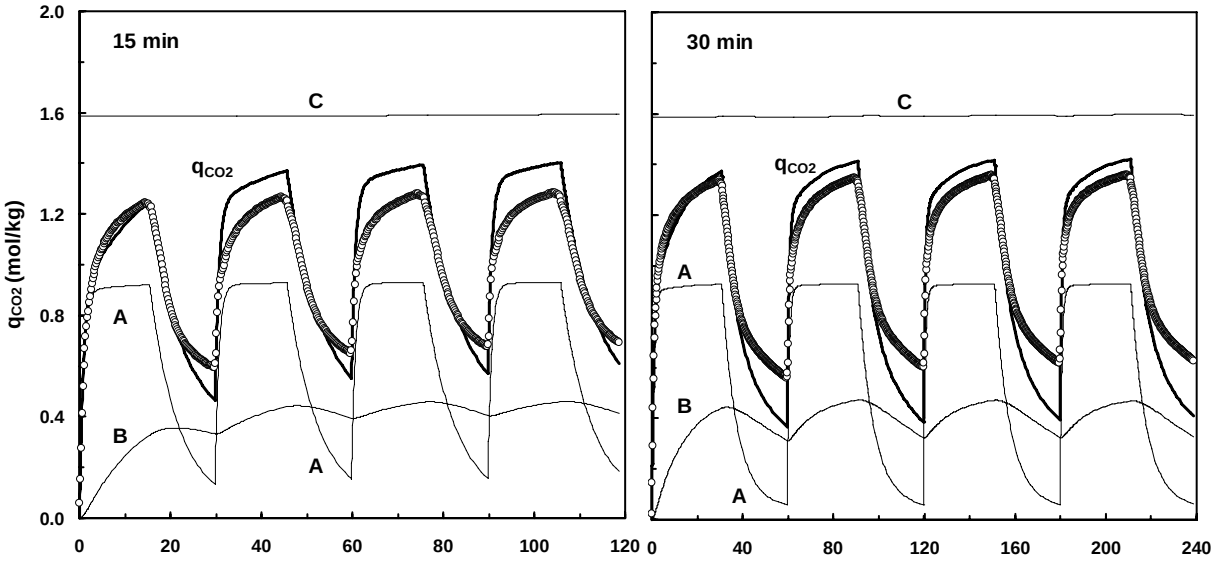

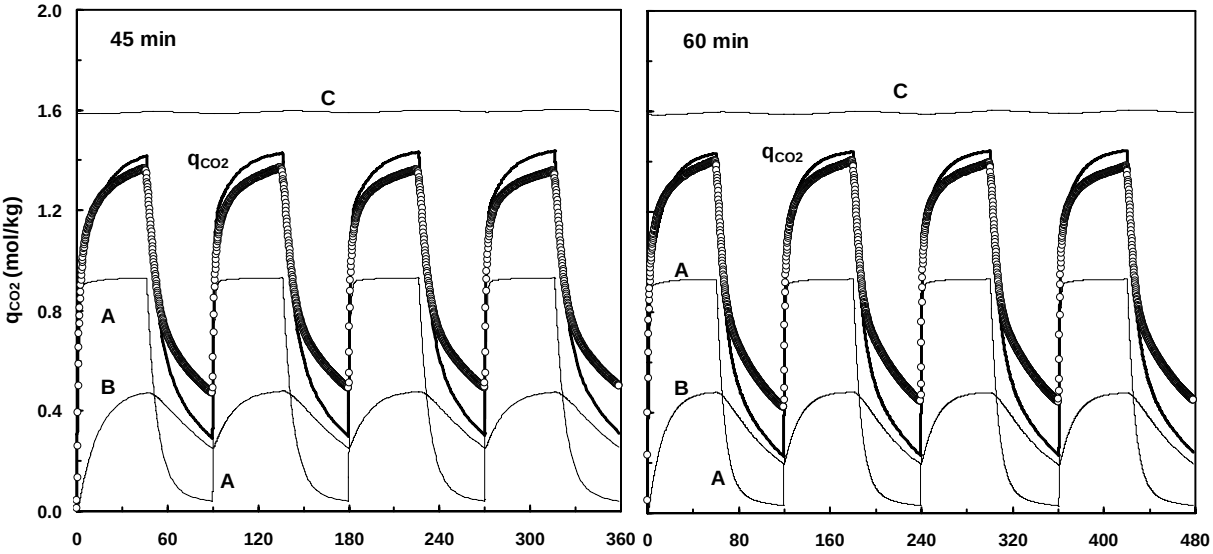

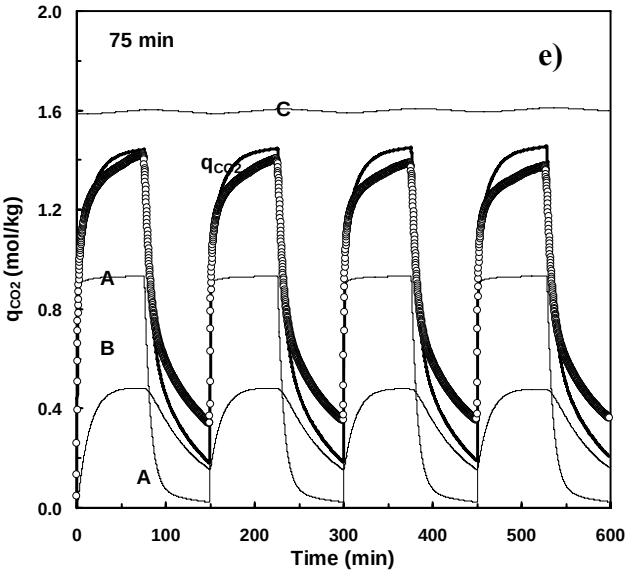

Figure 52. TGA experimental runs (empty circles) and model predictions (thick solid lines labeled q_{CO2}) of the CO_2 loadings in a K-promoted HTlc, and model predictions of the site concentrations of phases A, B and C (thin solid lines) during four CO_2 adsorption and desorption cycles with a) 15, b) 30, c) 45, d) 60 and e) 75 min half cycle times at 400 ^oC. This sample of K-promoted HTlc was activated in He at 400 ^oC for 12 hr.

Using the site concentration profiles of phases A, B and C, the model helped explain the significant difference between the initial adsorption step and those of subsequent cycles. Clearly, phase C did not contribute to this behavior, as its CO_2 loading did not change significantly during any of the runs, increasing only slightly after each cycle and oscillating more noticeably with longer cycle times (Figures 52d and 52e). This different behavior between the first and subsequent cycles was mainly due to phase B, with only a slight contribution from phase A. Both phases A and B displayed the largest increases in their CO_2 loadings during the first adsorption step. The initial CO_2 loadings observed experimentally were a result of these increases. The difference observed during the first adsorption step and those in subsequent ones tended to disappear for phase A with longer cycle times (Figures 52d and 52e). In contrast, the CO_2 loading of phase B became increasingly less periodic as the cycle time decreased. In fact, for the shortest half cycle time experiment of 15 min (Figure 52a), it continued to increase at the end of the adsorption step with cycling. This dynamic behavior associated with the slow kinetics of phase B during cycling at short times (Figure 52a) was not only predicted by the model, but it was also observed experimentally.

6.7 Modification of Kinetic Model for Temperature and Pressure Dependence

As discussed in the previous section, k_m represents the mass transfer coefficient for the process involving phase A and gaseous CO_2. In this mass transfer process, the LDF is defined between q_A and $q_{A,e}$, where $q_{A,e}$ represents the value of q_A at equilibrium with T and P_{CO2}, which is an independent parameter. Depending on whether the sample is under adsorption or desorption, $q_{A,e}$ is defined differently and k_m was allowed to take different values to account for the possibility of a loading dependent mass transfer process. For adsorption, $q_{A,e,a}$ is defined by equations (90), (91) and (92),

$$q_{A,e,a} = q_{A,\max}\theta_{A,e,a}(T,P) \tag{90}$$

$$q_{A,\max} = \eta(T)(q_B + 2q_E) \tag{91}$$

$$\eta(T) = ab(T - T_o)/[1 + b(T - T_o)] \tag{92}$$

Where, $q_{A,max}$ is the actual maximum concentration of site A formed after activation. $\theta_{A,e,a}$ is the fraction of coverage for phase A at equilibrium, in this case as all experiments were carried out at atmospheric pressure, which leads to $\theta_{A,e,a}$ being 1. η a function of temperature, is actually a fitting parameter, which physically means the ratio between actual reaction sites and the total sites that are available. Equation (92) shows the temperature dependence of η where a, b and T_o are parameters. The value of η ranges between 0 and 1. With increase in temperature, η also increases, which means that more reaction sites are available. For desorption, $q_{A,e,d} = 0$, since the equilibrium condition for site A at the end of desorption is a vacant site free of CO_2 molecule. Also, the mass transfer coefficient k_m of this process takes on values as shown by Eq (86).

Finally, through carefully examination of the predicted results with the experimental data, it was observed that a simple Langmuir model would best represent $\theta_{A,e,a}$.

$$\theta_{A,e,a} = \frac{bp}{1 + bp} \tag{93}$$

and

$$b = b_o \exp(-\frac{\Delta H}{RT}) \tag{94}$$

b_o is the pre-exponential coefficient, atm^{-1}, and ΔH is the heat of adsorption.

For this temperature and pressure dependent version of the model, the parameters that were made temperature dependent are:

$$k_{m,d} = A_{m,d} \exp(-Ea_{m,d}/RT) \tag{95}$$

$$k_{2,b} = A_{2,b} \exp(-Ea_{2,b}/RT);\ k_{2,f} = A_{2,f} \exp(-Ea_{2,f}/RT) \tag{96}$$

$$k_{1,b} = A_{1,b} \exp(-Ea_{1,b}/RT) \quad (97)$$

$$\eta = \frac{0.4048 \times 0.0103 \times (T - 270.1887)}{1 + 0.0103 \times (T - 270.1887)} \quad (98)$$

A series of adsorption and desorption cycling experiments were carried out in the TGA at different temperatures and partial pressures of CO_2. These data were used to extend the non-equilibrium model that describes the uptake and release of CO_2 on K-promoted HTlc to have both temperature and pressure dependence. The results are shown in Figures 53, 54 and 55. The conditions of the experiments are provided in the figure caption. After fitting these relationships to the experimental data, the following parameter values resulted:

$k_{m,a} = 1.2\ min^{-1}$

$A_{m,d} = 73.9556\ min^{-1}$

$Ea_{m,d} = 35.22\ kJ/mol$

$A_{2,b} = 4.237 \times 10^{-3}\ kgmol^{-1}min^{-1}$

$Ea_{2,b} = -9.843\ kJ/mol$

$A_{2,f} = 1.699\ min^{-1}$

$Ea_{2,f} = 27.8153\ kJ/mol$

$A_{1,b} = 2.691 \times 10^{-7}\ kgmol^{-1}min^{-1}$

$Ea_{1,b} = -46.2084\ kJ/mol$

$k_{1,f} = 2.75 \times 10^{-4}\ min^{-1}$

$q_{C,o} = 0.6245\ mol/kg$

$b_o = 0.1245\ atm^{-1}$

$\Delta H = 20.10\ kJ/mol$

Using these parameters, the model was able to fit the experiments quite well over a broad range of temperature and CO_2 partial pressure. It not only captured the adsorption and desorption kinetic behavior, but it also predicted the working capacity. The largest absolute deviations mostly occurred at the lowest CO_2 partial pressure; but, even there the model still predicted the working capacity. This is perhaps the most comprehensive model in the open literature that accurately describes the behavior of CO_2 on K-promoted HTlc.

6.8 Conclusions

A non-equilibrium kinetic model was developed to describe the reversible adsorption and desorption behavior of CO_2 in a K-promoted hydrotalcite like compound (HTlc) at 400 ^oC. The model consisted of three reversible reactions and four phases. Two of the reactions were of the Langmuir-Hinshelwood type with slow and intermediate kinetics, and one was a mass transfer limited chemisorption process with very fast kinetics. The first two reversible reactions represented the conversion of phase C ($Mg_6Al_2K_2O_{10}(CO_3)_2$) into phase B ($Mg_6Al_2K_2O_9(CO_3)$) and then the conversion of phase B into phase E ($Mg_6Al_2K_2O_{10}$). In each case, a CO_2 molecule was given up to form phase A (chemisorbed CO_2). The third reversible reaction represented the conversion of phase A into gaseous CO_2, which diffused through the K-promoted HTlc particle according to a mass transfer limited, linear driving force process. This model contained twelve parameters, four of which were known *a priori*.

To calibrate and test this model, a K-promoted HTlc was synthesized according to a recipe in the literature and then studied to determine its dynamic behavior during CO_2 adsorption and desorption cycles carried out at 400 ^oC. Three sets of dynamic cycling experiments were carried out. A long cycle time adsorption (700 min) and desorption (700 min) experiment was carried out that approached equilibrium with CO_2 in K-promoted HTlc at the end of each step. Prior to cycling in CO_2 and He, this sample was activated at 400 ^oC for 12 hr in He. Then, the effect of the half cycle time (15, 30, 45, 60 and 75 min) was studied with samples activated for 12 hr in He at 400 ^oC and cycled four times each. Finally, the effect of the activation time (8, 12, 16 and 20 hr) was studied with samples cycled twice with a 45 min half cycle time.

The eight parameter non-equilibrium kinetic model was fitted successfully to the long cycle time adsorption (700 min) and desorption (700 min) experiment. The model then predicted successfully the dynamic and cyclic behavior of both the much shorter cycle time experiments and the different activation time experiments. In all cases, it very accurately simulated the reversible adsorption and desorption behavior of the very fast mass transfer limited process associated with phase A, and the intermediate and slow kinetic processes associated with phases B and C, respectively. It also approached periodic behavior during cycling for different half cycle times in the same way the experiments did; and it showed independence between the CO_2 working capacity and the activation time of the sample, which was also consistent with the experimental findings. Overall, this non-equilibrium kinetic model revealed for the first time that the adsorption and desorption behavior of CO_2 in a K-promoted HTlc was associated with a combination of completely reversible adsorption, diffusion and reaction phenomena.

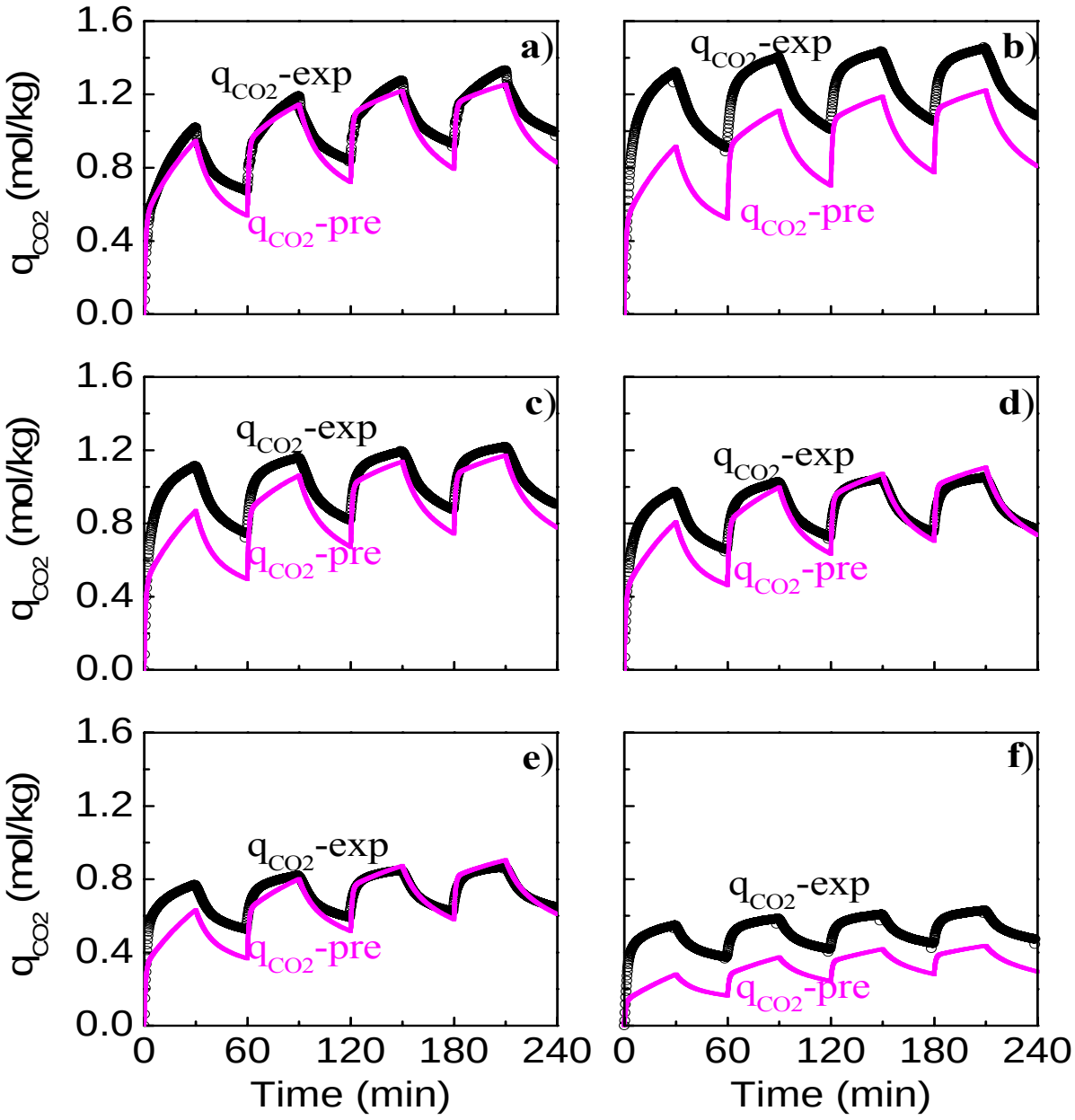

Figure 53. Comparison of experiment with model for K-promoted HTlc cycled at 360 ^{o}C and at different CO_2 partial pressures. The half cycle time is 30 min. The sample was activated at 500 ^{o}C with He, for 8 hours. P_{CO2} in (a) – (f) is 1, 0.79, 0.58, 0.42, 0.2, 0.05 atm, respectively. q_{CO2}-exp: experimental; q_{CO2}-pre: model prediction.

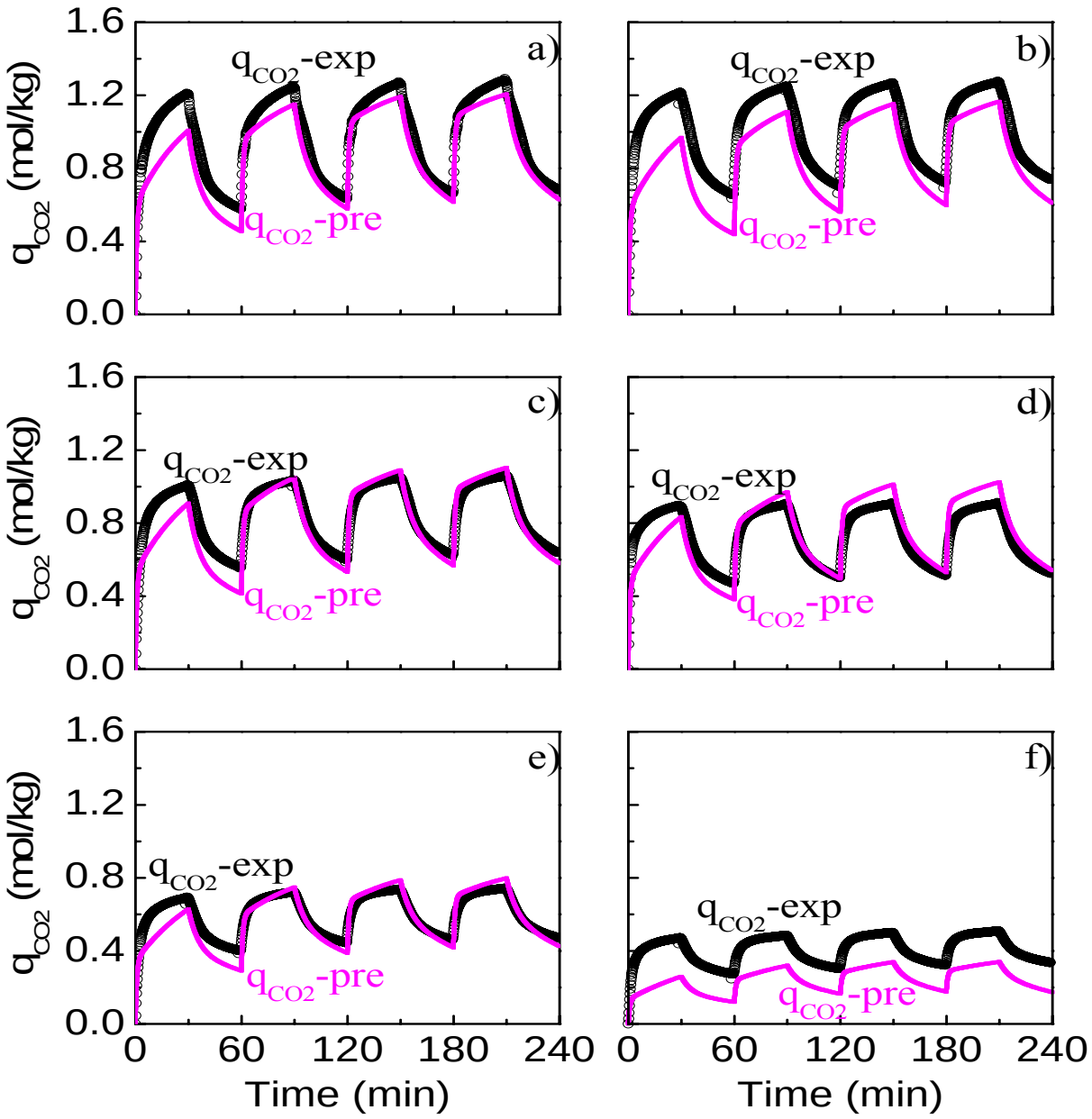

Figure 54. Comparison of experiment with model for K-promoted HTlc cycled at 400 ^{o}C and at different CO_2 partial pressures. The half cycle time is 30 min. The sample was activated at 500 ^{o}C with He, for 8 hours. P_{CO2} in (a) – (f) is 1, 0.79, 0.58, 0.42, 0.2, 0.05 atm, respectively. q_{CO2}-exp: experimental; q_{CO2}-pre: model prediction.

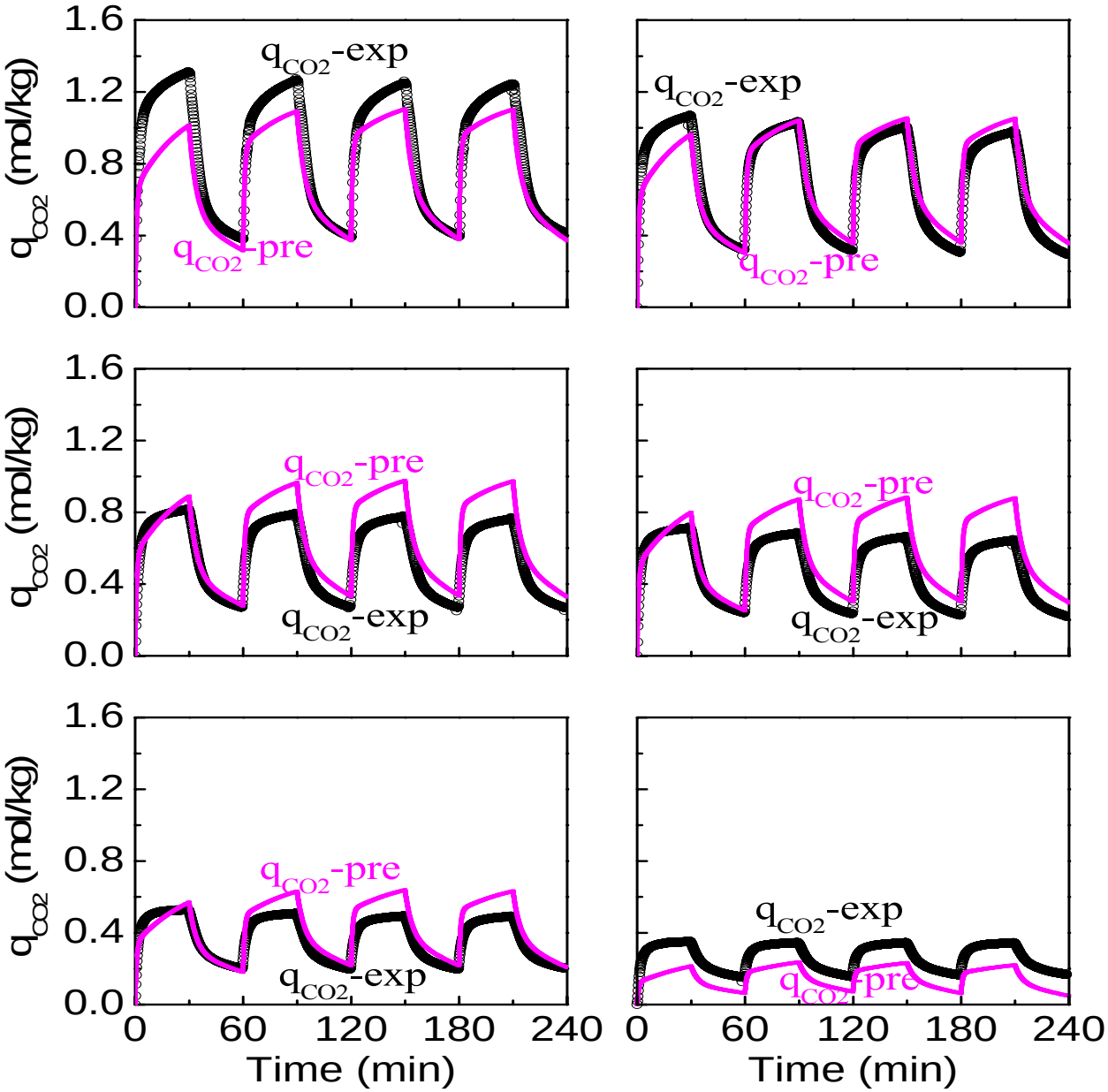

Figure 55. Comparison of experiment with model for K-promoted HTlc cycled at 460 ^{o}C and at different CO_2 partial pressures. The half cycle time is 30 min. The sample was activated at 500 ^{o}C with He, for 8 hours. P_{CO2} in (a) – (f) is 1, 0.79, 0.58, 0.42, 0.2, 0.05 atm, respectively. q_{CO2}-exp: experimental; q_{CO2}-pre: model prediction.

Finally, the non-equilibrium kinetic model was extended to account for temperature and pressure effects. This was done by incorporating Arrhenius-type expressions for all the kinetic parameters and a Langmuir isotherm for the mass transfer process. The extension was very successful, with the model now having the ability to predict the uptake and release of CO_2 over a wide range of conditions. This form of the model will be used in the PSA process simulator as a more realistic representation of the interaction of CO_2 with K-promoted HTlc.

7.0 Fixed Bed Adsorption Breakthrough and Desorption Elution Experiments with CO_2 on K-Promoted HTlc

7.1 Objective

The primary objective of this study was to carry out some larger scale experiments with K-promoted HTlc to verify some of the work done with smaller samples using the TGA. To this end, some preliminary fixed bed adsorption and desorption experiments were carried out with a newly implemented fixed bed apparatus. This bench-scale system utilized about 10,000 times more sample than in a TGA experiment.

7.2 Experimental Apparatus and Procedure

A schematic of the apparatus is provided in Figure 56. The system consists of a high temperature oven containing a 2 inch diameter by 22 inch long column packed with around 190 g of unactivated K-promoted HTlc. A preheated gas mixture of CO_2 and N_2 of a given composition and flow rate between 0.5 and 3.0 SLPM wase fed into this packed column for contact with the adsorbent. The composition and flow rate of the feed gas was controlled using two mass flow controllers located in the CO_2 and N_2 lines, as shown. The composition of the gas leaving the bed was analyzed using a mass spectrometer, while its flow rate was measured with a bubble flow meter located downstream of the oven.

First, the K-promoted HTlc sample was activated in 100% N_2 at 500 ^oC for 4 hrs. CO_2 adsorption breakthrough and desorption elution curves were then obtained on the Pural K-promoted HTlc (Sasol). The feed gas composition during adsorption was 15% CO_2 in balance of N_2. The feed gas composition during desorption was 100% N_2. The feed gas flow rate was 0.98 SLPM and the bed temperature was 400 ^oC.

7.3 Results and Discussion

Typical adsorption and desorption curves are shown in Figure 57. The bed capacity obtained from a number of such curves was the same at 0.39 mol CO_2/kg adsorbent. The fact that is was the same for adsorption and desorption indicates complete reversibility of CO_2 on this material. However, the adsorption rate appears to be faster than the desorption rate as indicated by the sharp breakthrough curve and less sharp elution curve. All of these results were consistent with the adsorption/desorption cycling experiments done with milligram samples of material in the TGA.

A modified version of the fixed bed system is shown in Figure 58. This single bed fixed-bed unit was designed to mimic all the steps of a complex multi-bed PSA cycle in a single unit. It will be used in the future to carry out experiments on various PSA cycles using K-promoted HTlc at temperatures between 400 and 500 ^oC.

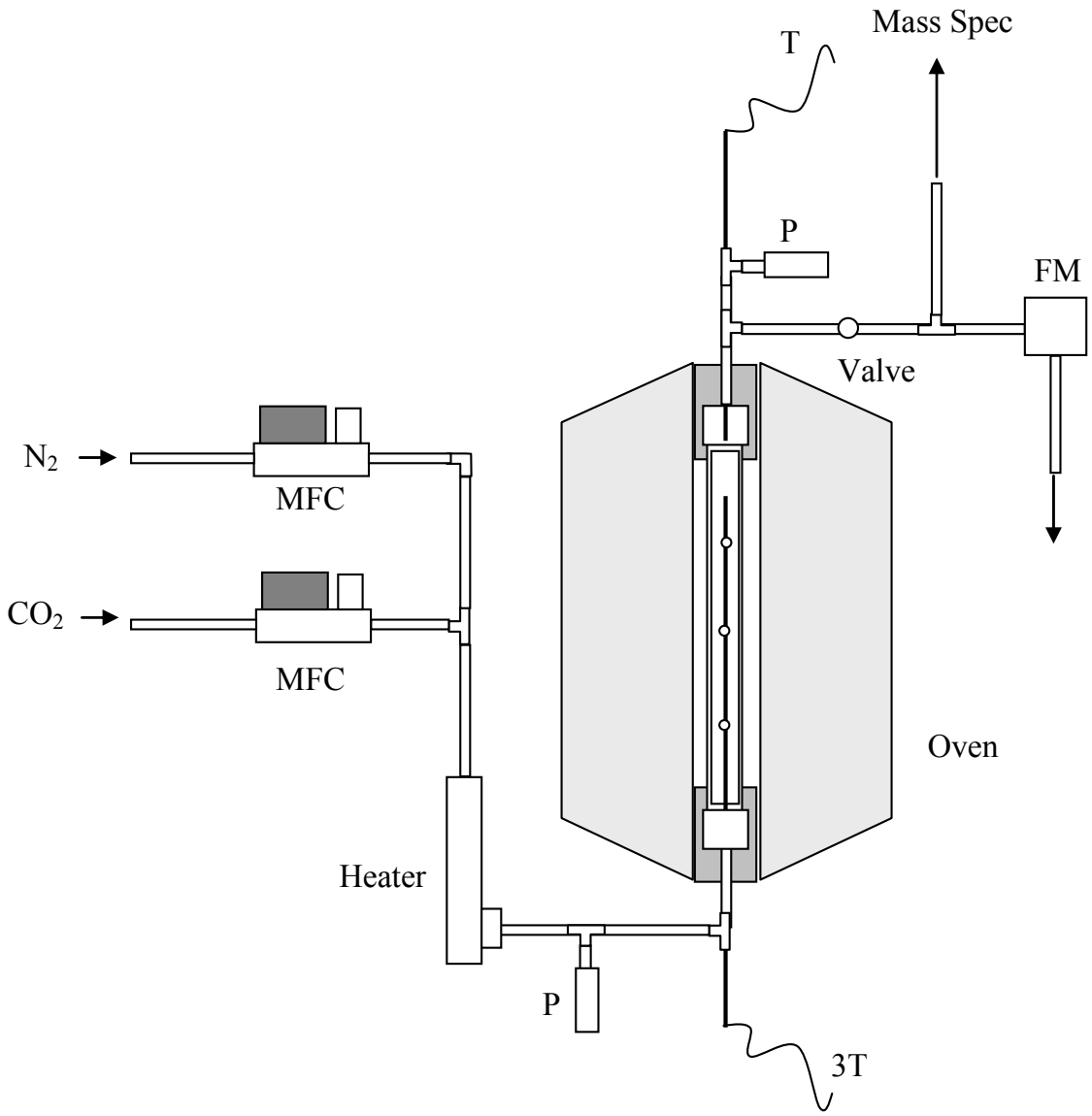

Figure 56. Schematic of the high temperature fixed-bed unit designed to obtain breakthrough and elution curves of CO_2 on K-promoted HTlc.

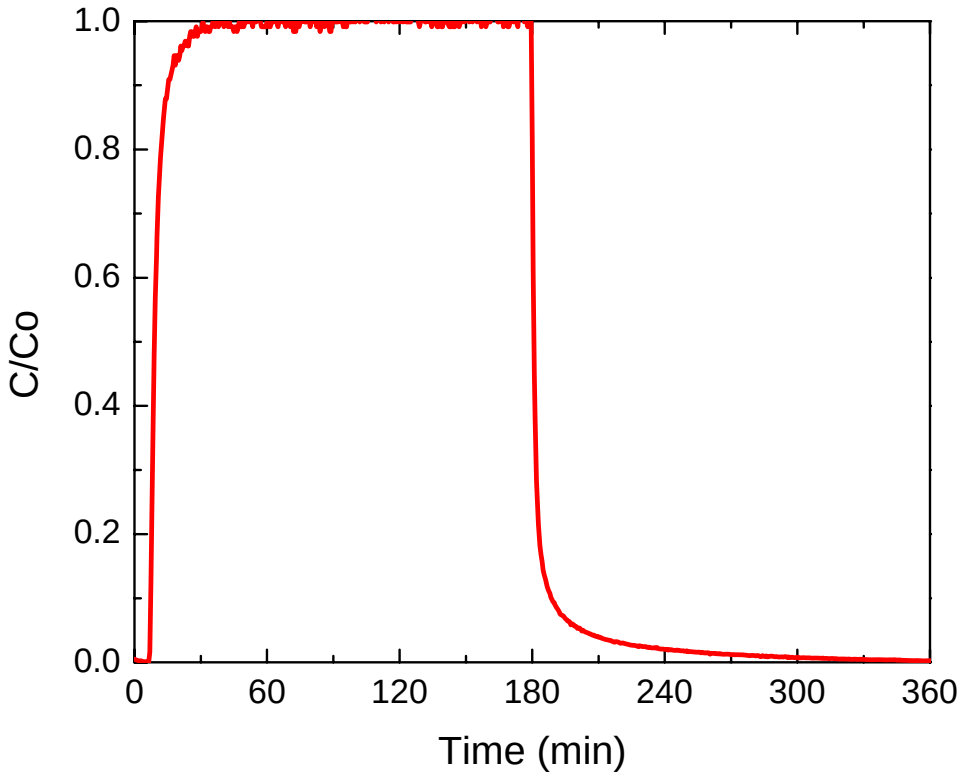

Figure 57. CO_2 adsorption breakthrough and desorption elution curves on Pural K-promoted HTlc (Sasol) in a fixed bed experiment: feed gas composition during adsorption: 15% CO_2 in balance of N_2; feed gas composition during desorption: 100% N_2; flow rate: 0.98 SLPM; bed temperature: 400 ^oC. The HTlc sample was activated in 100% N_2 at 500 ^oC for 4 hrs.

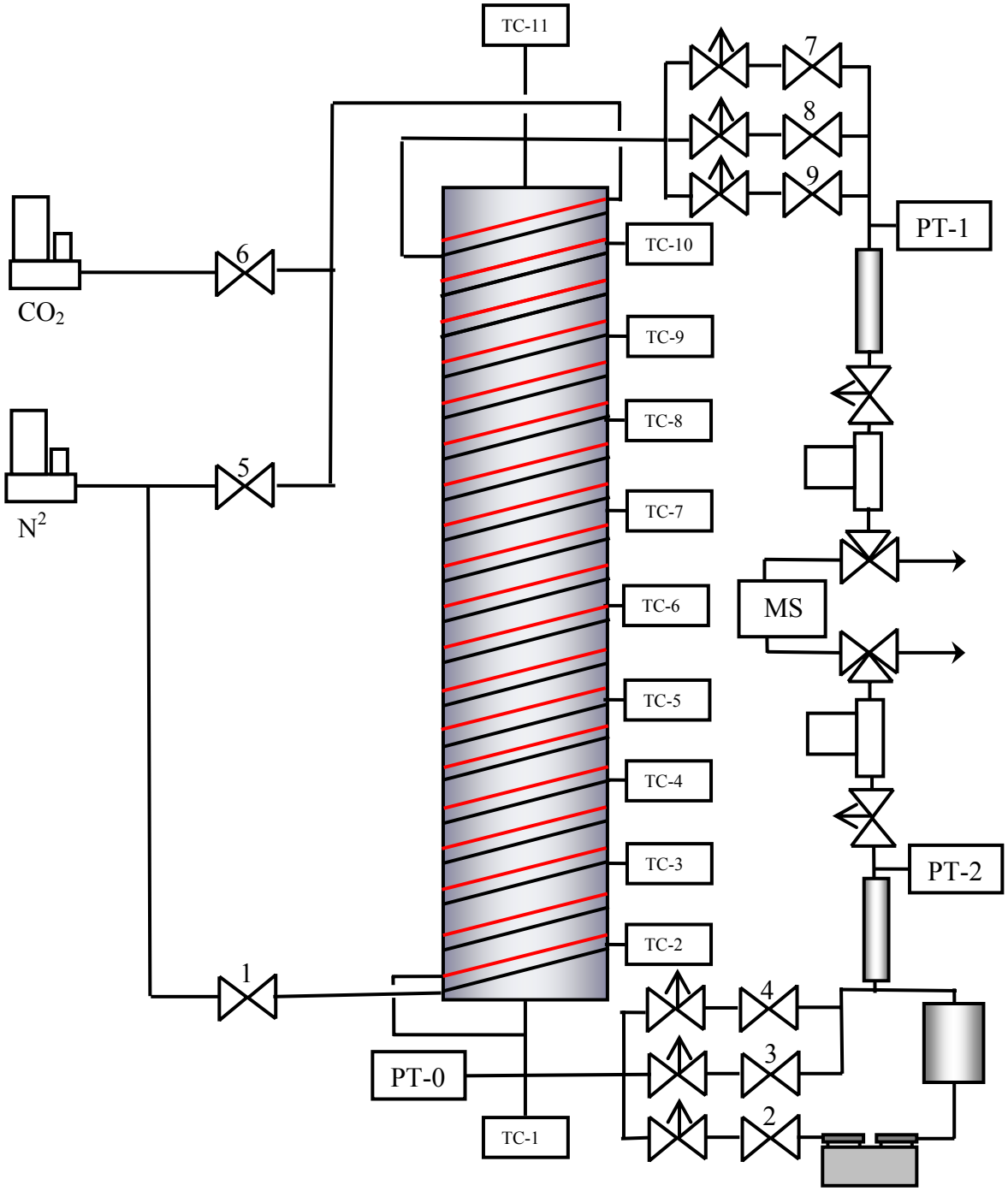

Figure 58. Schematic of a single bed fixed-bed unit designed to mimic all the steps of a complex multi-bed PSA cycle in a single bed.

7.4 Conclusions

Larger scale fixed bed adsorption experiments verified the extensive TGA cycling results. They showed complete reversibility of CO_2 at conditions of around 1 atm and 400 ^oC. The also

showed slower desorption kinetics than adsorption kinetics. These results were consistent with other smaller scale experiments.

8.0 Nomenclature

A_{cs}	bed cross section area, m^2
A_i	gas/adsorbed phase heat capacity parameter (kJ/mol/K)
A	reaction site for weakly chemisorbed CO_2 in a K-promoted HTlc.
B	reaction site for a single molecule of chemically bound CO_2 in a K-promoted HTlc, i.e., $Mg_6Al_2K_2O_9(CO_3)$.
B_i	gas/adsorbed phase heat capacity parameter ($kJ/mol/K^2$)
B_i^o	adsorption isotherm parameter (K)
b_i	adsorption isotherm parameter (kPa^{-1})
b_i^o	adsorption isotherm parameter (kPa^{-1})
C	reaction site for two molecules of chemically bound CO_2 in K-promoted HTlc, i.e., $Mg_6Al_2K_2O_8(CO_3)_2$.
C_i	gas/adsorbed phase heat capacity parameter ($kJ/mol/K^3$)
$C_{P,a,i}$	gas phase heat capacity of component i (kJ/mol/K)
$C_{P,g}$	gas phase heat capacity of the mixture (kJ/mol/K)
$C_{P,g,i}$	gas phase heat capacity of component i (kJ/mol/K)
$C_{P,p}$	heat capacity of the adsorbent particle (kJ/mol/K)
d_b	diameter of the bed (m)
D_i	gas/adsorbed phase heat capacity parameter ($kJ/mol/K^4$)
E	reaction site free of CO_2 in a K-promoted HTlc, i.e., $Mg_6Al_2K_2O_{10}$.
h	overall heat transfer coefficient ($kW/m^2/K$)
ΔH_i	isosteric heat of adsorption of component i (kJ/mol)
ΔH_i	isosteric heat of adsorption of component i (kJ/mol)
I	reaction site for two molecules of chemically bound CO_2 prior to dehydration and dehydroxylation, i.e., $[Mg_3Al(OH)_8](CO_3)\bullet K_2CO_3 \cdot nH_2O$
$k_{1,f}$	forward rate constant for the reaction C $\leftrightarrow$ A+B (min^{-1})
$k_{1,b}$	backward rate constant for the reaction C $\leftrightarrow$ A+B (kg/mol/min)
$k_{2,f}$	forward rate constant for the reaction B $\leftrightarrow$ A+E (min^{-1})
$k_{2,b}$	backward rate constant for the reaction B $\leftrightarrow$ A+E (kg/mol/min)
$k_{m,a}$	mass transfer coefficient for adsorption of CO_2 from the gas phase into phase A (min^{-1})
$k_{m,d}$	mass transfer coefficient for desorption of CO_2 from phase A into the gas phase (min^{-1})
k	Henry's law constant for species i, m^3 gas phase m^{-3} adsorbent
k_a	adsorption mass transfer coefficient of CO_2 (s^{-1})
k_d	desorption mass transfer coefficient of CO_2 (s^{-1})
k_i	mass transfer coefficient of component i (s^{-1})
L	length of the bed (m)
M_i	molecular weight of component i (kg/mol)
N_{total}	total number of reaction sites available for chemically bound CO_2 (mol of sites/kg of CO_2-free K-promoted HTlc).
n_i	concentration of species i in the adsorbed phase mol m^{-3} adsorbent

$N_{F(in)}$ total mass of adsorbates entering the bed during feed step, mol

$N_{F(out)}$ total mass of adsorbates leaving the bed during feed step, mol

$N_{HR(in)}$ total mass of adsorbates entering the bed during heavy reflux step, mol

$N_{HR(out)}$ total mass of adsorbates leaving the bed during heavy reflux step, mol

N_{CnD} total mass of adsorbates leaving the bed during blowdown step, mol

$N_{purge(in)}$ total mass of adsorbates entering the bed during light reflux step, mol

$N_{purge(out)}$ total mass of adsorbates leaving the bed during light reflux step, mol

$N_{P(out)}$ total mass of adsorbates leaving the bed during light reflux step with varying inlet feed concentration in the light reflux bed, mol

$N_{purge(A)}$ total mass of heavy component leaving the bed during light reflux step, mol

N_{press} total mass of adsorbates entering the bed during pressurization, mol

P total pressure, kg m^{-1} s^{-2}

P_i partial pressure of species i, kg m^{-1} s^{-2}

P_f final pressure (kPa)

P_H high pressure (kPa)

P_L low pressure (kPa)

Q flow rate (L STP/min)

Q_f flow rate of the feed (L STP/min)

q CO_2 loading relative to q_o (mol CO_2/kg of CO_2-free K-promoted HTlc).

q_i loading of component i (mol/kg)

q_i^* equilibrium loading of component i (mol/kg)

q_i^s adsorption isotherm parameter (mol/kg)

$q_{i,1}^s$ adsorption isotherm parameter (mol/kg/K)

$q_{i,2}^s$ adsorption isotherm parameter (mol/kg)

$q_{A,e}$ concentration of site A at equilibrium (mol of sites/kg of CO_2-free K-promoted HTlc)

$q_{A,e,a}$ concentration of site A at equilibrium during adsorption (mol of sites/kg of CO_2-free K-promoted HTlc)

$q_{A,e,d}$ concentration of site A at equilibrium during desorption (mol of sites/kg of CO_2-free K-promoted HTlc)

q_{CO2} CO_2 loading relative to q_o (mol CO_2/kg of CO_2-free K-promoted HTlc).

q_o CO_2 loading after activation (mol CO_2/kg of CO_2-free K-promoted HTlc).

q_T total number of reaction sites available for chemically bound CO_2 (mol of sites/kg of CO_2-free K-promoted HTlc).

q_X concentration of site X, with X = A, B, C or E (mol of sites/kg of CO_2-free K-promoted HTlc).

$q_{X,o}$ concentration of site X after activation, with X = A, B, C or E (mol of sites/kg of CO_2-free K-promoted HTlc).

r_b radius of the bed (m)

R ideal gas constant, 8.314 J mol^{-1} K^{-1}

R_R heavy product recycle ratio

t_1^* dimensionless time taken for breakthrough during heavy reflux

t_2^* dimensionless time taken for breakthrough during light reflux

T	temperature (K)
T_F	temperature of the feed (K)
T_w	temperature of the wall (K)
T	time (s)
t_c	total cycle time (s)
t_s	cycle step time (s)
t_{act}	activation time (h)
u	interstitial velocity, m sec^{-1}
u_F	interstitial velocity at the inlet of the feed bed, m sec^{-1}
$u_{F(out)}$	interstitial velocity at the exit of the feed bed, m sec^{-1}
u_R	interstitial velocity at the inlet of the heavy reflux bed, m sec^{-1}
u_{CnD}	interstitial velocity at the exit of the blowdown bed, m sec^{-1}
u_1	interstitial velocity at the exit of the heavy reflux bed during no breakthrough, m sec^{-1}
u_2	interstitial velocity at the exit of the heavy reflux bed during breakthrough, m sec^{-1}
u_{press}	interstitial velocity at the inlet of the pressurization bed, m sec^{-1}
$u_{purge(in)}$	interstitial velocity at the inlet of the light reflux bed, m sec^{-1}
$u_{purge(out)}$	interstitial velocity at the exit of the light reflux bed, m sec^{-1}
x	experimental mass obtained from the TGA (g).
x	position of the feed concentration wave at end of feed step, m
x_o	experimental mass obtained from the TGA just after activation (g).
[X]	concentration of site X, with X = A, B, C or E (mol of sites/kg of CO_2-free K-promoted HTlc)
$[X]_o$	concentration of site X after activation, with X = A, B, C or E (mol of sites/kg of CO_2-free K-promoted HTlc)
y_i	gas phase mole fraction of component i
y_F	gas phase mole fraction of the heavy component in feed
$y_{CO2,HP}$	average gas phase mole fraction of CO_2 in the heavy product
$\overline{y_P}$	gas phase mole fraction of the heavy component leaving the light reflux bed
z	axial coordinate in the column, m

8.1 Greek Letters

α	fractional bed length not occupied by the concentration wave at end of feed step
ε	bed porosity, m^3 gas phase m^{-3} bed
γ	light product purge to feed ratio
χ	porosity of the adsorbent particle
ψ	fraction of the bed length covered by concentration y = 1
ϕ	total mass of adsorbate in the bed saturated with heavy component at the end of blowdown, mol
φ	fraction of χ occupied by the adsorbed phase
Ω_i	recovery of the species i

Ξ_i	purity of species i
π	high-to-low pressure ratio
$\Delta\tau$	dimensionless time
Δt	step time, sec
θ	feed throughput (L STP/hr/kg)
ε_b	porosity of the bed
ρ_p	density of the particle (kg/m^3)
$\rho_{a,i}$	adsorbed phase density of component i (kg/m^3)
γ	light product purge to feed ratio
π_T	high to low pressure ratio
θ	feed throughput (L STP/hr/kg)

8.2 Subscripts

A	heavy component
B	heavy component
CnD	countercurrent depressurization step
CoD	cocurrent depressurization step
f	feed
F	feed step
F+R	feed plus recycle step
HR	heavy reflux step
i	component i (i = CO_2, H_2O or N_2)
LPP	light product pressurization step
LR	light reflux step
REC	recovery step
y	mole fraction

8.3 Acronyms

CnD	countercurrent depressurization step
CoD	cocurrent depressurization step
E	enrichment of the heavy product
F	feed step
F+R	feed plus recycle step
HR	heavy reflux step
HP	heavy product
HTlc	hydrotalcite-like compound
LP	light product
LPP	light product pressurization step
LR	light reflux step
PSA	pressure swing adsorption
R	recovery of the heavy product
REC	recovery step
TSA	temperature swing adsorption

9.0 References

Cassidy, R. T., and E. S. Holmes, Twenty-Five Years of Progress in Adiabatic Adsorption Processes. *AIChE Symp. Ser.*, 80(233), 68, 1984.

Chiang, A. S. T., Arithmetic of PSA process scheduling. *AIChE J*., 34, 1910-1912, 1988.

Chou, C.T.; Chen, C.Y. Carbon Dioxide Recovery by Vacuum Swing Adsorption. *Separ. Purif. Technol.*, *39*, 51-65, 2004.

Choi, W.-K.; Kwon, T.-I.; Yeo, Y.-K.; Lee, H.; Song, H.-K.; Na, B.-K. Optimal Operation of the Pressure Swing Adsorption (PSA) Process for CO_2 Recovery. *Korean J. Chem. Eng.*, 20, 617-623, 2003.

Chue, K.T., J.N. Kim, Y.J. Yoo, S.H. Cho, and R.T. Yang, "Comparison of Activated Carbon and Zeolite 13X for CO_2 Recovery from Flue Gas by Pressure Swing Adsorption," *Ind. Eng. Chem. Res.*, 34, 591-598, 1995.

Ding, Y.; Alpay, E. Adsorption-Enhanced Steam-Methane Reforming. *Chem. Eng. Sci.*, *55*, 3929-3940, 2000.

Ding, Y. and E. Alpay, "Equilibria and Kinetics of CO_2 Adsorption on Hydrotalcite Adsorbent," *Chem. Eng. Sci.*, 55, 3461-3474, 2000.

Ding, Y. and E. Alpay, "High Temperature Recovery of CO_2 from Flue Gases Using Hydrotalcite Adsorbent," *Trans IChemE*, 79, 45-51, 2001.

Dinsmore, H. L.; Young, Jr., J. W., Process and Apparatus for Removing Hydrocarbons from Air-Hydrocarbon Vapor Mixtures. U. S. Patent 4,462,811, 1984.

Ebner, A.D.; Ritter, J.A. Equilibrium Theory Analysis of Rectifying PSA for Heavy Component Production. *AIChE J.*, *48*, 1679-1691, 2002.

Ebner, A.D., S.P. Reynolds, and J.A. Ritter, "Understanding the Adsorption and Desorption Behavior of CO_2 on a K-Promoted HTlc through Non-Equilibrium Dynamic Isotherms," *Ind. Eng. Chem. Res.*, 45, 6387-6392, 2006.

Ebner, A. D. and J. A. Ritter, "State-of-the-Art Adsorption and Membrane Separation Processes for Carbon Dioxide Production in the Chemical and Petrochemical Industries," *Adsorption*, submitted, 2007.

Ebner, A.D., S.P. Reynolds, and J.A. Ritter, "Non-Equilibrium Kinetic Model that Describes the Reversible Adsorption and Desorption Behavior of CO_2 in a K-Promoted Hydrotalcite-like Compound," *Ind. Eng. Chem. Res.*, 46, 1737-1744, 2007.

Fuderer, A.; Rudelstorfer, E.; Selective Adsorption Process. U. S. Patent 3,986,849, 1976.

Gomes, V.G. and K.W.K. Yee, "Pressure Swing Adsorption for Carbon Dioxide Sequestration from Exhaust Gases," *Separ. Purif. Technol.*, 28, 161-171, 2002.

Hufton, J. R., S. Mayorga, and S. Sicar, "Sorption-Enhanced Reaction Process for Hydrogen Production," *AIChE J.*, 45, 248-256, 1999.

Hufton, J. R.; Allam, R. J.; Chiang, R.; Middleton, P.; Weist, E. L.; White V. Development of a Process for CO_2 Capture Gas Turbines using a Sorption Enhamced Water Gas Shift Reactor System. Presented at the *7th International Conference on Green House Control Technologies*. Vancouver Canada, 2004.

Hutson N. D.; Speakman S. A.; Payzant E. A. Structural Effects on the High Temperature Adsorption of CO_2 on a Synthetic Hydrotalcite. *Chem. Mater.*, *16*, 4135-4143, 2004.

International Energy Agency, "Carbon Dioxide Capture from Power Stations," www.ieagreen.org.uk/sr2p.htm, 1994.

Kikkinides, E.S., R.T. Yang, and S.H. Cho, "Concentration and Recovery of CO_2 from Flue Gas

by Pressure Swing Adsorption," *Ind. Eng. Chem. Res.*, 32, 2714-2720, 1993.
Knaebel, K. S., and F. B. Hill, "Pressure Swing Adsorption: Development of an Equilibrium Theory," Chem. Eng. Sci.. 40, 2351, 1985.
Ko, D., R. Siriwardane, and L.T. Biegler, "Optimization of a Pressure-Swing Adsorption Process Using Zeolite 13X for CO_2 Sequestration," *Ind. Eng. Chem. Res.*, 42, 339-348, 2003.
Ko, D.; Siriwardane, R.; Biegler, L.T. Optimization of Pressure Swing Adsorption and Fractionated Vacuum Pressure Swing Adsorption Processes for CO_2 Capture. *Ind. Eng. Chem. Res.*, 44, 8084-8094, 2005.
Liu, Y.; Ritter, J.A. Pressure Swing Adsorption-Solvent Vapor Recovery: Process Dynamics and Parametric Study. *Ind. Eng. Chem. Res.*, *35*, 2299-2312, 1996.
Liu, Y., C.E. Holland, J.A. Ritter, "Solvent Vapor Recovery by Pressure Swing Adsorption. I. Experimental Study on the Transient and Periodic Dynamics of the Butane-Activated Carbon System," *Sep. Sci. Technol.*, 33, 2311-2334, 1998.
Liu, Y., C.E. Holland, J.A. Ritter, "Solvent Vapor Recovery by Pressure Swing Adsorption. III. Comparison of Simulation with Experiment for the Butane-Activated Carbon System," *Sep. Sci. Technol.*, 34, 1545-1576, 1999.
Matz, M. J. and Knaebel, K. S., "PSA: effects of incomplete purge". *A.I.Ch.E J., 34,* 1486 - 1492., 1988.
Mehrotra A., S.P. Reynolds, A.D. Ebner, and J.A. Ritter, "Heavy Reflux PSA Cycles for CO_2 Recovery from Flue Gas: Part II. Interpretation of Trends," *Ind. Eng. Chem. Res.*, submitted., 2007.
Moreira, R. F. P. M.; Soares, J. L.; Casarin G. L.; Rodrigues, A. E. Adsorption of CO_2 on Hydrotalcite-Like Compounds in a Fixed Bed. *Sep. Sci. Technol.*, *41*, 341-357, 2006.
Nataraj, S. et al. Process for Operating Equilibrium Controlled Reactions. Canadian Patent 2,235,928., 1998.
Na, B.-K.; Koo, K.-K.; Eum, H.-M.; Lee, H.; Song, H.-K. CO_2 Recovery from Flue Gas by PSA Process using Activated Carbon. *Korean J. Chem. Eng.*, 18, 220-227, 2001.
Na, B.-K.; Lee, H.; Koo, K.-K.; Song, H.K. Effect of Rinse and Recycle Methods on the Pressure Swing Adsorption Process to Recover CO_2 from Power Plant Flue Gas Using Activated Carbon. *Ind. Eng. Chem. Res.*, , *41*, 5498-5503., 2002.
Park, J.-H.; Beum, H.-T.; Kin, J.-N. ; Cho, S.-H. Numerical Analysis on the Power Consumption of the PSA Process for Recovering CO_2 from Flue Gas. *Ind. Eng. Chem. Res.*, 41, 4122-4131, 2002.
Reichle, D. et al., "Carbon Sequestration Research and Development", U.S. DOE.,1999.
Reynolds, S.P., A.D. Ebner, and J.A. Ritter, "New Pressure Swing Adsorption Cycles for Carbon Dioxide Sequestration," *Adsorption.* 11, 531-536, 2005.
Reynolds, S.P., A.D. Ebner, and J.A. Ritter, "Stripping PSA Cycles for CO_2 Recovery from Flue Gas at High Temperature Using a Hydrotalcite-Like Adsorbent," *Ind. Eng. Chem. Res.*, 45, 4278-4294, 2006a.
Reynolds, S.P., A.D. Ebner, and J.A. Ritter, "Carbon Dioxide Capture from Flue Gas by PSA at High Temperature using a K-Promoted HTlc: Effects of Mass Transfer on the Process Performance," *Env. Prog.* 25, 334-342, 2006b.
Reynolds, S.P.; Mehrotra, A.; Ebner, A.D.; Ritter, J.A., Heavy reflux PSA Cycles for CO_2 Recovery from Flue Gas: Part I. Performance evaluation. *Adsorption.*, 14, 399-413, 2008.
Ritter, J. A., and R. T. Yang, ''Equilibrium Adsorption of Multicomponent Gas-Mixtures at Elevated Pressures,'' *Ind. Eng. Chem. Res.*, 26, 1679., 1987.

Rousar, I. and Ditl, P., "Pressure swing adsorption analytical solution for optimum purge" *Chem. Engng Sci.* 48, 723-734, 1993.

Ruthven, D.M., S. Farooq, and K.S. Knaebel, Pressure Swing Adsorption, VCH Publishers, Inc., New York, 1994.

Shendalman, L. H. and Mitchell, J. E., "A study of heatless adsorption in the model system CO_2 in He-I." *Chem. Engng Sci.* 27, 1449-1458, 1972.

Skarstrom, C. W., Method and Apparatus for Fractionating Gaseous Mixtures by Adsorption. U. S. Patent 3,082,166, 1960.

Smith, O. J. IV; Westerberg, A. W., Mixed-Integer Programming for Pressure Swing Adsorption Cycle Scheduling. *Chem. Eng Sci.*, 45, 2833-2842, 1990.

Suzuki, T.; Sakoda, A.; Suzuki, M.; Izumi, J. Recovery of Carbon Dioxide from Stack Gas by Piston-Driven Ultra-Rapid PSA. *J. Chem. Eng. Japan*, *30*, 1026-1033, 1997.

Soares, J. L.; Grande, C. A.; Yong, Z; Moreira, R. F. P. M.; Rodrigues, A. E. Adsorption of Carbon Dioxide at High Temperatures onto Hydrotalcite-Like Compounds (HTlcs). *Fundamentals of Adsorption 7*. Eds. Kaneko, K.; Kanoh, H.; Hanzawa, Y. IK International, Ltd.: Chibu-City, Japan, 763-770, 2002.

Soares, J.L., R.F.P.M. Moreira, H.J. Jose, C.A. Grande, and A.E. Rodrigues, "Hydrotalcite Materials for Carbon Dioxide Adsorption at High Temperatures: Characterization and Diffusivity Measurements," *Sep. Sci. Technol.*, 39, 1989-2010, 2004.

Soares, J. L., Moreira, R. F. P .M., Jose, H. J., Grande, C. A., Rodrigues, A. E. Hydrotalcite Materials for Carbon Dioxide Adsorption at High Temperatures: Characterization and Diffusivity Measurements. Sep. Sci. Technol., 39, 1989-2010, 2004.

Subramanian, D.; Ritter, J.A. Equilibrium Theory for Solvent Vapor Recovery by Pressure Swing Adsorption: Analytical Solution for Process Performance. *Chem. Eng. Sci.*, *52*, 3147-3160, 1997.

Takamura, Y.; Narita, S.; Aoki, J.; Hironaka, S.; Uchida, S. Evaluation of Dual-Bed Pressure Swing Adsorption for CO_2 Recovery from Boiler Exhaust Gas. *Separ. Purif. Technol. 24*, 519-528, 2001.

White C.M., B. R. Strazisar, E. J. Granite, J. S. Hoffman, and H. W. Pennline, "Separation and capture of CO_2 from large stationary sources and sequestration in geological formations - Coalbeds and deep saline," J.Air & Waste Management Association, 53, 645-715, 2003.

Xu, J.; Weist, L. E. Jr., Six Bed Pressure Swing Adsorption Process with Four Steps of Pressure Equalization. U. S. Patent 6,454,838, 2002.

Yong, Z., V. Mata, A.E. Rodrigues, "Adsorption of Carbon Dioxide on Basic Alumina at High Temperatures," *J. Chem. Eng. Data*, 45, 1093-1095, 2000.

Yong, Z; Mata V.; Rodrigues, A. E. Adsorption of Carbon Dioxide onto Hydrotalcite-Like Compounds (HTlcs) at High Temperature. *Ind. Eng. Chem. Res.*, *40*, 204-209, 2001.

Yong, Z.; Rodrigues, A. E. Hydrotalcite-Like Compounds as Adsorbents for Carbon Dioxide. *Energy Convers. Mgmt.*, *43*, 1865-1876, 2002.

Yong, Z., V. Mata, A.E. Rodrigues, "Adsorption of Carbon Dioxide at High Temperature – A Review," *Separ. Purif. Technol.*, 26, 195-205, 2002.

Yoshida, M.; Ritter, J.A.; Kodama, A.; Goto, M.; Hirose, T. Enriching Reflux and Parallel Equalization PSA Process for Concentrating Trace Components in Air. *Ind. Eng. Chem. Res.*, *42*, 1795-1803, 2003.